

STRUCTURAL, ELECTRONIC, AND OPTICAL PROPERTIES OF FUNCTIONAL METAL OXIDES

GUEST EDITORS: JIANHUA HAO, NIAN X. SUN, JIANRONG QIU, AND DANYANG WANG





Structural, Electronic, and Optical Properties of Functional Metal Oxides

Advances in Condensed Matter Physics

Structural, Electronic, and Optical Properties of Functional Metal Oxides

Guest Editors: Jianhua Hao, Nian X. Sun, Jianrong Qiu,
and Danyang Wang



Copyright © 2014 Hindawi Publishing Corporation. All rights reserved.

This is a special issue published in “Advances in Condensed Matter Physics.” All articles are open access articles distributed under the Creative Commons Attribution License, which permits unrestricted use, distribution, and reproduction in any medium, provided the original work is properly cited.

Editorial Board

A. S. Alexandrov, UK
Dario Alfe, UK
Bohdan Andraka, USA
Daniel Arovas, USA
V. Awana, India
Arun Bansil, USA
Ward Beyersmann, USA
G. M. Bhuiyan, Bangladesh
Luis L. Bonilla, Spain
Mark Bowick, USA
Gang Cao, USA
Ashok Chatterjee, India
Ram N. P. Choudhary, India
Kim Chow, Canada
Oleg Derzhko, Ukraine
Gayanath Fernando, USA
J. Fink, Germany
Yuri Galperin, Norway

Russell Giannetta, USA
Gabriele F. Giuliani, USA
James L. Gole, USA
P. Guptasarma, USA
Da-Ren Hang, Taiwan
M. Zahid Hasan, USA
Yurij Holovatch, Ukraine
Chia-Ren Hu, USA
David Huber, USA
Nigel E. Hussey, UK
Philippe Jacquod, USA
Jan A. Jung, Canada
Feo V. Kusmartsev, UK
Rosa Lukaszew, USA
Dmitrii Maslov, USA
Y. N. Mohapatra, India
A. Mookerjee, India
V. V. Moshchalkov, Belgium

Charles Myles, USA
V. A. Osipov, Russia
Rolfe Petschek, USA
Joseph S. Poon, USA
Ruslan Prozorov, USA
Leonid Pryadko, USA
C. Rosenblatt, USA
Mohindar S. Seehra, USA
S. Sergeenkov, Brazil
Ivan Smalyukh, USA
Daniel L. Stein, USA
Michael C. Tringides, USA
Sergio E. Ulloa, USA
A. Virosztek, Hungary
M. R. Wagner, Germany
Gary Wysin, USA
Gongnan Xie, China
Fajun Zhang, Germany

Contents

Structural, Electronic, and Optical Properties of Functional Metal Oxides, Jianhua Hao, Nian X. Sun, Jianrong Qiu, and Danyang Wang
Volume 2014, Article ID 134951, 2 pages

Progress in ZnO Acceptor Doping: What Is the Best Strategy?, Judith G. Reynolds and C. Lewis Reynolds
Volume 2014, Article ID 457058, 15 pages

Synthesis and Dielectric Studies of Monoclinic Nanosized Zirconia, I. Flavia Princess Nesamani, V. Lakshmi Prabha, Aswathy Paul, and D. Nirmal
Volume 2014, Article ID 828492, 7 pages

Synthesis, Tunable Multicolor Output, and High Pure Red Upconversion Emission of Lanthanide-Doped Lu_2O_3 Nanosheets, Lingzhen Yin, Tianmei Zeng, Zhigao Yi, Chao Qian, and Hongrong Liu
Volume 2013, Article ID 920369, 6 pages

Temperature Dependence of Electrical Properties and Crystal Structure of $0.29\text{Pb}(\text{In}_{1/2}\text{Nb}_{1/2})\text{O}_3 \cdot 0.44\text{Pb}(\text{Mg}_{1/3}\text{Nb}_{2/3})\text{O}_3 \cdot 0.27\text{PbTiO}_3$ Single Crystals, Qian Li, Yun Liu, Andrew Studer, Zhenrong Li, Ray Withers, and Zhuo Xu
Volume 2013, Article ID 382140, 5 pages

A Facile Synthesis and Optical Properties of Bundle-Shaped $\text{TbPO}_4 \cdot \text{H}_2\text{O}$ Nanorods, Dan Yue, Wen Luo, Wei Lu, Ruiyong Wang, Chunyang Li, Jiazhong Chang, and Zhenling Wang
Volume 2013, Article ID 673945, 5 pages

Synthesis and Downconversion Emission Property of $\text{Yb}_2\text{O}_3 \cdot \text{Eu}^{3+}$ Nanosheets and Nanotubes, Chao Qian, Tianmei Zeng, and Hongrong Liu
Volume 2013, Article ID 519869, 5 pages

Structural Disorder in the Key Lead-Free Piezoelectric Materials, $\text{K}_x\text{Na}_{1-x}\text{NbO}_3$ and $(1-x)\text{Na}_{0.5}\text{Bi}_{0.5}\text{TiO}_3 + x\text{BaTiO}_3$, Jason Schiemer, Ray Withers, Yun Liu, Yiping Guo, Zhiguo Yi, and Jian Wang
Volume 2013, Article ID 296419, 5 pages

The Influence of Surface Morphology of Buffer Layer on the Critical Current Density in YBCO Coated Conductors, Jie Xiong, Yudong Xia, Fei Zhang, Yan Xue, Kai Hu, Xiaohui Zhao, and Bowan Tao
Volume 2013, Article ID 673948, 6 pages

Decomposition and Oriented Growth of $\text{YBa}_2\text{Cu}_3\text{O}_{7-x}$ Films Prepared with Low Fluorine TFA-MOD Approach, Xiaohui Zhao, Pan Zhang, Yabing Wang, Jie Xiong, and Bowan Tao
Volume 2013, Article ID 532181, 5 pages

Hydrothermal Synthesis and Tunable Multicolor Upconversion Emission of Cubic Phase Y_2O_3 Nanoparticles, Haibo Wang, Chao Qian, Zhigao Yi, Ling Rao, Hongrong Liu, and Songjun Zeng
Volume 2013, Article ID 347406, 6 pages

Intense Red Upconversion Emission and Shape Controlled Synthesis of $\text{Gd}_2\text{O}_3 \cdot \text{Yb}/\text{Er}$ Nanocrystals, Zhigao Yi, Boyun Wen, Chao Qian, Haibo Wang, Ling Rao, Hongrong Liu, and Songjun Zeng
Volume 2013, Article ID 509374, 5 pages

Phase Transition and Optical Properties for Ultrathin KNbO_3 Nanowires, Shulin Yang, Yongming Hu, Shengfu Wang, Haoshuang Gu, and Yu Wang
Volume 2013, Article ID 567420, 5 pages

Simulation and Analysis of GaN Wafer Bowing on Sapphire Substrate, Wang Bin, Qu Yu-xuan, Hu Shi-gang, Tang Zhi-jun, Li Jin, and Hu Ying-lu
Volume 2013, Article ID 465498, 5 pages

Effect of Annealing Temperature on the Morphology and Piezoresponse Characterisation of Poly(vinylidene fluoride-trifluoroethylene) Films via Scanning Probe Microscopy, K. Lau, Y. Liu,

H. Chen, and R. L. Withers

Volume 2013, Article ID 435938, 5 pages

Phase Relations in $\text{Ba}_{6-3x}\text{Ln}_{8+2x}\text{Ti}_{18}\text{O}_{54}$ (Ln = Nd & Sm) Electroceramics, Amanda L. Snashall, Yun Liu, Frank Brink, Ray L. Withers, and Steven Cooper

Volume 2013, Article ID 373079, 7 pages

Effect of Electric Field and Temperature on Average Structure and Domain Wall Motion in $0.93\text{Bi}_{0.5}\text{Na}_{0.5}\text{TiO}_3$ - 0.07BaTiO_3 Ceramic, Jian Wang, Yun Liu, Andrew Studer, Lasse Norén, and Ray Withers

Volume 2013, Article ID 830971, 4 pages

Editorial

Structural, Electronic, and Optical Properties of Functional Metal Oxides

Jianhua Hao,¹ Nian X. Sun,² Jianrong Qiu,³ and Danyang Wang⁴

¹ Department of Applied Physics, The Hong Kong Polytechnic University, Hong Kong

² Electrical and Computer Engineering Department, Northeastern University, Boston, MA, USA

³ State Key Laboratory of Luminescent Materials and Devices, South China University of Technology, Guangzhou, China

⁴ School of Materials Science and Engineering, The University of New South Wales, Sydney, NSW, Australia

Correspondence should be addressed to Jianhua Hao; jh.hao@polyu.edu.hk

Received 21 July 2014; Accepted 21 July 2014; Published 31 August 2014

Copyright © 2014 Jianhua Hao et al. This is an open access article distributed under the Creative Commons Attribution License, which permits unrestricted use, distribution, and reproduction in any medium, provided the original work is properly cited.

In the past few decades, metal-oxides have drawn considerable attention and have been applied in diverse fields of applications because of their full spectrum of various behaviors, such as dielectrics, ferroelectricity, magnetism, superconductivity, optical spectroscopy, and light emission. The research interest in functional metal oxides is reflected by the rapid growth of publications in this field. Many metal-oxide materials are usually wideband gap compounds. The conductivity of oxides can vary from insulator to semiconductor to conductor. Due to their varied electronic and optical properties, metal oxides have been used for a wide variety of applications, such as smart sensor, data storage, energy, catalysis, and optical and display devices. The key to these device applications is an improved understanding of fundamental structural, electronic, dielectric, optical, and luminescent properties. In this special issue, we have invited authors to submit original research and review articles that will stimulate the continuing efforts to investigate the basic physical properties.

One of the papers of this special issue investigates lanthanide codoped oxide Y_2O_3 with body-centered cubic structure. The oxide nanoparticles exhibit strong red and light yellow upconversion emissions. It is expected that these oxide materials with tunable multicolor output and intense red upconversion emission may have potential application in color displays and biolabels. Other papers present the studies on the typical oxide superconductors of $YBa_2Cu_3O_{7-x}$ (YBCO). The effects of the sintering temperature on the microstructure and oriented growth of the YBCO film are

discussed. The impact of the surface morphologies of buffer layers on the superconducting properties in YBCO films is investigated. Another paper of this special issue presents nice work on the synthesis of $KNbO_3$ nanowires with perovskite structures by hydrothermal treatment at low temperature. The phase transition and photoluminescence (PL) properties of $KNbO_3$ nanowires are investigated. The studies completed by the researchers in China show that the $KNbO_3$ nanowires may be a promising candidate for fabricating ferroelectric and piezoelectric nanodevices.

One paper has examined the local structure and disorder in promising lead-free piezoelectric ceramic systems of NBT-BT and KNN. The studies reported by the Australian National University and University of Cambridge may supply information about the origins of high electrostrictive response and antiferroelectric behavior. Another paper reports the synthesis and characterization of nanocrystallite monoclinic zirconia powder. This work performed by the researchers in India will be useful in the applications of high- κ gate dielectric materials. Other papers report the synthesis and luminescent characteristics of various types of rare-earth doped oxide-based nanomaterials. These reported materials have potential applications in many fields such as lighting and optoelectronic devices with nanometer dimensions.

Another paper is a review article written by J. G. Reynolds and C. L. Reynolds in North Carolina State University. This review summarizes recent reports on the p-type behavior of ZnO for the various potential doping schemes. It is suggested that an understanding of the reaction pathways and specific

model to explain the acceptor level is the key to stable and reproducible p-type ZnO. Some papers have focused on the fabrication, crystal structural, and electrical properties of several kinds of dielectric ceramics based on oxides. One paper performs the simulation and analysis of GaN wafer bowing on sapphire substrate. The bowing deformation of the wafer on sapphire substrate is studied using finite element analysis software. Another paper reports on the nanoscale characterization of the morphology, polarization switching, and local piezoresponse hysteresis loops for ferroelectric PVDF-TrFE film.

We hope that the publication of this special issue will be of reference value for readers to understand the current status and future research direction in the research field on metal oxides materials and devices.

*Jianhua Hao
Nian X. Sun
Jianrong Qiu
Danyang Wang*

Review Article

Progress in ZnO Acceptor Doping: What Is the Best Strategy?

Judith G. Reynolds¹ and C. Lewis Reynolds²

¹ Department of Physics, North Carolina State University, Raleigh, NC 27695, USA

² Department of Materials Science and Engineering, North Carolina State University, Raleigh, NC 27695, USA

Correspondence should be addressed to C. Lewis Reynolds; lew_reynolds@ncsu.edu

Received 13 November 2013; Revised 23 April 2014; Accepted 23 April 2014; Published 22 May 2014

Academic Editor: Jianrong Qiu

Copyright © 2014 J. G. Reynolds and C. L. Reynolds. This is an open access article distributed under the Creative Commons Attribution License, which permits unrestricted use, distribution, and reproduction in any medium, provided the original work is properly cited.

This paper reviews the recent progress in acceptor doping of ZnO that has been achieved with a focus toward the optimum strategy. There are three main approaches for generating p-type ZnO: substitutional group IA elements on a zinc site, codoping of donors and acceptors, and substitution of group VA elements on an oxygen site. The relevant issues are whether there is sufficient incorporation of the appropriate dopant impurity species, does it reside on the appropriate lattice site, and lastly whether the acceptor ionization energy is sufficiently small to enable significant p-type conduction at room temperature. The potential of nitrogen doping and formation of the appropriate acceptor complexes is highlighted although theoretical calculations predict that nitrogen on an oxygen site is a deep acceptor. We show that an understanding of the growth and annealing steps to achieve the relevant acceptor defect complexes is crucial to meet requirements.

1. Introduction

Although zinc oxide has been investigated for many years, its potential for photonic and electronic applications has led to significant resurgence in interest during the last decade. Its use as a widely diverse functional material is enhanced by the fact that it can be grown in bulk, thin film, and nanostructures, examples of the latter being nanowires, nanobelts, and other morphologies that are dependent upon growth conditions. Although bulk substrates are readily available, ZnO thin films can also be grown heteroepitaxially across the misfit scale via the paradigm of domain matching epitaxy [1, 2]. This is relevant for fabrication of next generation devices in which multiple functionalities are integrated on a given substrate. Potential applications of ZnO are blue/UV LEDs and lasers, photodetectors, transparent thin film transistors, transparent conducting oxides, gas sensors, and nanostructured piezoelectric nanogenerators, and substantial markets have been predicted. Many of the potential device applications, however, require both donor and acceptor doping, and growth of reproducible and stable p-type ZnO has been difficult to achieve. This doping asymmetry problem in which n-type doping is easily achieved while p-type is quite problematic is well known [3], and

thus widespread development of ZnO-based devices has been inhibited. For this special issue on structural, electronic, and optical properties of functional metal oxides, we do not intend to provide an exhaustive review of ZnO materials and devices as many review articles [3–9] have already been published but instead to focus on recent progress in acceptor doping in ZnO and to provide our assessment of the strategies pursued thus far.

Zinc oxide is a wide band gap semiconductor that typically crystallizes in the hexagonal wurtzite structure with a 3.37 eV band gap at 300 K that is comparable to GaN, both of which are suitable for UV and blue photonic devices. Zinc oxide also has several other characteristics that make it an attractive semiconducting material. As a consequence of its less than ideal $c/a = \sqrt{8/3} = 1.633$ ratio in the ZnO wurtzite structure and tetrahedral coordination, it exhibits spontaneous polarization along the c -axis, the strength of which is related to the deviation from ideality. Strains in thin film heterostructures can also give rise to an additional piezoelectric polarization. On the basis of the Pauling electronegativity scale, the Zn–O bond has a significant, 60%, ionic nature instead of being considered a covalent compound. Furthermore, substitution of Mg or Cd

ions on the Zn cation sublattice enables band gap tuning above and below the nominal 3.37 eV band gap for growth of heterostructures. Advantages that ZnO has in comparison to GaN are availability of a native substrate, relative ease of wet chemical etching for device fabrication, its large exciton binding energy of approximately 60 meV [10] and biexciton binding energies on the order of the 25 meV thermal energy at room temperature [11]. These latter characteristics make it attractive for low threshold and large differential quantum efficiency photonic devices in the UV and blue portion of the electromagnetic spectrum. While current microelectronic, nanoelectronic, and optoelectronic devices are based on the flow of electric charge, integration of true multifunctionality on a chip will only be achieved when the spin of the electron can also be taken into consideration. Spin of the electron can be manipulated by an applied magnetic field and has relatively long relaxation times, which implies that devices can be smaller, use less energy, and provide logic operations. Zinc oxide has been predicted to exhibit ferromagnetic behavior at room temperature via a hole-mediated exchange mechanism [12], and thus stable p-type behavior is a requirement for successful demonstration of ZnO spintronics in electronic and photonic applications. While the above points to the significant promise of ZnO-based devices, two major issues must be resolved: high defect densities and doping asymmetry. The former is readily addressed by fabrication of ZnO-based structures that have been grown homoepitaxially. As stated above, however, the doping asymmetry problem is the dominant issue that limits ZnO-based materials and devices.

There are three fundamentally different approaches for growth of p-type ZnO: substitution of Group IA impurities, for example, Li, Na, or K on a Zn site, substitution of Group VA impurities such as N, P, As, and Sb on the O site, and codoping with donors and acceptors. It is clear that the successful approach will be that which enables substantial p-type conduction at room temperature; that is, the acceptor ionization energy must be relatively shallow and compensation by background impurities and/or defects must be minimized. Here, we attempt to summarize the recent accomplishments that have been achieved via each of these methods and to assess the trends in order to postulate what we believe to be the optimum strategy for both thin film heterostructures and nanostructures. Below, we will first address the origin of background donors, which is highly dependent upon whether the material is grown in a Zn-rich or an O-rich environment, the role of H as a donor in ZnO, and the issue of the acceptor ionization energy of substitutional N on the O sublattice. We follow this with a summary of recent reports on the p-type behavior for the various potential doping schemes and then conclude with our outlook.

2. Origin of Background Donors in ZnO

In order to be able to achieve the high ($>10^{17} \text{ cm}^{-3}$) acceptor concentration necessary for useful p-type conductivity, the solid solubility of the acceptor impurity must be relatively

high while the self-compensating defects and acceptor ionization energies must be low. Nominally undoped ZnO is n-type with carrier concentrations ranging from 10^{14} to mid- 10^{16} cm^{-3} . Traditionally, the underlying cause of the unintentional n-type conductivity has been assigned to the formation of zinc interstitials (Zn_i) and oxygen vacancies (V_O) [13]. Comprehensive calculations [13, 14] of the formation energies of dilute native point defects in ZnO via first principles density functional theory (DFT) within the local density approximation (LDA) [15, 16] have thus been performed. The pseudopotential plane-wave method [17] employed uses constant volume supercells and a pair potential approach. At equilibrium, the concentration, c , of a defect in the crystal lattice as a function of its formation energy, E^f , is as follows:

$$c = N_{\text{sites}} \exp\left(-\frac{E^f}{k_B T}\right), \quad (1)$$

where N_{sites} is the concentration of sites in the crystal where the defect can occur and k_B and T are the Boltzmann constant and temperature, respectively. Hence, a low E^f implies a high equilibrium concentration of the defect and a high E^f means that defect formation is less likely to occur. Additionally, the formation energy E^f of a point defect in a charge state q is given by [13]

$$E^f(q) = E^{\text{tot}}(q) - n_{\text{Zn}}\mu_{\text{Zn}} - n_{\text{O}}\mu_{\text{O}} - qE_F, \quad (2)$$

where $E^{\text{tot}}(q)$ is the total energy of a system containing n_{Zn} and n_{O} zinc and oxygen atoms, μ_{Zn} and μ_{O} are the chemical potentials for zinc and oxygen, respectively; and E_F is the Fermi energy. The chemical potentials depend upon the growth conditions. For high zinc partial pressure, $\mu_{\text{Zn}} = \mu_{\text{Zn}(\text{bulk})}$, while for high oxygen partial pressure, $\mu_{\text{O}} = \mu_{\text{O}_2}$. For intermediate II-VI ratios, $\mu_{\text{Zn}} < \mu_{\text{Zn}(\text{bulk})}$ and $\mu_{\text{O}} < \mu_{\text{O}_2}$. Since Zn and O are in equilibrium within ZnO, their chemical potentials are not independent necessitating $\mu_{\text{Zn}} + \mu_{\text{O}} < \mu_{\text{ZnO}}$.

All native point defect formation energies in ZnO have been calculated [13]. Figure 1 summarizes the E^f 's as a function of the Fermi energy E_F [13] for zinc-rich conditions including those for octahedral Zn_i , Zn antisites, Zn_O , and zinc vacancies V_{Zn} , in various charge states. For oxygen-rich conditions, E^f 's as a function of E_F for octahedral O_i , and O antisites, O_{Zn} , and V_{Zn} in various charge states are presented in Figure 2.

As the incorporation of donors or acceptors shifts the Fermi energy, spontaneous formation of these charged defects acts to compensate the prevailing conductivity in ZnO. The formation energy of Zn_i across most of the Fermi level range is high making them an unlikely self-compensating species in n-type material. However, in p-type material, the formation energies for charged species, Zn_i^{+1} and Zn_i^{+2} are more favorable, but the strain energy introduced by the self-interstitial limits their concentration. The absence of the charged V_O^+ and V_O^{2+} species in the energy diagram in Figure 2 reflects their high formation energy near the conduction band minimum (CBM). Since the formation energy of V_O^+ is always higher than either V_O^{2+}

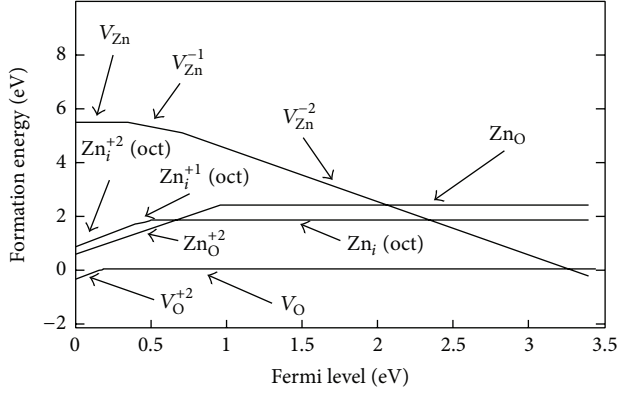


FIGURE 1: Calculated defect formation energy for selected defects as a function of the Fermi level and for $\mu_{\text{Zn}} = \mu_{\text{Zn}}^{\text{O}}$ (high zinc partial pressure). Only the lowest formation energy values are shown. The zero of the Fermi level is set to the top of the valence band. Reprinted with permission from [13]. Copyright 2000 by the American Physical Society.

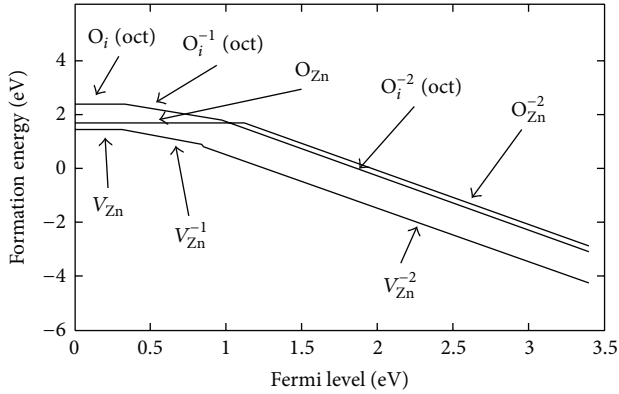


FIGURE 2: Calculated defect formation energy for selected defects as a function of the Fermi level and for $\mu_{\text{Zn}} = \mu_{\text{Zn}}^{\text{O}} + \Delta E_f^{\text{ZnO}}$ (low zinc partial pressure). Only the lowest formation energy values are shown. The zero of the Fermi level is set to the top of the valence band. Reprinted with permission from [13]. Copyright 2000 by the American Physical Society.

or V_{O} , the positive charge state is never thermodynamically stable [14]. However, by virtue of their low E_f^f 's, V_{O}^{2+} or V_{O} may be self-compensating species across the Fermi energy range.

Since hydrogen is unintentionally incorporated during MOVPE growth processes, it is also a plausible contributor to n-type conductivity in ZnO films. The formation energy of the hydrogen interstitial in charge state q is defined by [14]

$$E^f(\text{H}^q) = E^{\text{tot}}(\text{H}^q) - E^{\text{tot}}(\text{bulk}) - \mu_{\text{H}} + qE_F, \quad (3)$$

where $E^f(\text{H}^q)$ is the total energy derived from a supercell calculation for the hydrogen interstitial, $E^{\text{tot}}(\text{bulk})$ is the total energy for a supercell containing only bulk ZnO, μ_{H} is the hydrogen chemical potential, and E_F is the Fermi level which is set to 0 at the top of the valence band [14]. Defect species H^0 and H^- are never stable in ZnO because they are at a much higher energy level in the band structure than

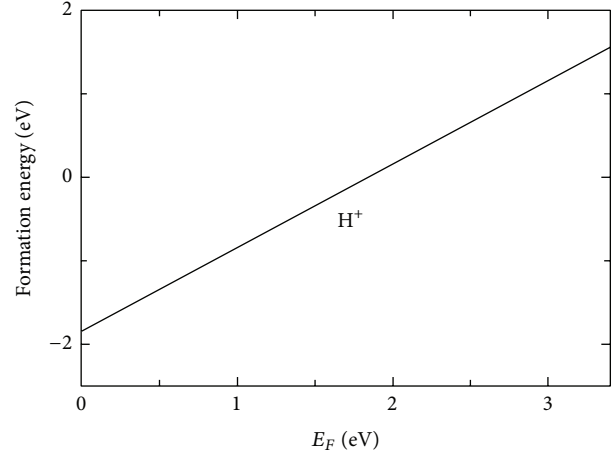


FIGURE 3: Formation energy of interstitial hydrogen in ZnO as a function of Fermi level, obtained from DFT-LDA calculations and referenced to the energy of a free H_2 molecule. Zero-point energies are included. The zero of Fermi energy is chosen at the top of the valence band. Reprinted with permission from [14]. Copyright 2001 by Elsevier Science B.

H^+ [14]. The calculated formation energy for H^+ in ZnO is shown in Figure 3. The lowest energy position for H is at the bond-center (BC) site with the antibonding (AB_{O}) position slightly higher in energy [14]. When H is at the AB_{Zn} site, the corresponding state is localized near the H atom. When H is at the BC and AB_{O} sites, the occupied state becomes an *extended* state because it is at a higher energy level [14].

The formation energy of interstitial H shows that the solubility of H^+ is higher under p-type conditions than under n-type conditions. While that may seem deleterious to accomplishing p-type conductivity in ZnO, hydrogen does have the beneficial effect of increasing acceptor solubility and suppressing compensation by native defects in GaN [18]. Also, since H^+ prefers positions where the charge density is high and it remains close to the donated electron [18], it may easily form complexes with double acceptor species resulting in single acceptor complexes. Additionally, H^+ can be removed from the ZnO lattice during high temperature post-growth anneals.

3. Strategies for p-Type Doping

As mentioned above, there are three primary different approaches that have been investigated to generate appreciable hole conduction in ZnO at room temperature: substitution of Group IA impurities on the Zn sublattice, codoping of donors and acceptors, and substitution of Group VA impurities on the O sublattice. And multiple growth techniques for thin films, for example, molecular beam epitaxy (MBE), magnetron sputtering, metalorganic vapor phase epitaxy (MOVPE), pulsed laser deposition (PLD), and sol-gel, have been utilized. In this section, we will address recent progress in each of these approaches. On the basis of Hall measurements that have been reported, it is clear that in general the hole concentrations are relatively low and

TABLE 1: Summary of room temperature Hall data for p-type ZnO.

Growth technique	Structure ^a	Acceptor doping scheme	Hole concentration (10^{18} cm^{-3})	Mobility ($\text{cm}^2 \text{ V}^{-1} \text{ s}^{-1}$)	Resistivity ($\Omega\text{-cm}$)	Reference
CVD	U	NH_3 and excess Zn	0.015	12	34	Minegishi et al. [19]
MBE	SC	RF plasma N_2	0.09	2	40	Look et al. [20]
RF diode sputtering	SC	Ga, N codoping	0.09	6	11.77	Singh et al. [21]
MBE (ECR O source)	U	Sb-doped + 800°C anneal	1.7	20	0.2	Xiu et al. [22]
DC reactive magnetron sputtering	PC ^b	Li-doped	0.14	2.65	16.4	Zeng et al. [23]
RF magnetron sputtering	SC	Ga and N codoping (N_2 sputtering gas)	0.39	0.4	38	Kumar et al. [24]
Plasma assisted MOVPE	U	NO plasma as O and N source	2.29	1.59	1.72	Zeng et al. [25]
Sol-gel	PC	Al and N codoping + O anneal	0.08–0.2	1.6–1.73	19–45	Dutta et al. [26]
RF magnetron sputtering	SC	O and As dual implantation	6.8–19.8	19–32.9	0.05–0.55	Kim et al. [27]
MOVPE	U	P-doped	0.21	1.2	—	Du et al. [28]
PLD	PC	Na-doped + 254 nm illumination	0.21	7.9	3.8	Lin [29]
PLD	SC	N^+ implantation + dynamic annealing	0.024–0.52	0.7–3.71	18–71	Myers et al. [30]
Plasma assisted MBE	U	Sb-doped + 800°C anneal	0.06	—	—	Huang et al. [31]
MOVPE	SC	As-doped via outdiffusion	0.35	0.79	—	Shi et al. [32]
Magnetron sputtering	U	P and N codoping + 800°C anneal	1.16	1.35	3.98	Sui et al. [33]
Plasma assisted MBE	SC	Na doping	0.002	0.4	8575	Ding et al. [34]
Spin coating	PC	N, Al codoping + double anneal in NH_3 and N_2	0.61	198.8	0.05	Kalyanaranan et al. [35]
MOVPE	SC	3% NO in N_2	3.6	0.4	4.4	Reynolds et al. [36]

^aU: undefined; SC: single crystal; PC: polycrystalline. All are thin films.

^b(002) preferential orientation.

that mobility values indicate that the thin films are quite compensated. A summary of the recent data in chronological order is given in Table 1. The fundamental goal is significant p-type conduction at room temperature, which implies that one must achieve shallow acceptor ionization energies with minimal compensation by unintentional impurities and/or defects.

3.1. Group IA Li and Na on a Zinc Site. While Park et al. [37] have predicted Li and Na to exhibit relatively shallow, $\sim 0.1\text{--}0.17 \text{ eV}$, acceptor levels in ZnO, a more recent hybrid

density functional investigation [38] has shown the ionization energy to be $0.6\text{--}1.1 \text{ eV}$ above the valence band maximum, that is, becomes significantly deeper. The latter attributed this discrepancy to the well-known band gap error in DFT and its influence on the energy of the Li_{Zn} acceptor level. As the band gap widens, the acceptor level shifts upward away from the VBM due to becoming more localized. However, there have been limited reports of successful acceptor behavior that is based on Group IA doping. Using DC reactive magnetron sputtering, Zeng et al. [23] have demonstrated hole concentrations of $\sim 10^{17} \text{ cm}^{-3}$ at a growth

temperature of 550°C in Li-doped thin films; however, the acceptor concentration decreases an order of magnitude as the growth temperature decreases or increases 50°C on either side of the optimum. They also suggest that Li_{Zn} may be relatively unstable because of a higher Madelung energy. As we will see later, a lowered Madelung energy is suggested as being fundamental to understanding why codoping should result in p-type behavior. For Na-doped ZnO, p-type ZnO has been reported for thin films grown by PLD [29] and plasma assisted MBE [34]. In the former, it was suggested that adsorbed O species at grain boundaries are deleterious to p-type behavior, and thus, it was necessary to subject films to 254 nm UV illumination to remove these species to obtain a p-type film. Nevertheless, they were able to achieve a mobility of $7.9 \text{ cm}^2 \text{ V}^{-1} \text{ s}^{-1}$ at a hole concentration of $2.1 \times 10^{17} \text{ cm}^{-3}$, and the acceptor ionization energy was estimated to be 110 meV from temperature-dependent Hall data. For the plasma assisted MBE ZnO, nonpolar a-plane films were grown on r-plane sapphire. The relatively low hole concentration of $\sim 2 \times 10^{15} \text{ cm}^{-3}$ was attributed to compensation by oxygen vacancies. Such weak p-type behavior is not anticipated to yield substantial hole conduction at room temperature. In general, the low mobilities observed in these investigations indicate that the films are most likely compensated. Group IA elements are relatively reactive, and thus we expect that anomalous p-n junction behavior may be an issue as observed for Group IIA dopants in traditional III-V semiconductors.

3.2. Codoping of Donors and Acceptors. Performing *ab initio* electronic band structure calculations, Yamamoto and Katayama-Yoshida [39] showed that substitutional N-doping alone increases the Madelung energy resulting in localization of N states. They thus suggested that codoping with Al or Ga and N leads to energetically favorable acceptor-donor-acceptor complexes that lead to a reduction in the Madelung energy with delocalized N states and equally important enhanced incorporation of N acceptors. More recent density functional theory calculations support this suggestion showing that codoping of N with Al or Ga leads to a strong attractive interaction between Al_{Zn} or Ga_{Zn} donors and nearest neighbor N_{O} acceptors. Although (Al-2N) or (Ga-2N) complexes form at higher concentrations of nitrogen, their behavior is predicted to be quite different with regard to nitrogen solubility [40]. That is, Duan et al. [40] predicted enhanced nitrogen solubility when using NO as the nitrogen source and codoping with Ga and N, which should lead to improved p-type conductivity. However, the relatively weak interaction between Al and N and N on a substitutional O site suggested that N solubility is not enhanced via Al and N codoping. Furthermore, the estimated acceptor ionization energies are 0.17 and 0.14 eV for Al and Ga codoped with N, respectively, which is substantially less than their predicted ionization energy of 0.33 eV for substitutional N_{O} only. They have also shown that codoping with the transition metals (Zr, Ti, Y, and Sc) and nitrogen can lead to complexes with levels above the valence band maximum that indicate lower ionization energies than the isolated N acceptor [41].

Although codoping of donors and acceptors has been predicted to lead to improved p-type conduction via the presence of shallow acceptor levels in comparison to the isolated nitrogen on an oxygen site, experimentally, relatively low hole concentrations, $< \sim 10^{17} \text{ cm}^{-3}$, with low mobilities are observed (see Table 1) [21, 24, 26, 35]. Singh et al. [21] demonstrated p-type ZnO thin films for (Ga, N) codoped films grown by RF diode sputtering but found that the observation of p-type behavior depended upon the oxygen partial pressure to total pressure ratio. For films grown with less than 50% O partial pressure, n-type conduction was observed, but films grown with 50% and above exhibited p-type behavior that appeared to saturate at 60% O partial pressure. P-type conduction was attributed to suppression of V_{O} and Zn_i and the associated compensation with codoping. In addition, films exhibiting p-type behavior revealed both (002) and (100) reflections in X-ray diffraction (XRD) patterns. Most likely, this is related to N incorporation in the films as we will discuss in the next section for substitutional N on an O site. They claim a reduction in band gap to 3.27 eV for p-type films; however, this emission peak is most likely related to an acceptor-related transition [21]. Using RF magnetron sputtering, Kumar et al. [24] have reported p-type behavior for (Ga, N) codoped films grown on both sapphire and Si in which N_2O was used as the sputtering gas. For films grown below 450°C, conduction was n-type. At a growth temperature of 550°C, they achieved a resistivity of $38 \Omega\text{-cm}$ with a hole concentration of $3.9 \times 10^{17} \text{ cm}^{-3}$. Somewhat puzzling though is the $1.3 \times 10^{19} \text{ cm}^{-3}$ hole concentration reported for films grown on Si. In spite of the significant difference in misfit and thermal expansion coefficients between ZnO and sapphire and between ZnO and Si (see, e.g., [6]) and resultant defect densities, it is most likely that the high hole concentration is not representative of the film but is indicative of an issue with the Hall measurements on the p-type substrate. Although these authors claim that only (002) and (004) diffraction peaks are observed in the XRD spectra for films grown on both substrates, close examination of the spectrum on Si reveals a (101) ZnO reflection. As we will discuss in the next subsection, we believe that this reflection is associated with N incorporation in the film.

Other codoped films have utilized (Al, N) codoping and have been deposited via sol-gel [26] and spin coat [35] processes. Dutta et al. [26] reported that films that were only N-doped exhibited mixed n and p conduction while the Al and N codoped films were stable p-type with hole concentrations of $(0.8\text{--}2) \times 10^{17} \text{ cm}^{-3}$ that were dependent upon the Zn/N/Al ratios. All films were annealed in an oxygen ambient. While their undoped and solely N-doped films were polycrystalline, their codoped (Al, N) ones exhibited a strong (002) diffraction peak with much weaker (100) and (101) peaks. We believe that presence of the latter weak reflection is related to N incorporation. Grain sizes were in the range 25–75 nm. Although the (Al, N) codoped ZnO films grown by spin coating were polycrystalline with grain sizes ~ 25 nm, they exhibited reasonably high hole concentrations, $6 \times 10^{17} \text{ cm}^{-3}$, and extraordinarily high mobility, $198.8 \text{ cm}^2 \text{ V}^{-1} \text{ s}^{-1}$ [35]. This is the highest mobility that we

have been reported for holes in ZnO and seems unreasonable considering the polycrystalline nature of the films. A 550°C anneal in NH₃ served as the N-dopant source, and films were subjected to another post-growth anneal at 700°C to remove H. This last step is crucial as it has been suggested that H is the dominant donor in ZnO [42, 43]. Comparison of Ga and N versus Al and N codoped films enables one to make an interesting observation that seems counter to first-principles DFT calculations [40]. For (Ga, N) codoped films, the reported [21, 24] hole concentrations are in the range of $0.9\text{--}3.9 \times 10^{17} \text{ cm}^{-3}$, whereas those [26, 35] codoped with Al and N are $0.8\text{--}6 \times 10^{17} \text{ cm}^{-3}$; that is, there appears to be no significant difference between codoping with Ga or Al and N with regard to N dopant solubility and/or acceptor ionization energy. As mentioned in the beginning of this subsection, DFT calculations implied that Ga and N codoping should increase N solubility compared to Al and N codoping because the interaction between (Al-2N) and a neighboring N on an oxygen site is weak in comparison to that between two (Ga-N) complexes and the binding between (Ga-2N) and a nearest neighbor N [40]. A more recent investigation [44] on p-type conduction for N and Te codoped ZnO films has reinforced the proposed role [39] of codoping for generating p-type behavior; that is, N/Te codoping lowers the Madelung energy for enhanced N incorporation. However, it was necessary to subject the codoped films to a 700°C/30 min anneal in an O₂ environment in order to reduce donor-related defects and enable n- to p-type conversion in the films. However, the luminescence data are somewhat puzzling with regard to the relative importance of N₂ flow and anneal related to the Hall data (see Figure 6 in Park et al. [44] in relation to carrier concentration data in Table 1). An added benefit of the thermal anneal step is that it improves crystal quality that had been degraded by codoping as evidenced by the increase in the FWHM of the (0002) X-ray reflection with increasing N₂ flow. Their highest reported hole concentration of $1.6 \times 10^{16} \text{ cm}^{-3}$ after the anneal occurred for the highest N₂ flow and also exhibited a mobility of $1.8 \text{ cm}^2 \text{ V}^{-1} \text{ s}^{-1}$, the latter implying that the films are heavily compensated.

3.3. Group VA Elements on an Oxygen Site. Although the Group VA elements (N, P, As, and Sb) have predicted acceptor ionization energies greater than those of the Group IA elements on the zinc site, the Group VAs have been the most extensively investigated. Of the Group VA elements, nitrogen seems to be the most suitable because of its electronic structure, and its ionic radius, 0.168 nm, is closer to that of oxygen, 0.138 nm, than the other elements for which the ionic radii differences are >50% [3]. One might anticipate that such a larger ionic radius compared to that of oxygen would introduce considerable strain into the wurtzite lattice. More importantly, the ionization energies are predicted to be $\sim 1 \text{ eV}$ for P, As, and Sb [45]. However, an acceptor ionization energy of 197–227 meV has been reported for Sb-doped ZnO grown by MBE [22]. Substitutional nitrogen on an oxygen site alone is particularly interesting. Ionization energies of 0.33 [40], ~ 0.4 [37, 46], and 1.3 eV [47] have been predicted, none of which would be compatible with appreciable hole

TABLE 2: Reported acceptor ionization energies for Group VA elements on an oxygen site.

Dopant	E_A (meV)	Reference
N	100	Minegisha et al. [19]
N	170–200	Look et al. [20]
N	165	Myers et al. [30]
N	209	Wang and Giles [48]
N	180	Zeng et al. [25]
N	160	Stehr et al. [49]
N	134	Reynolds et al. [36]
Sb	197–227	Xiu et al. [22]

conduction at room temperature. Nevertheless, on the basis of Hall measurements, p-type conduction has been reported for nitrogen and the other Group VA dopant elements. Reported ionization energies for N_O are in the range of 100–200 meV (see Table 2 for a summary of the ionization energies). In view of these results, it seems clear that complexes involving nitrogen are mainly responsible for p-type behavior as we will discuss below. We begin first though with a brief summary of p-type conduction for P-, As-, and Sb-doped ZnO. Recall that a summary of relatively recent room temperature Hall data are given in Table 1.

P-type behavior for P-doped ZnO has been reported for films grown by MOVPE [28] and magnetron sputtering [33]. In the latter reference, Sui et al. demonstrated that P and N codoping provided an order of magnitude increase to the hole concentration compared to P-doping alone. They attributed this to the addition of nitrogen to a neutral P_{Zn}-3N_O complex to form a P_{Zn}-4N_O acceptor complex, which gives rise to formation of an impurity band above the valence band maximum similar to the discussion above for donor-acceptor codoping. Their optimum hole concentration of $1.16 \times 10^{18} \text{ cm}^{-3}$ was achieved after a post-growth anneal at 800°C for 30 min at a pressure of 10^{-4} Pa . The low mobility of $1.35 \text{ cm}^2 \text{ V}^{-1} \text{ s}^{-1}$ implies that the films are heavily compensated. Du et al. [28] confirmed their p-type Hall data with C-V measurements and claimed their films to be stable for four months. Of particular relevance in the latter investigation is that they were able to demonstrate lasing under electrical pumping for a P-doped p-ZnO/n-GaN heterostructure; the FWHM of the electroluminescence spectrum narrowed to $\leq 1 \text{ nm}$ at 9 mA and above. However, other resistivity and luminescence data have suggested that phosphorous doping for p-type behavior in ZnO is more problematic. Von Wenckstern et al. [50] have grown P-doped ZnO heteroepitaxially and homoepitaxially and found quite varying results. For example, as-grown heteroepitaxial films were semi-insulating to n-type, whereas scanning capacitance microscopy of homoepitaxial films indicated regions of mixed carrier type; both results are consistent with the predictions of Park et al. [37], based on the amphoteric behavior of P in ZnO.

As-doped films have been achieved via MOVPE [32] and (O, As) dual implantation [27] into a film that was grown by magnetron sputtering. In the former, Shi et al. [32]

formed p-ZnO by As outdiffusion from a neighboring GaAs layer. They reported a hole concentration of $3.56 \times 10^{17} \text{ cm}^{-3}$, which was attributed to formation of an $\text{As}_{\text{Zn}}-2\text{V}_{\text{Zn}}$ complex, and also demonstrated electroluminescence from a p-n junction light emitting diode type structure based on As-doped ZnO. For the implanted films [27], mixed conduction was observed for As implantation alone, whereas dual implantation followed by an 800°C anneal in N_2 resulted in hole concentrations $\sim 10^{19} \text{ cm}^{-3}$ with relatively high hole mobilities that depended upon the fluence of As and O. The observation of hole conduction in As-doped ZnO however is contrary to the predictions of Park et al. [37], who based their analysis on the amphoteric nature of these dopants. In spite of the large ionic radii size difference between Sb and O, hole conduction has been observed in Sb-doped ZnO [31, 45]. For the Group VA elements P, As, and Sb, Xiu et al. have reported the highest hole concentration, $1.7 \times 10^{18} \text{ cm}^{-3}$, with a corresponding mobility of $20 \text{ cm}^2 \text{ V}^{-1} \text{ s}^{-1}$ for Sb-doped ZnO [22]. Their films were grown by MBE with elemental Zn and Sb sources and an oxygen plasma electron-cyclotron resonance source for the oxygen. Growth was followed by an 800°C *in situ* anneal; the hole concentration increased with the Sb effusion cell temperature. Huang et al. [31] used plasma assisted MBE to grow their films and also required an 800°C *in situ* anneal to activate their Sb. Earlier though, Friedrich et al. [51] reported a deterioration of the sample surface with an increase in the Sb concentration due to the increase in lattice stress. They claim that there is a tendency for Sb-O precipitate formation, which suppresses formation of $\text{Sb}_{\text{Zn}}-2\text{V}_{\text{Zn}}$ complexes for p-type behavior. More recently, it was demonstrated that the conduction type in Sb-doped ZnO depended upon the concentration of Sb in films grown by plasma enhanced MBE [52]. Liu et al. demonstrated that films with Sb concentrations in the doping regime (varied by changing the Sb flux) exhibited n-type behavior for electron concentrations in the 10^{16} -mid- 10^{19} cm^{-3} range while films with ~ 1 at % Sb revealed compensating acceptor-like defects with a resultant decrease in electron concentration. It was suggested that Sb incorporates on the Zn site for relatively low Sb concentrations but the observed sudden increase in the *c*-lattice parameter suggested that Sb begins to reside on the O site at higher concentrations, ~ 1 at % [52]. Structural degradation of the films was also observed to occur with increasing Sb as also reported by Friedrich et al. [51] above. Yankovich et al. [53] have reported that stable acceptor conduction is observed in Sb-doped ZnO nanowires in which Sb decorates basal plane inversion domain boundaries. This electron acceptor behavior was related to the phenomenon of Sb and O codoping and shown to be consistent with density functional theory calculations. This suggests however that acceptor behavior via Sb-doping is not necessarily simple formation of an isolated acceptor level but involves defect complexes within the material, which we believe to be the relevant mechanism for appreciable room temperature hole conduction.

There have been considerable calculations on substitutional Group VA impurities, mostly nitrogen, on the oxygen site. Although the magnitude of the ionization energies varies from 0.33 to 1.3 eV, all are consistent with a deep acceptor

for a single N_O . This strongly suggests that the experimental observation of p-type conduction in N-doped ZnO is predominantly related to complexes involving nitrogen. As mentioned above, Park et al. [37] performed first principles DFT calculations using the pseudopotential method within the LDA [15]. Since their calculations included a nonlinear partial core correction (NPC) [54], they gave a 2x correction of the bandgap for ZnO compared to those that only included the Zn-3d states as valence electrons. Their underestimate of the bandgap, 1.56 eV, is a characteristic error in the LDA approach and their 25% underestimate of the calculated heat of formation of ZnO follows. However, their calculations do reveal the trend for the increase in defect energy levels when Group VA elements are substituted on the O site compared to Group IA defects substituted on the Zn site. Since Group IA elements lack an active *d* orbital, they have reduced *p* – *d* coupling which lowers their defect energies. The higher defect energy levels for Group VA elements are a result of increasing impurity *p*-orbital energy from $\text{N} \rightarrow \text{P} \rightarrow \text{As}$ [37]. The key point revealed by their calculations was the importance of AX centers, which are deep defect complexes that compensate for acceptors. The positive energy required to form positively charged AX centers from the substitutional acceptors on a Zn site indicates that Group IA elements are only metastable in ZnO [37]. The negative energy for Group VA elements, P and As, means they are more stable as AX centers than substitutional states on the O site [37]. Their calculations thus suggested that only N is a viable substitutional acceptor in ZnO. Another consequence of their calculations is the formation of complexes between Zn_i and N_O as a function of growth environment. For example, the formation energy E_f of $(\text{Zn}_i + \text{N}_\text{O})$ under O-rich conditions is 6.58 eV but can be as low as 0.8 eV at the Zn-rich limit [37].

Lee et al. [46] also used first principles pseudopotential calculations within the LDA to describe the localized nature of the Zn 3*d* and O 2*p* wave functions to explain compensation mechanisms in N-doped ZnO. The conclusion from Lee's calculations mirrors others [13, 14] in that V_{Zn} is the most stable defect under O-rich conditions from midgap to the CBM. While V_{Zn} acts as an acceptor, his focus is on the compensating species such as V_O , Zn_i , Zn_O , and the shallow double donor, $(\text{N}_2)_\text{O}^{2+}$, as E_F changes from the CBM to the VBM. The low formation energies for complexes of those defects with N_O suggest that N-doping is inefficient under O-rich conditions because the total atomic concentration, $[\text{N}]$, of incorporated N impurities is below $8 \times 10^{12} \text{ cm}^{-3}$ which leads to very low hole densities [46]. In the Zn-rich limit however, since the E_f of N_O decreases significantly, both hole and N concentrations increase, leading to $[\text{N}] \sim 10^{15} - 2 \times 10^{17} \text{ cm}^{-3}$ with resultant hole carrier densities that saturate at $\sim 2 \times 10^{15} \text{ cm}^{-3}$. For growth processes using a N_2 source in an electron cyclotron resonance, ECR, and plasma, N solubility is expected to increase under O-rich conditions. However, $(\text{N}_2)_\text{O}$ molecules are the dominant compensating species. So even though $[\text{N}]$ increases with this active source, the hole carrier density decreases because of compensation by $(\text{N}_2)_\text{O}$ molecules and unintentional H impurities from H_2O within the growth system. Lee et al. [46] concludes that for low $[\text{N}]$,

N_O acceptors are compensated by V_O , while for high [N], N_O acceptors are compensated by N_O -ZnO complexes.

Troubled by acceptor levels for N in ZnO generated by DFT calculations within the LDA or generalized gradient approximation (GGA) [37, 46], Lyons et al. [47] performed first principles calculations using hybrid functionals. These calculations lead to a band gap of ZnO of 3.4 eV. They found that N_O can be stable in either the neutral or -1 charge states, with the acceptor level occurring at 1.3 eV above the VBM [47], as mentioned above. The discrepancy between their calculations and those of Park et al. [37] and Lee et al. [46] in which N is predicted to be a more shallow acceptor were attributed to the downward shift of the VBM on an absolute energy scale. They verified their calculations for N_O in ZnO by repeating them for N_{Se} in ZnSe. Their calculations were consistent with experimental findings that the ionization energy for N_{Se} is 100 meV [47]. They assigned the difference in ionization energies of the N acceptors to the band structure of the host as follows. In ZnO, the VBM is derived from the O $2p$ orbitals. In ZnSe, the VBM is derived from the Se $4p$ orbitals. Since N $2p$ orbitals are ~ 3 eV lower than Se $4p$ orbitals in ZnSe, but ~ 3 eV higher than O $2p$ orbitals in ZnO, it follows that the transfer of an electron from the VBM to the N acceptor is more energetically favorable in ZnSe, but nearly impossible in ZnO [47]. Experimental confirmation of N as a deep acceptor in bulk ZnO grown in an NH_3 ambient was reported by Tarun et al. [55] based on two key observations: (1) an IR absorption peak at 3148 cm^{-1} attributed to a N-H complex and (2) a broad PL emission centered at 1.7 eV, the intensity of which increased with the activated N concentration. Activation of N as a deep acceptor was accomplished by annealing in a 0.5 atm O_2 ambient, which dissociated N-H pairs to form the isolated N_O . Presence of the broad 1.7 eV emission was claimed to be in agreement with the deep acceptor model [47] for an isolated substitutional N in ZnO proposed by Lyons, et al. Nevertheless, numerous publications have reported N-related relatively shallow acceptor levels (see Table 2) that are consistent with p-type conduction. As discussed below, these shallow acceptor levels are related to defect complexes involving N_O and not an isolated N on the oxygen site.

Minegishi et al. [19] was the first to realize p-type conduction at room temperature in ZnO films by incorporating N during chemical vapor deposition (CVD) of ZnO on (0001) sapphire substrates. Secondary ion mass spectroscopy (SIMS) was used to confirm the presence, but not absolute concentration, of N in those films given the simultaneous addition of NH_3 to the H carrier gas and a 10 mol% mixture of metallic Zn and ZnO powder. Their N-doped films exhibited resistivities that ranged from 34 to $175\ \Omega\text{-cm}$ with Hall mobilities of $12\text{--}30\text{ cm}^2\text{ V}^{-1}\text{ s}^{-1}$ for substrate temperatures of $650\text{--}750^\circ\text{C}$, respectively. However, there was a very narrow temperature window in which the excess Zn was able to catalyze N to combine with H in the film to form ZnNH, resulting in the activation of the N acceptor [19]. For the film that did invert to p-type conduction, the acceptor ionization energy was estimated to be 100 meV which is the lowest reported to date (see Table 2) and seems low for the N incorporation suggested

by a hole carrier density of only $1.5 \times 10^{16}\text{ cm}^{-3}$. If one assumes that their estimate of the ionization energy is correct, then one can only conclude that their nitrogen incorporation is quite low.

Probably the results that have stimulated the most renewed interest in ZnO were those by Look et al. [20]. They were the first to show reproducible N-doped p-type ZnO grown by MBE on Li-doped semi-insulating ZnO substrates by adding N_2 to the O_2 gas flow in the RF plasma source. SIMS measurements revealed the nitrogen concentration, [N], at the surface of $\sim 9 \times 10^{18}\text{ cm}^{-3}$ with a corresponding hole concentration of $9 \times 10^{16}\text{ cm}^{-3}$, which implied a 1% activation of the N acceptor. Van der Pauw Hall measurements also gave average values of $\rho = 40\ \Omega\text{-cm}$ and $\mu_p = 2\text{ cm}^2\text{ V}^{-1}\text{ s}^{-1}$. Their low temperature (4 K) PL reported the acceptor-bound exciton (A^0X) associated with N_O at 3.315 eV, and the acceptor ionization energy was estimated to be 0.17–0.20 eV [20]. Their hole concentrations were consistent with the estimated ionization energy and were in agreement with those predicted by the nondegenerate, single-donor/single-acceptor model [56]. SIMS, Hall, and PL measurements were also consistent with those for p-type GaN and other p-type II-VI compounds.

Zeng et al. [25] grew N-doped ZnO thin films on a-plane (11–20) sapphire substrates by plasma-assisted low-pressure (5 Pa) MOVPE. An NO plasma was used as the source for both the oxygen source and the N dopant source. Growth temperatures ranged from 250 to 500°C in 50°C increments. All films were grown at 450°C and below exhibited p-type behavior. Room temperature (RT) van der Pauw Hall characteristics were optimal for a growth temperature of 400°C . Resistivity was lowest ($1.72\ \Omega\text{-cm}$) as was hole mobility ($1.59\text{ cm}^2\text{ V}^{-1}\text{ s}^{-1}$). Hole concentrations were also maximized at $2.29 \times 10^{18}\text{ cm}^{-3}$. Scanning electron microscopy (SEM) of surfaces of films grown at 300°C , 400°C , and 500°C supported Zeng et al.'s [25] assertion that less N is incorporated at higher temperatures as did the relative intensities from RT photoluminescence. The free electron-to-neutral-acceptor (e, A^0) transition was most pronounced for their 400°C film. From the (e, A^0) peak position, the acceptor ionization was estimated to be 180 meV. The very impressive aspect of this study was the wide range of temperature and the repetitive consistency with which p-type conductivity was achieved.

As mentioned in the codoped section above, Dutta et al. [26] used a sol gel process to investigate both N-doped and (Al, N) codoped ZnO. The sol-gel film was spin coated, post-baked, and then heated at 550°C in an oxygen ambient for 30 min. The decomposition pathway of the ammonium acetate gave NO and NO_2 to act as the N source. X-ray diffraction (XRD) patterns of their ZnO:N showed (002) as well as (101) plane reflections. However, their N-doped only films showed unstable behavior. Hall measurements fluctuated between p- and n-type with concentrations and mobilities in the range of $(-)\ 6.53 \times 10^{13}\text{ cm}^{-3}$ to $(+)\ 5.95 \times 10^{14}\text{ cm}^{-3}$ and $66.5\text{ cm}^2\text{ V}^{-1}\text{ s}^{-1}$ to $6.4\text{ cm}^2\text{ V}^{-1}\text{ s}^{-1}$. The anomalous Hall behavior is consistent with their low XRD c -axis value of 0.5218 nm suggesting <0.1 atomic % N in the film [57].

Myers et al. [30] used PLD and ion implantation of N^+ ions at three different fluences $3 \times 10^{14}\text{ cm}^{-2}$, $6 \times 10^{14}\text{ cm}^{-2}$,

and $1.2 \times 10^{15} \text{ cm}^{-2}$ and dynamic annealing at 300, 380, and 460°C for each fluence. Simulations predicted maximum implanted concentration of $8 \times 10^{19} \text{ cm}^{-3}$ at a depth of $\sim 120 \text{ nm}$ for the highest implant fluence of $1.2 \times 10^{15} \text{ cm}^{-2}$. All samples implanted at 300 and 380°C were n-type except for the lowest fluence at 380°C . However, samples for all fluences implanted at 460°C exhibited p-type conductivity and their resistivity decreased from $71 \Omega\text{-cm} \rightarrow 50 \Omega\text{-cm} \rightarrow 18 \Omega\text{-cm}$ as fluence increased. As resistivity decreased, hole carrier concentration increased from $2.4 \times 10^{16} \text{ cm}^{-3} \rightarrow 1.9 \times 10^{17} \text{ cm}^{-3} \rightarrow 2.4 \times 10^{17} \text{ cm}^{-3}$. Hall mobilities ranged from 0.7 to $3.7 \text{ cm}^2 \text{ V}^{-1} \text{ s}^{-1}$. Transmission electron microscopy (TEM) of films that exhibited n-type conductivity confirmed that low temperature implantation created defect clusters and damage instead of substitutional incorporation of dopants. Conversely, stacking faults were a characteristic of all the p-type samples. Based on their simulations, at an implant temperature of 460°C , they were able to activate 0.3% of the implanted N^+ ions.

Ion implantation provides a means of incorporating controllable amounts of dopant into the ZnO matrix to help elucidate the relevant mechanisms for p-type conduction. Recently, Stehr et al. [49] used this technique to maximize the formation of certain intrinsic defects by coimplanting N^+ with O^+ or Zn^+ into bulk ZnO crystals at 300 K. Following implantation, crystals were annealed in either N_2 or O_2 at 800°C for 2 min. Raman spectra of their crystals contained local vibration modes at 277 cm^{-1} , 511 cm^{-1} , and 581 cm^{-1} which have been previously associated with N [58, 59]. The PL spectra of their codoped ion implanted samples revealed three major points. First, the I_4 line normally present for undoped ZnO disappeared after codoping implantation with either N and O or N and Zn. They attributed this to consumption of H by the formation of complexes with N in the implanted ZnO. Secondly, PL lines at 3.3128 and 3.2405 eV appeared after implantation. These lines have been assigned to the recombination of excitons bound to a neutral acceptor (A^0X) [20, 60] and also to free electron to acceptor (FA) transitions [61]. The presence of these PL signatures is consistent with the observations of Look et al. [20]; however, the interpretation of the origin, single N_O versus an acceptor complex, remains quite controversial. Stehr et al. [49] suggested that this defect is most likely a complex that contains a N atom because the acceptor energies estimated by Stehr et al. [49] and Look et al. [20] are too small to be substitutional nitrogen on the oxygen site. Thirdly, the intensity of the A^0X emission for ZnO samples implanted with N and Zn was highest for those annealed in O_2 and lowest for those annealed in N_2 . This annealing behavior suggested that while defect formation was favored under Zn-rich conditions, it was also suppressed by oxygen deficiency [49]. For those samples coimplanted with N and O, a PL band at 3.23 eV accompanied by an LO-assisted transition was assigned as the donor to acceptor pair (DAP) transitions related to a nitrogen acceptor. Assuming a shallow (52 meV) donor is participating in the DAP transitions, the ionization energy (160 meV) suggests this N-related acceptor is also a complex defect. This binding energy is similar to the energy

level of a $\text{N}_{\text{Zn}}\text{-}2\text{V}_{\text{Zn}}$ complex seen in Zn-deficient conditions [49]. Their optically detected magnetic resonance (ODMR) measurements of samples with coimplantation of N and O gave insight about another defect. When studied in the visible spectrum, the ODMR signal for samples annealed in N_2 was broad and its intensity was diminished relative to those annealed in O_2 or the reference ZnO crystal. The angular dependence of that broad signal suggested the defect was related to the deep donor, N_{Zn} , which has favorable formation energy under oxygen-rich conditions [62]. However, when studied under near-IR emission, that same deep donor signal was detected but was paired with an additional defect, a deep acceptor N_O . These same defects were not present for samples coimplanted with N and Zn. These ODMR signals present the first evidence for the N antisite that Liu et al. [63] suggested and is fundamental to the work done by Reynolds et al. [36].

Sui et al. [33] codoped ZnO films with Group VA elements P and N by magnetron sputtering and post-growth annealing to generate p-type material. Their source material was a mixture of argon and nitrogen used to (RF) sputter ZnO and 2 wt.% P_2O_5 powders onto quartz substrates at 500°C . Post-growth annealing was performed in a tube furnace for 30 min at 800°C . Their RT resistivity was found to be $3.98 \Omega\text{-cm}$ with a Hall mobility of $1.35 \text{ cm}^2 \text{ V}^{-1} \text{ s}^{-1}$ and a hole concentration of $1.16 \times 10^{18} \text{ cm}^{-3}$. The electrical properties for ZnO:(P, N) were greatly improved, 10x and 100x, over those samples doped with P or N alone, respectively. The ZnO:P and ZnO:N resistivities were an order of magnitude lower and their carrier concentrations were $2.3 \times 10^{17} \text{ cm}^{-3}$ and $1.18 \times 10^{16} \text{ cm}^{-3}$, respectively. The higher mobility ($10.8 \text{ cm}^2 \text{ V}^{-1} \text{ s}^{-1}$) for the ZnO:N sample is consistent with the lower carrier concentration. All samples showed p-type conductivity. Sui et al. [33] also presented I - V characteristics for their homojunction of undoped n-type ZnO and p-type ZnO, which used Ni/Au for the p-contacts and In for the n-contacts. The rectifying behavior is clearly present albeit the current is low ($-2 \mu\text{A} < I < 2 \mu\text{A}$) for a drive voltage from $-15 \text{ V} < V < 15 \text{ V}$. Using SIMS, they compared the N incorporation in a film that was codoped with N and P with one doped with N alone. While no absolute concentrations were given, the relative incorporation of N is an order of magnitude higher in the (P, N) codoped sample. Their P_{2p} XPS spectra gave a binding energy of between 133.3 and 133.8 meV for the ZnO:(P, N) sample indicating that P did not substitute for O but rather occupied a Zn site. The N_{1s} XPS spectrum showed two peaks, one at 397.6 eV and another at 402.5 eV. The lower peak indicates that the N atom substitutes for the O atom to form the N_O acceptor in the ZnO:(P, N) sample. The higher, less intense peak is attributed to $(\text{N}_2)_\text{O}$ which is considered a double donor. Their PL data over the temperature range from 83 to 300 K showed the FA transition at 3.310 eV, a DAP transition at 3.241 eV, and its longitudinal optical (LO) phonon replica separated by 72 meV at 3.168 eV. Their FA peak exhibits the characteristic redshift while the DAP emission continually shows a blueshift as shallow donors are ionized with increasing temperature as the ionized free electrons in the conduction band prefer to recombine with acceptors to form FA [64]. The formation

mechanism for the p-type ZnO : (P, N) is that P occupies the Zn site, P_{Zn} , and N occupies the O site (N_O) forming a neutral passive $P_{Zn}-3N_O$ complex which may form an additional fully occupied impurity band above the VBM. When additional N is introduced into the system with the $P_{Zn}-3N_O$ defect complex, the N and $P_{Zn}-3N_O$ combine to form more energetically favored $P_{Zn}-4N_O$ complex acceptors. As a consequence, the electrons transit from the impurity band which lowers the ionization energy, and the p-conduction arises from the $P_{Zn}-4N_O$ acceptor complex.

The fact that low experimental acceptor ionization energies for Group VA on an oxygen site have been reported suggests that the origin of p-conductivity in ZnO is most likely not associated with a single VA substitution on an O site but must be explained by a more complex and multistep approach. Catlow et al. [65] showed that the fundamental reactions necessary to generate defect species V_{Zn}^{-2} , V_O^{+2} , O_i^{-2} , Zn_i^{+2} , and hole formation require energy while reactions for electron generation and ZnO(s) formation release energy. So, from a thermodynamic perspective, except under conditions of very high chemical potential, defect compensation is more favorable than hole compensation under equilibrium conditions [65]. However, experimental data suggests that by controlling the growth conditions, defect solubility may be coerced such that donor defect species provide metastable routes to acceptor complexes capable of providing mobile holes in ZnO. Liu et al. [63] suggested that since the absorption energy for N_{Zn} is 0.08 eV for the hexagonal close packed structure of the Zn-polar surface, it may be possible for N to absorb to bulk Zn sites, resulting in N_{Zn} bonded to 3 neighboring O atoms on the zinc-polar oxygen surface. This suggestion is consistent with the formation energies for V_{Zn}^{-2} under O-rich conditions as shown in Figure 2. But it necessitates the amphoteric behavior of N in ZnO under O-rich conditions leading to the formation of N_{Zn} antisites.

Reynolds et al. [36] suggested that if the MOVPE growth conditions were alternated from O-rich to Zn-rich, it would be energetically less favorable for O to bond to the N_{Zn} than to form an V_O^0 since its E_f is ~ 0.1 eV across the entire Fermi level range. The result would be the formation of $N_{Zn}-V_O$ which according to Liu et al. [63] are metastable double donors. By repeating the O-rich then Zn-rich growth environment in a cyclic manner, ZnO films containing high concentrations of $N_{Zn}-V_O$ can be achieved. During the cool down after growth, the metastable nature of these donors requires an input of energy via an *in situ* anneal that must satisfy two criteria. The first is that the ambient gas must create sufficient overpressure to minimize nitrogen from leaving the film. Secondly, the thermal energy must be sufficient to promote the N on the Zn site to hop to the adjacent vacant O site, the result of which is to convert the double donor complex, $N_{Zn}-V_O$, to a double acceptor complex, $V_{Zn}-N_O$. The first condition can be met with an 450°C *in situ* anneal in N_2O since the change in the Gibbs free energy, ΔG_f , favors formation of NO and N rather than N_2 . Since the thermal energy will also break bonds between H and native defects, H^+ will diffuse through the lattice to compensate

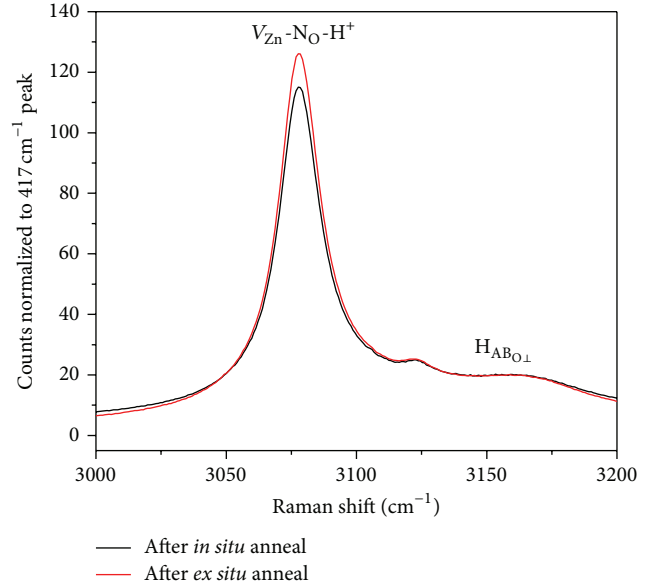


FIGURE 4: Raman spectra of a N-doped ZnO film exhibits the $V_{Zn}-N_O-H^+$ single acceptor complex at a vibration frequency of 3078 cm^{-1} after the *in situ* anneal (black) as well as after an *ex situ* 800°C O_2 anneal.

other defects. Reynolds et al. [36] used Raman spectroscopy to reveal a local vibration mode consistent with a $V_{Zn}-N_O-H^+$ single acceptor complex at a vibration frequency of the 3078 cm^{-1} (see Figure 4) that is present after the *in situ* anneal. Since H^+ always acts as a donor and its diffusivity in ZnO is high, an additional 800°C *ex situ* anneal was necessary to remove excess H^+ bound to $O_i^{-1(\text{oct})}$ and $Zn_i^{-1(\text{oct})}$ from the film as shown in Figure 5. The duration of the *ex situ* anneal is critical because the acceptor complex $V_{Zn}-N_O-H^+$ can be isochronally reduced, depending on the annealing ambient, while defects contributing to n-type conductivity are reduced. This suggests that net doping is determined by the relative rate at which acceptor and donor complexes are reduced. As long as the binding and dissociation energies are higher for the $V_{Zn}-N_O-H^+$ complex than for other H^+ -decorated species, (Figure 6) p-type conductivity prevails. Indeed, a 30 s, 800°C *ex situ* anneal in N_2 has been shown to reduce the compensating species in order to realize significant p-type conductivity, $p \sim 3.4 \times 10^{18}\text{ cm}^{-3}$, at room temperature. Consistent p-type polarity was observed on thirty Hall measurements over a range of currents within the linear regime of the IV curve. Contacts on all samples were placed at the corners; the relevance of this to correct determination of carrier type is discussed later within the context of remaining challenges. More recent preliminary magnetic data [66] show that our samples remain p-type after approximately one year, suggesting that our proposed $V_{Zn}-N_O-H^+$ complex is stable with time. Contrary to our data, others [67] have reported that p-type behavior in N-doped ZnO degrades over a period of several months becoming n-type when grown on *c*-plane sapphire. However, when grown on *a*-plane sapphire, Chen et al. [67] demonstrated p-type conduction

for more than one year. They attributed this instability for ZnO on *c*-plane sapphire to disappearance of nitrogen on the oxygen site due to compressive stresses associated with lattice misfit. Low temperature (11.6 K) PL studies of a N-doped film exhibiting RT p-type conductivity, shown in Figure 7, determined that the dominant peak is the neutral donor bound exciton (D^0X) transition at 3.361 eV [68] and the FA transition at 3.314 eV [69] that undergoes a continuous redshift with increasing temperature. The acceptor ionization energy assigned (using the method described by Wang and Giles [48]) to the $V_{Zn}-N_O-H^+$ complex is 134 meV, which is sufficiently low to allow appreciable room temperature hole conduction as we reported. The structural quality and N incorporation in our films can be assessed by X-ray diffraction scans. Figure 8 compares patterns for a N-doped film to a nominally undoped one for ZnO grown on sapphire. Both the sapphire (0006) and (0002) and (0004) reflections for ZnO are observed. Furthermore, the N-doped sample also exhibits additional (10-11) and (20-22) reflections. In all samples investigated thus far, the FWHM of the (0002) and (0004) reflections for N-doped material are slightly wider, for example, 13.0 min versus 11.5 min for nominally undoped. Using the Scherrer formula for X-ray broadening, we estimate the average crystallite size to be 50.2 nm for nominally undoped material and 44.5 nm for N-doped films. On the basis of the d-spacing for the (0004) reflection (see Figure 3.3 in [7]), we conclude that our alternating O-rich to Zn-rich growth scheme enables us to incorporate ~ 0.3 – 0.5 at % N in the films. Many have reported inferior crystalline quality of heavily N-doped films, which has led some to suggest that these films are actually polycrystalline and thus attribute p-type conduction in ZnO to be associated with grain boundaries [70]. These authors discuss segregation of impurities to grain boundaries and subsequent formation of an interfacial complex under O-rich conditions that behaves as an acceptor. Once again this appears to reinforce the concept that complex formation is required for p-type ZnO as opposed to simple impurity incorporation.

4. Summary, Conclusions, and Outlook

Zinc oxide is a fascinating material with numerous potential applications as we have discussed above. Wang et al. [71] has referred to ZnO as a unique material that has the “richest family of nanostructures among all materials, both in structure and in properties with novel applications in optoelectronics, sensors, transducers, and biomedical sciences.” These nanostructures include nanowires, nanobelts, nanorings, and nanocages, for example, and they have succeeded in fabricating a ZnO nanowire nanogenerator that is able to convert mechanical energy into electrical energy via piezoelectric to semiconductor coupling [71]. Yang et al. [72] have also described fabrication of N-doped ZnO nanowire arrays in which a DAP recombination has been observed. Although thin strain-free films of ZnO can be grown homoepitaxially, physical properties of the films can depend on uniformity of crystal quality and presence of defects over the ZnO substrate and details of the growth

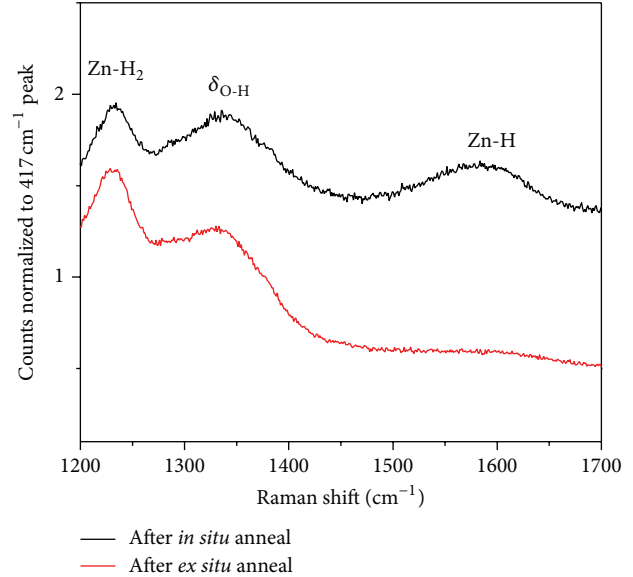


FIGURE 5: Raman spectra of a N-doped ZnO film show that excess H^+ bound to the $O_i^{-1(oct)}$ and $Zn_i^{-1(oct)}$ present after the *in situ* anneal (black) is removed from the film after the *ex situ* 800°C O_2 anneal (red).

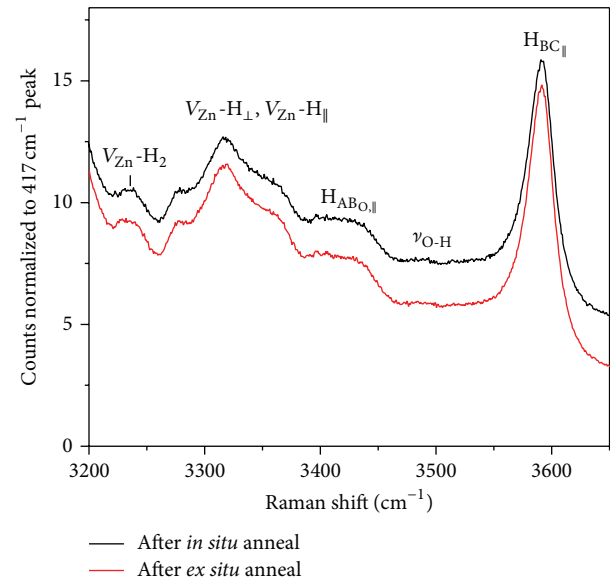


FIGURE 6: Raman spectra of a H-decorated native defects present after the *in situ* anneal (black) that are reduced after the *ex situ* 800°C O_2 anneal (red).

conditions. For example, homoepitaxial MOVPE growth of ZnO on (11–20) ZnO substrates revealed the existence of two different morphologies dependent upon the growth ambient [73]. At a growth temperature of 480°C, a needle microstructure was observed when grown in a N or $N_2O + O_2$ environment, whereas a network structure occurred in a $NO_2 + O_2$ ambient. Both films coalesced however after 15 min at 800°C. More importantly, the nitrogen atomic concentration varied by two orders of magnitude for films grown in the

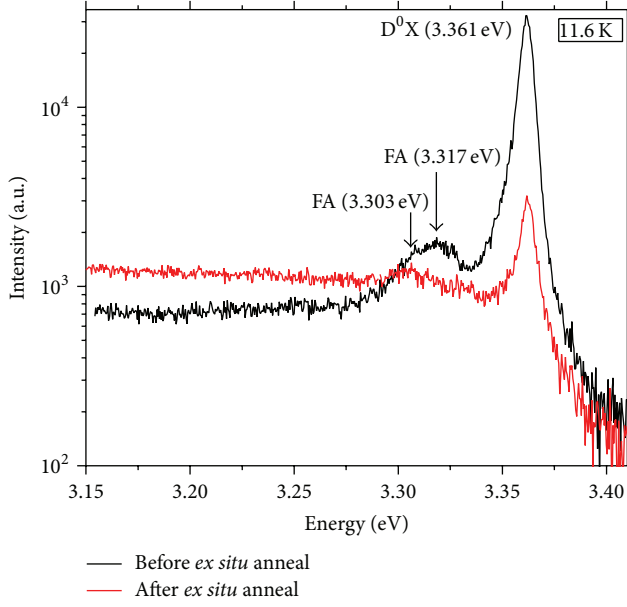


FIGURE 7: 11.6 K PL spectra of p-type ZnO before and after the *ex situ* 800°C O₂ anneal.

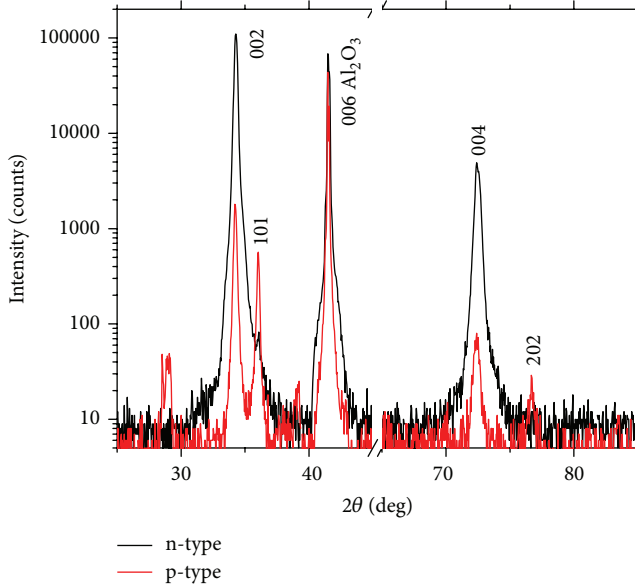


FIGURE 8: Comparison of X-ray spectra for nominally undoped (black) and N-doped (red) ZnO films grown using an alternating growth scheme.

different ambients ($5 \times 10^{17} \text{ cm}^{-3}$ for $\text{N}_2\text{O} + \text{O}_2$ and $9 \times 10^{19} \text{ cm}^{-3}$ for $\text{NO}_2 + \text{O}_2$). Using the concept of domain matching epitaxy [1, 2], ZnO thin films are also grown heteroepitaxially across the misfit scale on nonnative substrates such as sapphire and Si with misfits up to 18%. It is the latter that is particularly exciting as this would enable integration of electronics and optoelectronics on a substrate for multiple functionality. As discussed above, the dominant drawback of ZnO as an optoelectronic material has been the lack of stable and reproducible p-type conduction at room temperature. To

achieve this, one must have sufficient incorporation of the impurity species of interest with relatively shallow ionization energies without significant compensation by unintentional impurities and/or native defects. Satisfying both of these criteria is challenging.

As discussed above, there are three primary strategies that have been investigated to generate appreciable hole conductivity in ZnO at room temperature: substitution of Group IA impurities on the Zn sublattice, codoping of donors and acceptors, and substitution of Group VA impurities on the O sublattice. Recent room temperature Hall measurements are summarized in Table 1. On the basis of our analysis above regarding these data, we believe that we are able to assess the likelihood of success for functional devices utilizing each of these approaches, which enables us to postulate several conclusions that have significant impact on the promising outlook for zinc oxide.

With regard to Group IA impurities on a zinc site, the relatively low hole concentrations suggest that Li and Na are not optimum dopants in ZnO in spite of their relatively low ionization energies. The best that has been reported for Na-doped ZnO is $2.1 \times 10^{17} \text{ cm}^{-3}$ after 254 nm UV illumination [29]. Such a low doping level is marginal at best for fabricating efficient lasers and/or LEDs. Similarly, codoping of donors and acceptors has resulted in only slightly higher hole concentrations in the low- to mid- 10^{17} cm^{-3} range [21, 24, 26, 35], and it was necessary to incorporate post-growth annealing in the (Al, N) codoped films. The latter especially suggests to us that the observed p-type conductivity may be related more to formation of complexes, as discussed above for N-doping of ZnO, during an anneal than codoping per se. In spite of DFT calculations [40] that imply Ga and N codoping should be more effective for p-type behavior than Al and N codoping, a comparison of the experimental data in Table 1 reveals no difference between the two. This certainly suggests that a complete understanding of donor/acceptor codoping has thus far not been achieved.

On the basis of analysis above of recent data, it appears in general that Group VA impurities on the oxygen site and more specifically complexes involving nitrogen on an oxygen site, N_O , are the most likely to yield significant p-type conduction. While Sb-doped ZnO has resulted in an appreciable hole concentration of $1.7 \times 10^{18} \text{ cm}^{-3}$ after an 800°C post-growth *in situ* anneal and the hole concentration increased with the Sb effusion cell temperature [45], Friedrich et al. [51] recently reported that increased Sb concentrations resulted in Sb-O phase separation while Liu et al. [52] found that lower doping level concentrations lead to donor behavior. This suggests then that a fundamental doping phase space exists for Sb-doped ZnO, which can be deleterious to electronic and photonic devices.

Our view then is that N-doped ZnO holds the most promise for stable and reproducible p-type behavior. However, as we have described, it cannot be a sole substitutional nitrogen on an oxygen site as the predicted ionization energies are greater than 0.3 eV, suggesting N_O is a deep acceptor without appreciable p-type behavior at 300 K. We thus conclude that p-type conductivity in N-doped ZnO involves

formation of complexes that are shallow acceptors with ionization energies that are consistent with those reported in Table 2. It was Liu et al. [63] who used density functional theory and first suggested evolution of a shallow acceptor from a $N_{Zn}-V_O$ double donor to a N_O-V_{Zn} double acceptor. They based their analysis on the surface reaction pathways for N-doped ZnO. The initial step however was contrary to the statement by Park et al. [37] that nitrogen antisites, that is, N_{Zn} , do not exist in ZnO. But, the recent experimental results by Reynolds et al. [36] imply that formation of the initial double donor complex in an oxygen rich environment is crucial and thus support the pathway suggested by Liu et al. [63] with the caveat related to the significance of hydrogen. The significance of hydrogen in ZnO has been well documented by Van de Walle [42, 43]. Reynolds et al. [36] have recently shown that p-type conduction in ZnO thin films grown by MOVPE is associated with a three-step process in which one employs an alternating Zn-rich and O-rich growth environment to incorporate sufficient nitrogen as a metastable double donor, $N_{Zn}-V_O$, on the zinc site, an *in situ* anneal that supplies sufficient activation energy for the nitrogen to hop to the adjacent oxygen site to form the shallow acceptor complex, $V_{Zn}-N_O-H^+$, and lastly, an *ex situ* anneal to eliminate hydrogen from native defects without removing the acceptor complex. Basically then, one can view formation of p-type conduction during the *ex situ* anneal as a competition between removing H-decorated native defects without significant reduction of the $V_{Zn}-N_O-H^+$ acceptor complex, having a resultant ionization energy of ~ 134 meV. Raman spectroscopy was used to follow the reaction pathways under different growth and annealing conditions that enabled the authors to identify [36] the specific complexes involved, which are consistent with the model [63] suggested by Liu, et al. However, there are competing models [74, 75] for hole conduction, which our existing data cannot definitively exclude. These models are based on N_O pairs complexed with a hydrogen atom [74] and N_2 on a Zn site [75]. The latter in particular is intriguing considering that the deduced acceptor ionization energy of 165 meV is reasonably close to that which we have estimated. Both Liu et al. [63] and Boonchun and Lambrecht [75] are in agreement that growth on the Zn-polar surface is critical for sufficient nitrogen incorporation. Additional EPR and Raman data may help to elucidate the nature of the relevant complexes. It seems clear to us that routine observations of p-type N-doped ZnO is based on a complete understanding of the fundamental mechanisms involved and general acceptance of the applicable model.

One might ask what the outstanding challenges that remain for p-type behavior in zinc oxide are. The dominant issue that remains is demonstration of the stability and reproducibility of p-type ZnO, which can only be accomplished by additional growth under the conditions described and subsequent Hall and Raman measurements over time. There must be a critical assessment of the Hall measurements and associated data. It is generally recognized that it is difficult to make contacts to ZnO, and, hence, one might question interpretation of Hall results. One of the issues that have been discussed with regard to interpretation of Hall measurements for polarity is sample uniformity and placement of contacts.

Ohgaki et al. [76] showed that false positive Hall coefficients can be observed on n-type ZnO crystals and attributed this behavior to sample inhomogeneity. A subsequent analysis by Bierwagen et al. [77] of various sample nonuniformities and contact placement supported the results in [76]. In particular, they showed that an incorrect polarity type can be deduced in the presence of a nonuniform carrier concentration when contacts are placed in the interior of the sample. Most importantly though, they demonstrated that the correct carrier type can be inferred if contacts are placed at sample corners even if inhomogeneities exist. Recently, Macaluso et al. [78] have also questioned assignment of carrier type in not-intentionally doped ZnO grown on an InP substrate based on conflicting results from Hall data and photocurrent and C-V measurements. While their Hall measurements suggested conversion from n-type to p-type material after a post-growth anneal, the latter two techniques indicated that the material remained n-type. Thus, they attributed the anomalous Hall results to a highly conducting p-type layer at the ZnO/InP interface formed during a post-growth 600°C anneal. This may not be surprising if the defect structure in the ZnO film allowed P outdiffusion during the anneal, which would render the interfacial region to be p-type. Lastly, heteroepitaxial growth of ZnO on various substrates and orientations across the misfit scale may influence the incorporation of dopants as observed in the InP-based system [79].

In summary, recent results described herein strongly suggest that p-type conduction in zinc oxide is feasible based on nitrogen doping on the oxygen sublattice. An understanding of the reaction pathways and specific model to explain the acceptor level is the key to stable and reproducible p-type ZnO. This indeed implies a promising future for zinc oxide based thin film and nanostructured electronic and photonic devices.

Conflict of Interests

The authors declare that there is no conflict of interests regarding the publication of this paper.

References

- [1] J. Narayan and B. C. Larson, "Domain epitaxy: a unified paradigm for thin film growth," *Journal of Applied Physics*, vol. 93, no. 1, pp. 278–285, 2003.
- [2] J. Narayan, "Recent progress in thin film epitaxy across the misfit scale," *Acta Materialia*, vol. 61, no. 8, pp. 2703–2724, 2013.
- [3] V. Avrutin, D. J. Silversmith, and H. Morkoç, "Doping asymmetry problem in ZnO: current status and outlook," *Proceedings of the IEEE*, vol. 98, no. 7, pp. 1269–1280, 2010.
- [4] D. C. Look and B. Claflin, "p-type doping and devices based on ZnO," *Physica Status Solidi B*, vol. 241, no. 3, pp. 624–630, 2004.
- [5] Y. W. Heo, D. P. Norton, L. C. Tien et al., "ZnO nanowire growth and devices," *Materials Science and Engineering R*, vol. 47, no. 1–2, pp. 1–47, 2004.
- [6] Ü. Özgür, Y. I. Alivov, C. Liu et al., "A comprehensive review of ZnO materials and devices," *Journal of Applied Physics*, vol. 98, no. 4, Article ID 041301, 2005.

- [7] C. Jagadish and S. Pearton, Eds., *Zinc Oxide Bulk, Thin Films and Nanostructures*, Elsevier, New York, NY, USA, 2006.
- [8] H. Morkoc and U. Ozgur, *Zinc Oxide: Fundamentals, Materials and Device Technology*, Wiley-VCH, Weinheim, Germany, 2009.
- [9] A. Janotti and C. G. Van de Walle, "Fundamentals of zinc oxide as a semiconductor," *Reports on Progress in Physics*, vol. 72, no. 12, Article ID 126501, 2009.
- [10] Y. Segawa, H. D. Sun, T. Makino, M. Kawasaki, and H. Koinuma, "Exciton related stimulated emission in ZnO-based multiple-quantum wells," *Physica Status Solidi A*, vol. 192, no. 1, pp. 14–20, 2002.
- [11] C. H. Chia, T. Makino, K. Tamura et al., "Confinement-enhanced biexciton binding energy in ZnO/ZnMgO multiple quantum wells," *Applied Physics Letters*, vol. 82, no. 12, pp. 1848–1850, 2003.
- [12] T. Dietl, H. Ohno, F. Matsukura, J. Cibert, and D. Ferrand, "Zener model description of ferromagnetism in zinc-blende magnetic semiconductors," *Science*, vol. 287, no. 5455, pp. 1019–1022, 2000.
- [13] A. F. Kohan, G. Ceder, D. Morgan, and C. G. Van de Walle, "First-principles study of native point defects in ZnO," *Physical Review B*, vol. 61, no. 22, pp. 15019–15027, 2000.
- [14] C. G. Van de Walle, "Defect analysis and engineering in ZnO," *Physica B*, vol. 308–310, pp. 899–903, 2001.
- [15] P. Hohenberg and W. Kohn, "Inhomogeneous electron gas," *Physical Review*, vol. 136, no. 3, pp. B864–B871, 1964.
- [16] W. Kohn and L. J. Sham, "Self-consistent equations including exchange and correlation effects," *Physical Review*, vol. 140, no. 4, pp. A1133–A1138, 1965.
- [17] M. Bockstedte, A. Kley, J. Neugebauer, and M. Sheffler, "Density-functional theory calculations for poly-atomic systems: electronic structure, static and elastic properties and ab initio molecular dynamics," *Computer Physics Communications*, vol. 107, no. 1–3, pp. 187–222, 1997.
- [18] J. Neugebauer and C. G. Van de Walle, "Hydrogen in GaN: novel aspects of a common impurity," *Physical Review Letters*, vol. 75, no. 24, pp. 4452–4455, 1995.
- [19] K. Minegishi, Y. Koiwai, Y. Kikuchi, K. Yan, M. Kasuga, and A. Shimizu, "Growth of *p*-type zinc oxide films by chemical vapor deposition," *Japanese Journal of Applied Physics*, vol. 36, no. 11, Article ID L1453, 1997.
- [20] D. C. Look, D. C. Reynolds, C. W. Litton, R. L. Jones, D. B. Eason, and G. Cantwell, "Characterization of homoepitaxial *p*-type ZnO grown by molecular beam epitaxy," *Applied Physics Letters*, vol. 81, no. 10, pp. 1830–1832, 2002.
- [21] A. V. Singh, R. M. Mehra, A. Wakahara, and A. Yoshida, "*p*-type conduction in codoped ZnO thin films," *Journal of Applied Physics*, vol. 93, no. 1, pp. 396–399, 2003.
- [22] F. X. Xiu, Z. Yang, L. J. Mandalapu, D. T. Zhao, J. L. Liu, and W. P. Beyermann, "High-mobility Sb-doped *p*-type ZnO by molecular-beam epitaxy," *Applied Physics Letters*, vol. 87, no. 15, Article ID 152101, 2005.
- [23] Y. J. Zeng, Z. Z. Ye, W. Z. Xu et al., "Dopant source choice for formation of *p*-type ZnO: Li acceptor," *Applied Physics Letters*, vol. 88, no. 6, Article ID 062107, 2006.
- [24] M. Kumar, T.-H. Kim, S.-S. Kim, and B.-T. Lee, "Growth of epitaxial *p*-type ZnO thin films by codoping of Ga and N," *Applied Physics Letters*, vol. 89, no. 11, Article ID 112103, 2006.
- [25] Y. J. Zeng, Z. Z. Ye, W. Z. Xu et al., "Study on the Hall-effect and photoluminescence of N-doped *p*-type ZnO thin films," *Materials Letters*, vol. 61, no. 1, pp. 41–44, 2007.
- [26] M. Dutta, T. Ghosh, and D. Basak, "N doping and Al-N co-doping in sol-gel ZnO films: studies of their structural, electrical, optical, and photoconductive properties," *Journal of Electronic Materials*, vol. 38, no. 11, pp. 2335–2342, 2009.
- [27] C. O. Kim, D. H. Shin, S. Kim, S.-H. Choi, K. Belay, and R. G. Elliman, "Effect of (O, As) dual implantation on *p*-type doping of ZnO films," *Journal of Applied Physics*, vol. 110, no. 10, Article ID 103708, 2011.
- [28] G.-T. Du, W. Zhao, G.-G. Wu et al., "Electrically pumped lasing from *p*-ZnO/*n*-GaN heterojunction diodes," *Applied Physics Letters*, vol. 101, no. 5, Article ID 053503, 2012.
- [29] S. S. Lin, "Robust low resistivity *p*-type ZnO:Na films after ultraviolet illumination: the elimination of grain boundaries," *Applied Physics Letters*, vol. 101, no. 12, Article ID 122109, 2012.
- [30] M. A. Myers, M. T. Myers, M. J. General, J. H. Lee, L. Shao, and H. Wang, "P-type ZnO thin films achieved by N⁺ ion implantation through dynamic annealing process," *Applied Physics Letters*, vol. 101, no. 11, Article ID 112101, 2012.
- [31] J. Huang, Z. Li, S. Chu, and J. Liu, "P-type behavior of Sb doped ZnO from *p*-*n*-*p* memory structures," *Applied Physics Letters*, vol. 101, no. 23, Article ID 232102, 2012.
- [32] Z. Shi, Y. Zhang, B. Wu et al., "Vertical conducting ultraviolet light-emitting diodes based on *p*-ZnO:As/*n*-GaN/*n*-SiC heterostructures," *Applied Physics Letters*, vol. 102, no. 16, Article ID 161101, 2013.
- [33] Y. Sui, B. Yao, L. Xiao et al., "Effects of (P, N) dual acceptor doping on band gap and *p*-type conduction behavior of ZnO films," *Journal of Applied Physics*, vol. 113, no. 13, Article ID 133101, 2013.
- [34] P. Ding, X. H. Pan, Z. Z. Ye et al., "Realization of *p*-type non-polar *a*-plane ZnO films via doping of Na acceptors," *Solid State Communications*, vol. 156, pp. 8–11, 2013.
- [35] S. Kalyanaraman, R. Thangavel, and R. Vettumperumal, "High mobility formation of *p*-type Al doped ZnO:N films annealed under NH₃ ambient," *Journal of Physics and Chemistry of Solids*, vol. 74, no. 3, pp. 504–508, 2013.
- [36] J. G. Reynolds, C. L. Reynolds, A. Mohanta, J. F. Muth, J. E. Rowe, and D. E. Aspnes, "Shallow acceptor complexes in *p*-type ZnO," *Applied Physics Letters*, vol. 102, no. 15, Article ID 152114, 2013.
- [37] C. H. Park, S. B. Zhang, and S. H. Wei, "Origin of *p*-type doping difficulty in ZnO: the impurity perspective," *Physical Review B*, vol. 66, Article ID 073202, 2002.
- [38] A. Carvalho, A. Alkauskas, A. Pasquarello, A. K. Tagantsev, and N. Setter, "A hybrid density functional study of lithium in ZnO: stability, ionization levels, and diffusion," *Physical Review B*, vol. 80, no. 19, Article ID 195205, 2009.
- [39] T. Yamamoto and H. Katayama-Yoshida, "Solution using a codoping method to unipolarity for the fabrication of *p*-type ZnO," *Japanese Journal of Applied Physics*, vol. 38, no. 2, pp. L166–L169, 1999.
- [40] X. M. Duan, C. Stampfl, M. M. M. Bilek, and D. R. McKenzie, "Codoping of aluminum and gallium with nitrogen in ZnO: a comparative first-principles investigation," *Physical Review B*, vol. 79, no. 23, Article ID 235208, 2009.
- [41] X. M. Duan, C. Stampfl, M. M. M. Bilek, D. R. McKenzie, and S.-H. Wei, "Design of shallow acceptors in ZnO through early transition metals codoped with N acceptors," *Physical Review B*, vol. 83, no. 8, Article ID 085202, 2011.
- [42] C. G. Van de Walle, "Hydrogen as a cause of doping in ZnO," *Physical Review Letter*, vol. 85, article 1012, 2000.

- [43] C. G. Van de Walle and A. Janotti, "Hydrogen in oxides and nitrides: unexpected physics and impact on devices," *IOP Conference Series: Materials Science and Engineering*, vol. 15, Article ID 012001, 2010.
- [44] S.-H. Park, T. Minegishi, D.-C. Oh et al., "*p*-type conductivity of heteroepitaxially grown ZnO films by N and Te codoping and thermal annealing," *Journal of Crystal Growth*, vol. 363, pp. 190–194, 2013.
- [45] D. C. Look and B. Claffin, "High-quality melt-grown ZnO single crystals," *Physica Status Solidi B*, vol. 241, no. 3, pp. 624–630, 2004.
- [46] E.-C. Lee, Y.-S. Kim, Y.-G. Jin, and K. J. Chang, "Compensation mechanism for N acceptors in ZnO," *Physical Review B*, vol. 64, no. 8, Article ID 085120, 2001.
- [47] J. L. Lyons, A. Janotti, and C. G. Van de Walle, "Why nitrogen cannot lead to *p*-type conductivity in ZnO," *Applied Physics Letters*, vol. 95, no. 25, Article ID 252105, 2009.
- [48] L. Wang and N. C. Giles, "Determination of the ionization energy of nitrogen acceptors in zinc oxide using photoluminescence spectroscopy," *Applied Physics Letters*, vol. 84, no. 16, pp. 3049–3051, 2004.
- [49] J. E. Stehr, X. J. Wang, S. Filippov et al., "Defects in N, O, and N, Zn implanted ZnO bulk crystals," *Journal of Applied Physics*, vol. 113, no. 10, Article ID 103509, 2013.
- [50] H. von Wenckstern, G. Benndorf, S. Heitsch et al., "Properties of phosphorus doped ZnO," *Applied Physics A*, vol. 88, no. 1, pp. 125–128, 2007.
- [51] F. Friedrich, I. Sieber, C. Klimm, M. Klaus, C. Genzel, and N. H. Nickel, "Sb-doping of ZnO: phase segregation and its impact on *p*-type doping," *Applied Physics Letters*, vol. 98, no. 13, Article ID 131902, 2011.
- [52] H. Y. Liu, N. Izyumskaya, V. Avrutin et al., "Donor behavior of Sb in ZnO," *Journal of Applied Physics*, vol. 112, no. 3, Article ID 033706, 2012.
- [53] A. B. Yankovich, B. Puchala, F. Wang et al., "Stable *p*-type conduction from Sb-decorated head-to-head basal plane inversion domain boundaries in ZnO nanowires," *Nano Letters*, vol. 12, no. 3, pp. 1311–1316, 2012.
- [54] S. G. Louie, S. Froyen, and M. L. Cohen, "Nonlinear ionic pseudopotentials in spin-density-functional calculations," *Physical Review B*, vol. 26, no. 4, pp. 1738–1742, 1982.
- [55] M. C. Tarun, M. Z. Iqbal, and M. D. McCluskey, "Nitrogen is a deep acceptor in ZnO," *AIP Advances*, vol. 1, no. 2, Article ID 022105, 2011.
- [56] D. C. Look, *Electrical Characterization of GaAs Materials and Devices*, John Wiley & Sons, New York, NY, USA, 1989.
- [57] T. J. Coutts, X. Li, T. M. Barnes et al., "Chapter 3—synthesis and characterization of nitrogen-doped ZnO films grown by MOCVD," in *Zinc Oxide Bulk, Thin Films and Nanostructures*, C. Jagadish and S. Pearton, Eds., pp. 43–83, Elsevier, New York, NY, USA.
- [58] A. Kaschner, U. Haboeck, M. Strassburg et al., "Nitrogen-related local vibrational modes in ZnO:N," *Applied Physics Letters*, vol. 80, no. 11, pp. 1909–1911, 2002.
- [59] J. B. Wang, H. M. Zhong, Z. F. Li, and W. Lu, "Raman study of N⁺-implanted ZnO," *Applied Physics Letters*, vol. 88, no. 10, Article ID 101913, 2006.
- [60] M. Schirra, R. Schneider, A. Reiser et al., "Acceptor-related luminescence at 3.314 eV in zinc oxide confined to crystallographic line defects," *Physica B*, vol. 401–402, pp. 362–365, 2007.
- [61] Y. R. Ryu, T. S. Lee, and H. W. White, "Properties of arsenic-doped *p*-type ZnO grown by hybrid beam deposition," *Applied Physics Letters*, vol. 83, no. 1, pp. 87–89, 2003.
- [62] P. Li, S. Deng, G. Liu, and K. Hou, "Comprehensive investigations on the feasibility of nitrogen as a *p*-type dopant in ZnO," *Chem Phys. Lett*, vol. 543, pp. 92–95, 2012.
- [63] L. Liu, J. Xu, D. Wang et al., "*p*-Type conductivity in N-doped ZnO: the role of the N_{Zn}-V_O complex," *Physical Review Letters*, vol. 108, Article ID 215501, 2012.
- [64] J. D. Ye, S. L. Gu, F. Li et al., "Correlation between carrier recombination and *p*-type doping in P monodoped and In-P codoped ZnO epilayers," *Applied Physics Letters*, vol. 90, no. 15, Article ID 152108, 2007.
- [65] C. R. A. Catlow, A. A. Sokol, and A. Walsh, "Microscopic origins of electron and hole stability in ZnO," *Chemical Communications*, vol. 47, no. 12, pp. 3386–3388, 2011.
- [66] C. L. Reynolds Jr. and J. G. Reynolds, "Preliminary magnetization vs applied field indicate that films are *p*-type," unpublished.
- [67] X. Chen, Z. Zhang, B. Yao et al., "Effect of compressive stress on stability of N-doped *p*-type ZnO," *Applied Physics Letters*, vol. 99, no. 9, Article ID 091908, 2011.
- [68] B. K. Meyer, H. Alves, D. M. Hofmann et al., "Bound exciton and donor-acceptor pair recombinations in ZnO," *Physica Status Solidi B*, vol. 241, no. 2, pp. 231–260, 2004.
- [69] J. W. Sun, Y. M. Lu, Y. C. Liu et al., "Nitrogen-related recombination mechanisms in *p*-type ZnO films grown by plasma-assisted molecular beam epitaxy," *Journal of Applied Physics*, vol. 102, no. 4, Article ID 043522, 2007.
- [70] J. M. Carlsson, H. S. Domingos, P. D. Bristowe, and B. Hellsing, "An interfacial complex in ZnO and its influence on charge transport," *Physical Review Letters*, vol. 91, no. 16, Article ID 165506, 2003.
- [71] X. Wang, J. Song, J. Liu, and Z. L. Wang, "Direct-current nanogenerator driven by ultrasonic waves," *Science*, vol. 316, no. 5821, pp. 102–105, 2007.
- [72] B. Yang, P. Feng, A. Kumar, R. S. Katiyar, and M. Achermann, "Structural and optical properties of N-doped ZnO nanorod arrays," *Journal of Physics D*, vol. 42, no. 19, Article ID 195402, 2009.
- [73] J. M. Pierce, B. T. Adekore, R. F. Davis, and F. A. Stevie, "Homoepitaxial growth of dense ZnO (0001) and ZnO (11–20) films via MOVPE on selected ZnO substrates," *Journal of Crystal Growth*, vol. 283, no. 1–2, pp. 147–155, 2005.
- [74] S. Lautenschlaeger, M. Hofmann, S. Eisermann et al., "A model for acceptor doping in ZnO based on nitrogen pair formation," *Physica Status Solidi B*, vol. 248, no. 5, pp. 1217–1221, 2011.
- [75] A. Boonchun and W. R. Lambrecht, "Electronic structure of defects and doping in ZnO: oxygen vacancy and nitrogen doping," *Physica Status Solidi B*, vol. 250, no. 10, pp. 2091–2101, 2013.
- [76] T. Ohgaki, N. Ohashi, S. Sugimura et al., "Positive Hall coefficients obtained from contact misplacement on evident n-type ZnO films and crystals," *Journal of Materials Research*, vol. 23, no. 9, pp. 2293–2295, 2008.
- [77] O. Bierwagen, T. Ive, C. G. Van de Walle, and J. S. Speck, "Causes of incorrect carrier-type identification in Van der Pauw-Hall measurements," *Applied Physics Letters*, vol. 93, no. 24, Article ID 242108, 2008.
- [78] R. Macaluso, M. Mosca, C. Cali et al., "Erroneous *p*-type assignment by Hall effect measurements in annealed ZnO films grown on InP substrate," *Journal of Applied Physics*, vol. 113, no. 16, Article ID 164508, 2013.
- [79] C. L. Reynolds Jr. and J. A. Grenko, "Crystallographic plane dependent Fe and Si dopant incorporation and activation in InP," *Physica Status Solidi A*, vol. 206, no. 4, pp. 691–696, 2009.

Research Article

Synthesis and Dielectric Studies of Monoclinic Nanosized Zirconia

I. Flavia Princess Nesamani,¹ V. Lakshmi Prabha,² Aswathy Paul,¹ and D. Nirmal¹

¹ Department of Electronics and Communication Engineering, Karunya University, Coimbatore 641114, India

² Department of Electronics and Communication Engineering, Government College of Technology, Coimbatore 641013, India

Correspondence should be addressed to I. Flavia Princess Nesamani; flavia@karunya.edu

Received 11 October 2013; Revised 22 December 2013; Accepted 5 January 2014; Published 16 February 2014

Academic Editor: Nian X. Sun

Copyright © 2014 I. Flavia Princess Nesamani et al. This is an open access article distributed under the Creative Commons Attribution License, which permits unrestricted use, distribution, and reproduction in any medium, provided the original work is properly cited.

Zirconium dioxide is a prospective high- κ material that can replace silicon dioxide. Zirconium dioxide nanoparticle has been synthesized using sol-gel process at room temperature. The structural and morphological characterization of the nanoscaled zirconium dioxide is done using FTIR, SEM, X-ray diffraction, and TEM. The particle size of the synthesized ZrO_2 is observed in the range of 50–80 nm with an average crystallite size of 2–10 nm. The results are compared with commercial coarse zirconia which showed a particle size in the range of 900 nm–2.13 μ m and crystallite size of 5.3 nm–20 nm. It is expected that both nanoscaling and the high dielectric constant of ZrO_2 would be useful in replacing the low- κ SiO_2 dielectric with high- κ ZrO_2 for CMOS fabrication technology. The synthesized ZrO_2 is subjected to impedance analysis and it exhibited a dielectric constant of 25 to find its application in short channel devices like multiple gate FinFETS and as a suitable alternative for the conventional gate oxide dielectric SiO_2 with dielectric value of 3.9, which cannot survive the challenge of an end of oxide thickness ≤ 1 nm.

1. Introduction

The ever growing semiconductor industry has turned towards nanoscaled devices with high- κ metal oxide gate dielectrics along with tuneable metal gates in transistor manufacturing processes to meet the need for high speed transistors, while maintaining low power consumption. The best metal oxide to replace Silicon dioxide is hafnia or zirconia (HfO_2/ZrO_2). The particles when synthesized in the magical dimension scale of nanometer [1] have wide applications with the improvement of the electrical, mechanical, and optical properties of any compound due to the increase in surface area. Zirconia, a metal oxide, is expected to be invariant with higher thermal expansion ratio in an FET configuration. A figure of merit to judge a high- κ gate dielectric layer is the equivalent oxide thickness (EOT) = $(\kappa_{SiO_2}/\kappa_{high-\kappa})d\kappa$. If a dielectric material with a higher dielectric constant (high- κ) can replace SiO_2 ,

the dielectric layer thickness can be increased proportionally while keeping the same gate capacitance [2, 3]. Since a thicker layer is used for insulation, the tunnelling current is drastically reduced in the tunnelling region. Meanwhile, before incorporating a new high- κ material into the present ULSI process flow, many requirements, like particle size, capacitance at different thickness of the material, and so forth, need to be optimized [4–8]. One of the most crucial elements that allow the successful scaling is certainly the material and electrical properties of ZrO_2 [4, 5, 9–11] offsets compared to the reported band gap of 5.16 to 7.8 eV for ZrO_2 . Among the high- κ materials, ZrO_2 is a promising candidate in multiple gate FinFETS and a lot of research works focus on this material [2]. Pure zirconia exhibits three stages of polymorphism. The monoclinic, tetragonal, and cubical symmetries are stable up to the temperature range of 1100°C, between 1100 and 2370°C, and above 2370°C, respectively.

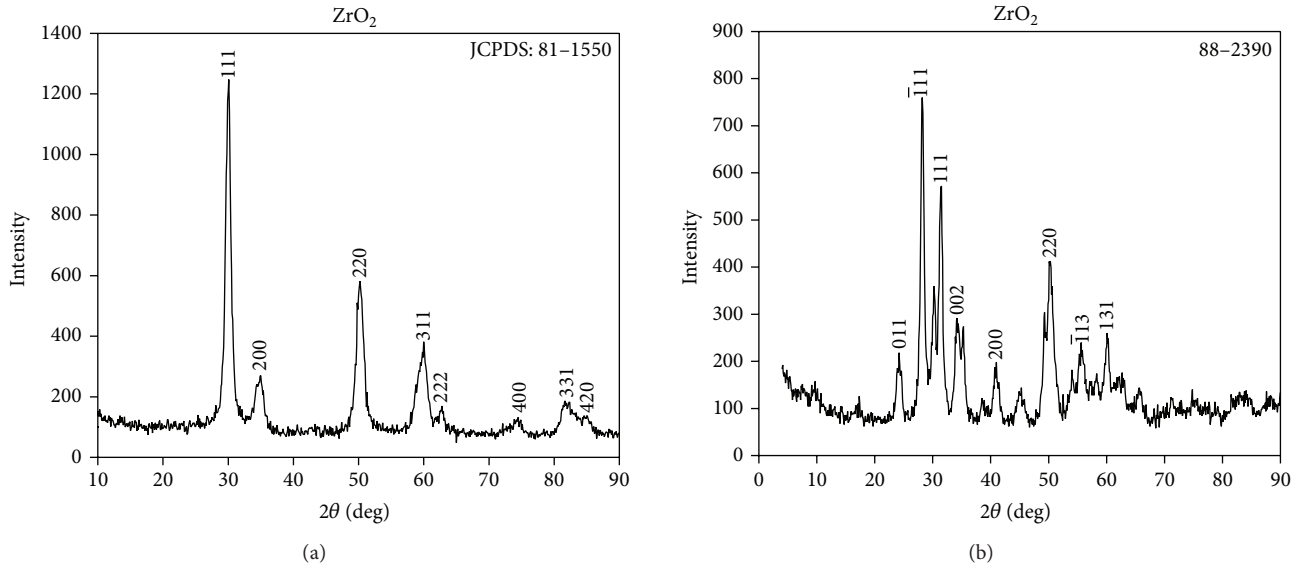
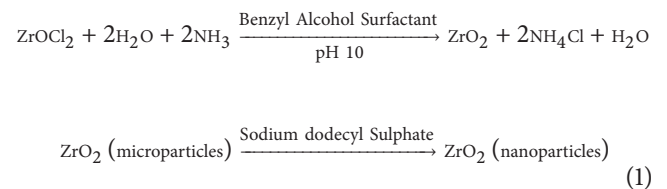


FIGURE 1: (a) and (b): XRD pattern of coarse zirconia and synthesized zirconia.

Zirconium dioxide, from the group of ceramic semiconductors, possesses special transition-metal oxide properties. The ceramic based zirconia is used in variety of applications such as technological and commercial applications, for example, catalyst, oxygen sensors, and high dielectric constant material for large scale integrated circuit. Zirconium dioxide has good thermal stability, high strength, low thermal conductivity, and high corrosion resistance. It is an excellent high- κ gate oxide dielectric widely accepted in high- κ /metal gate stacks for CMOS fabrication technology. Zirconium oxide can be prepared by sol-gel technique (Brinker and Scherer, 1990 [12]) using inorganic precursors like $ZrOCl_2$ or metal organic precursors like zirconium alkoxides [13]. Considering the development of new materials, the experimental conditions can be adjusted in order to get stable or metastable compounds. Most studies performed in the field focus on the synthesis of materials with mixed composition [14–17]. The physical and chemical properties of mixed oxides prepared through sol-gel process are of great interest due to their thermal and chemical stability. Besides they are highly acidic because of the presence of OH groups on the surface [18]. Stable dispersions, or sols, of small particles (less than 0.1 micrometre) are formed from precursor chemicals such as metal alkoxides or other metalorganics [18]. By partial evaporation of the liquid or addition of a suitable initiator, a polymer-like, three-dimensional bonding takes place within the sol to form a gelatinous network or gel. The gel can then be dehydrated and calcined to obtain a fine, intimately mixed ceramic powder. This paper presents the synthesis using solgel process and material characterization of the nanoscaled zirconia through FTIR, SEM, TEM, and XRD analysis along with the evaluation of dielectric constant through impedance spectroscopy test.

2. Experimental

2.1. Synthesis Method. In this work, one of the widely used cost effective sol-gel method [1, 5, 14, 16, 18] is employed for the preparation of ZrO_2 . The powders with different particle size, morphology, and phase composition can be prepared by varying parameters such as temperature, duration of the processing, and concentration of chemical species to solution [1]. 15 mmol of zirconium oxychloride ($ZrOCl_2$ Sigma Aldrich) is dissolved in distilled water and aqueous ammonia is added drop by drop under constant stirring using magnetic stirrer to form gel-like precipitate until it reached a pH value of 10. The chemical equation is given as



30 mmol of benzyl alcohol was added as surfactant to reduce the surface tension. 30 mmol of sodium dodecyl sulphate is used as phase transition catalyst to form nanoparticle size. Then, the precipitate is filtered through high grade Whatman filter of nanopore size and thoroughly washed with water until elimination of chloride using deionized water. The precipitate is then dried in an oven for 24 hr at 120°C. The solid zirconium dioxide is calcined at 750°C for 2 hrs twice to obtain zirconium dioxide in the white powder form.

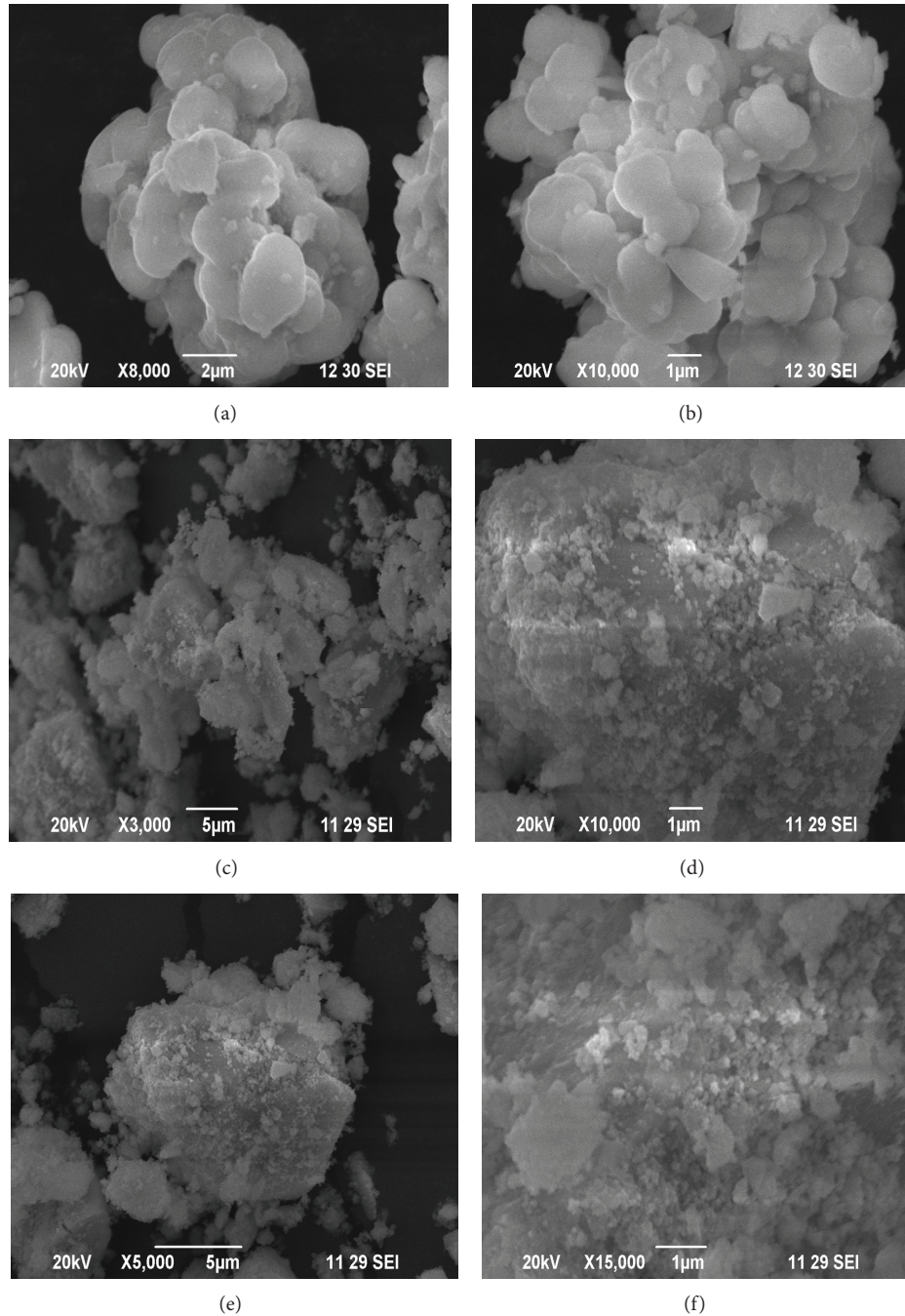


FIGURE 2: [(a)-(b)]: SEM images of coarse zirconia; [(c)-(f)]: SEM images of synthesized zirconium dioxide.

2.2. Characterization. The particle size distribution was analyzed by Fourier Transform Infrared Spectroscopy done using Shimadzu IR Prestige-21 using KBR pelletizer in the wavelength range of $400\text{--}4000\text{ cm}^{-1}$ with a resolution of 2 cm^{-1} . X-ray diffraction was taken with Shimadzu, Japan Model XRD 6000 at room temperature using target of $\text{CuK}\alpha$ with a voltage of 40.0 (kV) and a current of 30.0 (mA) for 2θ between 10° and 90° with a sampling pitch of 1° in scan mode

of continuous scan and scan speed of 10 (deg/min). SEM microstructural analysis was performed using a JEOL JSM-6390 microscope. The samples were ultrasonically dispersed in ethanol, deposited on a carbon film supported on a copper grid, and subjected for SEM analysis. TEM microstructural analysis was performed using JOEL JM 2010. Advanced analytical high resolution enables us to give morphological, chemical, and structure information. Electron diffraction

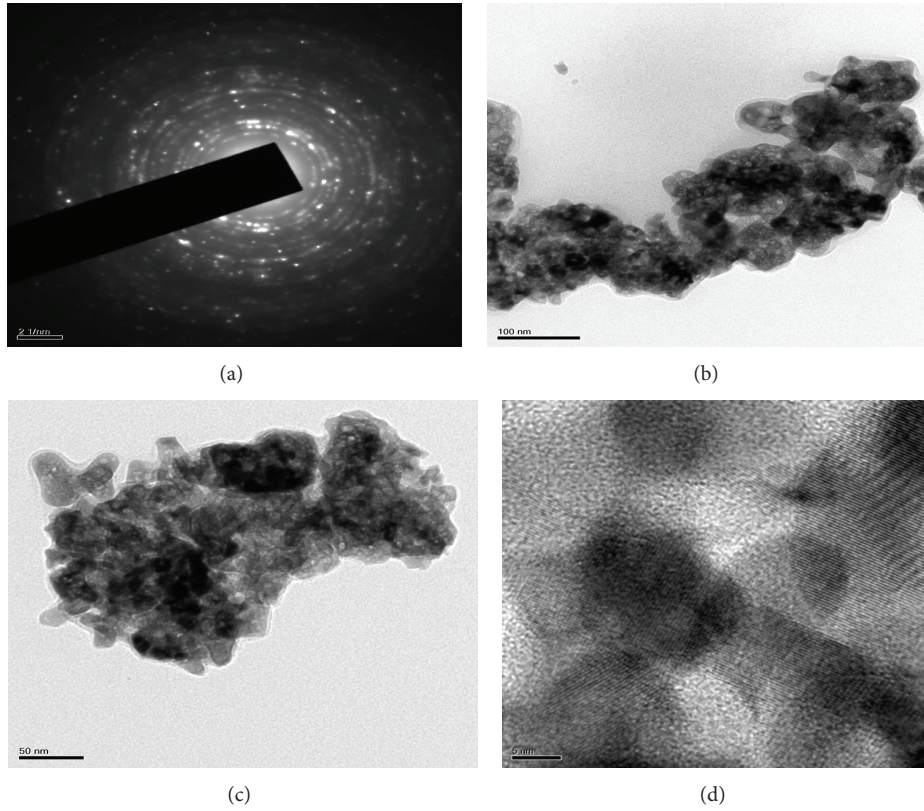


FIGURE 3: (a) Corresponding selected area diffraction, (b) 100 nm, (c) 50 nm, and (d) 5 nm. TEM images of sol-gel synthesized zirconium dioxide.

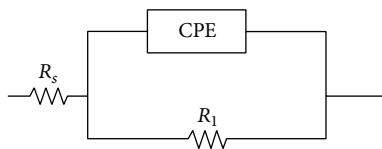


FIGURE 4: Equivalent circuit of impedance fit.

crystallographic studies were done on synthesized zirconia powder and SAED (selected area electron diffraction) pattern and CBED (convergent beam electron diffraction) pattern were taken for the sample. The sample was mixed with ethanol and ultrasonically vibrated for 5 minutes and it is coated on carbon coated copper grid and the powder is allowed to dry for 5 minutes before taking the patterns. For the impedance analysis, the powder is sprayed in a die of diameter 10 mm and the thickness of 1.29 mm applying a pressure of 200 Psi. The pellet was sintered at 300°C for 1 hr. Then, the pellet is calcined at various temperatures upto a maximum of 750°C. Increase in processing temperatures (sintering and calcining) results in increase of grain size and reduction of pores or vacancies. Increase in temperature increases the grain size which in turn influences the dielectric

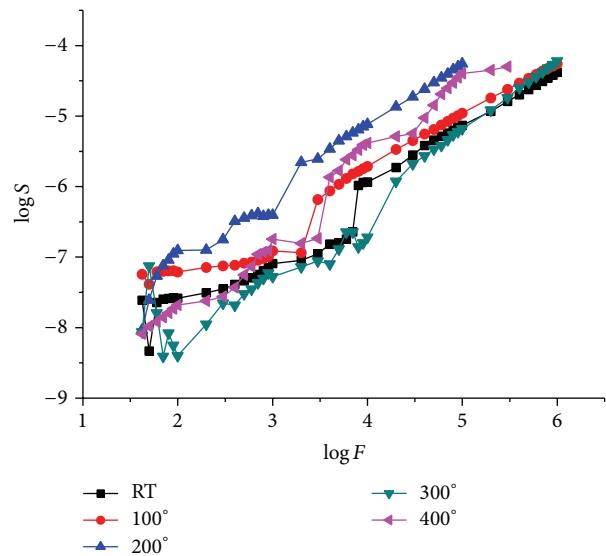


FIGURE 5: Comparison of conductivity graph versus $\log \sigma$ for the results ranging from room temperature to 400°C.

and electrical properties of the sample. The growth of grain size is not seen after 750°C and, hence, the dielectric constant

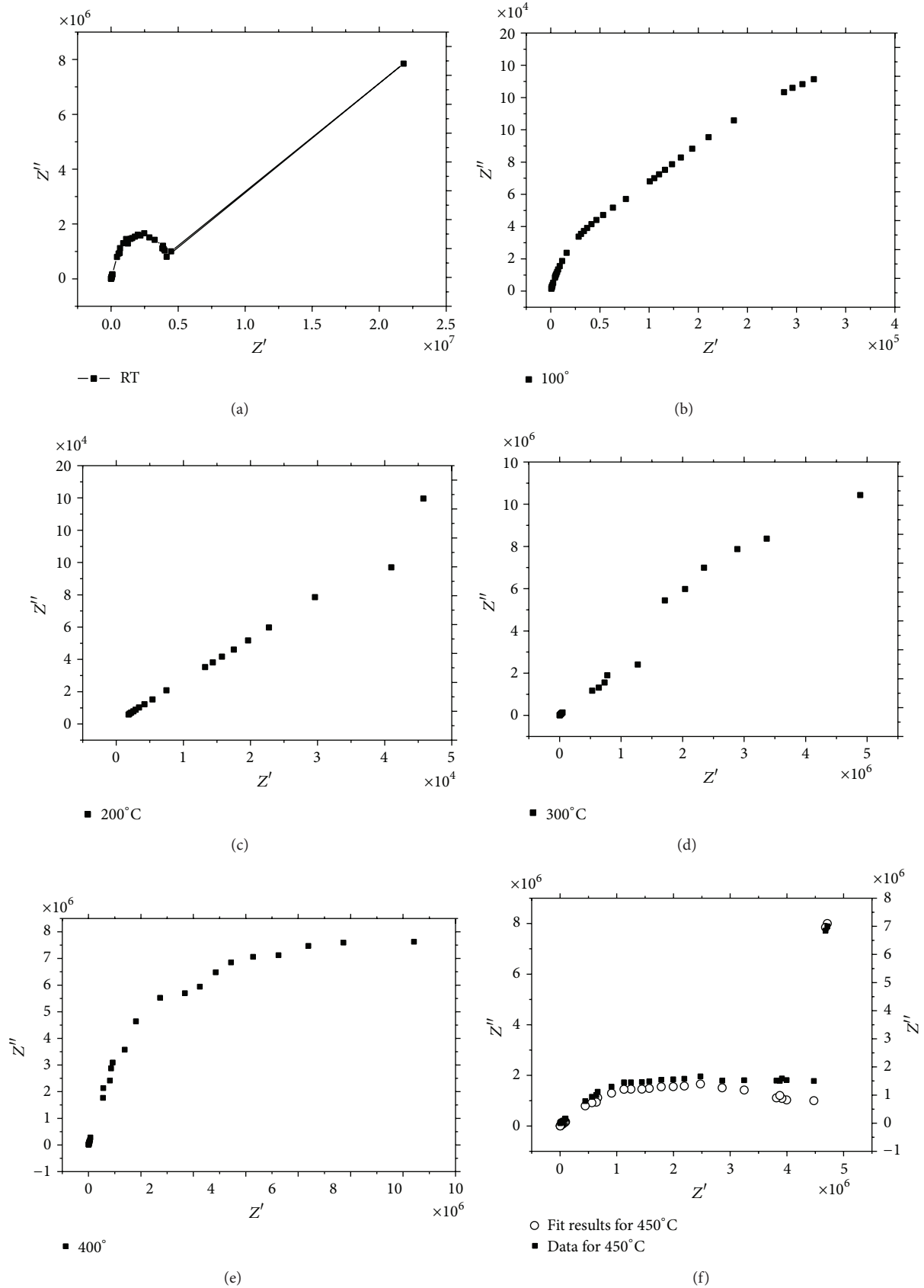


FIGURE 6: (a)–(e) Cole-cole plot of synthesized zirconia at different temperatures. (f) Impedance spectra plot of zirconium oxide with fit results at 450°C.

also remains constant after this temperature. The grain size growth was observed upto 750°C [19–23] and also it is confirmed that the grain did not grow bigger in size after 750°C [2]. This helps zirconia to have a constant dielectric. The impedance measurements were made with the Impedance Analyzer Hioki 3532-50 LCR Hi Tester with a frequency range of 42 Hz–5 MHz at room temperature as well at elevated temperatures from 50°C to 550°C at the intervals of 50°C. To avoid any diffusion problems, electrodes were not applied on the substrate but the sample was ensured to make complete contact with the electrodes by pressure contact.

3. Results and Discussion

The results of Fourier Transform Infrared Spectroscopy of coarse zirconia showed a strong peak of absorption at 1082.07 cm⁻¹ and two weak peaks at 856.39 cm⁻¹ and 877.61 cm⁻¹ ensuring that the commercial sample is cubic zirconia; however, the synthesized zirconia after calcination at 750°C for two hours twice showed none of the major peaks except a small peak at 860.1 cm⁻¹. Structural and morphological elucidations were checked using XRD (Figure 1), SEM (Figure 2), and TEM (Figure 3). The crystallite size of ZrO₂ was estimated by XRD peaks. The reduction of size by sol-gel procedure was confirmed by different trials and all samples exhibit only peaks corresponding to typical ZrO₂, [111], [200], and [220] planes. Using the diffraction peaks the crystallite size was calculated through Scherrer's equation $D = (0.9\lambda/\beta \cos \theta)$ and was found to fall in a range from 2 nm to 10 nm.

The size of the particles of sol-gel synthesized zirconia, an average diameter of 50 to 80 nm particles sampled at random, was assessed from the corresponding SEM micrographs, whereas for coarse zirconia, the particle size was found to be in the range of 900 nm to 2.13 μm (Figures 2(a) and 2(b)).

Coarse zirconia has a cubical structure which is inferred from the lattice parameters as indicated from JCPDS file “a = b = c = 5.129 Å” with a crystallite size of 5.3 nm to 20 nm and particle size of 900 nm–2.13 μm and the synthesized zirconia after calcination at 750°C for 4 hours showed monoclinic structure with the lattice parameters indicated from JCPDS file as “a = 5.25, b = 5.204 and c = 5.213 Å” with particle size of 50 nm–80 nm and crystallite size of 2–10 nm determined by Debye-Scherrer method calculated using formula $D = k\lambda/\beta \cos \theta$. The XRD pattern (Figure 1) of resulting synthesized zirconia is of monoclinic structure that is stable up to 1100°C preferable for CMOS fabrication and it can replace SiO₂ which has same stability. The SEM and TEM micrographs indicate that the ZrO₂ nanoparticles after calcination were small, monoclinic crystallites in [111], [200], and [220] planes, and that they agglomerated to some extent because of nanocrystalline size and particles getting closer to each other. The obtained impedance spectra were fit to the theoretical equivalent circuit (Figure 4) using Z-Plot software [2, 24]. The values obtained from the fit and the actual data at 550°C are as follows. The equivalent circuit is obtained using the fit and consists of $R_s = 1.5K \Omega$, $R_1 = 3.05 \times 10^6 \Omega$, $C_{PEIT} = 1.174 \times 10^{-11} F$, and $C_{PEIP} = 0.98$ with the peak frequency $f = 3 \times 10^4$ Hz, where $\omega\tau = 1$. The capacitance

and dielectric loss were also measured at this frequency and is found to be $C_p = 1.7376 \times 10^{-11} F$. The same analysis has been made for all the temperatures from room temperature to 550°C. The dielectric constant of zirconia was found from the formula $C = \epsilon_0 \epsilon_r A/d$, where ϵ_0 is permittivity of vacuum, ϵ_r is permittivity of zirconia, A is Area of the pellet, and d is diameter of the pellet. The calculated value of nanosized zirconium oxide obtained from the results is 25. Also the conductivity values were verified using log F versus log σ plot (Figure 5) and cole-cole plot (Figures 6(a)–2(f)) and the conductivity was found to be equal at room temperature and at 450°C. The resistance was in the range of 10⁶–10⁷ proving that the nanosized synthesized zirconia has good dielectric constant of 25 [2, 25–28].

4. Conclusion

In this paper, nanocrystallite monoclinic zirconia powder with particle size of 50–100 nm and crystallite size of 2 nm–10 nm is obtained by sol-gel method, whereas coarse zirconia has a particle size of 1 μm to 2 μm with a crystallite size of 50 nm–90 nm. The significant divergence of the phase composition, morphology, and the particle size has been found. The monoclinic phase is found to be predominant for the calcination temperatures up to 750°C [29]. The impedance profile of the nanosized zirconia gave a dielectric constant of 25 [2, 23, 26–28]. This work will be useful in the fabrication of nanosized zirconia as thin films to the required equivalent oxide thickness and analyzing the same for the high- κ gate dielectric materials. When compared with HfO₂, a rare earth metal, ZrO₂, is cheaper and exhibits the same electrical properties as that of HfO₂, which made it viable to be used in designing a high- κ /metal gate, multigate MOSFET, with improved electrical characteristics.

Conflict of Interests

The authors declare that there is no conflict of interests regarding the publication of this paper.

Acknowledgments

The authors would like to thank Dr. Haris for the valuable suggestions and Karunya University, Coimbatore, for providing the facilities to carry out this work.

References

- [1] M. R. H. Siddiqui, A. I. Al-Wassil, A. M. Al-Otaibi, and R. M. Mahfouz, “Effects of precursor on the morphology and size of ZrO₂ nanoparticles, synthesized by sol-gel method in non-aqueous medium,” *Materials Research*, vol. 15, no. 6, pp. 986–989, 2012.
- [2] D. Nirmal, B. Nalini, and P. Vijaya Kumar, “Nanosized high κ dielectric material for FINFET,” *Integrated Ferroelectrics*, vol. 121, no. 1, pp. 31–35, 2010.
- [3] M. N. Tahir, L. Gorgishvili, J. Li et al., “Facile synthesis and characterization of monocrySTALLINE cubic ZrO₂ nanoparticles,” *Solid State Sciences*, vol. 9, no. 12, pp. 1105–1109, 2007.

- [4] R. M. C. de Almeida and I. J. R. Baumvol, "Diffusion-reaction Modeling of silicon oxide interlayer growth during thermal annealing of high dielectric constant materials on silicon," *Surface Science Reports*, vol. 49, p. 1, 2003.
- [5] J. A. Wang, M. A. Valenzuela, J. Salmones, A. Vázquez, A. García-Ruiz, and X. Bokhimi, "Comparative study of nanocrystalline zirconia prepared by precipitation and sol-gel methods," *Catalysis Today*, vol. 68, no. 1–3, pp. 21–30, 2001.
- [6] M. Balog, M. Schieber, M. Michman, and S. Patai, "The chemical vapour deposition and characterization of ZrO_2 films from organometallic compounds," *Thin Solid Films*, vol. 47, no. 2, pp. 109–120, 1977.
- [7] B. Králik, E. K. Chang, and S. G. Louie, "Structural properties and quasiparticle band structure of zirconia," *Physical Review B*, vol. 57, no. 12, pp. 7027–7036, 1998.
- [8] P. Abelard and J. Baumard, "The electrical conductivity of cubic stabilized zirconia," *Pure and Applied Chemistry*, vol. 67, no. 11, pp. 1891–1940, 1995.
- [9] M. S. Lundstrom and J. Guo, *Nano Scale Transistors: Device Physics, Modelling and Simulation*, vol. 39 of *Silicon Moore's Law*, Springer, New York, NY, USA, 2006.
- [10] P. M. Zeitzoff, J. A. Hutchby, G. Bersuker, and H. R. Huff, "Integrated circuit technologies: from conventional CMOS to nanoscale era," in *Nano and Giga Challenges in Microelectronics*, J. Greer, A. Korkein, and J. Labanowski, Eds., pp. 1–25, Elsevier, New York, NY, USA, 2003.
- [11] <http://www.itrs.net/Links/2008ITRS/Home2008.htm>.
- [12] C. Jeffrey Brinker and G. W. Scherer, *Sol-Gel Science: The Physics and Chemistry of Sol-Gel Processing*, 1990.
- [13] L. E. Davies, N. A. Bonini, S. Locatelli, and E. E. Gonzo, "Characterization and catalytic activity of zirconium dioxide prepared by sol-gel," *Latin American Applied Research*, vol. 35, no. 1, pp. 23–28, 2005.
- [14] M. D. Curran, D. D. Pooré, and A. E. Stiegman, "Vanadia-silica sol-gel derived glass: factors affecting homogeneity and morphology," *Chemistry of Materials*, vol. 10, no. 10, pp. 3156–3166, 1998.
- [15] K. Yanagisawa, Y. Yamamoto, Q. Feng, and N. Yamasaki, "Formation mechanism of fine anatase crystals from amorphous titania under hydrothermal conditions," *Journal of Materials Research*, vol. 13, no. 4, pp. 825–829, 1998.
- [16] Z. Zhan and H. C. Zeng, "A catalyst-free approach for sol-gel synthesis of highly mixed ZrO_2 - SiO_2 oxides," *Journal of Non-Crystalline Solids*, vol. 243, no. 1, pp. 26–38, 1999.
- [17] V. Santos, M. Zeni, C. P. Bergmann, and J. M. Hohemberger, "Correlation between thermal treatment and tetragonal/monoclinic nanostructured zirconia powder obtained by sol-gel process," *Reviews on Advanced Materials Science*, vol. 17, no. 1-2, pp. 62–70, 2008.
- [18] C. J. Brinker, G. C. Frye, A. J. Hurd, and C. S. Ashley, "Fundamentals of sol-gel dip coating," *Thin Solid Films*, vol. 201, no. 1, pp. 97–108, 1991.
- [19] G. D. Wilk, R. M. Wallace, and J. M. Anthony, "High- κ gate dielectrics: current status and materials properties considerations," *Journal of Applied Physics*, vol. 89, no. 10, pp. 5243–5275, 2001.
- [20] A. Manan, Y. Iqbal, and I. Qazi, "The effect of sintering temperature on phase, microstructure and properties of $Sr_5Nb_4TiO_{17}$," *Journal of Physics*, vol. 241, no. 1, Article ID 012028, 2010.
- [21] R. Pandu, K. L. Yadav, A. Kumar, P. Ravinder Reddy, and A. V. S. S. K. S. Gupta, "Effect of sintering temperature on structural and electrical properties of $BiFeO_3$ multiferroics," *Indian Journal of Engineering and Materials Sciences*, vol. 17, no. 6, pp. 481–485, 2010.
- [22] G.-Y. Guo and Y.-L. Chen, "A nearly pure monoclinic nanocrystalline zirconia," *Journal of Solid State Chemistry*, vol. 178, no. 5, pp. 1675–1682, 2005.
- [23] K. Geethalakshmi, T. Prabhakaran, and J. Hemalatha, "Dielectric studies on nano zirconium dioxide synthesized through coprecipitation process, world academy of science," *Engineering and Technology*, vol. 64, pp. 179–182, 2012.
- [24] <http://www.gamry.com/>.
- [25] D. Nirmal, P. Vijayakumar, D. M. Thomas, B. K. Jebalin, and N. Mohankumar, "Subthreshold performance of gate engineered FinFET devices and circuit with high K dielectrics," *Microelectronics Reliability*, vol. 53, pp. 499–504, 2013.
- [26] P. J. Harrop and J. N. Wanklyn, "The dielectric constant of zirconia," *British Journal of Applied Physics*, vol. 18, no. 6, article 305, pp. 739–742, 1967.
- [27] Y. Ma, Y. Ono, L. Stecker, D. R. Evans, and S. T. Hsu, "Zirconium oxide based gate dielectrics with equivalent oxide thickness of less than 1.0 nm and performance of submicron MOSFET using a nitride gate replacement process," in *Proceedings of the IEEE International Devices Meeting (IEDM '99)*, pp. 149–152, December 1999.
- [28] J. Robertson, "High dielectric constant oxides," *The European Physical Journal*, vol. 28, no. 3, pp. 265–291, 2004.
- [29] S. Asadi, H. Abdizadeh, and Y. Vahidshad, "Effect of crystalline size on the structure of copper doped zirconia nanoparticles synthesized via sol-gel," *Journal of Nanostructures*, vol. 2, pp. 205–212, 2012.

Research Article

Synthesis, Tunable Multicolor Output, and High Pure Red Upconversion Emission of Lanthanide-Doped Lu₂O₃ Nanosheets

Lingzhen Yin, Tianmei Zeng, Zhigao Yi, Chao Qian, and Hongrong Liu

College of Physics and Information Science and Key Laboratory of Low-Dimensional Quantum Structures and Quantum Control of the Ministry of Education, Hunan Normal University, Changsha, Hunan 410081, China

Correspondence should be addressed to Hongrong Liu; hrliu@hunnu.edu.cn

Received 9 October 2013; Accepted 22 November 2013

Academic Editor: Jianhua Hao

Copyright © 2013 Lingzhen Yin et al. This is an open access article distributed under the Creative Commons Attribution License, which permits unrestricted use, distribution, and reproduction in any medium, provided the original work is properly cited.

Yb³⁺ and Ln³⁺ (Ln = Er, Ho) codoped Lu₂O₃ square nanocubic sheets were successfully synthesized via a facile hydrothermal method followed by a subsequent dehydration process. The crystal phase, morphology, and composition of hydroxide precursors and target oxides were characterized by X-ray diffraction (XRD), field emission scanning electron microscope (FE-SEM), and energy-dispersive X-ray spectroscopy (EDS). Results present the as-prepared Lu₂O₃ crystallized in cubic phase, and the monodispersed square nanosheets were maintained both in hydroxide and oxides. Moreover, under 980 nm laser diode (LD) excitation, multicolor output from red to yellow was realized by codoped different lanthanide ions in Lu₂O₃. It is noteworthy that high pure strong red upconversion emission with red to green ratio of 443.3 of Er-containing nanocrystals was obtained, which is beneficial for *in vivo* optical bioimaging.

1. Introduction

In the past few decades, lanthanide-doped upconversion phosphors have received considerable attention due to their application in display systems [1], optical processing sensors [2], solid-state lasers [3], fluorescent detection, and label of biomolecules [4]. More importantly, as the applications in biological assays and medical imaging, the conventional semiconductor quantum dots were limited due to cytotoxicity, photobleaching, photodamage and low signal-to-noise ratio for excitation with short wavelength (usually ultraviolet and visible light) [5, 6]. Upconversion nanocrystals (UCNCs), which overcome those problems and absorb long wavelength (usually near infrared (NIR) light) and emit short wavelength, were believed to be a new kind of fluorescence materials [7, 8]. Besides, UCNCs have low radiation damage, chemical stability, and deep penetration of NIR excitation source compared with conventional fluorescent materials [9, 10].

It is well known that the luminescence property of UCNCs is affected by a combination of different host/activator, doping concentrations, nanocrystal size, shape, and the coatings [11–13]. Therefore, it is important to select appropriate host matrixes for achieving excellent luminescence

property. Lutetium oxides are one of the excellent host matrix for ionizing radiation detection and X-ray phosphors because of their unique properties: high atomic number of Lu (71) and high density (9.42 g/cm³) [14, 15]. Besides, the ionic radius of Lu³⁺ (1.117 Å) is closer to the radius of Yb³⁺ (1.125 Å) than that of other lanthanide ions [16], which may improve the stability of UCNCs while doping high concentration Yb³⁺. More importantly, the energy levels of Lu, especially the 4f orbital, make Lu-containing structure of stronger luminescence intensity than Y-containing crystal [17–19], which was known as very efficient phosphors.

As a potential host matrix, lutetium oxides have received many research interests. Studies on the synthesis of Lu₂O₃ with controlled size and various morphologies have been extensively carried out [20–22]. In addition, the luminescence properties of Lu-containing nanocrystals, for example, multicolor output manipulation by changing the reaction temperature, doping different lanthanide ions, and tuning the concentration of sensitizer or activator ions, have been widely investigated [23–25]. However, most of those researches are about lutetium fluorides, and the study on lanthanide ions-doped Lu₂O₃ was still limited. Furthermore, the lutetium oxide nanocubic sheets have rarely been mentioned.

Herein, we have prepared Yb^{3+} , Ln^{3+} ($\text{Ln} = \text{Er}, \text{Ho}$) codoped Lu_2O_3 via a simple and green hydrothermal method followed by a dehydration process [26]. Moreover, under the excitation of 980 nm laser diode, strong eye-visible red and yellow lights were observed. And the mechanism of the pure red upconversion emission was discussed in detail.

2. Experimental Section

Rare earth nitrates $\text{RE}(\text{NO}_3)_3 \cdot 6\text{H}_2\text{O}$ ($\text{RE} = \text{Lu}, \text{Yb}, \text{Er}, \text{Ho}$, 99.99%) were purchased from Sinopharm Chemical Reagent Co., Ltd (China). All other materials are of analytical grade and used directly without further purification.

2.1. Sample Preparation. Yb^{3+} and Ln^{3+} ($\text{Ln} = \text{Er}, \text{Ho}$) codoped Lu_2O_3 with a composition of $\text{Lu}_{1.60-x}\text{Yb}_{0.40}\text{Ln}_x\text{O}_3$ ($x = 0.04$) was prepared by using a facile hydrothermal method followed by a dehydration process [26]. As for the synthesis of $\text{Lu}_2\text{O}_3:\text{Yb}^{3+}$, Er^{3+} , the corresponding amount of rare earth nitrate (total amount: 1 mmol) was thoroughly mixed with 20 mL distilled water, then NaOH solution with $[\text{OH}^-] = 5 \text{ mol/L}$ was gradually added to obtain the hydroxide precipitates and adjust the pH to 14 under strong stirring. After being stirred 10 mins, the mixed solution was transferred into autoclaves to carry out a hydrothermal treatment at 180°C for about 12 h, and after cooling down to room temperature the hydroxide precursor was purified by centrifugation, washed with distilled water several times, and then dried at 80°C . At last, the corresponding rare earth-doped oxides were prepared successfully through the subsequent dehydration at 800°C for about 4 hours. The Yb/Ho codoped Lu_2O_3 was prepared in a similar procedure.

2.2. Characterization. Power X-ray diffraction (XRD) patterns of the samples were measured with D/max 2500/PC diffractometer using $\text{Cu-K}\alpha$ radiation ($\lambda = 1.5406 \text{ \AA}$) at 40 kV and 250 mA. The morphology and composition of the samples were recorded on a FE-SEM equipped by an EDS system (FEI NanoSEM 450). The upconversion spectra were recorded using R-500 spectrophotometer under an unfocused 980 nm LD excitation at room temperature, and the corresponding digital photographs were taken by a digital camera under 980 nm infrared irradiation.

3. Results and Discussion

3.1. Phase and Morphology. Figure 1 shows the XRD patterns of $\text{Lu}_2\text{O}_3:\text{Yb}^{3+}$, Ho^{3+} and the standard cubic phase Lu_2O_3 (JCPDS no. 86-2475) for comparison. As demonstrated, all diffraction peaks of Yb-Ho codoped Lu_2O_3 are perfectly indexed to the pure cubic phase Lu_2O_3 and no other impurity peaks are detected, implying the high purity cubic phase structure is obtained via the facile hydrothermal approach. Moreover, compared with the standard diffraction peaks, there are very little deviations because the radius of main doped ion Yb^{3+} (1.125 Å) is very close to that of Lu^{3+} (1.117 Å) [16].

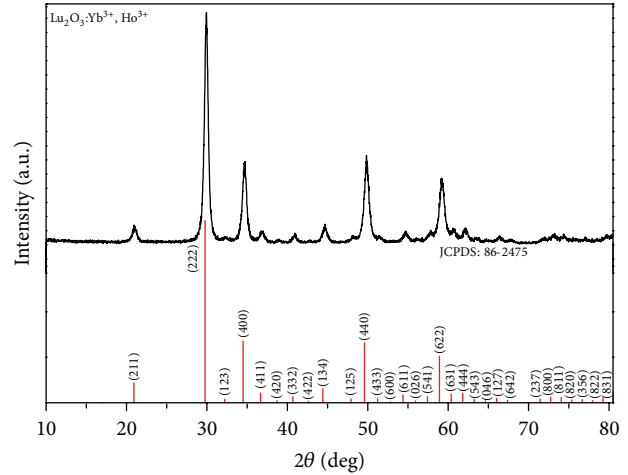


FIGURE 1: XRD patterns of Yb^{3+} and Ho^{3+} codoped Lu_2O_3 powder obtained via a hydrothermal approach (black line); the red lines indicate the standard data of pure cubic Lu_2O_3 structure (JCPDS: 86-2475).

More information about morphology and composition can be obtained by FE-SEM observation and EDS analysis. Figure 2 shows the FE-SEM images of precursor $\text{Lu}(\text{OH})_3$ (Figures 2(a) and 2(b)) and $\text{Lu}_2\text{O}_3:\text{Yb}^{3+}$, Ho^{3+} (Figures 2(c) and 2(d)). As shown in FE-SEM images, all of these two samples present square nanosheets structure and no obvious difference between the two samples in the morphology is founded, implying the samples have well thermal stability. The corresponding EDS (Figure 2(e)) shows the main elements components are Lu, O, Yb, and Ho, implying the Yb and Ho ions are doped into the host matrix successfully.

3.2. Upconversion Luminescent Properties. Figure 3(a) demonstrates the upconversion luminescence spectra of Yb-Er codoped Lu_2O_3 nanocrystals. Under the excitation of 980 nm laser diode, an intense red emission band centered at 655 nm and a very weaker green emission area are observed. After magnifying 350 times (left inset in Figure 3(a)), the green emission area includes two weak bands centered at 526 nm and 542 nm, respectively. Moreover, the red to green (R/G) ratio is measured to a very large value of 443.3, resulting in a pure red upconversion emission, which is also verified by the digital photograph (right inset of Figure 3(a)) and CIE chromaticity coordinates ($X = 0.6312$, $Y = 0.33346$) illustrated in Figure 3(b). When codoped Yb-Ho ions to Lu_2O_3 nanocrystals, the as-prepared structure has both intense green and red emissions (Figure 3(c)). Therefore, bright eye-visible yellow light was observed (inset of Figures 3(c) and 3(d)), differing from the red light seen from the Yb-Er codoped samples. Therefore, the multicolor tuning from red to yellow can be achieved by simply doping different activator ions such as Er^{3+} and Ho^{3+} . More importantly, the pure red upconversion emission with large R/G ratio of 443.3 was realized, which is more beneficial for optical bioimaging for deep tissue penetration.

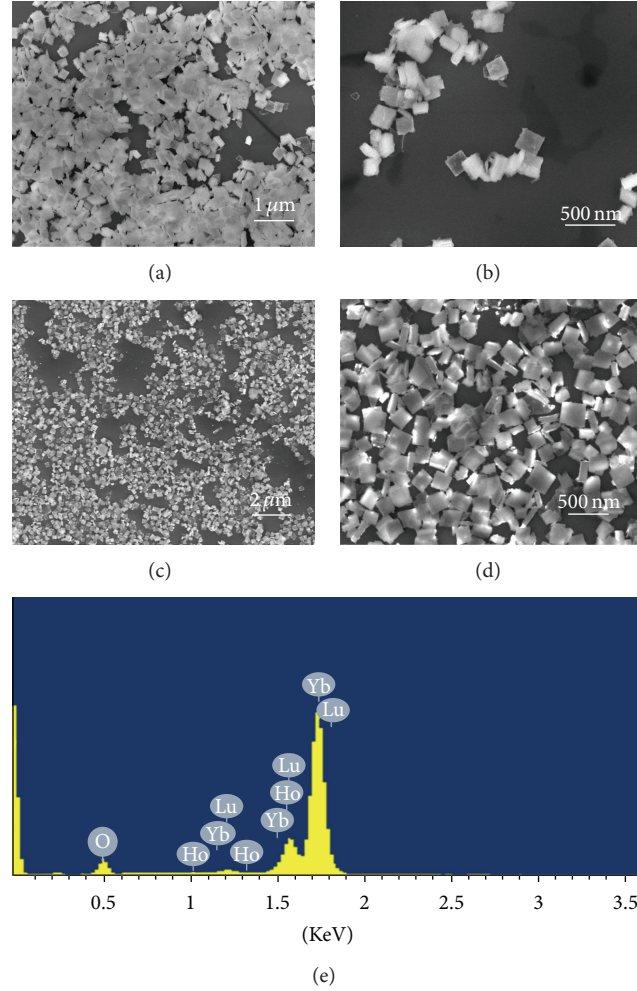


FIGURE 2: FE-SEM images of the as-prepared precursor $\text{Lu}(\text{OH})_3\text{:Yb}^{3+}, \text{Ho}^{3+}$: (a) low magnification, (b) high magnification and obtained FE-SEM images of target $\text{Lu}_2\text{O}_3\text{:Yb}^{3+}, \text{Ho}^{3+}$, (c) low magnification, (d) high magnification, and (e) EDS of the obtained $\text{Lu}_2\text{O}_3\text{:Yb}^{3+}, \text{Ho}^{3+}$ nanocubic sheets.

To reveal the possible upconversion mechanism, a simplified energy level diagram with indicated pathways is presented (Figure 4). As shown, the two weak green emissions of Yb-Er co-doped samples are assigned to the ${}^2\text{H}_{11/2} \rightarrow {}^4\text{I}_{15/2}$ (526 nm) and ${}^4\text{S}_{3/2} \rightarrow {}^4\text{I}_{15/2}$ (542 nm) transitions of Er^{3+} , and the red emission is attributed to the ${}^4\text{F}_{9/2} \rightarrow {}^4\text{I}_{15/2}$ transition of Er^{3+} . The high intensity ratio of the red to green emission can be explained from Figure 4. One reason of the red emission enhancement is that energy transfer from sensitizer ion Yb^{3+} at ${}^2\text{F}_{5/2}$ state to activator ion Er^{3+} through ${}^4\text{I}_{15/2} \rightarrow {}^4\text{I}_{11/2}$ transition, and then perform a nonradiative decay, which increase the number of Er^{3+} at ${}^4\text{I}_{13/2}$ level, at last, energy transfer from Yb^{3+} at ${}^2\text{F}_{5/2}$ state to Er^{3+} through ${}^4\text{I}_{13/2} \rightarrow {}^2\text{F}_{9/2}$. Another reason is the efficient cross-relaxation (CR) process of Er^{3+} : ${}^4\text{I}_{11/2} + {}^4\text{F}_{7/2} \rightarrow {}^4\text{F}_{9/2} + {}^4\text{F}_{9/2}$ illustrated in Figure 4. The CR process strengthens the red band and weakens the green emission because most of the ions at

${}^4\text{F}_{7/2}$ state transfer to ${}^4\text{F}_{9/2}$ directly bypassing the ${}^2\text{H}_{11/2}$ and ${}^4\text{S}_{3/2}$, which contribute to the green emission [23–25].

On the other hand, the green and red upconversion emissions of Ho containing sample are mainly attributed to the transitions ${}^5\text{F}_4 \rightarrow {}^5\text{I}_8$ (541 nm), ${}^5\text{S}_2 \rightarrow {}^5\text{I}_8$ (551 nm), ${}^5\text{F}_5 \rightarrow {}^5\text{I}_8$ (640–678 nm) of Ho^{3+} (Figure 4). As illustrated in Figure 4, all the processes need two-photo energy transfer; the red emission state ${}^5\text{F}_5$ is attributed to phonon-assisted energy transfer: ${}^5\text{I}_7(\text{Ho}^{3+}) \rightarrow {}^5\text{F}_5(\text{Ho}^{3+})$ and non-radiative decay from ${}^5\text{S}_2$. When doping high concentration Yb^{3+} (20%), all the three emissions are enhanced and lead to an intense eye-visible yellow light with CIE chromaticity coordinates at $X = 0.419$, $Y = 0.5318$.

4. Conclusion

In summary, monodispersed Lu_2O_3 co-doped with Yb^{3+} and Ln^{3+} ($\text{Ln} = \text{Er}, \text{Ho}$) square nanocubic sheets were successfully fabricated with a simple hydrothermal method.

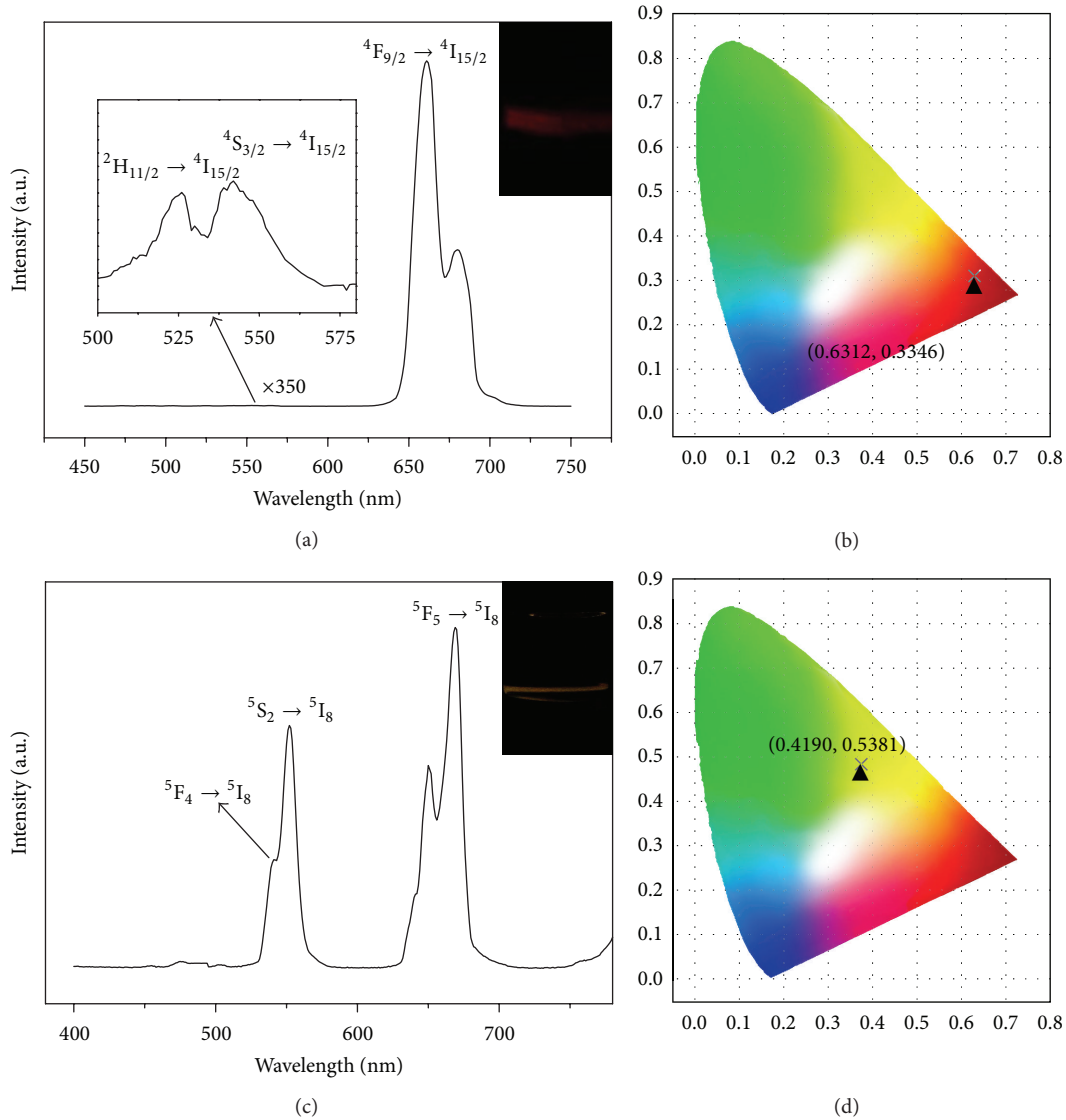


FIGURE 3: (a) UC spectra of $\text{Lu}_2\text{O}_3:\text{Yb}/\text{Er}$, (b) CIE chromaticity coordinates diagram of $\text{Lu}_2\text{O}_3:\text{Yb}/\text{Er}$, (c) UC spectra of $\text{Lu}_2\text{O}_3:\text{Yb}/\text{Ho}$, and (d) CIE chromaticity coordinates diagram of $\text{Lu}_2\text{O}_3:\text{Yb}/\text{Ho}$; the right insets of (a) and (c) are the corresponding digital photographs of 1 wt% water soluble of the samples.

The upconverted luminescence properties of as-prepared samples were well investigated under excitation of 980 nm laser diode. By changing the doped ions from Er to Ho, the upconversion emissions transform from eye-visible red to bright yellow light. Moreover, high pure red upconversion emission was obtained in Yb/Er codoped sample, which is suitable for high contrast optical bioimaging with absence of autofluorescence owing to the low tissue absorption at red light area (655 nm).

Acknowledgments

This work was supported by the National Natural Science Foundation of China (no. 51102202), New Century Excellent

Talents in University (NCET-13-0787), Specialized Research Fund for the Doctoral Program of Higher Education of China (no. 20114301120006) and Hunan Provincial Natural Science Foundation of China (nos. 12JJ4056 and 13JJ1017), the Scientific Foundation of Ministry of Education (212119), and Scientific Research Fund of Hunan Provincial Education Department (13B062).

References

- [1] E. Downing, L. Hesselink, J. Ralston, and R. Macfarlane, "A three-color, solid-state, three-dimensional display," *Science*, vol. 273, no. 5279, pp. 1185–1189, 1996.
- [2] B. M. van der Ende, L. Aarts, and A. Meijerink, "Lanthanide ions as spectral converters for solar cells," *Physical Chemistry*

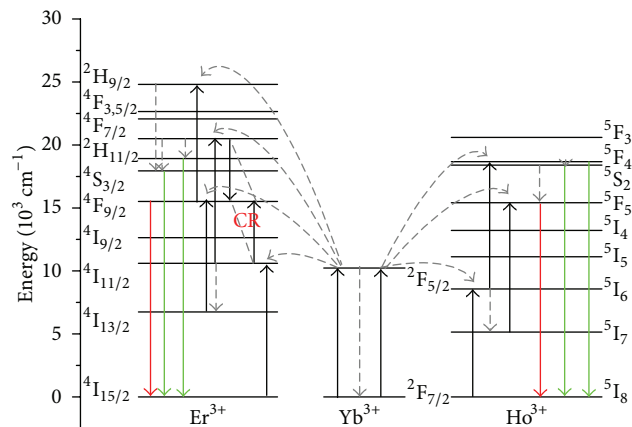


FIGURE 4: Schematic energy level diagrams of Yb^{3+} , Er^{3+} , and Ho^{3+} ions and proposed upconversion mechanism.

Chemical Physics, vol. 11, no. 47, pp. 11081–11095, 2009.

- [3] G. F. Wang, Q. Peng, and Y. D. Li, “Lanthanide-doped nanocrystals: synthesis, optical-magnetic properties, and applications,” *Accounts of Chemical Research*, vol. 44, no. 5, pp. 322–332, 2011.
- [4] H. R. Liu, W. Lu, H. B. Wang et al., “Simultaneous synthesis and amine-functionalization of single-phase $\text{BaYF}_5:\text{Yb}/\text{Er}$ nanoprobe for dual-modal *in vivo* upconversion fluorescence and long-lasting X-ray computed tomography imaging,” *Nanoscale*, vol. 5, no. 13, pp. 6023–6029, 2013.
- [5] N. Lewinski, V. Colvin, and R. Drezek, “Cytotoxicity of nanoparticles,” *Small*, vol. 4, no. 1, pp. 26–49, 2008.
- [6] J. M. Klostranec and W. C. W. Chan, “Quantum dots in biological and biomedical research: recent progress and present challenges,” *Advanced Materials*, vol. 18, no. 15, pp. 1953–1964, 2006.
- [7] S. J. Zeng, M. K. Tsang, C. F. Chan, K. L. Wong, and J. H. Hao, “PEG modified $\text{BaGdF}_5:\text{Yb}/\text{Er}$ nanoprobe for multi-modal upconversion fluorescent, *in vivo* X-ray computed tomography and biomagnetic imaging,” *Biomaterials*, vol. 33, no. 36, pp. 9232–9238, 2012.
- [8] F. Auzel, “Upconversion and anti-stokes processes with f and d ions in solids,” *Chemical Reviews*, vol. 104, no. 1, pp. 139–174, 2004.
- [9] S. J. Zeng, J. J. Xiao, Q. B. Yang, and J. H. Hao, “Bi-functional $\text{NaLuF}_4:\text{Gd}^{3+}/\text{Yb}^{3+}/\text{Tm}^{3+}$ nanocrystals: structure controlled synthesis, near-infrared upconversion emission and tunable magnetic properties,” *Journal of Materials Chemistry*, vol. 22, no. 19, pp. 9870–9874, 2012.
- [10] J. C. Boyer, F. Vetrone, L. A. Cuccia, and J. A. Capobianco, “Synthesis of colloidal upconverting NaYF_4 nanocrystals doped with Er^{3+} , Yb^{3+} and Tm^{3+} , Yb^{3+} via thermal decomposition of lanthanide trifluoroacetate precursors,” *Journal of the American Chemical Society*, vol. 128, no. 23, pp. 7444–7445, 2006.
- [11] G. Z. Ren, S. J. Zeng, and J. H. Hao, “Tunable multicolor upconversion emissions and paramagnetic property of monodispersed bifunctional lanthanide-doped NaGdF_4 nanorods,” *Journal of Physical Chemistry C*, vol. 115, no. 41, pp. 20141–20147, 2011.
- [12] F. Wang and X. G. Liu, “Recent advances in the chemistry of lanthanide-doped upconversion nanocrystals,” *Chemical Society Reviews*, vol. 38, no. 4, pp. 976–989, 2009.
- [13] S. J. Zeng, G. Z. Ren, C. F. Xu, and Q. B. Yang, “Modifying crystal phase, shape, size, optical and magnetic properties of monodispersed multifunctional NaYbF_4 nanocrystals through lanthanide doping,” *CrystEngComm*, vol. 13, no. 12, pp. 4276–4281, 2011.
- [14] J. Trojan-Piegza, E. Zych, D. Hreniak, W. Stręk, and L. Kepiński, “Structural and spectroscopic characterization of $\text{Lu}_2\text{O}_3:\text{Eu}$ nanocrystalline spherical particles,” *Journal of Physics Condensed Matter*, vol. 16, no. 39, pp. 6983–6994, 2004.
- [15] J. C. Boyer, F. Vetrone, J. A. Capobianco, A. Speghini, and M. Bettinelli, “Variation of fluorescence lifetimes and judd-ofelt parameters between Eu^{3+} doped bulk and nanocrystalline cubic Lu_2O_3 ,” *Journal of Physical Chemistry B*, vol. 108, no. 52, pp. 20137–20143, 2004.
- [16] R. D. Shannon, “Revised effective ionic radii and systematic studies of interatomic distances in halides and chalcogenides,” *Acta Crystallographica A*, vol. 32, no. 5, pp. 751–767, 1976.
- [17] P. Rambaldi, R. Moncorgé, J. P. Wolf, C. Pédrini, and J. Y. Gesland, “Efficient and stable pulsed laser operation of $\text{Ce}:\text{LiLuF}_4$ around 308 nm,” *Optics Communications*, vol. 146, no. 1–6, pp. 163–166, 1998.
- [18] V. Sudesh and K. Asai, “Spectroscopic and diode-pumped-laser properties of $\text{Tm},\text{Ho}:\text{YLF}$; $\text{Tm},\text{Ho}:\text{LuLF}$; and $\text{Tm},\text{Ho}:\text{LuAG}$ crystals: a comparative study,” *Journal of the Optical Society of America B*, vol. 20, no. 9, pp. 1829–1837, 2003.
- [19] C. Maunier, J. L. Doualan, R. Moncorgé, A. Speghini, M. Bettinelli, and E. Cavalli, “Growth, spectroscopic characterization, and laser performance of $\text{Nd}:\text{LuVO}_4$, a new infrared laser material that is suitable for diode pumping,” *Journal of the Optical Society of America B*, vol. 19, no. 8, pp. 1794–1800, 2002.
- [20] H. J. Qiu, Y. Shi, J. J. Xie, J. Xie, L. L. Zhang, and F. F. Xu, “Hydrothermal route to Eu doped $\text{LuO}(\text{OH})$ and Lu_2O_3 nanorods,” *Science China Technological Sciences*, vol. 53, no. 6, pp. 1576–1582, 2010.
- [21] H. Guo, M. Yin, N. Dong, M. Xu, L. R. Lou, and W. P. Zhang, “Effect of heat-treatment temperature on the luminescent properties of $\text{Lu}_2\text{O}_3:\text{Eu}$ film prepared by Pechini sol-gel method,” *Applied Surface Science*, vol. 243, no. 1–4, pp. 245–250, 2005.
- [22] P. P. Yang, S. L. Gai, Y. C. Liu, W. X. Wang, C. X. Li, and J. Lin, “Uniform hollow $\text{Lu}_2\text{O}_3:\text{Ln}$ ($\text{Ln} = \text{Eu}^{3+}/\text{Tb}^{3+}$) spheres: facile synthesis and luminescent properties,” *Inorganic Chemistry*, vol. 50, no. 6, pp. 2182–2190, 2011.
- [23] N. Niu, P. P. Yang, F. He et al., “Tunable multicolor and bright white emission of one-dimensional $\text{NaLuF}_4:\text{Yb}^{3+}, \text{Ln}^{3+}$

- (Ln = Er, Tm, Ho, Er/Tm, Tm/Ho) microstructures,” *Journal of Materials Chemistry*, vol. 22, no. 21, pp. 10889–10899, 2012.
- [24] E. W. Barrera, M. C. Pujol, F. Díaz et al., “Emission properties of hydrothermal Yb^{3+} , Er^{3+} and Yb^{3+} , Tm^{3+} -codoped Lu_2O_3 nanorods: upconversion, cathodoluminescence and assessment of waveguide behavior,” *Nanotechnology*, vol. 22, no. 7, Article ID 075205, 2011.
- [25] Y. P. Li, J. H. Zhang, Y. S. Luo, X. Zhang, Z. D. Hao, and X. J. Wang, “Color control and white light generation of upconversion luminescence by operating dopant concentrations and pump densities in Yb^{3+} , Er^{3+} and Tm^{3+} tri-doped Lu_2O_3 nanocrystals,” *Journal of Materials Chemistry*, vol. 21, no. 9, pp. 2895–2900, 2011.
- [26] X. Wang and Y. D. Li, “Rare-earth-compound nanowires, nanotubes, and fullerene-like nanoparticles: synthesis, characterization, and properties,” *Chemistry*, vol. 9, no. 22, pp. 5627–5635, 2003.

Research Article

Temperature Dependence of Electrical Properties and Crystal Structure of $0.29\text{Pb}(\text{In}_{1/2}\text{Nb}_{1/2})\text{O}_3-0.44\text{Pb}(\text{Mg}_{1/3}\text{Nb}_{2/3})\text{O}_3-0.27\text{PbTiO}_3$ Single Crystals

Qian Li,¹ Yun Liu,¹ Andrew Studer,² Zhenrong Li,³ Ray Withers,¹ and Zhuo Xu³

¹ Research School of Chemistry, The Australian National University, ACT 0200, Australia

² Bragg Institute, Australian Nuclear Science and Technology Organization (ANSTO), NSW 2232, Australia

³ Electronic Materials Research Laboratory, Xi'an Jiaotong University, Shanxi 710049, China

Correspondence should be addressed to Yun Liu; yliu@rsc.anu.edu.au

Received 31 May 2013; Revised 3 October 2013; Accepted 7 October 2013

Academic Editor: Jianhua Hao

Copyright © 2013 Qian Li et al. This is an open access article distributed under the Creative Commons Attribution License, which permits unrestricted use, distribution, and reproduction in any medium, provided the original work is properly cited.

We characterized the temperature dependent ($\sim 25-200^\circ\text{C}$) electromechanical properties and crystal structure of $\text{Pb}(\text{In}_{1/2}\text{Nb}_{1/2})\text{O}_3-\text{Pb}(\text{Mg}_{1/3}\text{Nb}_{2/3})\text{O}_3-\text{PbTiO}_3$ single crystals using *in situ* electrical measurement and neutron diffraction techniques. The results show that the poled crystal experiences an addition phase transition around 120°C whereas such a transition is absent in the unpoled crystal. It is also found that the polar order persists above the maximum dielectric permittivity temperature at which the crystal shows a well-defined antiferroelectric behavior. The changes in the electrical properties and underlying crystal structure are discussed in the paper.

1. Introduction

Lead-based relaxor ferroelectric single crystals (RFSCs) have been intensely studied over recent decades due to their exceptional electromechanical coupling performance. Typical RFSCs include binary systems $\text{Pb}(\text{Zn}_{1/3}\text{Nb}_{2/3})\text{O}_3-\text{PbTiO}_3$ (PZN-PT) and $\text{Pb}(\text{Mg}_{1/3}\text{Nb}_{2/3})\text{O}_3-\text{PbTiO}_3$ (PMN-PT) [1, 2], as well as a ternary system, $\text{Pb}(\text{In}_{1/2}\text{Nb}_{1/2})\text{O}_3-\text{Pb}(\text{Mg}_{1/3}\text{Nb}_{2/3})\text{O}_3-\text{PbTiO}_3$ (PIN-PMN-PT), which possess enhanced properties in terms of high Curie temperature T_C and coercive field E_c . The origin of high piezoelectricity of RFSCs has long been an important issue. In this regard a widely accepted theory, proposed by Fu and Cohen [3], is the polarization rotation mechanism, the essence of which is that the polarization vectors can rotate freely within a lattice plane instead of being restricted to certain directions. This theory is supported by the observations of intermediate phases near the morphotropic phase boundary (MPB), for example, monoclinic M_A and M_C phases (space group Cm and Pm, resp.) [4].

On the other hand, the structure evolution of RFSCs under external fields of thermal, electrical, and/or mechanical stress is another important issue. From a viewpoint of application, as many piezoelectric devices are employed under a multi-field coupled environment, their electromechanical behavior usually deviates from a simple linear constitutive relationship, and as a result, those devices may suffer from failures that are unexpected based on individual factors. Therefore, it is of great importance to understand the structural evolution of RFSCs that governs their macroscopic properties using *in situ* techniques.

In this paper, we aim to study the electromechanical properties and crystal structure evolution with temperature for $\text{Pb}(\text{In}_{1/2}\text{Nb}_{1/2})\text{O}_3-\text{Pb}(\text{Mg}_{1/3}\text{Nb}_{2/3})\text{O}_3-\text{PbTiO}_3$ single crystals, via *in situ* single crystal neutron diffraction in conjunction with electrical characterization methods. The result leads to a good understanding of the phase transition behaviour in this material and associated RFSCs.

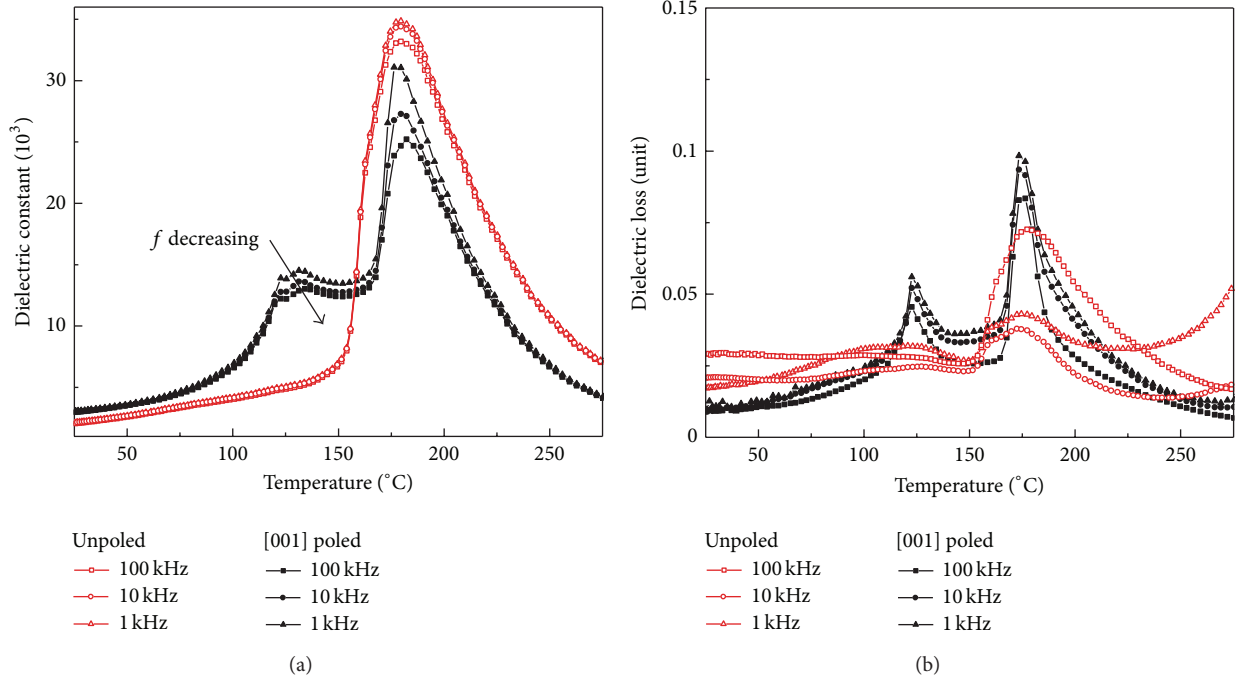


FIGURE 1: Temperature dependent dielectric constant (a) and loss (b) at several frequency points for the unpoled and [001]-poled 0.29PIN-0.44PMN-0.27PT single crystals.

2. Experiment

The near-MPB composition 0.29PIN-0.44PMN-0.27PT single crystals were grown using the vertical Bridgman technique [5]. Several [001]-oriented samples with dimension $\sim 5 \times 5 \times 0.5$ mm were cut from the near position in the crystal boule so as to minimize composition deviations (note that all pseudocubic crystallographic indexes are used throughout this paper). These crystals were silver-electroded on the 5×5 mm faces and two of them were poled along the [001] direction under an electric field of 10 kV/cm at room temperature. This poling method was found to sufficiently produce a high piezoelectric constant, d_{33} , of ~ 2000 pC/N, similar to the prevailing field-cooling method. In light of this, we neglected in the current study the issue of the dependence of the structure and electrical properties on poling electric fields. Temperature dependent dielectric spectra of both the states of crystals were measured in a furnace with a computer-interfaced LCR meter (Agilent 4284A) using 1 V_{rms} ac test signals. A ferroelectric analyzer system (TF2000, AixCCCT), including a bulk sample heating holder and a laser interferometer, was used to measure the electrical field-polarization (P - E) hysteresis loops and strain-field (S - E) curves on an unpoled sample. The P - E and S - E measurements were performed from room temperature to 200 $^{\circ}\text{C}$ at every 5 $^{\circ}\text{C}$ interval. *In situ* single crystal diffraction experiments were performed at ANSTO, using Wombat high intensity neutron diffractometer [6]. One of the poled crystals was fixed into a cryostat and then mounted at a four-circle Eulerian cradle which allowed quick crystal alignment. The sample was heated up to 200 $^{\circ}\text{C}$ during the first run, and

after cooling to 25 $^{\circ}\text{C}$ now the depoled/unpoled crystals was again heated for the second run. The (002) reflections were mesh-scanned in the HOL scattering plane using a neutron wavelength of 1.838 \AA .

3. Result and Discussion

Figures 1(a) and 1(b) show the dielectric constant and loss spectra, respectively, of 0.29PIN-0.44PMN-0.27PT single crystals as a function of temperature and frequency. As can be seen, both the [001]-poled and unpoled crystals exhibit a dielectric maximum temperature $T_m \sim 182^{\circ}\text{C}$. Generally this peak position is attributed to the Curie temperature T_C where a transition from ferroelectric phases to paraelectric phases occurs, and it can well confirm the nominal composition for the crystals [2]. Aside from the same T_m , the poled and unpoled crystals display different characteristics; for example, the unpoled crystal only exhibits a broad T_m peak within the measured temperature range. It is therefore believed that the unpoled crystal is more typical of relaxor ferroelectric. This can be well understood since in RFSCs the relaxor nature of PMN (and PIN and others) competes with the normal ferroelectric order favoured by PT component.

By comparison, the poled crystal has an additional dielectric peak below T_m . Looking at it closely, two peaks may also be claimed from the permittivity spectra (Figure 1(a)), which are not found correspondingly from the loss spectra (Figure 1(b)). However, there is not a unanimous assignment of the associated phases in the literature. This is mainly due to the fact that the lattice parameters for the intermediate phases are quite close and even metrically the same. Another

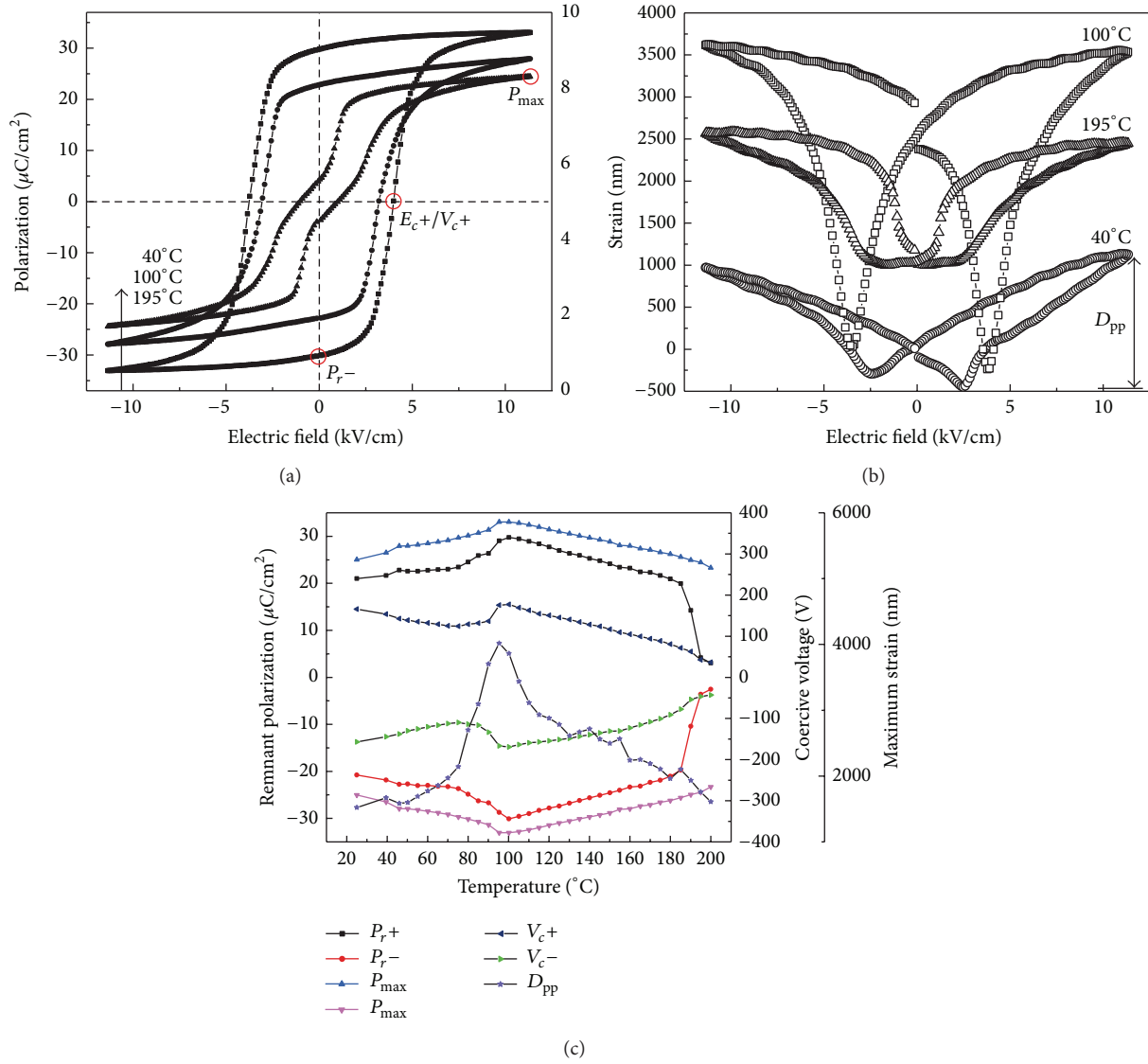


FIGURE 2: (a) P - E and (b) S - E hysteresis loops of 0.29PIN-0.44PMN-0.27PT single crystals, at three selected temperatures and (c) temperature dependence of the parameters deduced from those loops. Note that for clarity the S - E loops in (b) are vertically offset.

possible reason is that the stabilities of those phases are fragile and sensitive to many factors, for example, composition deviations [7]. In our case, it is believed that a transition sequence of R (rhombohedral)- M_A - M_C - T (tetragonal)- C is induced by heating, consistent with the polarization rotation pathway discussed by Noheda et al. [4]. The jump from M_A to M_C , which is different from the continuous R - M_A and M_C - T phase transitions, occurs in a wide temperature range 120–132°C. Besides, in this temperature range a frequency dependence of the dielectric permittivity can be observed (Figure 1(a)), which may therefore indicate diffuse characteristics for such a structural transition.

Figures 2(a) and 2(b) show the P - E hysteresis loops and S - E curves, respectively, at three selected temperatures, and the parameters drawn from those hysteresis loops versus temperature are plotted in Figure 2(c). An unpoled crystal

was used for this series of measurements. At 40°C, a square P - E loop can be obtained with a saturated polarization P_s value of $28 \mu\text{C}/\text{cm}^2$ and a coercive field E_c around 3.2 kV/cm. The corresponding S - E curve has a typical butterfly shape, and the maximum strain (defined as peak-to-peak displacement D_{pp} , see Figure 3(b)) can reach 1500 nm (0.3%). The strain curve shows a slight asymmetry as the positive half cycle is larger than the negative half, indicating that the domains are easier to switch to the positive E field direction. This could be due to the pinning effect of defects inside the crystal. With the temperature increases, the saturated/remnant polarization values gradually increase, and after reaching their maxima at $\sim 100^\circ\text{C}$, they change into an opposite dependence and finally drop quickly near the T_m (Figure 2(c)). A similar trend can be found for the maximum strain, and the field-induced strain is significantly enhanced near 100°C . The strain curve

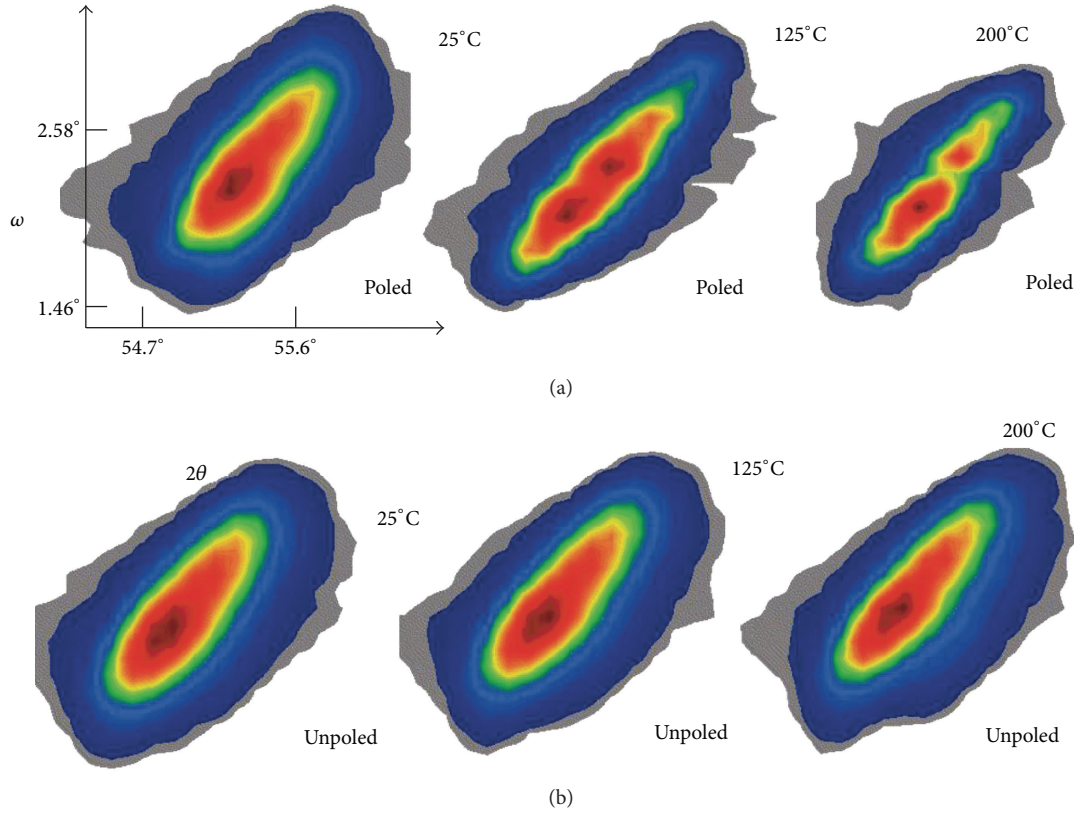


FIGURE 3: Contour of (002) reflection for [001]-poled (upper row) and unpoled (lower row) 0.29PIN-0.44PMN-0.27PT single crystals, at three selected temperatures.

at 100°C (Figure 2(b)) reveals that a great portion of strain is achieved during the course of domain switching, suggesting that domain switching is highly facilitated by the M_A - M_C transition where the polarization vector jumps from the (110) plane to (100) plane. However, it is also very likely that such a transition itself can make an important contribution to the total strain due to a discontinuous change in lattice dimensions. In contrast, the variation of coercive field shows a different behavior; basically it always decreases with temperature except for a jump occurring near 100°C. It is evident that all those parameters reflect a phase transition point at 100°C, near the M_A - M_C transition temperature range, in good agreement with the dielectric spectroscopic results. The difference in the transition temperature obtained from these two techniques may be because the electrical field strength levels are remarkably different.

Another interesting phenomenon observed is that near T_m , the spontaneous polarization does not disappear instantly. Instead an antiferroelectric behavior can be induced at this critical temperature. As shown in Figure 2(a), the P - E hysteresis loop at 195°C develops into a double loop shape. The remnant polarization value is not zero, suggesting the coexistence of ferroelectric order to a certain extent. Besides, the strain curve obtained here is more typical of an antiferroelectric as no negative strain can be induced by electric field; that is, the crystal cannot contract relative to a zero-field state. Zhao et al. [8] reported a similar

phenomenon in 0.76PMN-0.24PT single crystals near the M_A - M_C temperature (which they called T_d , depolarization temperature). They explained that a macrodomain state to microdomain state transition occurs when heating the poled crystal across T_d and that this transition is responsible for their observed “triple-like” loops. Compared to this report, our result is different since in our case the double P - E loops are observed only near T_m .

Figure 3 shows the evolution of the contours of (002) reflection resulting from *in situ* neutron diffraction measurements. Generally, single diffraction examines only one Bragg peak at each reflection position, irrespective of the symmetry of a crystal. For ferroelectric materials, however, due to the presence of ferroelectric domains which act as a certain type of structure twinning, multiple twinned Bragg peaks can possibly be present for one reflection [9, 10]. In this case, at 25°C, the (002) reflection contours appear to have a single component for both the unpoled and poled states. This agrees with the rhombohedral symmetry of the crystals as known from the previous discussion on electrical measurements. When the crystals are heated up to 200°C, the (002) reflection for the unpoled state changes only a little in position as a result of thermal expansions, while basically remains a single component profile. Note that the small overall shift of the reflections and the underlying lattice changes are not addressed here. By contrast, for the poled crystal two components with similar magnitude can be observed on the (002)

reflection measured at 125°C. The two components have different 2θ diffraction angles as well as different ω rocking angle, implying that the three lattice vectors herein are no longer equivalent as in an R symmetry. We believe that such a splitting is a clear evidence for the tetragonal symmetry that the poled crystal possesses around this critical temperature. The aforementioned monoclinic symmetries, however, also possibly give rise to such a diffraction result; that is, it is not sufficient to assign a T symmetry from this (002) reflection alone. Moreover, the (002) reflection for the poled crystal measured at 200°C, a temperature well above T_m , shows a weak peak component together with a main component, implying that the crystal has not totally been of a cubic phase at the current temperature. A very possible scenario is that there are some polar domains/regions coexisting with the major nonpolar paraelectric phase in the crystal, and this may provide a structural basis for the apparent antiferroelectric behavior shown in the P - E and S - E hysteresis loops. On the other hand, it is difficult to ascertain an actual length scale for the residual polar domains based upon the current diffraction results. Real space ferroelectric domain imaging techniques, for example, piezoresponse force microscopy, might be employed to probe this information at the nanoscale [11].

4. Summary

The dielectric property, ferroelectric polarization, and strain hysteresis loop as well as crystal structure for relaxor ferroelectric 0.29PIN-0.44PMN-0.27PT single crystals are characterized over a temperature region from about room temperature to 200°C. A combinational analysis of those characterization results has revealed the phase transition behavior within this temperature region, and very good agreement can be found between the structure of the crystals and their macroscopic electrical properties.

Acknowledgments

Qian Li, Yun Liu, and Ray Withers acknowledge financial support from the Australian Research Council (ARC) in the form of an ARC Discovery Grant. Yun Liu also acknowledges support from the ARC Future Fellowships program. The authors also thank the Australian Institute of Nuclear Science and Engineering (ANSIE) for financial support to access the national neutron facilities at ANSTO.

References

- [1] S.-E. Park and T. R. Shrout, "Ultra-high strain and piezoelectric behavior in relaxor based ferroelectric single crystals," *Journal of Applied Physics*, vol. 82, no. 4, pp. 1804–1811, 1997.
- [2] X. Li and H. Luo, "The growth and properties of relaxor-based ferroelectric single crystals," *Journal of the American Ceramic Society*, vol. 93, no. 10, pp. 2915–2928, 2010.
- [3] H. Fu and R. E. Cohen, "Polarization rotation mechanism for ultra-high electromechanical response in single-crystal piezoelectrics," *Nature*, vol. 403, no. 6767, pp. 281–283, 2000.
- [4] B. Noheda, D. E. Cox, G. Shirane, S.-E. Park, L. E. Cross, and Z. Zhong, "Polarization rotation via a monoclinic phase in the piezoelectric 92% $\text{PbZn}_{1/3}\text{Nb}_{2/3}\text{O}_3$ -8% PbTiO_3 ," *Physical Review Letters*, vol. 86, no. 17, pp. 3891–3894, 2001.
- [5] X. Wang, Z. Xu, Z. Li, F. Li, H. Chen, and S. Fan, "Growth of the relaxor based ferroelectric single crystals $\text{Pb}(\text{In}_{1/2}\text{Nb}_{1/2})\text{O}_3$ - $\text{Pb}(\text{Mg}_{1/3}\text{Nb}_{2/3})\text{O}_3$ - PbTiO_3 by vertical Bridgman technique," *Ferroelectrics*, vol. 401, no. 1, pp. 173–180, 2010.
- [6] A. J. Studer, M. E. Hagen, and T. J. Noakes, "Wombat: the high-intensity powder diffractometer at the OPAL reactor," *Physica B*, vol. 385, pp. 1013–1015, 2006.
- [7] Z. Li, Z. Xu, X. Yao, and Z.-Y. Cheng, "Phase transition and phase stability in [110]-, [001]-, and [111]-oriented 0.68 $\text{Pb}(\text{Mg}_{1/3}\text{Nb}_{2/3})\text{O}_3$ -0.32 PbTiO_3 single crystal under electric field," *Journal of Applied Physics*, vol. 104, no. 2, Article ID 024112, 2008.
- [8] X. Zhao, J. Wang, Z. Peng, H. L. W. Chan, C. L. Choy, and H. Luo, "Triple-like hysteresis loop and microdomain-macrodomain transformation in the relaxor-based 0.76 $\text{Pb}(\text{Mg}_{1/3}\text{Nb}_{2/3})\text{O}_3$ -0.24 PbTiO_3 single crystal," *Materials Research Bulletin*, vol. 39, no. 2, pp. 223–230, 2004.
- [9] Q. Li, Y. Liu, J. Wang et al., "Structural transitions in [001]/[111]-oriented 0.26 $\text{Pb}(\text{In}_{1/2}\text{Nb}_{1/2})\text{O}_3$ -0.46 $\text{Pb}(\text{Mg}_{1/3}\text{Nb}_{2/3})\text{O}_3$ -0.28 PbTiO_3 single crystals probed via neutron diffraction and electrical characterization," *Journal of Applied Physics*, vol. 113, Article ID 154104, 2013.
- [10] Z.-G. Ye, B. Noheda, M. Dong, D. Cox, and G. Shirane, "Monoclinic phase in the relaxor-based piezoelectric/ferroelectric $\text{Pb}(\text{Mg}_{1/3}\text{Nb}_{2/3})\text{O}_3$ - PbTiO_3 system," *Physical Review B*, vol. 64, no. 18, Article ID 184114, 2001.
- [11] Q. Li, Y. Liu, R. L. Withers, Y. Wan, Z. Li, and Z. Xu, "Piezoresponse force microscopy studies on the domain structures and local switching behavior of $\text{Pb}(\text{In}_{1/2}\text{Nb}_{1/2})\text{O}_3$ - $\text{Pb}(\text{Mg}_{1/3}\text{Nb}_{2/3})\text{O}_3$ - PbTiO_3 single crystals," *Journal of Applied Physics*, vol. 112, Article ID 052006, 2012.

Research Article

A Facile Synthesis and Optical Properties of Bundle-Shaped $\text{TbPO}_4 \cdot \text{H}_2\text{O}$ Nanorods

Dan Yue,^{1,2} Wen Luo,² Wei Lu,³ Ruiyong Wang,¹ Chunyang Li,²
Jiazhong Chang,² and Zhenling Wang²

¹ The College of Chemistry and Molecular Engineering, Zhengzhou University, Zhengzhou 450001, China

² The Key Laboratory of Rare Earth Functional Materials and Applications, Zhoukou Normal University, Zhoukou 466001, China

³ Department of Applied Physics and Materials Research Center, The Hong Kong Polytechnic University, Hong Kong

Correspondence should be addressed to Ruiyong Wang; wangry@zzu.edu.cn and Zhenling Wang; wangzhenling@zkn.edu.cn

Received 14 November 2013; Accepted 1 December 2013

Academic Editor: Jianhua Hao

Copyright © 2013 Dan Yue et al. This is an open access article distributed under the Creative Commons Attribution License, which permits unrestricted use, distribution, and reproduction in any medium, provided the original work is properly cited.

Bundle-shaped $\text{TbPO}_4 \cdot \text{H}_2\text{O}$ nanorods have been prepared by a facile hydrothermal technique and characterized by XRD, SEM, TEM, UV-Vis diffuse reflectance spectrum (DRS), photoluminescence (PL) spectrum, and lifetime. The results indicate that the obtained sample has hexagonal structure of $\text{TbPO}_4 \cdot \text{H}_2\text{O}$ and is composed of nanorods bundles which is assembled from many single crystalline nanorods with the diameter of around 45 nm and the length of 2.3 μm . The growth of the single crystalline nanorod is along the (001) plane direction. Under the UV light irradiation, $\text{TbPO}_4 \cdot \text{H}_2\text{O}$ nanorods bundles exhibit bright green emission corresponding to the $^5\text{D}_4 \rightarrow ^7\text{F}_j$ ($J = 6, 5, 4, 3$) transitions of the Tb^{3+} ions, and the lifetime is determined to be about 0.24 ms.

1. Introduction

In recent years, inorganic nanostructures with well-defined shapes and sizes have attracted growing attention because of their unique size- and shape-dependent properties [1–3]. Among many kinds of nanostructured materials, lanthanide orthophosphates (LnPO_4) with uniform size and various morphologies have been prepared by some mild and controllable methods [4, 5] and attracted great interest because of their unique properties including very low solubility in water (The solubility product constant, $pK_{\text{sol}} = 25\text{--}27$) [6], high thermal stability, high index of refraction, and high luminescent efficiency [7, 8]. These materials have been used as active components in a wide range of applications such as phosphors, laser hosts, and biolabeling [9–12]. The chemical and optical properties of one-dimensional (1D) LnPO_4 nanostructures (e.g., $\text{CePO}_4 : \text{Tb}^{3+}$ nanowires, LaPO_4 nanorods, CePO_4 peanut-like nanostructures, etc.) can be successfully tailored, which makes these materials have significant potential applications in fabricating the next generation of information storage, optoelectronic, sensing devices, and nanoscale devices [13–15].

As an important sort of lanthanide phosphates, TbPO_4 has been investigated mainly focusing on its physical low-temperature properties (magnetic properties, birefringence measurements, and mean-field calculations) in previous literatures [16, 17]. Recently, much attention has been focused on the synthesis and properties of the TbPO_4 with various morphologies. It is known that the hydrothermal technique is a common method in the field of material science. Using this technique, many materials with uniform morphology and satisfying crystallinity can be obtained at relatively low reaction temperature, usually without any further calcinations at high temperature [18, 19]. For example, $\text{TbPO}_4 : \text{Eu}^{3+}$ square-like particles were prepared by hydrothermal method with citric acid as the organic additive, and the reaction temperature is as low as 160°C [20]. As a contrast, TbPO_4 hollow spheres can be obtained through solid state method when the annealing temperature is increased to 1150°C [21, 22]. In this work, uniform $\text{TbPO}_4 \cdot \text{H}_2\text{O}$ bundle-shaped nanostructures composed of single crystalline nanorods were synthesized at 180°C through a facile hydrothermal technique and characterized by XRD, SEM, TEM DRS, PL spectra, and so forth. The possible mechanism leading to

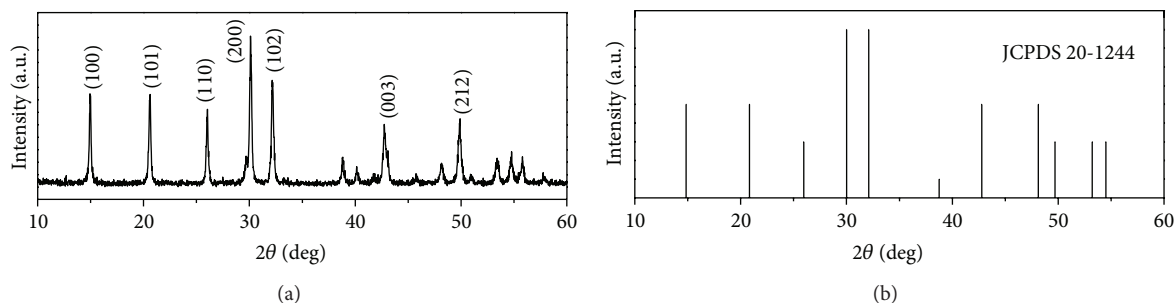


FIGURE 1: XRD patterns of bundle-shaped $\text{TbPO}_4 \cdot \text{H}_2\text{O}$ nanorods (a) and standard data of bulk $\text{TbPO}_4 \cdot \text{H}_2\text{O}$ ((b), JCPDS card 20-1244).

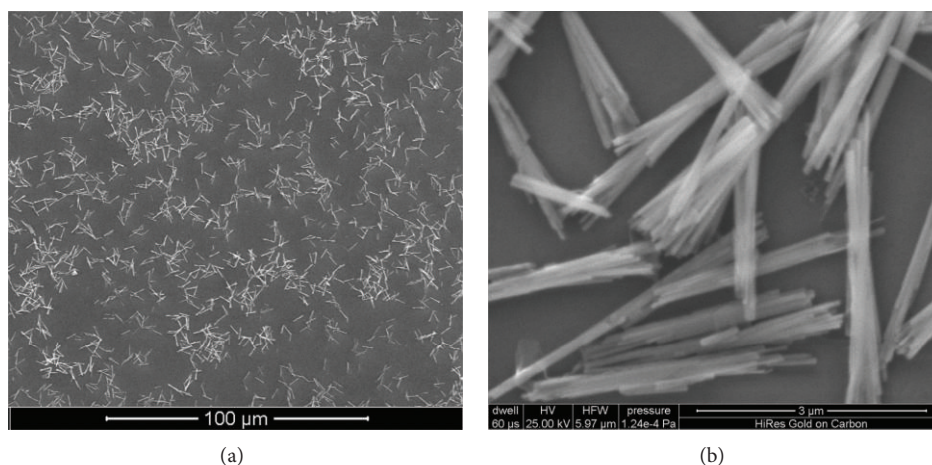


FIGURE 2: SEM images (a) and (b) of $\text{TbPO}_4 \cdot \text{H}_2\text{O}$ nanorods bundles.

bundle-shaped structures, phase structure, morphology, and optical properties were discussed in detail.

2. Experimental Section

2.1. Synthesis of Bundle-Shaped $\text{TbPO}_4 \cdot \text{H}_2\text{O}$ Nanorods. Tb_4O_7 (99.99%) and $(\text{NH}_4)_2\text{HPO}_4$ ($\geq 98.5\%$) were used as starting materials without any further purification. $\text{Tb}(\text{NO}_3)_3$ was prepared by dissolving Tb_4O_7 in diluted nitric acid, and the water in the solutions was distilled off by heating. Bundle-shaped $\text{TbPO}_4 \cdot \text{H}_2\text{O}$ nanorods were prepared by hydrothermal technique. Typically, 2 mmol of $(\text{NH}_4)_2\text{HPO}_4$ was added to 20 mL of 0.1 mol/L $\text{Tb}(\text{NO}_3)_3$ aqueous solution and the mixture was continuously stirred for 2 h. The obtained suspension was then transferred into a Teflon bottle held in a stainless steel autoclave, which was sealed and hydrothermally treated at 180°C for 24 h. After the autoclave was cooled to room temperature naturally, the precipitates were separated by centrifugation, washed with ethanol and distilled water twice, respectively, and dried at 70°C for 24 h to obtain the sample.

2.2. Characterization. Phase structure was characterized by a Bruker D8 Advance X-ray diffractometer (XRD) with $\text{Cu-K}\alpha$ radiation ($\lambda = 0.15406 \text{ nm}$). The accelerating voltage and emission current were 40 kV and 40 mA, respectively.

Morphology of the samples was observed using a scanning electron microscope (SEM, Quanta 200) with an acceleration voltage of 25 kV. The TEM image and selected area electron diffraction (SAED) pattern were obtained on a JEOL-2010 transmission electron microscope at an accelerating voltage of 200 kV. UV-Vis diffuse reflectance spectrum (DRS) was obtained using a UV/Vis Spectrophotometer (Lambda35, PerkinElmer) equipped with an integrating sphere attachment. Photoluminescence (PL) spectra and lifetime were recorded using an FLS920P Edinburgh Analytical Instrument apparatus equipped with a 450 W xenon lamp and a μF900H high-energy microsecond flash lamp as the excitation sources.

3. Results and Discussion

3.1. Phase Structure and Morphology. Figure 1 shows the XRD patterns of bundle-shaped $\text{TbPO}_4 \cdot \text{H}_2\text{O}$ nanorods (Figure 1(a)) and standard data of $\text{TbPO}_4 \cdot \text{H}_2\text{O}$ powders (Figure 1(b)). It can be seen that all of the diffraction peaks of the bundle-shaped $\text{TbPO}_4 \cdot \text{H}_2\text{O}$ nanorods are in agreement with the standard data of hexagonal structure $\text{TbPO}_4 \cdot \text{H}_2\text{O}$ (JCPDS No. 20-1244), with the space group of $P3_121$ (152). Figures 2(a) and 2(b) show the low- and high-magnification SEM images of $\text{TbPO}_4 \cdot \text{H}_2\text{O}$ nanorods bundles, respectively. It can be seen that these bundle-shaped

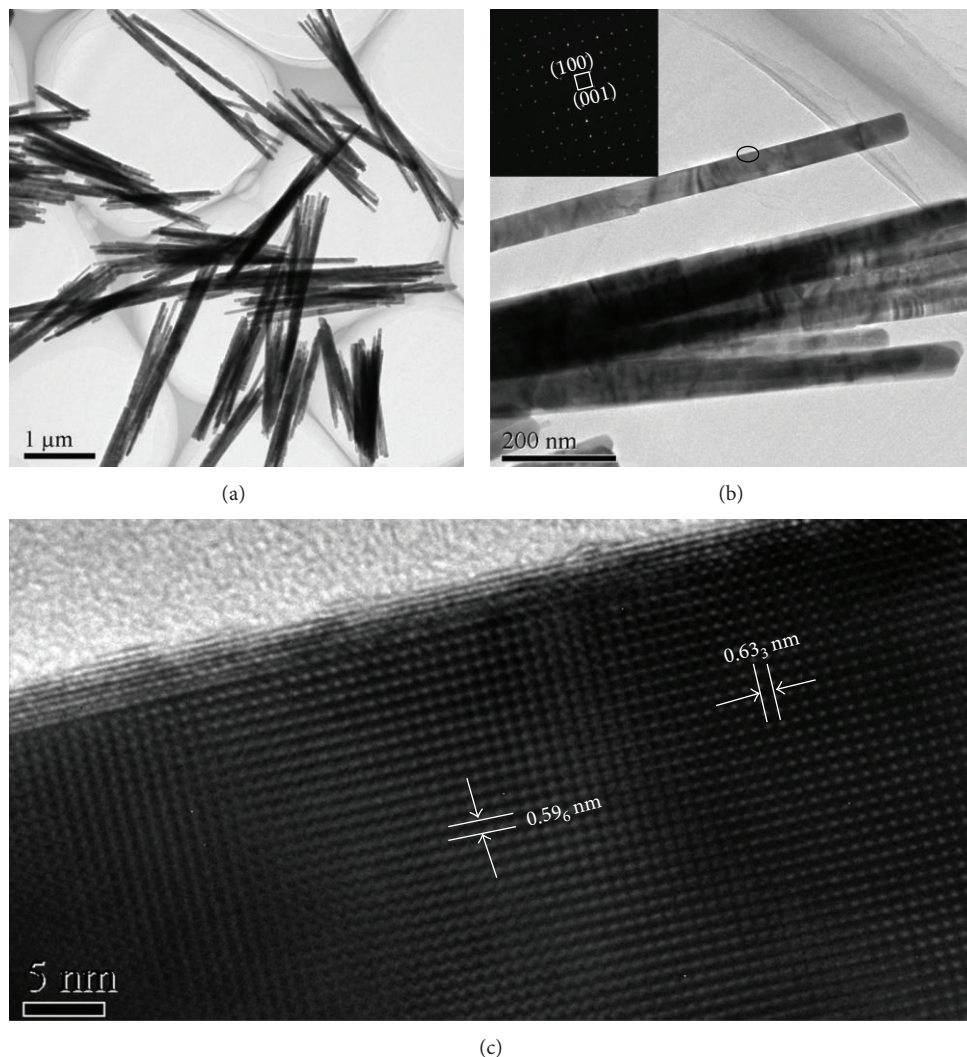


FIGURE 3: TEM images of bundle-shaped $\text{TbPO}_4 \cdot \text{H}_2\text{O}$ nanorods (a) and (b), SAED pattern (inset in (b)), and HRTEM image (c) of the single nanorod.

structures are homogeneous in the large field of vision (Figure 2(a)), the magnified image (Figure 2(b)) indicates that the bundle-shaped structures are actually composed of nanorods, and most of the nanorods are linked together by side-by-side conjunction.

To investigate the growth mechanism and microstructure of bundle-shaped structures in detail, the obtained sample was observed by the TEM and high resolution TEM (HRTEM) images equipped with selected area electron diffraction (SAED) pattern (Figure 3). It can be clearly seen from Figure 3(a) that the obtained sample is composed of bundle-shaped morphology, which is assembled by many $\text{TbPO}_4 \cdot \text{H}_2\text{O}$ nanorods with the diameter of ~ 45 nm and the length of ~ 2.3 μm . A high-magnified image of bundled nanorods (Figure 3(b)) indicates that these single crystalline nanorods as the primary construction unit are relatively uniform. The SAED pattern (Figure 3(b), inset) taken from the upper single nanorod can be indexed to the (100) and (001)

planes of $\text{TbPO}_4 \cdot \text{H}_2\text{O}$ single crystalline with the hexagonal phase structure. These findings are consistent with the XRD result mentioned above. The HRTEM image (Figure 3(c)) of the single $\text{TbPO}_4 \cdot \text{H}_2\text{O}$ nanorod marked as an oval in Figure 3(b) displays singlecrystalline nature. The values of interplanar spacing of $\text{TbPO}_4 \cdot \text{H}_2\text{O}$ nanorod are 0.596 and 0.633 nm, which is identical to the (100) and (001) facet distance of bulk $\text{TbPO}_4 \cdot \text{H}_2\text{O}$ powders, respectively. It can be seen that the growth direction of $\text{TbPO}_4 \cdot \text{H}_2\text{O}$ single-crystalline nanorod is along (001) plane. According to the experimental results and analysis, the growth mechanism of $\text{TbPO}_4 \cdot \text{H}_2\text{O}$ nanorods bundles was proposed. Generally, $\text{TbPO}_4 \cdot \text{H}_2\text{O}$ tends to grow as 1D nanorods, which is possibly due to the 1D characteristics of the infinite linear chains of hexagonal-structured TbPO_4 [7]. And then, the surface energy of these nanorods may change under the hydrothermal process [23], so these nanorods aggregates might be assembled and grown along the same direction

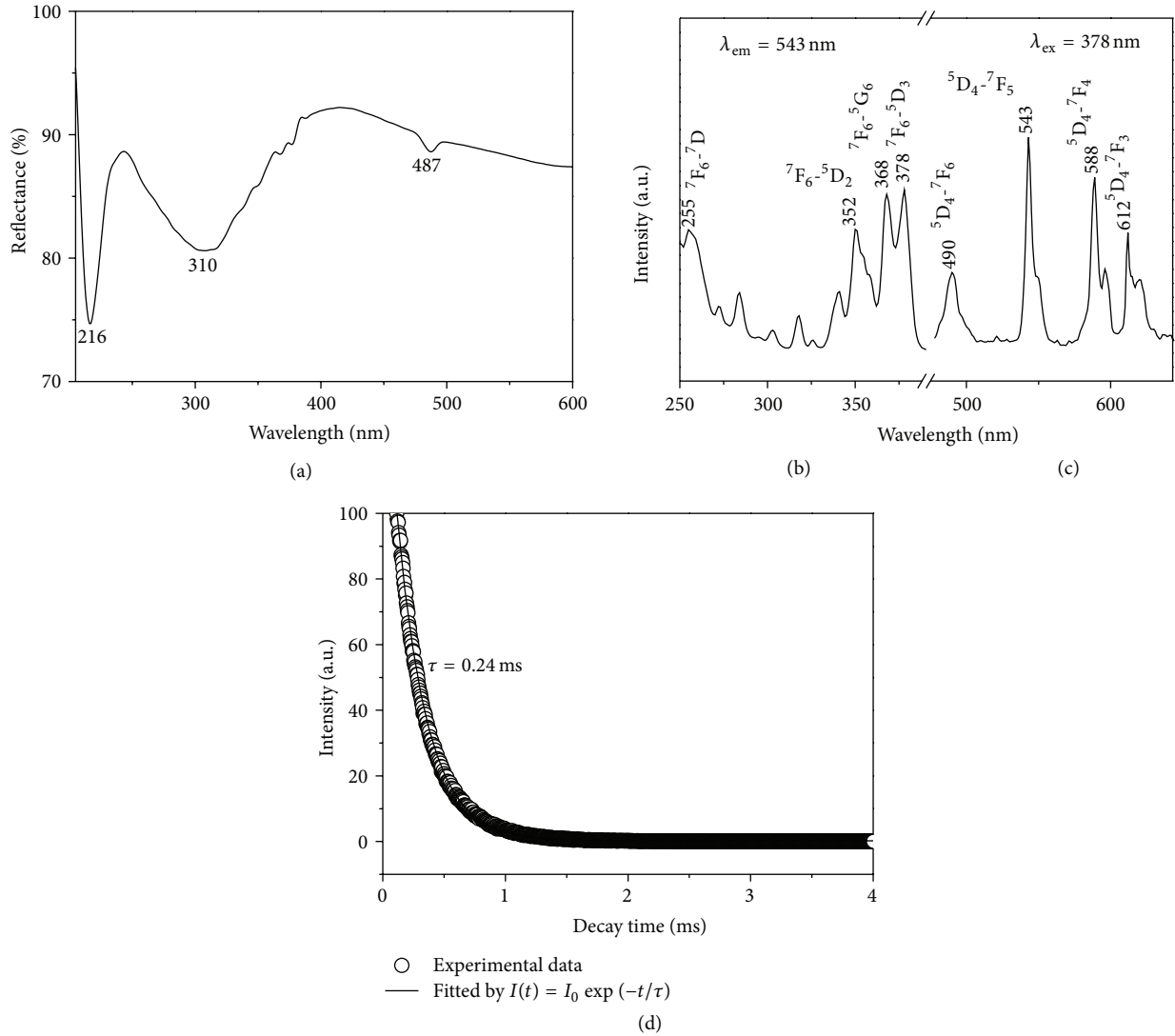


FIGURE 4: UV-Vis DRS (a), PL excitation (b), emission (c) spectra, and decay curve (d) of bundle-shaped TbPO₄·H₂O nanorods.

(oriented attachment) to form bundle-shaped structures. The formation process of TbPO₄·H₂O nanorods bundles is similar to that of In(OH)₃ rod bundles [24].

3.2. Optical Properties. Figure 4(a) shows the UV-Vis DRS spectrum of TbPO₄·H₂O nanorods bundles. The absorption peaks at 216 and 310 nm are due to the spin-allowed 4f-5d transition and the spin-forbidden transition of the Tb³⁺ ions, respectively. The absorption peak at 487 nm is assigned to the transitions from the ground level 7F_6 to the excited level 5D_4 of Tb³⁺ ion [25]. The excitation spectrum of TbPO₄·H₂O nanorods bundles was obtained by monitoring the emission of Tb³⁺ due to ${}^5D_4 \rightarrow {}^7F_5$ transition at 543 nm, as shown in Figure 4(b). It can be seen that the excitation peak at 255 nm is assigned to intra 4f⁸ transitions between the 4f⁷5d¹, and most of the excitation peaks can be clearly assigned (352 nm: ${}^7F_6 \rightarrow {}^5D_2$; 368 nm: ${}^7F_6 \rightarrow {}^5G_6$; and 378 nm: ${}^7F_6 \rightarrow {}^5D_3$). Under the UV light irradiation (378 nm), the emission spectrum is composed of four well-resolved peaks at 490, 543, 588,

and 612 nm, which is corresponding to the ${}^5D_4 \rightarrow {}^7F_J$ ($J = 6, 5, 4, 3$) transitions of Tb³⁺ ions as labeled in Figure 4(c). Figure 4(d) shows the PL decay curves of TbPO₄·H₂O nanorods bundles with the excitation wavelength (378 nm) and emission wavelength at 543 nm. The PL decay curve for Tb³⁺ in the TbPO₄·H₂O nanorods bundles can be well fitted into a single exponential function as $I(t) = I_0 \exp(-t/\tau)$ (τ is 1/e lifetime of Tb³⁺ ion) [26]. The lifetime for Tb³⁺ in TbPO₄·H₂O nanorods bundles is determined to be 0.24 ms.

4. Conclusion

In summary, the bundle-shaped TbPO₄·H₂O nanorods have been successfully prepared by the hydrothermal route. The reaction media are aqueous solution and free of any surfactants or templates, and the synthesis technique is simple and environmentally friendly. The bundle-shaped TbPO₄·H₂O nanostructures are assembled by many single crystalline TbPO₄·H₂O nanorods through side-by-side conjunction.

And these nanorods bundles yield green emission attributed to the transitions from the 5D_4 to the 7F_J ($J = 6, 5, 4, 3$) energy levels of Tb^{3+} , which makes these nanorods bundles have potential applications in many fields such as lighting and optoelectronic devices with nanometer dimensions.

Acknowledgments

This work is financially supported by the National Natural Science Foundation of China (nos. 21171179 and 21301200), the Excellent Youth Foundation of He'nan Scientific Committee (134100510018), and the Program for Science & Technology Innovation Talents in University of Henan Province (no. 2011HASTIT030).

References

- [1] G. Wang, Q. Peng, and Y. Li, "Lanthanide-doped nanocrystals: synthesis, optical-magnetic properties, and applications," *Accounts of Chemical Research*, vol. 44, no. 5, pp. 322–332, 2011.
- [2] S. J. Zeng, M. K. Tsang, C. F. Chan, K. L. Wong, and J. H. Hao, "PEG modified BaGdF₅: Yb/Er nanoprobe for multi-modal upconversion fluorescent, in vivo X-ray computed tomography and biomagnetic imaging," *Biomaterials*, vol. 33, pp. 9232–9238, 2012.
- [3] S. Zeng, J. Xiao, Q. Yang, and J. Hao, "Bi-functional NaLuF₄: Gd³⁺/Yb³⁺/Tm³⁺ nanocrystals: Structure controlled synthesis, near-infrared upconversion emission and tunable magnetic properties," *Journal of Materials Chemistry*, vol. 22, no. 19, pp. 9870–9874, 2012.
- [4] C. X. Li, Z. Y. Hou, C. M. Zhang et al., "Controlled synthesis of Ln³⁺ (Ln= Tb, Eu, Dy) and V⁵⁺ ion-doped YPO₄ nano/microstructures with tunable luminescent colors," *Chemistry of Materials*, vol. 21, no. 19, pp. 4598–4607, 2009.
- [5] R. Komban, R. Beckmann, S. Rode et al., "Surface modification of luminescent lanthanide phosphate nanorods with cationic "quat-primer" polymers," *Langmuir*, vol. 27, no. 16, pp. 10174–10183, 2011.
- [6] R. Yu, J. Bao, X. Yang et al., "Controlled synthesis of tetragonal terbium orthophosphate nanostructures through a solvothermal route," *Research on Chemical Intermediates*, vol. 37, no. 2-5, pp. 145–151, 2011.
- [7] J. Bao, R. Yu, J. Zhang et al., "Controlled synthesis of terbium orthophosphate spindle-like hierarchical nanostructures with improved photoluminescence," *European Journal of Inorganic Chemistry*, no. 16, pp. 2388–2392, 2009.
- [8] Y.-P. Fang, A.-W. Xu, R.-Q. Song et al., "Systematic synthesis and characterization of single-crystal lanthanide orthophosphate nanowires," *Journal of the American Chemical Society*, vol. 125, no. 51, pp. 16025–16034, 2003.
- [9] W. Di, M.-G. Willinger, R. A. S. Ferreira, X. Ren, S. Lu, and N. Pinna, "Citric acid-assisted hydrothermal synthesis of luminescent TbPO₄:Eu nanocrystals: controlled morphology and tunable emission," *Journal of Physical Chemistry C*, vol. 112, no. 48, pp. 18815–18820, 2008.
- [10] G. Phaomei, W. R. Singh, and R. S. Ningthoujam, "Solvent effect in monoclinic to hexagonal phase transformation in LaPO₄:RE (RE= Dy³⁺, Sm³⁺) nanoparticles: photoluminescence study," *Journal of Luminescence*, vol. 131, no. 6, pp. 1164–1171, 2011.
- [11] M. Ferhi, K. Horchani-Naifer, and M. Férid, "Hydrothermal synthesis and photoluminescence of the monophosphate LaPO₄:Eu(5%)," *Journal of Luminescence*, vol. 128, no. 11, pp. 1777–1782, 2008.
- [12] W. Bu, L. Zhang, Z. Hua, H. Chen, and J. Shi, "Synthesis and characterization of uniform spindle-shaped microarchitectures self-assembled from aligned single-crystalline nanowires of lanthanum phosphates," *Crystal Growth and Design*, vol. 7, no. 11, pp. 2305–2309, 2007.
- [13] Y. Liu, Z.-G. Lu, Y.-Y. Gu, and W. Li, "Hydrothermal-assisted ion exchange synthesis and photoluminescence of Li⁺ and Eu³⁺ codoped NaLa(WO₄)₂ as near-UV type red phosphors," *Journal of Luminescence*, vol. 132, no. 5, pp. 1220–1225, 2012.
- [14] Y.-F. Liu, Z.-P. Yang, and Q.-M. Yu, "Preparation and its luminescent properties of AlPO₄:Eu³⁺ phosphor for w-LED applications," *Journal of Alloys and Compounds*, vol. 509, no. 21, pp. L199–L202, 2011.
- [15] C. Wu and Y. Wang, "Hydrothermal synthesis and luminescent properties of (La,Gd)PO₄:Tb phosphors under VUV excitation," *Materials Letters*, vol. 61, no. 11-12, pp. 2416–2418, 2007.
- [16] P. Morin, J. Rouchy, and Z. Kazei, "Magnetic and magnetoelastic properties in tetragonal TbPO₄," *Physical Review B*, vol. 50, no. 17, pp. 12625–12634, 1994.
- [17] C. Anderer, G. Hess, and H. G. Kahle, "Extensive studies on the low-temperature properties of TbPO₄. II. Measurements of the Faraday rotation," *Journal of Physics: Condensed Matter*, vol. 5, no. 7, article 022, pp. 945–954, 1993.
- [18] Z. Wang, Z. Quan, and J. Lin, "Remarkable changes in the optical properties of CeO₂ nanocrystals induced by lanthanide ions doping," *Inorganic Chemistry*, vol. 46, no. 13, pp. 5237–5242, 2007.
- [19] Z. L. Wang, J. H. Hao, H. L. W. Chan, W. T. Wong, and K. L. Wong, "A strategy to simultaneously realizing the cubic-to-hexagonal phase transition and controlling small size of NaYF₄:Yb³⁺, Er³⁺ nanocrystals for in-vitro cell imaging," *Small*, vol. 8, no. 12, pp. 1863–1868, 2012.
- [20] J. Lü, T. Fan, J. N. Xie, and G. J. Chen, "Tunable luminescence and energy transfer of TbPO₄:Eu³⁺ nanocrystals," *Optics Communications*, vol. 286, no. 12, pp. 221–223, 2013.
- [21] L. H. Zhang, H. P. You, M. Yang, and Y. H. Song, "Facile one-pot synthesis and luminescence of hexagonal TbPO₄·nH₂O hollow spheres," *Materials Letters*, vol. 67, no. 1, pp. 256–258, 2012.
- [22] M. Yang, H. You, Y. Song et al., "Synthesis and luminescence properties of sheaflike TbPO₄ hierarchical architectures with different phase structures," *Journal of Physical Chemistry C*, vol. 113, no. 47, pp. 20173–20177, 2009.
- [23] X. D. Zhang and Y. Xie, "Recent advances in free-standing two-dimensional crystals with atomic thickness: design, assembly and transfer strategies," *Chemical Society Reviews*, vol. 42, no. 21, pp. 8187–8199, 2013.
- [24] J. Yang, C. Lin, Z. Wang, and J. Lin, "In(OH)₃ and In₂O₃ nanorod bundles and spheres: microemulsion-mediated hydrothermal synthesis and luminescence properties," *Inorganic Chemistry*, vol. 45, no. 22, pp. 8973–8979, 2006.
- [25] Z.-L. Wang, H. L. W. Chan, H.-L. Li, and J. H. Hao, "Highly efficient low-voltage cathodoluminescence of LaF₃: Ln³⁺ (Ln= Eu³⁺, Ce³⁺, Tb³⁺) spherical particles," *Applied Physics Letters*, vol. 93, no. 14, Article ID 141106, 2008.
- [26] Z.-L. Wang, J. Hao, and H. L. W. Chan, "Light emission due to energy transfer from Gd³⁺ to Eu³⁺ ions in paramagnetic NaGdF₄:Eu³⁺ submicrometer disks," *Journal of the Electrochemical Society*, vol. 157, no. 10, pp. J315–J318, 2010.

Research Article

Synthesis and Downconversion Emission Property of $\text{Yb}_2\text{O}_3:\text{Eu}^{3+}$ Nanosheets and Nanotubes

Chao Qian, Tianmei Zeng, and Hongrong Liu

College of Physics and Information Science and Key Laboratory of Low-Dimensional Quantum Structures and Quantum Control of the Ministry of Education, Hunan Normal University, Changsha, Hunan 410081, China

Correspondence should be addressed to Hongrong Liu; hrliu@hunnu.edu.cn

Received 11 October 2013; Accepted 22 November 2013

Academic Editor: Jianhua Hao

Copyright © 2013 Chao Qian et al. This is an open access article distributed under the Creative Commons Attribution License, which permits unrestricted use, distribution, and reproduction in any medium, provided the original work is properly cited.

Ytterbium oxide (Yb_2O_3) nanocrystals with different Eu^{3+} (1%, 2%, 5%, and 10%) doped concentrations were synthesized by a facile hydrothermal method, subsequently by calcination at 700°C . The crystal phase, size, and morphology of prepared samples were characterized by X-ray diffraction (XRD) and transmission electron microscopy (TEM). The results show that the as-prepared Yb_2O_3 nanocrystals with sheet- and tube-like shape have cubic phase structure. The Eu^{3+} doped Yb_2O_3 nanocrystals were revealed to have good down conversion (DC) property and intensity of the DC luminescence can be modified by Eu^{3+} contents. In our experiment the 1% Eu^{3+} doped Yb_2O_3 nanocrystals showed the strongest DC luminescence among the obtained Yb_2O_3 nanocrystals.

1. Introduction

Recently, rare earth (RE) doped luminescence materials have attracted considerable attention owing to their excellent applications in optics, biological labeling and imaging, new light source, catalyst and so on, owing to their unique properties such as narrow band of spectrum, monochromatism and bright of emission light, much stronger light absorb, good thermal and chemical stabilities, and low biotoxicity [1–8]. Much more investigations have focused on fluorides because of their unique advantages such as low phonon energy and high upconversion (UC) and DC luminescence [9, 10]. For example, dual-modal (UC/DC) luminescence has been successfully realized through lanthanide (Ln) ions doped NaGdF_4 core/shell nanocrystals by Chen's group [11]. In addition to fluorides, RE doped oxides with much better high temperature thermal stability have also attracted much interests and they are applied in thin films, fiber laser, capacitor and precision optical glass, and so forth [12–16]. Chen's group have investigated the phonon confinement effects on the luminescence dynamics in $\text{Gd}_2\text{O}_3:\text{Eu}^{3+}$ nanotubes and

provided experimental evidence of anomalous thermalization [14]. In addition, the synthesis process of RE oxide doped Ln ions is much more simple and controllable [17]. For example, the Tb_4O_7 and Y_2O_3 nanotubes with open ends were synthesized by a simple hydrothermal method without adding any template [18]. Via one-step hydrothermal method, the crystal phase, shape, and size controlling of these oxides can be easily obtained by changing the reaction parameters such as pH value of the solution, reaction temperature/time, and. As a result, DC luminescence of various RE oxides like Ln (Eu, Tb, Dy) doped Y_2O_3 , Ce_2O_3 and Gd_2O_3 has been widely investigated and the important applications of these RE oxides have been reported in recent years [19–22]. Although Yb_2O_3 is also a very promising matrix material [23], there is still lack of research about effect of Eu^{3+} dopant on the DC luminescence of Yb_2O_3 .

In this paper, we reported the controllable synthesis of Eu^{3+} doped Yb_2O_3 nanosheets and nanotubes with cubic structure by a general and facile hydrothermal method with combination of calcination. The yellow DC luminescence was displayed under ultraviolet (UV) excitation at 395 nm. Furthermore, intensity of DC luminescence can be modified

by varying Eu^{3+} content and it is observed in the emission spectra that 1% Eu^{3+} doped Yb_2O_3 nanocrystals emit the strongest DC light in our experiment.

2. Experimental

2.1. Materials. The following chemical reagents Yb_2O_3 , Eu_2O_3 , HNO_3 and NaOH were used in synthesis of Eu^{3+} doped Yb_2O_3 . Among them, Yb_2O_3 and Eu_2O_3 with purity of 99.99% were purchased from Sinopharm Chemical Reagent Co. Ltd. The analytical grade HNO_3 and NaOH were used as received without further purification.

2.2. Synthesis of Eu^{3+} Doped Rare-Earth Hydroxide/Oxide Nanosheets and Nanotubes. In order to prepare Eu^{3+} doped Yb_2O_3 , we have to first prepare $\text{Yb}(\text{NO}_3)_3$ (0.5 M) and $\text{Eu}(\text{NO}_3)_3$ (0.1 M) by dissolving the Yb_2O_3 and Eu_2O_3 in HNO_3 . Then the precursor $\text{Yb}(\text{OH})_3$ was prepared by mixing $\text{Yb}(\text{NO}_3)_3$ and $\text{Eu}(\text{NO}_3)_3$ with addition of NaOH for adjusting the pH value of the liquid mixture. Finally, the Eu^{3+} doped Yb_2O_3 nanosheets and nanotubes with Eu^{3+} concentrations of 1, 2, 5, and 10% were synthesized by calcination at 700°C . The experimental details are listed below.

1 mmol $\text{RE}(\text{NO}_3)_3$ with the designed concentration of $\text{Eu}(\text{NO}_3)_3$ of 1, 2, 5, and 10% was, respectively, added into 30 mL distilled water and pH value of the liquid mixture was then tuned to 14 by adding NaOH solution. The above mixture was stirred by magnetic stirring apparatus for 15 minutes at room temperature and colloidal precipitation appeared in the solution. Then the mixture was transferred into 50 mL stainless Teflon lined autoclave and heated at 180°C for 12 h. The as-prepared $\text{Yb}_2\text{O}_3:\text{Eu}^{3+}$ microcrystals were precipitated at the bottom of the vessel. The precipitates were taken out by pouring out the upper liquid and then washed with deionized water three times to remove impurities such as OH^- , NO_3^- and Na^+ . Then the precursor $\text{Yb}(\text{OH})_3$ precipitates were dried at 60°C for 6 h. Finally the different concentration Eu^{3+} doped Yb_2O_3 nanocrystals were obtained by calcination of these precursors at 700°C for 3 h.

2.3. Characterizations. The crystal phase of the products was identified by XRD using an X-ray diffractometer (model: D/max- γ A) with $\text{Cu-K}\alpha$ radiation ($\lambda = 1.5406 \text{ \AA}$), and the 2θ range was from 10° to 80° . The microstructure of the products was characterized by TEM (JEOL-2100F) together with energy-dispersive X-ray spectroscopy (EDS). The DC emission and excitation spectra were recorded by a SENS-9000 spectrophotometer equipped with xenon lamp that was used as the UV light source. All of the above tests were performed at room temperature.

3. Results and Discussion

XRD pattern of the as-prepared products was shown in Figure 1, in which all of the diffraction peaks are matched well with the standard cubic phase Yb_2O_3 structure (JCPDS: 87-2374). No extra diffraction peaks corresponding to other impurity phase were observed in this XRD pattern, indicating

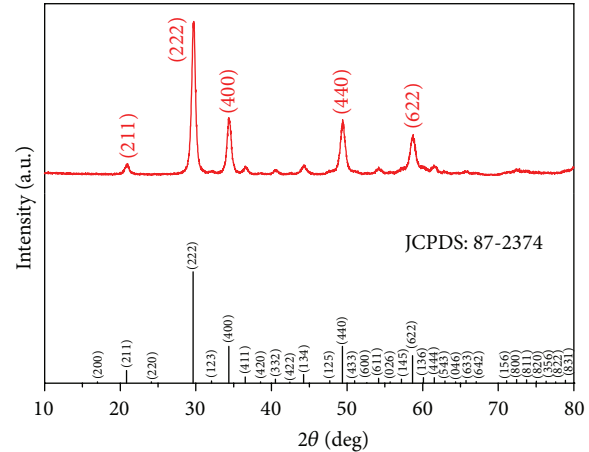


FIGURE 1: XRD pattern of $\text{Yb}_2\text{O}_3:1\% \text{Eu}^{3+}$ nanocrystals (top) and standard diffraction of cubic phase Yb_2O_3 (JCPDS: 87-2374, bottom for comparison).

the pure cubic phase Yb_2O_3 obtained at low temperature (180°C).

In order to establish the correlation between the Eu^{3+} doped $\text{Yb}(\text{OH})_3$ and Yb_2O_3 , the size and morphology of the precursors $\text{Yb}(\text{OH})_3:1\% \text{Eu}^{3+}$ and $\text{Yb}_2\text{O}_3:1\% \text{Eu}^{3+}$ were characterized by TEM, respectively. Figures 2(a) and 2(b) show the typical TEM images of $\text{Yb}(\text{OH})_3:1\% \text{Eu}^{3+}$. As demonstrated, the precursors have two typical shapes: sheet and tube-like structure. After calcination, $\text{Yb}_2\text{O}_3:1\% \text{Eu}^{3+}$ presents the similar morphologies (Figures 2(c) and 2(d)) as the precursor hydroxides. The inset image in Figure 2(d) shows the selected area electron diffraction (SAED) pattern of a single $\text{Yb}_2\text{O}_3:1\% \text{Eu}^{3+}$ nanosheet, which reveal the single-crystalline nature of the nanosheet and can be readily indexed to cubic phase structure. In addition, as shown in Figures 2(a) and 2(b), some sheets were curled into tube-like shape, indicating the formation mechanism of tube structure with open ends coincident with self-rolled model, which is similar to Zhang's report [24]. Figure 2(e) shows the EDS analysis of $\text{Yb}_2\text{O}_3:\text{Eu}^{3+}$ nanosheets, in which the Yb, Eu, and O except Cu resulting from copper grid are the major elements in sheets. As a result, the Eu^{3+} is successfully incorporated into the Yb_2O_3 . It should be noted that the compositions of the $\text{Yb}_2\text{O}_3:\text{Eu}^{3+}$ nanotubes were also analyzed by EDS equipped with the TEM and the similar results with nanosheets were obtained (data not shown).

Under UV light excitation, the DC luminescence properties of $\text{Yb}_2\text{O}_3:\text{Eu}^{3+}$ have been investigated. The photoluminescence excitation and emission spectra were recorded and shown in Figure 3, where the excitation spectrum of $\text{Yb}_2\text{O}_3:1\% \text{Eu}^{3+}$ nanocrystals was obtained by monitoring at 593 nm. Several wavelengths of UV light can excite emission with wavelength of 593 nm, but the strongest emission happened at the 395 nm UV light. Therefore, the 395 nm UV light is the best excitation wavelength. Meanwhile, the emission spectrum (Figure 3(b)) was measured under the excitation at 395 nm and eight emission peaks recorded at 470, 525, 530,

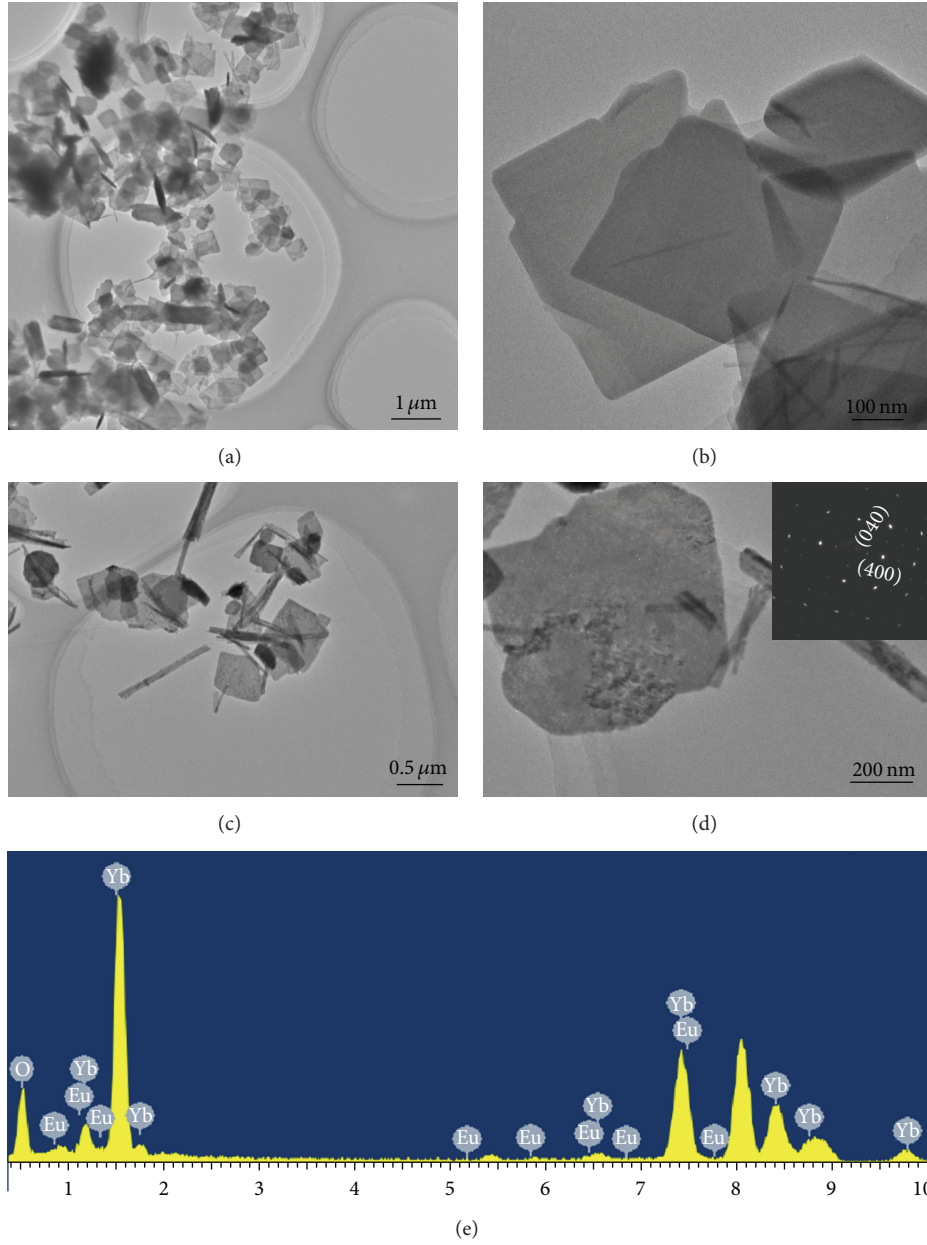


FIGURE 2: (a) TEM image of $\text{Yb}(\text{OH})_3:\text{Eu}^{3+}$ nanosheets; (b) highly magnified TEM image of individual $\text{Yb}(\text{OH})_3:\text{Eu}^{3+}$ nanosheets; (c) TEM image of $\text{Yb}_2\text{O}_3:\text{Eu}^{3+}$ nanosheets and nanotubes; (d) highly magnified TEM image of individual $\text{Yb}_2\text{O}_3:\text{Eu}^{3+}$ nanosheets and nanotubes; (e) EDS analysis of $\text{Yb}_2\text{O}_3:\text{Eu}^{3+}$ nanosheets. The inset of Figure 2(d) shows the SAED pattern of Yb_2O_3 nanosheets.

574, 593 610, 651, and 660 nm, respectively, were produced by the electron transition from $^5\text{D}_J$ to $^7\text{F}_{J'}$ levels ($J = 0, 1, 2$, and $J' = 1-4$) [6, 25]. The strongest DC emission was centered at 593 nm (due to the electron transition from $^5\text{D}_0$ to $^7\text{F}_1$ levels), leading to yellow emission light.

Possible mechanical energy level diagram for Eu^{3+} doped Yb_2O_3 nanocrystals after pumping at 395 nm is shown in Figure 4 [6, 25]. Under the excitation at 395 nm, the Eu^{3+} ion can be excited from the ground state to the excited state. The excited state Eu^{3+} ions will decay nonradiatively to the

$^5\text{D}_2$, $^5\text{D}_1$ and $^5\text{D}_0$ levels, resulting in the corresponding blue ($^5\text{D}_2 \rightarrow ^7\text{F}_0$), green ($^5\text{D}_1 \rightarrow ^7\text{F}_{0,1,3}$), yellow ($^5\text{D}_0 \rightarrow ^7\text{F}_1$) and red ($^5\text{D}_0 \rightarrow ^7\text{F}_{2,3,4}$) emissions, respectively.

The influence of Eu^{3+} concentration on the DC luminescence was investigated by comparison of the emission spectra (Figure 5) of the synthesized $\text{Yb}_2\text{O}_3:\text{X}\% \text{Eu}$ ($X = 1, 2, 5, 10$) samples. It can be seen that the strongest DC luminescence was achieved in 1% Eu doped sample. With further increasing the Eu^{3+} content, the DC luminescent intensity was decreased, which was mainly ascribed to the concentration quenching effect [26].

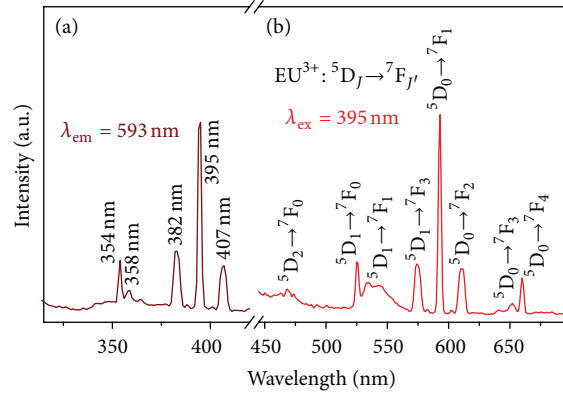


FIGURE 3: (a) Photoluminescence excitation spectrum of $\text{Yb}_2\text{O}_3:1\% \text{Eu}^{3+}$ nanocrystals by detecting the emission at 593 nm and (b) emission spectrum under the excitation at 395 nm.

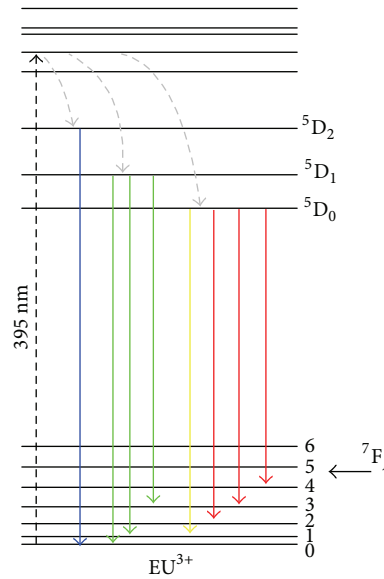


FIGURE 4: Scheme of energy levels of Eu^{3+} in Yb_2O_3 and possible mechanical energy level diagram for Eu^{3+} after pumping excitation at 395 nm.

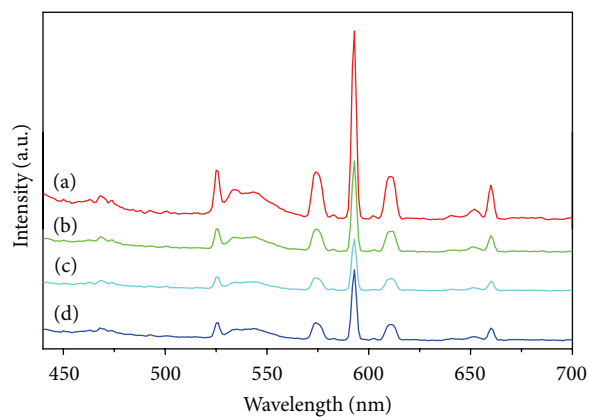


FIGURE 5: Photoluminescence emission spectra of different concentrations of Eu^{3+} doped Yb_2O_3 : (a) 1% Eu^{3+} , (b) 2% Eu^{3+} , (c) 5% Eu^{3+} , and (d) 10% Eu^{3+} by excitation at 395 nm.

4. Conclusions

$\text{Yb}_2\text{O}_3:\text{Eu}^{3+}$ nanosheets and nanotubes doped with different concentrations of Eu^{3+} were successfully synthesized by a facile controllable hydrothermal process followed by calcination at 700°C . The XRD confirms the synthesized $\text{Yb}_2\text{O}_3:\text{Eu}^{3+}$ with cubic structure. The TEM images revealed $\text{Yb}(\text{OH})_3:\text{Eu}^{3+}$ with sheet- and tube-like morphology, respectively. The DC emissions of the synthesized $\text{Yb}_2\text{O}_3:\text{Eu}^{3+}$ centered at 470, 525, 530, 574, 593, 610, 651 and 660 nm were observed under the strongest excitation at 395 nm. The intensity of DC emission can be tuned by adjusting the concentration of Eu^{3+} , while the strongest intensity yellow DC luminescence was obtained at 1% Eu^{3+} .

Acknowledgments

This work was supported by the National Natural Science Foundation of China (no. 51102202), the New Century Excellent Talents in University (NCET-13-0787), the Specialized Research Fund for the Doctoral Program of Higher Education of China (no. 20114301120006) and Hunan Provincial Natural Science Foundation of China (nos. 12JJ4056 and 13JJ1017), the Scientific Foundation of Ministry of Education (212119) and the Scientific Research Fund of Hunan Provincial Education Department (13B062 and YB2012B027).

References

- [1] R. Yan and Y. Li, "Down/up conversion in LnO^{3+} -doped YF_3 nanocrystals," *Advanced Functional Materials*, vol. 15, no. 5, pp. 763–770, 2005.
- [2] B. M. Tissue, "Synthesis and luminescence of lanthanide ions in nanoscale insulating hosts," *Chemistry of Materials*, vol. 10, no. 10, pp. 2837–2845, 1998.
- [3] Y. S. Liu, D. T. Tu, H. M. Zhu, and X. Y. Chen, "Lanthanide-doped luminescent nanoprobe: controlled synthesis, optical spectroscopy, and bioapplications," *Chemical Society Reviews*, vol. 42, no. 16, pp. 6924–6958, 2013.
- [4] P. A. Tanner, "Synthesis and luminescence of nano-insulators doped with lanthanide ions," *Journal of Nanoscience and Nanotechnology*, vol. 5, no. 9, pp. 1455–1464, 2005.
- [5] G.-Y. Adachi and N. Imanaka, "The binary rare earth oxides," *Chemical Reviews*, vol. 98, no. 4, pp. 1479–1514, 1998.
- [6] Y. Wang, Y. Liu, Q. Xiao, H. Zhu, R. Li, and X. Chen, " Eu^{3+} doped KYF_4 nanocrystals: synthesis, electronic structure, and optical properties," *Nanoscale*, vol. 3, no. 8, pp. 3164–3169, 2011.
- [7] Z. Bai, M. Fujii, T. Hasegawa, K. Imakita, M. Mizuhata, and S. Hayashi, "Efficient ultraviolet-blue to near-infrared downconversion in Bi-Dy-Yb-doped zeolites," *Journal of Physics D*, vol. 44, no. 45, Article ID 455301, 2011.
- [8] M. Bruchez Jr., M. Moronne, P. Gin, S. Weiss, and A. P. Alivisatos, "Semiconductor nanocrystals as fluorescent biological labels," *Science*, vol. 281, no. 5385, pp. 2013–2016, 1998.
- [9] G. Wang and Q. Peng, "Tunable photoluminescence of $\text{NaYF}_4:\text{Eu}$ nanocrystals by Sr^{2+} codoping," *Journal of Solid State Chemistry*, vol. 184, no. 1, pp. 59–63, 2011.
- [10] L. Wang and Y. Li, "Controlled synthesis and luminescence of lanthanide doped NaYF_4 nanocrystals," *Chemistry of Materials*, vol. 19, no. 4, pp. 727–734, 2007.
- [11] Y. Liu, D. Tu, H. Zhu, R. Li, W. Luo, and X. Chen, "A strategy to achieve efficient dual-mode luminescence of Eu^{3+} in lanthanides doped multifunctional NaGdF_4 nanocrystals," *Advanced Materials*, vol. 22, no. 30, pp. 3266–3271, 2010.
- [12] S. Ohmi, C. Kobayashi, I. Kashiwagi, C. Ohshima, H. Ishiwara, and H. Iwai, "Characterization of La_2O_3 and Yb_2O_3 thin films for high-k gate insulator application," *Journal of the Electrochemical Society*, vol. 150, no. 7, pp. F134–F140, 2003.
- [13] M. C. Paul, A. V. Kir'yanov, Y. O. Barmenkov et al., " Yb_2O_3 doped yttrium-alumino-silicate nano-particles based LMA optical fibers for high-power fiber lasers," *Journal of Lightwave Technology*, vol. 30, no. 13, pp. 2062–2068, 2012.
- [14] L. Liu, E. Ma, R. Li, G. Liu, and X. Chen, "Effects of phonon confinement on the luminescence dynamics of Eu^{3+} in Gd_2O_3 nanotubes," *Nanotechnology*, vol. 18, no. 1, Article ID 015403, 2007.
- [15] P. Zhang, Y. Ma, Z. Zhang et al., "Comparative toxicity of nanoparticulate/bulk Yb_2O_3 and YbCl_3 to cucumber (*Cucumis sativus*)," *Environmental Science and Technology*, vol. 46, no. 3, pp. 1834–1841, 2012.
- [16] A. Towata, M. Sivakumar, K. Yasui, T. Tuziuti, T. Kozuka, and Y. Iida, "Synthesis of europium-doped yttrium hydroxide and yttrium oxide nanosheets," *Journal of Materials Science*, vol. 43, no. 4, pp. 1214–1219, 2008.
- [17] X. Wang, J. Zhuang, Q. Peng, and Y. Li, "A general strategy for nanocrystal synthesis," *Nature*, vol. 437, no. 7055, pp. 121–124, 2005.
- [18] Y.-P. Fang, A.-W. Xu, L.-P. You et al., "Hydrothermal synthesis of rare earth (TB, Y) hydroxide and oxide nanotubes," *Advanced Functional Materials*, vol. 13, no. 12, pp. 955–960, 2003.
- [19] D. K. Williams, B. Bihari, B. M. Tissue, and J. M. McHale, "Preparation and fluorescence spectroscopy of bulk monoclinic $\text{Eu}^{3+}:\text{Y}_2\text{O}_3$ and comparison to $\text{Eu}^{3+}:\text{Y}_2\text{O}_3$ nanocrystals," *The Journal of Physical Chemistry B*, vol. 102, no. 6, pp. 916–920, 1998.
- [20] A. S. Ivanova, "Physicochemical and catalytic properties of systems based on CeO_2 ," *Kinetics and Catalysis*, vol. 50, no. 6, pp. 797–815, 2009.
- [21] J. Yang, C. Li, Z. Cheng et al., "Size-tailored synthesis and luminescent properties of one-dimensional $\text{Gd}_2\text{O}_3:\text{Eu}^{3+}$ nanorods and microrods," *Journal of Physical Chemistry C*, vol. 111, no. 49, pp. 18148–18154, 2007.
- [22] M. Nickkova, D. Dosev, S. J. Gee, B. D. Hammock, and I. M. Kennedy, "Microarray immunoassay for phenoxybenzoic acid using polymer encapsulated $\text{Eu}:\text{Gd}_2\text{O}_3$ nanoparticles as fluorescent labels," *Analytical Chemistry*, vol. 77, no. 21, pp. 6864–6873, 2005.
- [23] J. Ding, H. Gu, P. G. Qiu et al., "Creation of Yb_2O_3 Nanoprecipitates through an oxidation process in Bulk Yb-filled skutterudites," *Journal of Electronic Materials*, vol. 42, no. 3, pp. 382–388, 2013.
- [24] F. Zhang and D. Zhao, "Synthesis of uniform rare earth fluoride (NaMF_4) nanotubes by in situ ion exchange from their hydroxide [$\text{M}(\text{OH})_3$] parents," *ACS Nano*, vol. 3, no. 1, pp. 159–164, 2009.
- [25] M. Yu, J. Lin, and J. Fang, "Silica spheres coated with $\text{YVO}_4:\text{Eu}^{3+}$ layers via sol-gel process: a simple method to obtain spherical core-shell phosphors," *Chemistry of Materials*, vol. 17, no. 7, pp. 1783–1791, 2005.
- [26] F. Wang, Y. Han, C. S. Lim et al., "Simultaneous phase and size control of upconversion nanocrystals through lanthanide doping," *Nature*, vol. 463, no. 7284, pp. 1061–1065, 2010.

Research Article

Structural Disorder in the Key Lead-Free Piezoelectric Materials, $K_xNa_{1-x}NbO_3$ and $(1-x)Na_{0.5}Bi_{0.5}TiO_3 + xBaTiO_3$

Jason Schiemer,^{1,2} Ray Withers,¹ Yun Liu,¹ Yiping Guo,¹ Zhiguo Yi,¹ and Jian Wang¹

¹ Research School of Chemistry, Australian National University, Science Road, Acton, ACT 0200, Australia

² Department of Earth Sciences, University of Cambridge, Downing Street, Cambridge CB2 3EQ, UK

Correspondence should be addressed to Jason Schiemer; jas263@cam.ac.uk

Received 25 October 2013; Accepted 17 November 2013

Academic Editor: Danyang Wang

Copyright © 2013 Jason Schiemer et al. This is an open access article distributed under the Creative Commons Attribution License, which permits unrestricted use, distribution, and reproduction in any medium, provided the original work is properly cited.

Using electron diffraction, trends in the local structural behaviour of the $K_xNa_{1-x}NbO_3$ (KNN x) and the $(1-x)Na_{0.5}Bi_{0.5}TiO_3 + xBaTiO_3$ (NBT- x BT) systems are investigated. In KNN, electron diffraction shows a single plane of diffuse intensity perpendicular to [010] across the entire phase diagram, indicating the existence of ferroelectric disorder along this axis. An additional characteristic pattern of diffuse scattering is also observed, involving rods of diffuse intensity running along the $[100]_p^*$ and $[001]_p^*$ directions of the perovskite substructure and indicative of octahedral tilt disorder about these axes. Similarly, in the NBT- x BT system, rods of diffuse intensity running along the $\langle 100 \rangle_p^*$ directions of the perovskite substructure are observed, again indicating octahedral tilt disorder. Ferroelectric-like disorder is also observed in highly BT doped samples, and a continuous change from the “rhombohedral” structure of NBT to the “tetragonal” structure of NBT-12BT is seen from characteristic variation in observed superstructure reflections. A crystal chemical rationalisation of these results is performed, and the implications for structure and properties are discussed.

1. Introduction

$K_xNa_{1-x}NbO_3$ (KNN x) became known as a promising lead-free piezoelectric ceramic system when relatively high piezoelectric coefficients (up to ~ 300 pC/N) along with Curie temperatures of up to 400°C were reported by Saito et al. in 2004 [1]. $(1-x)Na_{0.5}Bi_{0.5}TiO_3 + xBaTiO_3$ (NBT- x BT) is similarly high performing. Its raw piezoelectric performance is not as high as in KNN, ~ 160 pm/V [2], but it can display huge electrostrictive strains, up to 0.48% [3], which show promise for electrostrictive actuators with zero strain, as long as they are designed to account for their nonlinear response. These materials are among the few lead-free piezoelectric materials that can compete with lead-based materials in specialized applications. Due to their performance, the structure of materials such as KNN and NBT-BT is of considerable interest in order to establish structure-property relationships and to engineer improvements.

At room temperature in the KNN system, there is long range ferroelectric order in the plane perpendicular to a particular parent perovskite $\langle 001 \rangle_p$ direction (usually taken

to be the $[010]_p$ direction in KNN). As long range ferroelectric order is established along both the $[100]_p$ and $[001]_p$ directions, the direction of the spontaneous polarization is then along a parent perovskite $\langle 101 \rangle_p$ direction, in the case of the end-member $KNbO_3$, and it might be expected to remain largely unchanged across the KNN phase diagram unless there is an unexpectedly strong coupling between ferroelectric ordering and octahedral tilt rotation. There is a pattern of octahedral tilting induced by the introduction of the smaller Na^+ ions into the perovskite A sites of the originally unrotated, $Amm2$, $KNbO_3$ structure type. According to the current phase diagram [4], the onset of b^+ tilting does not occur until a value of $x = 0.4$. b^+ tilting is then reported to occur from $x = 0.4$ to 0.2, below which a^- , b^+ , and c^- tilts are reported. The nature of the local structure has not been closely examined, as previous investigations involve powder diffraction using neutrons [5] and X-rays [4, 6], which are not very sensitive to short range order.

NBT-BT initially appears simpler than that in KNN. The end member, NBT, is rhombohedral, with ferroelectricity along a particular $[111]_p$ direction. Above $\sim 7\%$ BT

doping, the rhombohedral NBT structure transitions to a metrically tetragonal state when observed with powder diffraction methods, while a pseudocubic state exists in the “morphotropic phase boundary” between these two phases. Additionally, there are electric field dependent phase transitions in this system at 7% BT doping [7], from pseudocubic to metrically tetragonal, which are irreversible.

Very few electron diffraction or diffuse scattering investigations have been performed on these systems. This report seeks to examine disorder present in these materials, in particular, the correlations between the two system and the effects of this disorder on structure determination and properties.

2. Materials and Methods

Synthesis of KNN x was performed for samples of composition $x = 0.15, 0.21, 0.35, 0.46,$ and 0.75 . This was by solid-state reaction for $x = 0.15, 0.21, 0.35,$ and 0.75 . Starting reagents were $\text{K}_2\text{CO}_3, \text{Na}_2\text{CO}_3,$ and Nb_2O_5 . Mixing and homogenising of reagents were performed in a planetary ball mill, using yttrium stabilised zirconia balls in polymeric tanks. The reagents were ball-milled in stoichiometric ratios for 12 h under acetone followed by calcining at 900°C for 5 h to drive off carbon dioxide and begin the reaction to form KNN. Ball milling and calcination at 900°C were then repeated for homogeneity and complete decomposition. Finally, the powders were ball-milled again for 12 h and pressed into 20 mm pellets at 175 MPa in a uniaxial steel press, followed by sintering in a bed of loose powder on Pt foil, in lidded alumina crucibles for 4 h in the range of 1030°C for KNN, $x = 0.15$ to 1110°C for KNN, $x = 0.75$. The $x = 0.46$ sample was prepared by sol-gel synthesis as described in [8].

NBT- x BT ceramics of composition $x = 0, 0.04, 0.06, 0.07, 0.08, 0.10,$ and 0.12 were synthesized by solid-state reaction. These samples were from the same batch as described in [9]. Starting reagents were $\text{Na}_2\text{CO}_3, \text{Bi}_2\text{O}_3, \text{BaCO}_3,$ and nano- TiO_2 (~ 20 nm). These were ball-milled for 5 h in ethanol, followed by calcination at 800°C for 2 h. The calcined powder was ball-milled again for 2 h and dried, followed by the addition of poly(vinylalcohol) binder. This powder was then pressed into pellets with a diameter of 13 mm in a uniaxial steel press at 200 MPa. Finally, these pellets were sintered at 1150°C for 2 h in a covered alumina crucible.

The purity and apparent metric symmetry of the resultant ceramic samples were investigated by X-ray powder diffraction (Siemens D-5000, Cu radiation and Guinier-Hägg camera, $\text{Cu K}_{\alpha 1}$ radiation), and all samples were found to be pure and free from secondary phases. The Guinier-Hägg patterns collected on the solid-state synthesized KNN samples are shown in Figure 1, below, while the relevant patterns for the KNN 46 sample and the NBT- x BT samples are reported in [8, 9] respectively. Electron diffraction patterns (EDPs) were obtained using Philips EM 430 and Philips CM 30 Transmission Electron Microscopes (TEMs) operating at 300 kV on crushed sample powders dispersed onto holey carbon coated, copper grids.

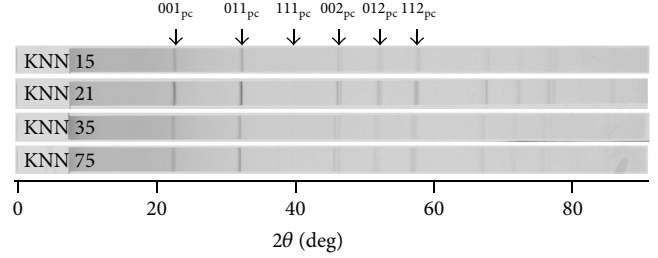


FIGURE 1: Guinier-Hägg X-ray diffraction patterns of solid-state reacted KNN, showing only the expected perovskite-related peaks. The subscript “pc” indicates pseudocubic indexing.

3. Results and Discussion

3.1. KNN Average Structure. In all discussions on EDPs, a subscript p denotes that the indexing is with respect to a parent perovskite subcell. EDPs of KNN as a function of composition are shown in Figures 2(a) and 2(b). We start with the unrotated, high x samples and then consider the octahedrally rotated phases that occur when x is reduced. With $x = 0.75$ (see Figure 2(a)), there are no additional superstructure reflections, and the structure appears to be $Amm2$, as is well known for KNbO_3 . There are, however, faint diffuse features, which will be discussed subsequently. From $x = 0.46$ down to $x = 0.21$, a $G_p \pm 1/2(101)_p$ type spot occurs, with the intensity of this spot increasing with decreasing potassium content. A sharp $G_p \pm 1/2(111)_p$ spot appears in $x = 0.15$ (Figure 2(b)) in addition to $G_p \pm 1/2(101)_p$. A diffuse feature exists at $G_p \pm 1/2(111)_p$ in all patterns from $x = 0.46$ to $x = 0.21$. Weak spots associated with a doubled b axis can be seen in the $x = 0.15$.

3.2. NBT-BT Average Structure. EDPs of NBT-BT as a function of BT dopant are shown in Figures 2(a) and 2(b). We start with the “rhombohedral” NBT end member and examine the superstructure reflections as BT is introduced. Previous refinements suggest that the structure remains rhombohedral with $x < 0.06$, going pseudocubic at $0.06 < 0.07$ and tetragonal for $x > 0.07$. Examination of the diffraction patterns does not reproduce these findings. There is, in fact, a continuous change of intensity between the “rhombohedral” $G_p \pm 1/2(111)_p$ spot and the “tetragonal” $G_p \pm 1/2(101)_p$ spot, both of which exist to some degree, even in pure NBT. Increasing the BT content reduces the intensity of the “rhombohedral” spot and increases the intensity of the “tetragonal” spot, but neither disappears completely. The width of the “tetragonal” peak is also noticeably higher than the parent reflections, even in NBT-12BT.

3.3. Diffuse Scattering. In all KNN EDPs, a single plane of diffuse scattering is observed perpendicular to $[010]$, as expected from being in the singly disordered ferroelectric (orthorhombic) state [11] (chevron-headed arrows with dashed tails in Figures 2(a) and 2(b)). This diffuse scattering indicates ordered ferroelectricity in the 101 plane,

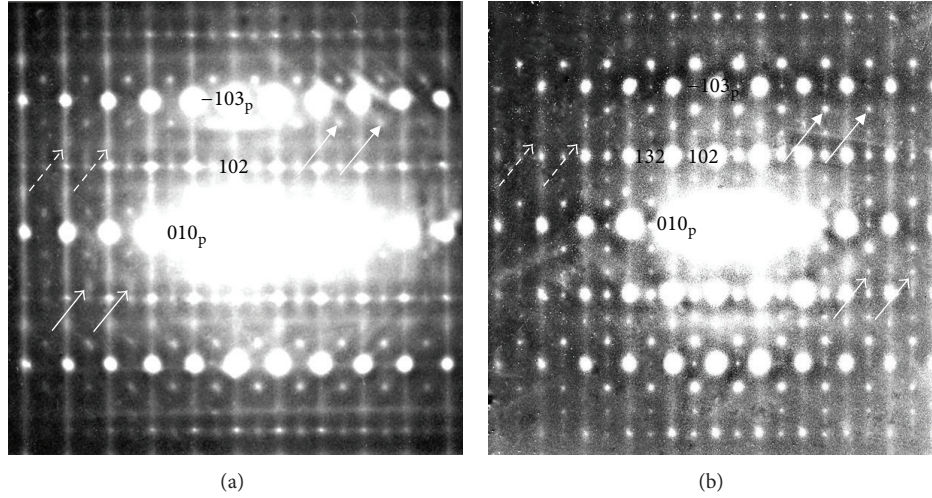


FIGURE 2: Electron diffraction patterns along a $-3, 0, -1_p$ axis in KNN x with (a) $x = 0.75$ and (b) $x = 0.15$.

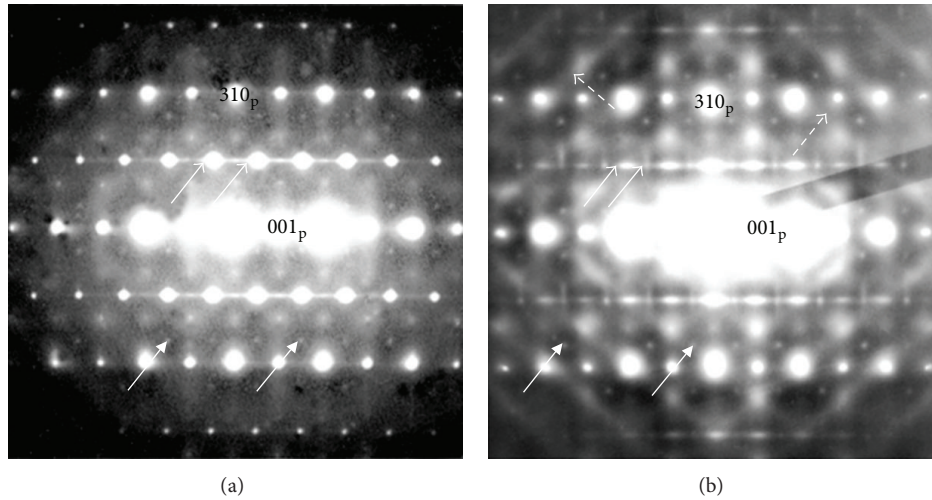


FIGURE 3: Electron diffraction patterns along a 301_p axis in NBT- x BT with (a) $x = 0$ and (b) $x = 0.12$.

with columnar disorder along $[010]$. In NBT, no ferroelectric diffuse is seen, again, as expected from being the fully ordered ferroelectric (rhombohedral) state. However, examination of the diffraction patterns from NBT-12BT (Figure 3(b)) shows planes of diffuse intensity perpendicular to $[111]_p$, indicating ferroelectric disorder along these axes (chevron-headed arrows with dashed tails), generated by the addition of BT. Additionally, $G_p \pm [1/2, 1/2, \xi]_p^*$ -type streaks of diffuse intensity, denoted by chevron-headed arrows with solid tails, are observed from $1/2(111)_p$ to $1/2(110)_p$ and to $1/2(011)_p$ at all compositions in KNN and from $1/2(111)_p$ to $1/2(110)_p$, to $1/2(101)_p$, and to $1/2(011)_p$ in NBT-BT. These one-dimensional rods of diffuse appear both in the plane and as diffuse “spots” (solid-headed arrows with solid tails) which arise from the Ewald sphere cutting through one of the rods of diffuse intensity. In KNN, these can be indexed as $G_p \pm [\xi, 1/2, 1/2]_p^*$ or $G_p \pm [1/2, 1/2, \xi]_p^*$ and in NBT-BT as $G_p \pm [\xi, 1/2, 1/2]_p^*$

or $G_p \pm [1/2, 1/2, \xi]_p^*$ or $G_p \pm [1/2, \xi, 1/2]_p^*$. This effect also gives rise to apparent “spots” of the type $G_p \pm [1/2, 1/2, 0]_p^*$ and $G_p \pm [1/2, 1/2, 1/2]_p^*$, which can be misleading in patterns which show no other evidence that the “reflections” originate from diffuse rods. In NBT-BT, the continuous movement of intensity between the “rhombohedral” $G_p \pm 1/2(111)_p$ spot and the “tetragonal” $G_p \pm 1/2(101)_p$ spot is accompanied by a continuous diffuse streak between these spots for all compositions and the $G_p \pm 1/2(101)_p$ spot remains diffuse and anisotropic, even when relatively strong. Denoyer et al. [12] observed streaking of the type $G_p \pm [\xi, 1/2, 1/2]_p^*$ in NaNbO_3 near a phase transition at 641 K and assigned it to oxygens in the structure. Indeed, the directions and locations of these streaks in both KNN and NBT-BT suggest octahedral tilt twin disorder along their axes, as does the absence of even harmonics of the type $G_p \pm [1, 1, 2\xi]_p^*/G_p \pm [2\xi, 1, 1]_p^*$.

In KNN, the diffuse rods are clearer for lower sodium compositions. This is unsurprising, as KNbO_3 is untilted,

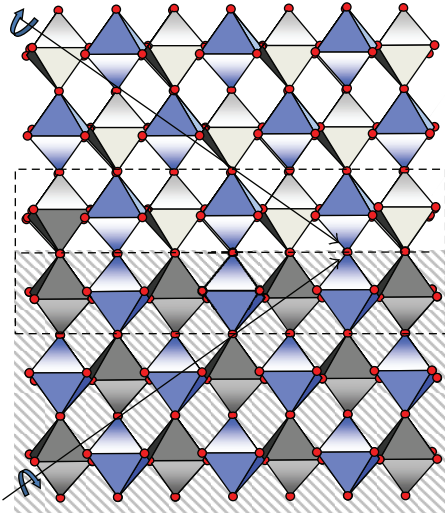


FIGURE 4: Tilt twin region in NBT/NBT-BT showing two rhombohedral twins with different polarization directions meeting in a tetragonal tilt twin region, as shown by the dashed box. Modified version reproduced with permission from [10].

while NaNbO_3 is highly tilted, and is due to the fact that tilts increase A site valence and decrease B site valence, and sodium is much smaller than potassium. Disorder in the tilts gives them zero amplitude in refinements of the average structure. The continuous nature of the changes of tilt in KNN implies that there are no phase boundaries with ferroelectric polarization rotation, which are known to lead to temperature independent phase boundaries with enhanced properties. Similarly in NBT, tilt disorder is likely to stem from the significant ionic site size requirement mismatch between a Bi^{III} and a Na^{I} ion. Performing bond valence sums on the ICSD structure, the valence for Na is found to be 0.12 v.u. high and Bi is found to be 0.60 v.u. low. Ordering of these ions may be expected, but this is likely to be frustrated by kinetic and ferroelectric requirements, and no superstructure is observed. Tilt twin disorder of the kind shown in Figure 4 may be occurring, with the larger twin boundary sites more likely to contain the sodium ion. The final question in NBT-BT is with regard to what occurs when BT is added to NBT, which is effectively the addition of Ba^{II} to the structure, which requires a much larger ionic cavity than Na^{I} or Bi^{III} . This effect is likely to force the Ba ions to occupy twin boundary regions, and it appears that the twin boundary region is able to expand to a multiple unit cell thickness, due to the driving force of accommodating Ba, creating layers of tetragonal BT-like material between twins of rhombohedral NBT-like material.

If the dopant concentration is sufficiently high, then this twin boundary region will become the “bulk” and the rhombohedral “bulk” region will become the twin boundary, giving a continuous intensity shift from rhombohedral-like reflections to tetragonal-like reflections, as is experimentally observed. This has been observed directly in NBT-6BT with 3% KNN [13], with polar nanoregions of $R3c$ and $P4bm$ structure reported. This mixing of structures induces disorder in the ferroelectric direction observed from diffuse scattering

and may lead to the reported antiferroelectric behaviour and giant strain in NBT-BT.

4. Conclusions

In this report we have examined the local structure and disorder in NBT-BT and KNN. This investigation has shown a single, undisturbed ferroelectric plane of diffuse scattering in all compositions of KNN. Additionally, KNN shows disordered octahedral tilting at all compositions due to the mismatch in size between K and Na atoms. This disordered tilting behaviour locks into some order at the composition dependent tilt transitions, but no polarisation rotation occurs.

NBT-BT is shown to also have octahedral tilt disorder at all compositions, but ferroelectric disorder only occurs with BT doping. Continuous transfer of intensity from the “rhombohedral” $G_p \pm 1/2(111)_p$ spot to the “tetragonal” $G_p \pm 1/2(101)_p$ spot with increasing BT content is explained as an expansion of the stacking fault boundary regions in the material due to the ionic size of Ba. This explanation also gives a reason for observed ferroelectric disorder in NBT-12BT and may supply information about the origins of high electrostrictive response and antiferroelectric behaviour in NBT-BT.

References

- [1] Y. Saito, H. Takao, T. Tani et al., “Lead-free piezoceramics,” *Nature*, vol. 432, no. 7013, pp. 84–87, 2004.
- [2] D. Maurya, C. W. Ahn, and S. Priya, “Structural and electrical characterization of lead-free $(1-x)(\text{Na}_{1/2}\text{Bi}_{1/2})\text{TiO}_{3-x}\text{BaTiO}_3$ piezoelectric ceramics,” in *Advances in Electroceramic Materials II: Ceramic Transactions*, pp. 47–54, Wiley, 2010.
- [3] Y. Guo, M. Gu, H. Luo, Y. Liu, and R. L. Withers, “Composition-induced antiferroelectric phase and giant strain in lead-free $(\text{Na}_y\text{Bi}_z)\text{Ti}_{1-x}\text{O}_{3(1-x)-x}\text{BaTiO}_3$ ceramics,” *Physical Review B*, vol. 83, Article ID 054118, 7 pages, 2011.
- [4] D. W. Baker, P. A. Thomas, N. Zhang, and A. M. Glazer, “A comprehensive study of the phase diagram of $\text{K}_x\text{Na}_{1-x}\text{NbO}_3$,” *Applied Physics Letters*, vol. 95, no. 9, Article ID 091903, 3 pages, 2009.
- [5] M. Ahtee and A. W. Hewat, “Structural phase transitions in sodium-potassium niobate solid solutions by neutron powder diffraction,” *Acta Crystallographica A*, vol. 34, pp. 309–317, 1978.
- [6] M. Ahtee and A. M. Glazer, “Lattice parameters and tilted octahedra in sodium-potassium niobate solid solutions,” *Acta Crystallographica A*, vol. 32, pp. 434–446, 1976.
- [7] J. E. Daniels, W. Jo, J. Rodel, and J. L. Jones, “Electric-field-induced phase transformation at a lead-free morphotropic phase boundary: case study in a 93% $(\text{Bi}_{0.5}\text{Na}_{0.5})\text{TiO}_3$ 7% BaTiO_3 piezoelectric ceramic,” *Applied Physics Letters*, vol. 95, Article ID 032904, 3 pages, 2009.
- [8] Z. Yi, Y. Liu, M. A. Carpenter, J. Schiemer, and R. L. Withers, “ $\text{K}_{0.46}\text{Na}_{0.54}\text{NbO}_3$ ferroelectric ceramics: chemical synthesis, electro-mechanical characteristics, local crystal chemistry and elastic anomalies,” *Dalton Transactions*, vol. 40, no. 18, pp. 5066–5072, 2011.
- [9] Y. Guo, Y. Liu, R. L. Withers, F. Brink, and H. Chen, “Large electric field-induced strain and antiferroelectric behavior in

- (1-x)(Na_{0.5}Bi_{0.5})TiO_{3-x}BaTiO₃ ceramics,” *Chemistry of Materials*, vol. 23, no. 2, pp. 219–228, 2011.
- [10] Y. Liu, L. Norén, A. J. Studer et al., “Response of intergrown microstructure to an electric field and its consequences in the lead-free piezoelectric bismuth sodium titanate,” *Journal of Solid State Chemistry*, vol. 187, pp. 309–315, 2012.
- [11] R. Comes, M. Lambert, and A. Guinier, “Désordre linéaire dans les cristaux (cas du silicium, du quartz, et des pérovskites ferroélectriques),” *Acta Crystallographica A*, vol. 26, pp. 244–254, 1970.
- [12] F. Denoyer, R. Comes, and M. Lambert, “X-ray diffuse scattering from NaNbO₃ as a function of temperature,” *Acta Crystallographica A*, vol. 27, pp. 414–420, 1971.
- [13] L. A. Schmitt and H. Kleebe, “Single grains hosting two space groups: a transmission electron microscopy study of a lead-free ferroelectric,” *Functional Materials Letters*, vol. 3, no. 1, pp. 55–58, 2010.

Research Article

The Influence of Surface Morphology of Buffer Layer on the Critical Current Density in YBCO Coated Conductors

Jie Xiong, Yudong Xia, Fei Zhang, Yan Xue, Kai Hu,
Xiaohui Zhao, and Bowan Tao

State Key Laboratory of Electronic Thin Film and Integrated Devices, University of Electronic Science and Technology of China, Chengdu 610054, China

Correspondence should be addressed to Jie Xiong; jiexiong@uestc.edu.cn and Yudong Xia; xiayudong1983@gmail.com

Received 28 October 2013; Accepted 7 November 2013

Academic Editor: Danyang Wang

Copyright © 2013 Jie Xiong et al. This is an open access article distributed under the Creative Commons Attribution License, which permits unrestricted use, distribution, and reproduction in any medium, provided the original work is properly cited.

1 μm -thick $\text{YBa}_2\text{Cu}_3\text{O}_{7-\delta}$ (YBCO) films were grown on the Y_2O_3 /yttria stabilized zirconia (YSZ)/ CeO_2 buffer layers with different surface morphologies using direct-current sputtering. The critical current density (J_c) value of YBCO was 1.1 MA/cm^2 when the root mean square surface roughness (R_{rms}) of the buffer layer was 2.5 nm. As the R_{rms} of the buffer layer increased to 15 nm, the J_c decreased to 0.3 MA/cm^2 . X-ray diffraction and scanning electron microscopy showed the strong relevance of the evolution of the structure and surface morphologies of YBCO films with the buffer layer of different R_{rms} . A model was proposed to explain the influence of surface morphology on the superconducting properties of YBCO films.

1. Introduction

Recently, there are more efforts focusing on the fabrication of high performance $\text{YBa}_2\text{Cu}_3\text{O}_{7-\delta}$ (YBCO) coated conductors on flexible metallic substrates [1, 2]. The application of 2nd generation coated conductors requires higher current carrying capacity. To reach this goal, a high critical current density (J_c) must be maintained in thick ($>1 \mu\text{m}$) YBCO coatings [3]. Unfortunately, YBCO films deposited on polycrystalline metal substrates showed high angle grain boundaries, leading that the YBCO had a very small critical current [4]. As a result, several methods had been investigated to prepare biaxially aligned templates, such as ion-beam-assisted deposition (IBAD) and rolling assisted biaxially textured substrates (RABiTS) [5, 6]. The RABiTS approach has been proven to be a simple and cost effective manufacturing technology for mass production of coated conductors.

In order to block the interdiffusion of the metal and oxygen, and minimize the lattice mismatch of YBCO and flexible metallic substrates, one or several layer thin films are deposited on the metallic substrates to serve as the buffer layer for the subsequent YBCO films. Typical tri-layer stack of CeO_2 /yttrium stabilized zirconia (YSZ)/ Y_2O_3 is one of the

mostly explored architectures [7]. In this architecture, the Y_2O_3 acts to transfer the biaxial texture from the RABiTS substrate to the YBCO layer; the YSZ layer is used as a barrier to prevent the interdiffusion between oxides and metal substrate; the CeO_2 cap layer on YSZ layer provides good lattice matching and an epitaxial growth template for depositing the YBCO layer. Therefore, buffer layers play a critical role in fabricating high performance coated conductors. So far, enormous efforts had been made toward the manufacture of the biaxial texture of buffer layers on the RABiTS tapes; however, the cap layer had not been paid enough attention [8–10]. In our previous work, we had reported the surface morphology evolution of the CeO_2 films deposited on the YSZ/ Y_2O_3 /Ni-alloy substrates [11, 12]. In this study, we investigated in detail the impact of the surface morphologies of buffer layers on the superconducting properties in YBCO films.

2. Experimental Details

Biaxially textured {100} <100> Ni-5at.%W alloy (NiW) tapes were used in this study, which were supplied from EVICO GmbH, Germany. The full width at half maximum (FWHM)

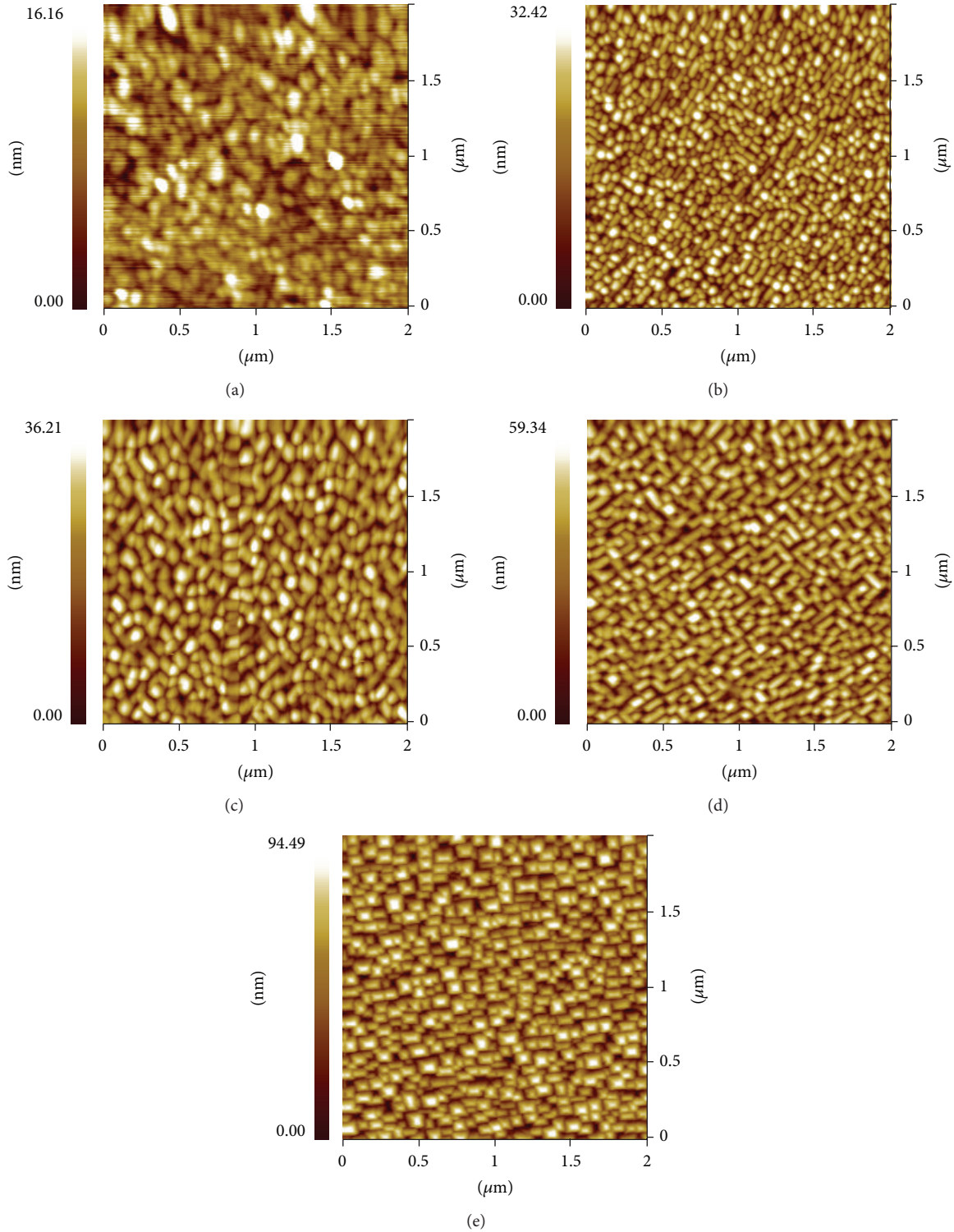


FIGURE 1: AFM images of different CeO_2 cap layers.

values of out-of-plane and in-plane were about 5.5° and 6° , respectively. The $\text{Y}_2\text{O}_3/\text{YSZ}/\text{CeO}_2$ multilayers with different surface morphologies were deposited on NiW tapes using reel-to-reel direct-current (DC) reactive magnetron sputtering by modulating the substrate temperature from 500°C to

680°C as reported in [12]. The thickness of all CeO_2 cap layers was 40 nm. The subsequent YBCO films were prepared by DC sputtering with the same conditions, which were initially optimized. Detailed conditions were reported elsewhere [3].

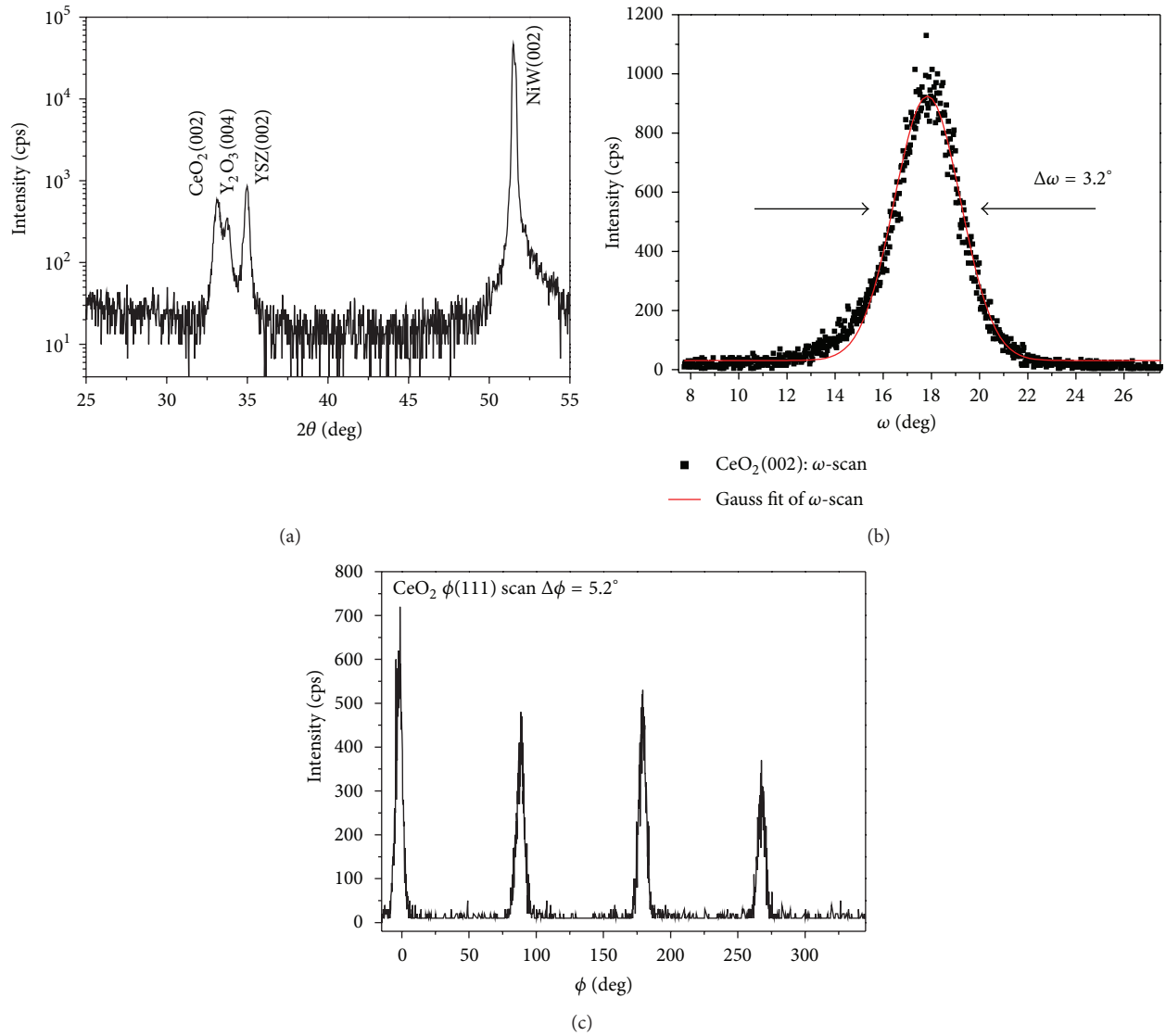


FIGURE 2: Typical XRD patterns of $\text{CeO}_2/\text{YSZ}/\text{Y}_2\text{O}_3$ buffer layer (a) θ - 2θ scan, (b) ω -scan of (002) CeO_2 , and (c) ϕ -scan of (111) CeO_2 .

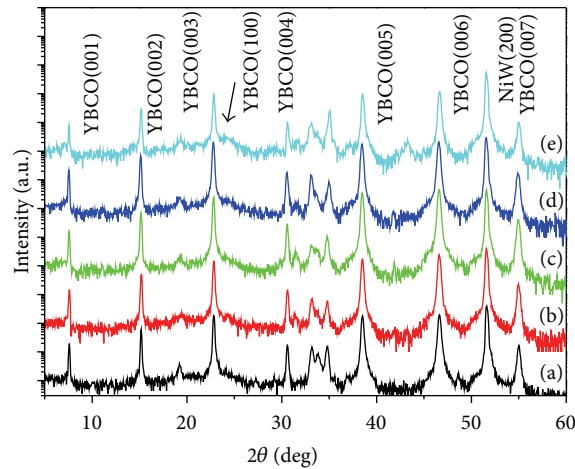


FIGURE 3: XRD θ - 2θ patterns of YBCO films deposited on the buffers of samples from (a) to (e).

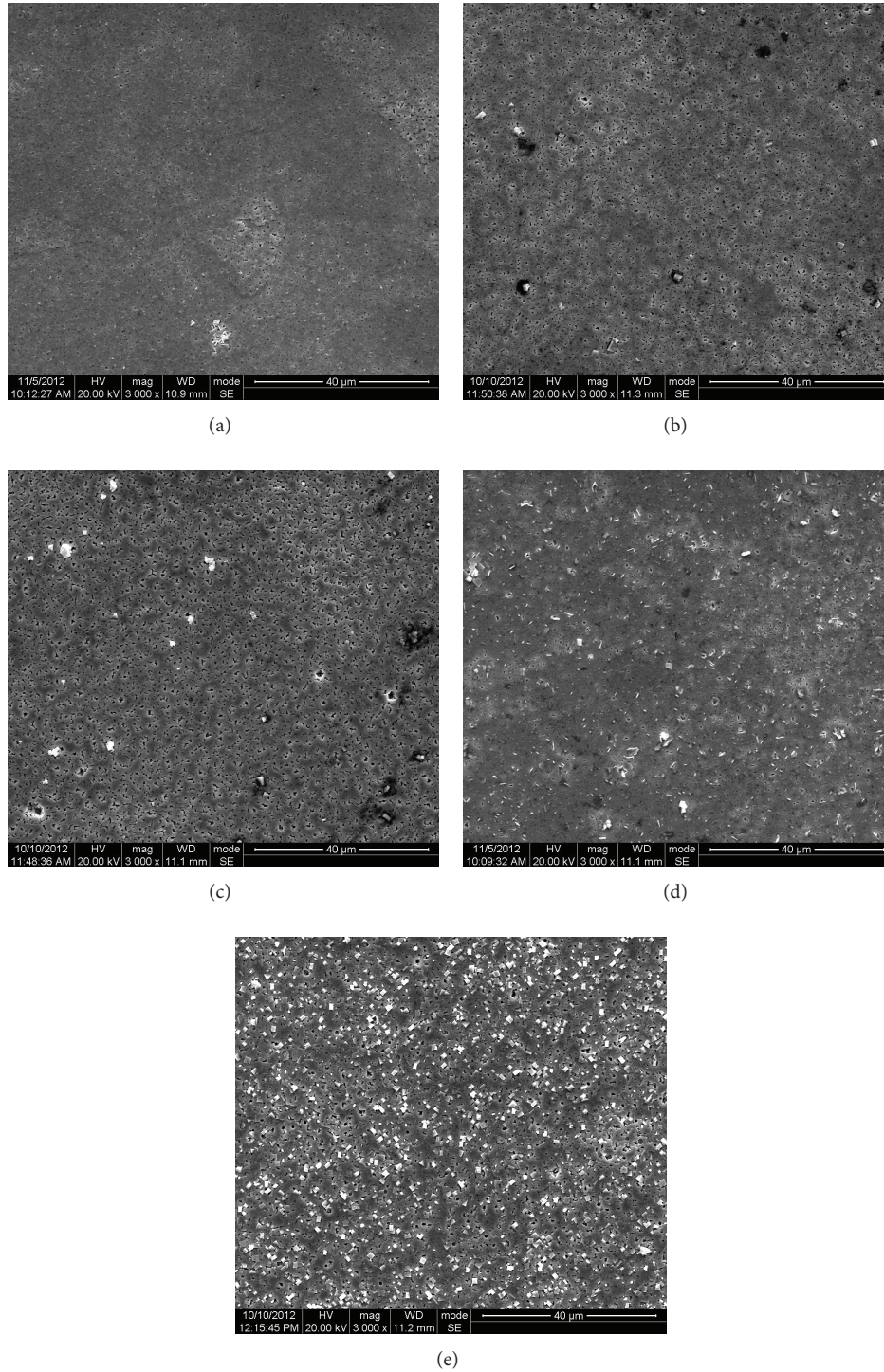


FIGURE 4: SEM images of YBCO films deposited on different surface morphologies of buffer layers.

The film structure was measured with Bede X-ray diffraction (XRD) system including θ - 2θ , ω , and ϕ -scan. Atomic force microscopy (AFM, SEIKO SPA300HA microscopy) and scanning electron microscopy (SEM, JSM-5900) were used to characterize the surface morphology and calculate the root mean square surface roughness (R_{rms}). J_c -Scan

system developed by Germany Leipzig University was used to measure the J_c values.

3. Results and Discussion

Figure 1 shows the surface morphologies of the different CeO_2 layers for this series experiments. The R_{rms} values of the

TABLE 1: The R_{rms} of the buffer layers and the values of out-of-plane and in-plane textures of the corresponding YBCO films.

Sample	a	b	c	d	e
R_{rms} of CeO_2	2.5 nm	4.6 nm	5.8 nm	9.5 nm	15.2 nm
$\Delta\omega$ of (002) YBCO	2.37°	2.98°	2.92°	2.97°	3.2°
$\Delta\phi$ of (103) YBCO	4.91°	4.77°	5.07°	4.72°	5.48°

CeO_2 films from (a) to (e) are shown in Table 1. The XRD θ - 2θ scan, ω -scan of CeO_2 (200) peak, and ϕ -scan of CeO_2 (111) plane are shown in Figures 2(a), 2(b), and 2(c), respectively; all the $\text{Y}_2\text{O}_3/\text{YSZ}/\text{CeO}_2$ films are completely c -axis oriented with representative in-plane FWHM value of 5.2° and out-of-plane FWHM value of 3.2° .

The XRD patterns of YBCO films deposited on the buffer samples from (a) to (e) are shown in Figure 3. The deposition time was 20 hours and the typical thickness of YBCO film was $1\ \mu\text{m}$. The 2θ peaks at 33.02° , 33.8° , and 34.9° were indexed as the (00 l) reflections of CeO_2 , Y_2O_3 , and YSZ, respectively. Weak NiO and NiWO_4 reflections were observed at the 2θ angles of 19.28° , 37.26° , and 43.29° . All of the patterns indicated pure c -axis orientation except for the sample (e), which had a small amount of a -axis grains. The out-of-plane and in-plane textures of YBCO films deposited on samples from (a) to (e) are documented in Table 1. With the exception of the YBCO deposited on sample (e), all the out-of-plane FWHM values of YBCO films were smaller than 3° , demonstrating good out-of-plane alignments. The FWHM values of sample (e) were slightly bigger than others, ascribed to the a -axis grains, and led to the formation of high angle grain boundaries in the YBCO film. The in-plane FWHM values of YBCO films were between 4.7° and 5.5° , indicating no obvious tendency on the in-plane texture when the YBCO films deposited on different buffer layers.

The SEM images of YBCO films deposited on different surface morphologies of CeO_2 cap layers are shown in Figure 4, which corresponded with (a) to (e) of Figure 1, respectively. Figure 4(a) showed the relative flattest surface morphology with typical small holes attributed to the rich yttrium in YBCO films [13]. As the R_{rms} of the buffer layers increased, the holes on the surface of the YBCO films became bigger, as observed in Figures 4(b) and 4(c). As the R_{rms} of the buffer layers increased more than 10 nm, the needle-like a -axis particles of YBCO films were distributed on the surface of YBCO film shown in Figures 4(d) and 4(e).

The relationship between the J_c of corresponding YBCO films is sketched in Figure 5. The J_c of YBCO deposited on the buffer of sample (a) was $1.1\ \text{MA}/\text{cm}^2$. The YBCO deposited on samples (b)–(d) showed J_c values of $0.9\ \text{MA}/\text{cm}^2$, $0.8\ \text{MA}/\text{cm}^2$, and $0.5\ \text{MA}/\text{cm}^2$, respectively. As the R_{rms} of the buffer layers increased to 15 nm, the J_c value of YBCO films continuously decreased to $0.3\ \text{MA}/\text{cm}^2$, revealing the strong relevance between the superconducting properties and the surface morphology.

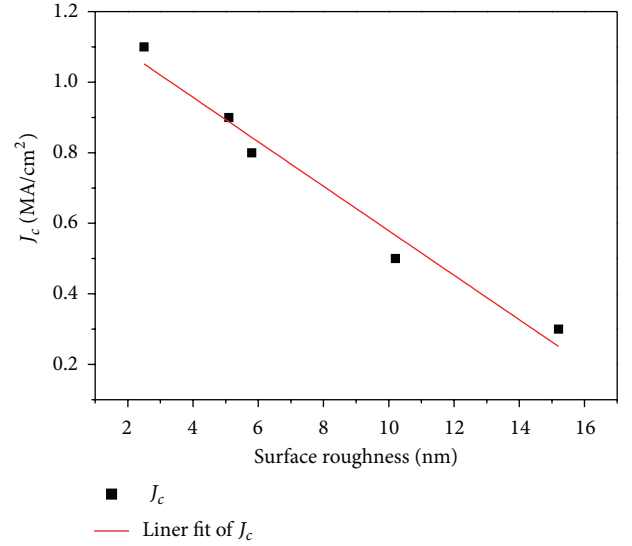


FIGURE 5: The relationship between the J_c of YBCO films and surface morphologies of CeO_2 layers.

In order to study the mechanism of the effect of the buffers' surface on the performance of YBCO films, the corresponding line profiles of CeO_2 films of samples (a) and (e) were plotted in Figures 6(a) and 6(b), respectively. As shown in Figure 6, the grain height was in the range of $\sim 50\ \text{nm}$ – $50\ \text{nm}$, and the gap between in grain boundaries of sample (a) was much smaller than that of sample (e). In the sputter process, the sputter atoms diffused and nucleated on the substrate surface. However, YBCO is a multielement oxide with different atom radii of Y, Ba, and Cu. For different surface morphologies of CeO_2 films such as sample (e), the gap between grain boundaries was deeper and the grain boundaries area was larger than that of sample (a). If metal atoms diffused from one grain of CeO_2 surface to another, it should overcome the superior potential barrier, while the potential barrier of a Ba atom is bigger than that of Cu and Y atoms. Therefore, if the grain boundary area was large, Ba atoms would be enriched on the grain boundaries, which led to the deviation of YBCO chemical contents, and as observed white particles formed on the surface in Figure 4(e), which was identified as the CuO nonconductive particles. Further demonstrations are necessary for a better understanding by transmission electron microscopy which is ongoing.

4. Conclusions

The influence of surface morphologies of CeO_2 cap layers on the microstructure and critical current density of YBCO films was systematically investigated. YBCO films on the flat surface revealed high quality epitaxial c -axis oriented growth and had much better superconducting properties. As the R_{rms} of the buffer layer increased, the nonconductive particles and a -axis grains on the surface of YBCO were observed, leading to deteriorating the J_c of YBCO films. A model was proposed to understand the phenomena, demonstrating

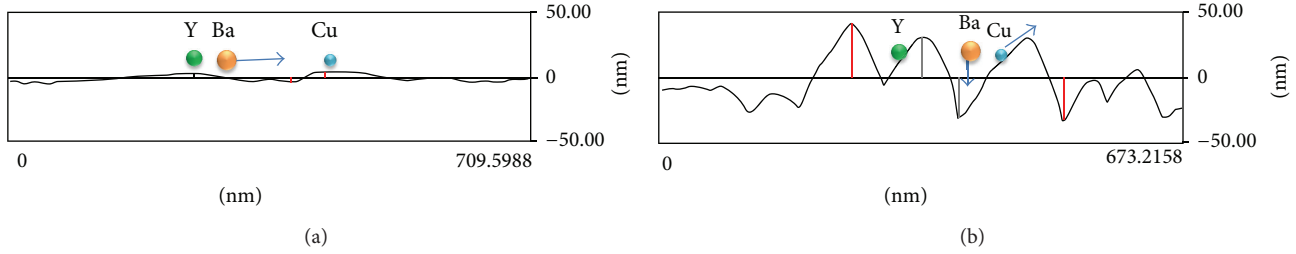


FIGURE 6: The corresponding line profiles of CeO_2 films (a) of sample (a) and (b) of sample (e).

that the surface morphology of buffer layers had a strong effect on the current carrying capacity of YBCO coated conductors.

Acknowledgments

The authors gratefully acknowledge the support of the National Natural Science Foundation of China under Grant no. 51002024, Sichuan Youth Science and Technology Innovation Research Team Funding (no. 2011JTD0006), and Fundamental Research Funds for the Central Universities (no. ZYGX2012J039 and ZYGX2011Z002) for this work.

References

- [1] D. P. Norton, A. Goyal, J. D. Budai et al., "Epitaxial $\text{YBa}_2\text{Cu}_3\text{O}_7$ on biaxially textured nickel (001): an approach to superconducting tapes with high critical current density," *Science*, vol. 274, no. 5288, pp. 755–757, 1996.
- [2] D. P. Norton, A. Goyal, J. D. Budai et al., "High critical current density superconducting tapes by epitaxial deposition of $\text{YBa}_2\text{Cu}_3\text{O}_x$ thick films on biaxially textured metals," *Applied Physics Letters*, vol. 69, no. 12, article 1795, 1996.
- [3] J. Xiong, B. W. Tao, W. F. Qin et al., "Reel-to-reel continuous simultaneous double-sided deposition of highly textured CeO_2 templates for $\text{YBa}_2\text{Cu}_3\text{O}_{7-8}$ coated conductors," *Superconductor Science and Technology*, vol. 21, no. 2, Article ID 025016, 2008.
- [4] D. Dimos, P. Chaudhari, and J. Mannhart, "Superconducting transport properties of grain boundaries in $\text{YBa}_2\text{Cu}_3\text{O}_7$ bicrystals," *Physical Review B*, vol. 41, no. 7, pp. 4038–4049, 1990.
- [5] Y. Iijima, N. Tanabe, O. Kohno et al., "In-plane aligned $\text{YBa}_2\text{Cu}_3\text{O}_{7-x}$ thin films deposited on polycrystalline metallic substrates," *Applied Physics Letters*, vol. 60, no. 6, article 769, 1992.
- [6] E. D. Specht, A. Goyal, D. F. Lee et al., "Cube-textured nickel substrates for high-temperature superconductors," *Superconductor Science and Technology*, vol. 11, no. 10, article 945, 1998.
- [7] X. Li, M. W. Rupich, T. Kodenkandath et al., "High critical current YBCO films prepared by an MOD process on RABiTS templates," *IEEE Transactions on Applied Superconductivity*, vol. 17, no. 2, pp. 3553–3556, 2007.
- [8] T. Aytug, M. Paranthaman, H. Y. Zhai et al., "Single buffer layers of LaMnO_3 or $\text{La}_{0.7}\text{Sr}_{0.3}\text{MnO}_3$ for the development of $\text{YBa}_2\text{Cu}_3\text{O}_{7-8}$ -coated conductors: a comparative study," *Journal of Materials Research*, vol. 17, no. 9, pp. 2193–2396, 2002.
- [9] J. Xiong, Y. Chen, Y. Qiu et al., "A novel process for CeO_2 single buffer layer on biaxially textured metal substrates in YBCO coated conductors," *Superconductor Science and Technology*, vol. 19, no. 10, article 1068, 2006.
- [10] D. Q. Shi, R. K. Ko, K. J. Song et al., "Deposition of Y_2O_3 film on textured metal substrates for a single buffer layer of a YBCO coated conductor," *Superconductor Science and Technology*, vol. 18, no. 4, article 561, 2005.
- [11] Y. D. Xia, J. Xiong, F. Zhang et al., "Reel-to-reel deposition of epitaxial double-sided Y_2O_3 buffer layers for coated conductors," *Physica C*, vol. 476, pp. 48–53, 2012.
- [12] Y. D. Xia, J. Xiong, and F. Zhang, "Morphology evolution of CeO_2 cap layer for coated conductors," *Applied Surface Science*, vol. 263, pp. 508–512, 2012.
- [13] J. Xiong, W. F. Qin, J. L. Tang, B. Tao, X. Cui, and Y. Li, "Preparation and characterization of microcrack-free thick $\text{YBa}_2\text{Cu}_3\text{O}_{7-8}$ films," *Rare Metals*, vol. 26, no. 5, pp. 403–407, 2007.

Research Article

Decomposition and Oriented Growth of $\text{YBa}_2\text{Cu}_3\text{O}_{7-x}$ Films Prepared with Low Fluorine TFA-MOD Approach

Xiaohui Zhao, Pan Zhang, Yabing Wang, Jie Xiong, and Bowan Tao

State Key Laboratory of Electronic Thin Film and Integrated Devices, University of Electronic Science and Technology of China, Chengdu 610054, China

Correspondence should be addressed to Xiaohui Zhao; xzhao@uestc.edu.cn

Received 26 September 2013; Accepted 28 October 2013

Academic Editor: Jianhua Hao

Copyright © 2013 Xiaohui Zhao et al. This is an open access article distributed under the Creative Commons Attribution License, which permits unrestricted use, distribution, and reproduction in any medium, provided the original work is properly cited.

TFA-MOD approach of $\text{YBa}_2\text{Cu}_3\text{O}_{7-x}$ (YBCO) films has been approved to be the most promising method for mass production of low cost high temperature coated conductors. In order to reduce the decomposition time and improve the properties of YBCO films, copper propionate was used as the precursor and certain Lewis-bases were introduced into the precursor solution. The fluorine content of the solution was significantly reduced. High quality oriented YBCO films were prepared on LAO substrates with this low fluorine TFA-MOD approach. The effects of the sintering temperature on the oriented growth and properties of YBCO films were investigated. The preliminary results yielded the critical current density (J_c) of 2 MA/cm^2 and critical current (I_c) of 120 A/cm width at 77 K and self-field.

1. Introduction

Second generation $\text{YBa}_2\text{Cu}_3\text{O}_{7-x}$ (YBCO) high temperature superconducting materials have been considered as the most promising candidate for electric power applications due to their large critical current density (J_c) at liquid nitrogen temperature (77.3 K) and high irreversibility field. Among all kinds of fabrication methods, the metal organic deposition (MOD) [1, 2] could provide precise composition control and large area deposition accessibility with low cost, which makes it appealing for large scale production. The conventional MOD route used trifluoroacetate salts as the precursors. However, due to high fluorine content in the precursor, large amount of HF gas is generated during the decomposition. In order to avoid crack of the film, the heating rate during decomposition is generally kept below $1^\circ\text{C}/\text{min}$. This results in long term decomposition process over 20 hours. Seeking for reducing the decomposition time without degradation of the film quality, a different precursor has been introduced to substitute trifluoroacetate salts or modify the chemistry of the precursor solution [3–10]. Fuji et al. [3] and Tokunaga et al. [4] chose copper naphthenate as the copper precursor, the decomposition time was reduced, and high performance

YBCO film with I_c over 200 A/cm width was achieved. However, as a complex mixture distilled from petroleum, copper naphthenate comprises of certain petroleum by-products and contaminants. So the composition of copper naphthenate is not stable and the copper content varies, which makes the precise control of the film composition and fabrication of long tape with uniform performance almost impossible.

In this report, copper propionate was used to substitute copper trifluoroacetate, and with this substitution the fluorine content of the precursor was reduced around 50%. The decomposition process of the precursor film was adjusted accordingly. The effects of the sintering temperature on the microstructure and oriented growth of the YBCO film were discussed in detail.

2. Experimental

Y, Ba, and Cu acetate salts are used as the starting materials for the precursor solution preparation. Yttrium acetate and barium acetate were dissolved in water with Y/Ba ratio of 1:2 and reacted with excessive trifluoroacetate acid at 80°C for 6 hours. The resulting solution was refined under reduced

pressure to remove water and excessive acid. Meanwhile, Cu acetate was dissolved in methanol and reacted with excess propionate acid at 80°C for 2 hours. And appropriate amount of diethanolamine (DEA) and ammonia was added dropwise into the solution. Two solutions prepared above were mixed together with Y:Ba:Cu ratio of 1:2:3 at room temperature and concentrated under vacuum, resulting in a viscous and deep blue precursor solution. Only removal of volatile solvents was conducted during the whole process; therefore the content of metal ions in final precursor solution is consistent with the starting materials, which offers the feasibility of precise composition control. Methanol was used as the solvent and the total metal ion concentration of the solution was adjusted to 2 mol/L.

The precursor solution was spin-coated onto the (001) oriented LaAlO₃ single crystal substrate with spinning rate of 3000 rpm for 60 seconds. The precursor film was baked at hot plate for 60 seconds afterwards and decomposed in the tube furnace with 1.3% humidified oxygen. The heating profile was shown in Figure 2. The whole decomposition process takes less than 2 hours; comparing with more than 20 hours for conventional TFA-MOD, this is a significant improvement in efficiency and potentially reducing manufacturing cost. Homogeneous and crack-free film consisting intermediate phase, for example, Y₂O₃, BaF₂, and CuO, was achieved [11, 12]. And then the decomposed film was crystallized at 790–830°C for 1 hour under humid oxygen and argon balanced atmosphere. Afterwards the films were annealed at 500°C with dry oxygen to form superconducting phase.

Differential thermal analysis (DTA) and thermal gravimetric analysis (TGA) of precursor solution were performed in air with a 2°C/min heating rate. The phase purity and microstructure of YBCO film were characterized with X-ray diffraction θ -2 θ scans (HRXRD, Bede D1). The in-plane texture of YBCO film was quantified by measuring full width half maxima (FWHM) of YBCO (103) Φ -scans. The rocking curve of the YBCO (005) peaks was measured to characterize the out-of-plane texture (*c*-axis alignment) of the film. The oriented growth mode of the film was revealed by XRD Chi-scan of YBCO (102) peaks. Surface morphology of films was examined by scanning electron microscopy (SEM). Film thickness was measured by DEKTA surface profiler. Critical current density (J_c) of the film was determined by the J_c -scan Leipzig system. I_c was calculated from the J_c results and the thickness measured from the surface profiler.

3. Results and Discussion

In our precursor solution, copper propionate was used to substitute copper trifluoroacetate and the fluorine content of the precursor was reduced around 50%. So less HF gas will be generated with current approach.

3.1. Decomposition of the Precursor. In order to better understand the decomposition behavior of the precursor and redesign the heating profile of the decomposition process, DTA and TGA analyses were performed for gels dried from the precursor solution. As shown in Figure 1, there are two exothermic peaks in DTA curve located at 206°C and 240°C,

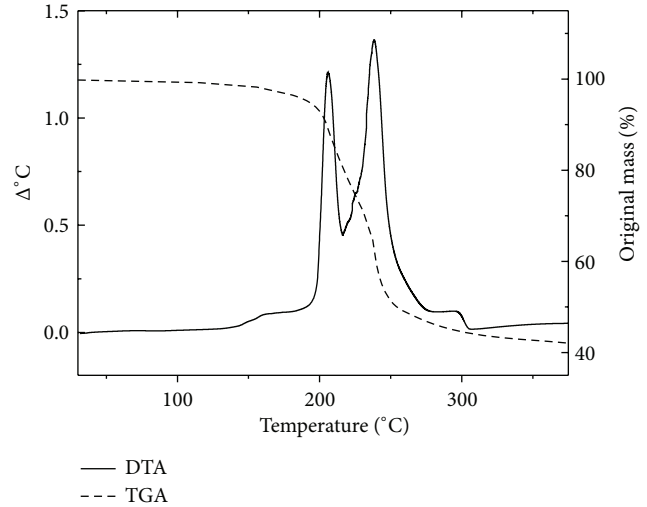
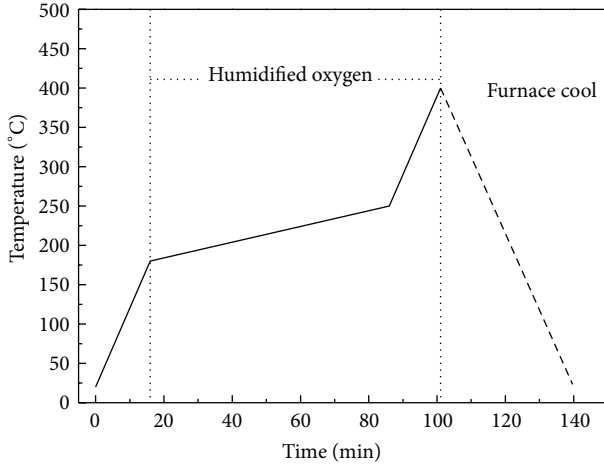


FIGURE 1: DTA and TGA curves for low fluorine TFA-MOD precursor gel decomposed in air.

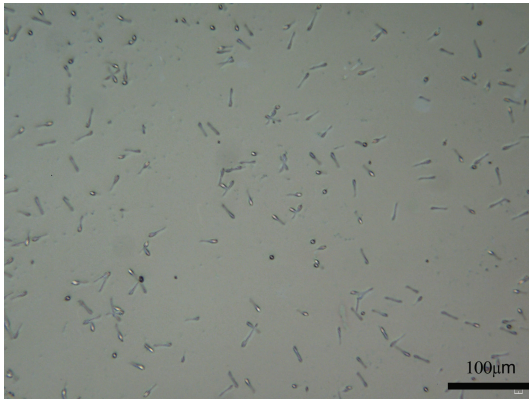
respectively. Compared with the traditional TFA-MOD precursor, which has only one intense exothermic peak at 260°C [13], the decomposition behavior becomes moderate. The first peak corresponds to Cu propionate decomposition, and the second exothermic peak at 240°C, which is believed to be resulting from the decomposition of Y- and Ba-trifluoroacetate. Surprisingly, both of these exothermic peaks shift to lower temperature in comparison with the expected value [13]. Significant weight loss between two exothermic peaks was observed and no substantial weight loss at higher temperatures, indicating that the decomposition of all the organic species was completed by 240°C. This phenomenon suggests that the introduction of DEA and Lewis-basic ammonia has dramatically affected the chemistry of the precursor solution.

Right after the volatile solvent evaporation at the beginning of the decomposition, the metal ions in the precursor film tend to cross-link with each other and aggregate to form clusters, especially for Cu, which have bigger ionic size. It is believed that the presence of Lewis-base can coordinate with metal ions, thereby reducing cross-linking of them during intermediate formation. Both DEA and ammonia has the Lewis-basic nature; after coordinating with metal ions, the cross-linking and aggregation of metal ions are significantly reduced. This is the key factor to account for that the decomposition becomes moderate and shifts to lower temperatures. In addition, less aggregation also reduces the segregation of the intermediate phase, and this ensures the chemical homogeneity and integrity of the film. On the other hand, the molecular weight of compound is increased by this coordination; as a consequence, the sublimation of Cu is suppressed, leading to reproducible stoichiometry of Y:Ba:Cu = 1:2:3.

The introduction of highly viscous DEA induced the viscosity increase of the precursor solution; however, the high boiling point of DEA (268°C) also makes it persistent in the film up to high temperature, leading to thermal



(a)



(b)

FIGURE 2: Heating profile of decomposition (a) and morphology (obtained with optical microscope) (b) of the precursor film.

stress relaxation of the precursor film. This explains that the smooth and crack free film still can be achieved even with faster heating rate. Both of these effects enable the rapid decomposition of precursor films with increased thickness.

Based on TGA and DTA results, the heating profile of decomposition was modified accordingly. The ramp rate of $1^{\circ}\text{C}/\text{min}$ was applied for the temperature range 200°C – 250°C in which major decomposition happened and fast ramp rate of $10^{\circ}\text{C}/\text{min}$ was used beyond this range. As shown in Figure 2(a), the modified decomposition process could be complete in two hours, which is much less than that of the conventional TFA-MOD method. And the decomposed film is smooth and crack free with only uniform submicron pores resulting from the generation of HF gas, as shown in Figure 2(b). The thickness of the final YBCO film was determined to be 600 nm, which was almost doubled in comparison with that of traditional TFA-MOD method.

3.2. Heating Rate Effect during Sintering. The resulting decomposed film was further heated to higher temperature to form YBCO superconducting phase. The temperature window for superconducting phase is relatively small and

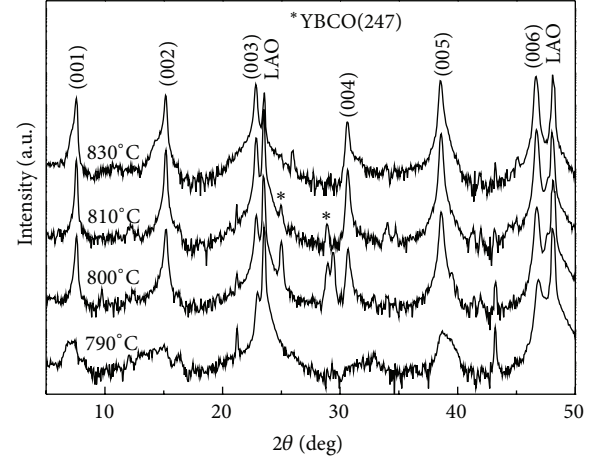


FIGURE 3: XRD θ - 2θ patterns of YBCO films with different sintering temperature. YBCO247 phase is marked with “**”.

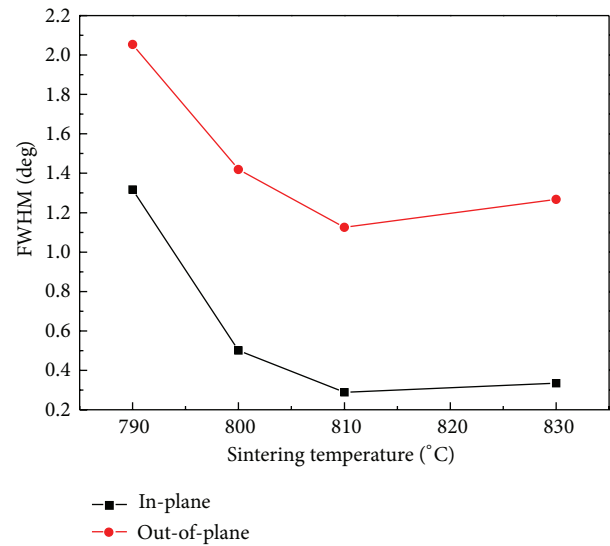


FIGURE 4: Temperature dependence of FWHM of in-plane and out-of-plane scan of YBCO films.

the sintering temperature is critical for the oriented growth of YBCO films. Different sintering temperatures ranging from 790 to 830°C were attempted while keeping other working conditions constant. XRD θ - 2θ scan of all the films was shown in Figure 3. The ordinate was put in log scale for details. All of the samples showed well-developed (001) growth with only slight amount of $\text{Y}_2\text{Ba}_4\text{Cu}_7\text{O}_{15-x}$ phase at certain temperature. The temperature dependence of FWHM of rocking curve and out-of-plane scan was shown in Figure 4. Both of them reduced substantially with increasing temperature. At 810°C , the FWHM values of in-plane and out-of-plane scan were 1.12° and 0.29° , indicating high quality oriented growth of YBCO films.

In order to further disclose the temperature effect on the oriented growth of YBCO films, XRD Chi-scan of YBCO (102) was also performed. As shown in Figure 5, the peak

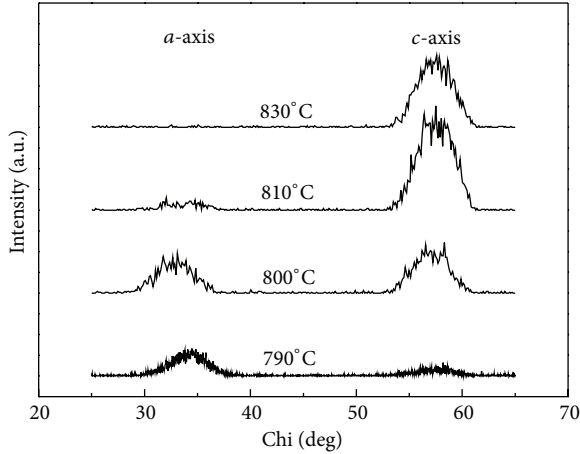


FIGURE 5: XRD Chi-scan of YBCO films with different sintering temperatures.

at 35° represents *a*-axis growth of YBCO. The intensity of the peak is dominant at 790°C , whereas the peak at 57° that indicating *c*-axis growth is weak at low temperature. However, the peak intensity at 57° was significantly enhanced with increasing temperature while the peak at 35° was gradually diminished. This peak intensity variation indicates that with increasing sintering temperature, the oriented growth mode changed from *a*-axis growth to *c*-axis growth. And pure *c*-axis growth was achieved at 830°C . This result is coincident with previous studies and the similar growth thermodynamic properties have also been observed in perovskite oxides such as SrTiO_3 and BaTiO_3 [14–16]. It is widely accepted that the oriented growth of YBCO starts from the interface between intermediate phase and LAO substrate [17]. The lattice mismatch of *a*-axis and *c*-axis growth with LAO substrate is 0.8% and 1.9%, respectively. And thereby *c*-axis growth of YBCO requires larger thermodynamic driving force than *a*-axis growth, leading to preferred *a*-axis growth at relatively low temperatures.

3.3. Properties of YBCO Films. YBCO films were sintered at different temperatures for 1 hour alongside with other tailored working conditions. Figure 6 shows the morphology of YBCO film sintered at 810°C . Despite the existence of few needle-like *a*-axis grains, most part of the film shows well-connected, pallet-like *c*-axis grains. This SEM observation is consistent with the XRD results above. The superconductivity of all the films was measured and the variation of critical current density (J_c) as a function of sintering temperature was shown in Figure 7. It is evident that J_c of YBCO films increased with sintering temperature, which can be ascribed to the increase of the *c*-axis growth. High J_c of 2 MA/cm^2 and I_c of 120 A/cm width at 77 K and self-field were obtained for YBCO film sintered at 810°C . However, only 1 MA/cm^2 was achieved at 830°C , which shows pure *c*-axis growth. This property degradation may be caused by other deteriorated features (such as interconnection) of YBCO grains after high temperature sintering. The relevant study is in progress.

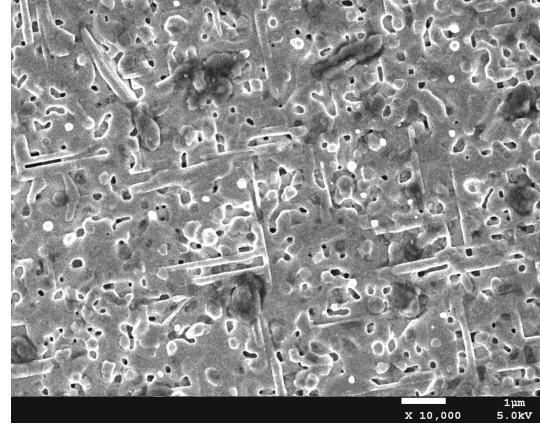


FIGURE 6: SEM (secondary electron) micrographs of the typical morphology of YBCO films sintered at 810°C .

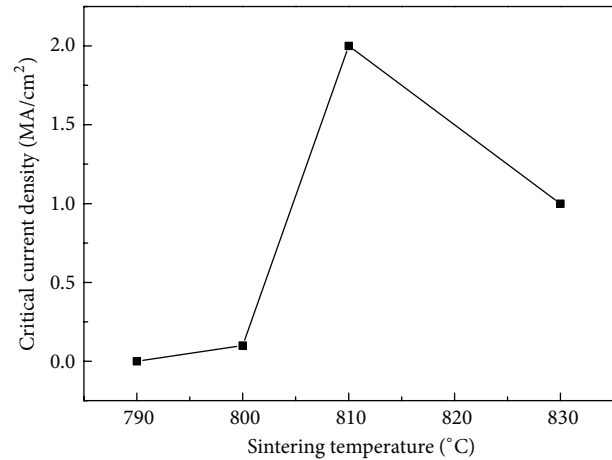


FIGURE 7: Critical current density (J_c) of YBCO films as a function of sintering temperature.

4. Conclusion

High quality single-coating YBCO films with 600 nm in thickness was prepared with low fluorine TFA-MOD approach. The decomposition process was shortened in 2 hours by Cu-propionate substitution and the introduction of Lewis-basic DEA and ammonia. Since the thermodynamic driving force for *c*-axis growth of YBCO is larger than that of *a*-axis growth, YBCO films undergo *a*-axis growth at low sintering temperature, whereas pure *c*-axis oriented growth is achieved at 830°C . High quality YBCO film with J_c of 2 MA/cm^2 and I_c of 120 A/cm width at 77 K and self-field was obtained.

Acknowledgments

This work was financially supported by National Natural Science Foundation of China (51002024), the Scientific Research Foundation of the State Human Resource Ministry, the Education Ministry for Returned Chinese Scholars, and the Fundamental Research Funds for the Central Universities. This work was also supported by a Grant to Dr. Wen Huang

from the National Natural Science Foundation of China (51002022).

References

- [1] A. Gupta, R. Jagannathan, E. I. Cooper, E. A. Giess, J. I. Landman, and B. W. Hussey, "Superconducting oxide films with high transition temperature prepared from metal trifluoroacetate precursors," *Applied Physics Letters*, vol. 52, no. 24, pp. 2077–2079, 1988.
- [2] P. C. McIntyre, M. J. Cima, J. J. A. Smith, R. B. Hallock, M. P. Siegal, and J. M. Phillips, "Effect of growth conditions on the properties and morphology of chemically derived epitaxial thin films of $\text{Ba}_2\text{Cu}_3\text{O}_{7-x}$ on (001) LaAlO_3 ," *Journal of Applied Physics*, vol. 71, no. 4, pp. 1868–1877, 1992.
- [3] H. Fuji, T. Honjo, R. Teranishi et al., "Processing for long YBCO coated conductors by advanced TFA-MOD process," *Physica C*, vol. 412–414, pp. 916–919, 2004.
- [4] Y. Tokunaga, H. Fuji, R. Teranishi et al., "High critical current YBCO films using advanced TFA-MOD process," *Physica C*, vol. 412–414, pp. 910–915, 2004.
- [5] Y. Xu, A. Goyal, K. Leonard, and P. Martin, "High performance YBCO films by the hybrid of non-fluorine yttrium and copper salts with Ba-TFA," *Physica C*, vol. 421, no. 1–4, pp. 67–72, 2005.
- [6] Y. R. Patta, D. E. Wesolowski, and M. J. Cima, "Aqueous polymer-nitrate solution deposition of YBCO films," *Physica C*, vol. 469, no. 4, pp. 129–134, 2009.
- [7] D. Shi, L. Wang, J. Kim et al., "YBCO film with Sm addition using low-fluorine TFA-MOD approach," *IEEE Transactions on Applied Superconductivity*, vol. 19, no. 3, pp. 3208–3211, 2009.
- [8] X. H. Zhao, C. Gao, Y. D. Xia et al., "Preparation of YBCO coated conductors on RABiTS substrate with advanced TFA-MOD method," *Rare Metal Materials and Engineering*, vol. 40, pp. 342–345, 2011.
- [9] Y. Xu, Z. Qian, Z. Xu, P. He, M. Massey, and R. Bhattacharya, "Nucleation study of $\text{YBa}_2\text{Cu}_3\text{O}_{7-x}$ (YBCO) films by modified tfa-mod approach," *IEEE Transactions on Applied Superconductivity*, vol. 19, no. 3, pp. 3127–3130, 2009.
- [10] X. Obradors, T. Puig, S. Ricart et al., "Growth, nanostructure and vortex pinning in superconducting $\text{YBa}_2\text{Cu}_3\text{O}_{7-x}$ thin films based on trifluoroacetate solutions," *Superconductor Science and Technology*, vol. 25, no. 12, Article ID 123001, 2012.
- [11] R. Feenstra, F. A. List, X. Li et al., "A modular ex situ conversion process for thick MOD-fluoride RBCO precursors," *IEEE Transactions on Applied Superconductivity*, vol. 19, no. 3, pp. 3131–3135, 2009.
- [12] K. Zalamova, A. Pomar, A. Palau, T. Puig, and X. Obradors, "Intermediate phase evolution in YBCO thin films grown by the TFA process," *Superconductor Science and Technology*, vol. 23, no. 1, Article ID 014012, 2010.
- [13] J. T. Dawley, P. G. Clem, T. J. Boyle, L. M. Ottley, D. L. Overmyer, and M. P. Siegal, "Rapid processing method for solution deposited $\text{YBa}_2\text{Cu}_3\text{O}_{7-x}$ thin films," *Physica C*, vol. 402, no. 1–2, pp. 143–151, 2004.
- [14] W. Huang, Z. P. Wu, and J. H. Hao, "Electrical properties of ferroelectric BaTiO_3 thin film on SrTiO_3 buffered GaAs by laser molecular beam epitaxy," *Applied Physics Letters*, vol. 94, no. 3, Article ID 032905, 2009.
- [15] W. Huang, J. Y. Dai, and J. H. Hao, "Structural and resistance switching properties of $\text{ZnO}/\text{SrTiO}_3/\text{GaAs}$ heterostructure grown by laser molecular beam epitaxy," *Applied Physics Letters*, vol. 97, no. 16, Article ID 162905, 2010.
- [16] J. S. Wu, C. L. Jia, K. Urban, J. H. Hao, and X. X. Xi, "Microstructure and misfit relaxation in $\text{SrTiO}_3/\text{SrRuO}_3$ bilayer films on $\text{LaAlO}_3(100)$ substrates," *Journal of Materials Research*, vol. 16, no. 12, pp. 3443–3450, 2001.
- [17] T. G. Holesinger, L. Civale, B. Maiorov et al., "Progress in nano-engineered microstructures for tunable high-current, high-temperature superconducting wires," *Advanced Materials*, vol. 20, no. 3, pp. 391–407, 2008.

Research Article

Hydrothermal Synthesis and Tunable Multicolor Upconversion Emission of Cubic Phase Y_2O_3 Nanoparticles

Haibo Wang,^{1,2} Chao Qian,¹ Zhigao Yi,^{1,2} Ling Rao,^{1,2} Hongrong Liu,¹ and Songjun Zeng¹

¹ College of Physics and Information Science and Key Laboratory of Low-Dimensional Quantum Structures and Quantum Control of the Ministry of Education, Hunan Normal University, Changsha, Hunan 410081, China

² Faculty of Materials, Optoelectronics and Physics, Key Laboratory of Low-Dimensional Materials and Application Technology (Ministry of Education), Xiangtan University, Xiangtan 411105, China

Correspondence should be addressed to Songjun Zeng; songjunz@hunnu.edu.cn

Received 29 September 2013; Accepted 12 November 2013

Academic Editor: Jianhua Hao

Copyright © 2013 Haibo Wang et al. This is an open access article distributed under the Creative Commons Attribution License, which permits unrestricted use, distribution, and reproduction in any medium, provided the original work is properly cited.

Highly crystalline body-centered cubic structure Y_2O_3 with lanthanide (Ln) codopants (Ln = Yb^{3+}/Er^{3+} and Yb^{3+}/Ho^{3+}) has been synthesized via a moderate hydrothermal method in combination with a subsequent calcination. The structure and morphology of $Y(OH)_3$ precursors and Y_2O_3 nanoparticles were characterized by X-ray diffraction and transmission electron microscopy. The results reveal that the Y_2O_3 nanoparticles possess cubic phase and form the quasispherical structure. The upconversion luminescence properties of Y_2O_3 nanoparticles doped with different Ln³⁺ (Yb^{3+}/Er^{3+} and Yb^{3+}/Ho^{3+}) ions were well investigated under the 980 nm excitation. The results show that the Yb^{3+}/Er^{3+} and Yb^{3+}/Ho^{3+} codoped Y_2O_3 nanoparticles exhibit strong red and light yellow upconversion emissions, respectively. It is expected that these Y_2O_3 nanoparticles with tunable multicolor output and intense red upconversion emission may have potential application in color displays and biolabels.

1. Introduction

In the last few years, upconversion (UC) nanoparticles have attracted great attention in many research areas owing to their unique antistokes emission processes of converting a longer wavelength radiation to short wavelength emission [1–3]. Lanthanide-doped rare-earth oxides and related materials are common phosphors in optical display devices and fluorescent bioimaging applications [4–12].

Y_2O_3 , as one of the most important rare-earth materials, was considered as an ideal candidate for biological applications, because of their higher mechanical, thermal, and chemical stability [13–15]. Rare-earth oxides were usually synthesized by thermal decomposition of their oxy salt precipitates such as hydroxide and oxalate at a certain temperature [16–19]. However, the thermal decomposition method requires high temperature and inert gases protection, resulting in complex experimental operations. Therefore, it is of significant importance to develop a simple method for the preparation of rare-earth oxide nanoparticles. Recently,

Ln-doped Y_2O_3 shows great potential application in optical display and lighting [20]. So, further investigations of tunable multicolor UC emission Y_2O_3 nanoparticles via codoping Ln ions (Yb^{3+}/Er^{3+} and Yb^{3+}/Ho^{3+}) are still of great interest. Up to now, there are many researches to regulate the multi-color output of UC nanomaterials via doping rare-earth ions [21–25]. For example, Garry's group have reported that Yb^{3+} , Er^{3+} , Ho^{3+} , and Tm^{3+} codoped Y_2O_3 nanocrystals can generate red, green, blue, and white light [25]. However, to the best of our knowledge, few studies have focused on the synthesis of spherical-like Y_2O_3 nanoparticles with tunable multicolor UC emissions by using facile hydrothermal method.

In this paper, different Ln³⁺ (Yb^{3+}/Er^{3+} and Yb^{3+}/Ho^{3+}) ions codoped $Y(OH)_3$ nanosheets have been successfully synthesized based on a facile and mild hydrothermal method. And the cubic phase Y_2O_3 nanoparticles were calcinated from these $Y(OH)_3$ precursors. In addition, the UC luminescence properties of the Y_2O_3 doped with different Ln ions (Yb^{3+}/Er^{3+} and Yb^{3+}/Ho^{3+}) were investigated under 980 nm

excitation. The UC mechanism and CIE (Commission Internationale de l'Éclairage 1931 chromaticity) chromaticity coordinates were studied in detail.

2. Experimental

$Y(NO_3)_3 \cdot 6H_2O$ (99.99%), $Er(NO_3)_3 \cdot 6H_2O$ (99.99%), $Yb(NO_3)_3 \cdot 5H_2O$ (99.99%), and $Ho(NO_3)_3 \cdot 5H_2O$ (99.99%) were purchased from Sinopharm Chemical Reagent Co., Ltd (China). All other chemical reagents are of analytical grade and used directly without further purification.

2.1. Synthesis of Different Ln^{3+} Codoped Y_2O_3 Nanoparticles.

$Y(OH)_3$ nanosheets were synthesized by a facile hydrothermal method [26, 27]. For a typical protocol, 1 mmol (total amounts) of $Ln(NO_3)_3$ ($Ln = Y, Yb, Er,$ and Ho) with designed molar ratio ($Y : Yb : Er = 78 : 20 : 2$ and $Y : Yb : Ho = 78 : 20 : 2$) was added into 20 mL deionized water. And then the obtained solution was rapidly adjusted to $pH = 14$ by adding 10 wt% NaOH solution. The obtained mixture was then transferred into a 50 mL stainless Teflon lined autoclave and reacted at $120^\circ C$ for 12 h. After reaction, the system was naturally cooled to room temperature. The resulting products were collected, washed several times with de-ionized water to remove residual NaOH, and then dried at $80^\circ C$ for 3 h. Y_2O_3 nanoparticles were synthesized by sintered $Y(OH)_3$ precursor at $500^\circ C$ for 6 h.

2.2. Characterizations.

X-ray powder diffraction (XRD) patterns were recorded by using a D/max 2500/PC system X-ray diffractometer at 40 kV and 250 mA using $Cu K\alpha$ radiation ($\lambda = 1.5406 \text{ \AA}$). The morphology and size of the samples were characterized by transmission electron microscopy (TEM, JEOL-2100F) equipped with an Oxford's energy dispersive X-ray spectroscopy (EDS). The UC emission spectra were recorded by a spectrophotometer (R 500) equipped with 980 nm laser diode as the excitation source. The digital photographs of the as-prepared samples were taken by a commercial digital camera (Canon 650D).

3. Results and Discussion

3.1. Crystal Phase and Morphology Analysis.

The phase composition of the as-prepared $Y_2O_3:Yb/Er$ was investigated by XRD analysis. As shown in Figure 1, the samples present characteristic diffraction peaks centered at 20.60° (211), 29.32° (222), 33.90° (400), 36.08° (411), 39.96° (332), 43.62° (134), 48.72° (440), 53.44° (611), 56.38° (541), 57.88° (622), 59.30° (136), 60.72° (444), 64.76° (127), 71.28° (800), and 72.52° (811), which is matched well with the standard body-centered cubic Y_2O_3 (JCPDS card no. 88-1040). In addition, no other impurity diffraction peaks are observed, indicating that pure cubic phase nanoparticles were synthesized with good crystallinity and a homogenous Y-Yb solid solution structure was formed.

To reveal the morphology and structure, the as-prepared samples were characterized by TEM (Figure 2). The as-prepared $Y(OH)_3:Yb/Er$ by hydrothermal method at

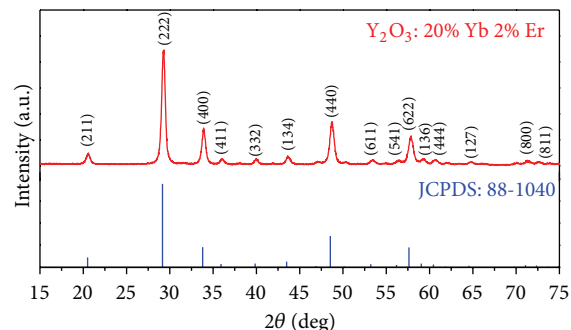


FIGURE 1: Typical XRD patterns of the $Y_2O_3:Yb/Er$ samples and the standard cubic phase Y_2O_3 (JCPDS: 88-1040).

$120^\circ C$ for 12 h consists of nanosheet and frizzy nanosheet (Figure 2(a)). $Y_2O_3:Yb/Er$ calcinated from the precursor of $Y(OH)_3:Yb/Er$ at $500^\circ C$ for 6 h present agglutinate structure of sphere-like nanoparticles (Figures 2(b) and 2(c)). As shown in Figure 2(d), the obvious lattice fringes in the high resolution transmission electron microscopy (HRTEM) images confirm the high crystallinity of the as-prepared $Y_2O_3:Yb/Er$ nanoparticles. The interplanar distances between the adjacent lattices were measured to 2.64 \AA , matching well with the d_{400} spacing of the cubic phase Y_2O_3 (JCPDS 88-1040). From the above results, we can see that rare-earth hydroxides are unstable compounds. When the temperature reached a certain value, the nanosheet and frizzy nanosheet hydroxides were burnt to stable sphere-like nanoparticles. During the TEM measurement, the elemental components of the $Y_2O_3:Yb/Er$ nanoparticles were detected by EDS. The sphere-like nanoparticles are mainly composed of Y, Er, Yb, and O, indicating that the doped Yb^{3+} and Er^{3+} were successfully incorporated into the Y_2O_3 host (Figure 2(e)). It is noted that the signals of Cu are attributed to the TEM copper grid.

3.2. Upconversion Luminescence Properties.

It is well known that multicolor UC luminescence can be achieved by doping various sensitizers and active Ln ions. Here, we discuss the UC luminescence properties of Y_2O_3 nanoparticles through codoping Yb^{3+}/Er^{3+} and Yb^{3+}/Ho^{3+} ions. Under 980 nm excitation, the corresponding UC luminescence spectra and the proposed energy transfer mechanism are shown in Figure 3. As demonstrated in Figure 3(a), the UC spectra of $Y_2O_3:Yb/Er$ nanoparticles show the characteristic Er^{3+} UC emissions including the green emission peaks (522 nm and 541 nm) and the red emission peak centered at 660 nm. More importantly, it can be seen that the $Y_2O_3:Yb/Er$ nanoparticles possess significant stronger red luminescence at 660 nm, which is different from previously reported $NaYF_4$ host that is usually presenting green UC emission [28]. Figure 3(c) shows the energy level diagram of the possible energy transfer processes between Yb^{3+} and Er^{3+} . With absorbing 980 nm photon, the Yb^{3+} is excited to the $^2F_{5/2}$ energy level and then transfers its energy to the nearby Er^{3+} ion. Immediately

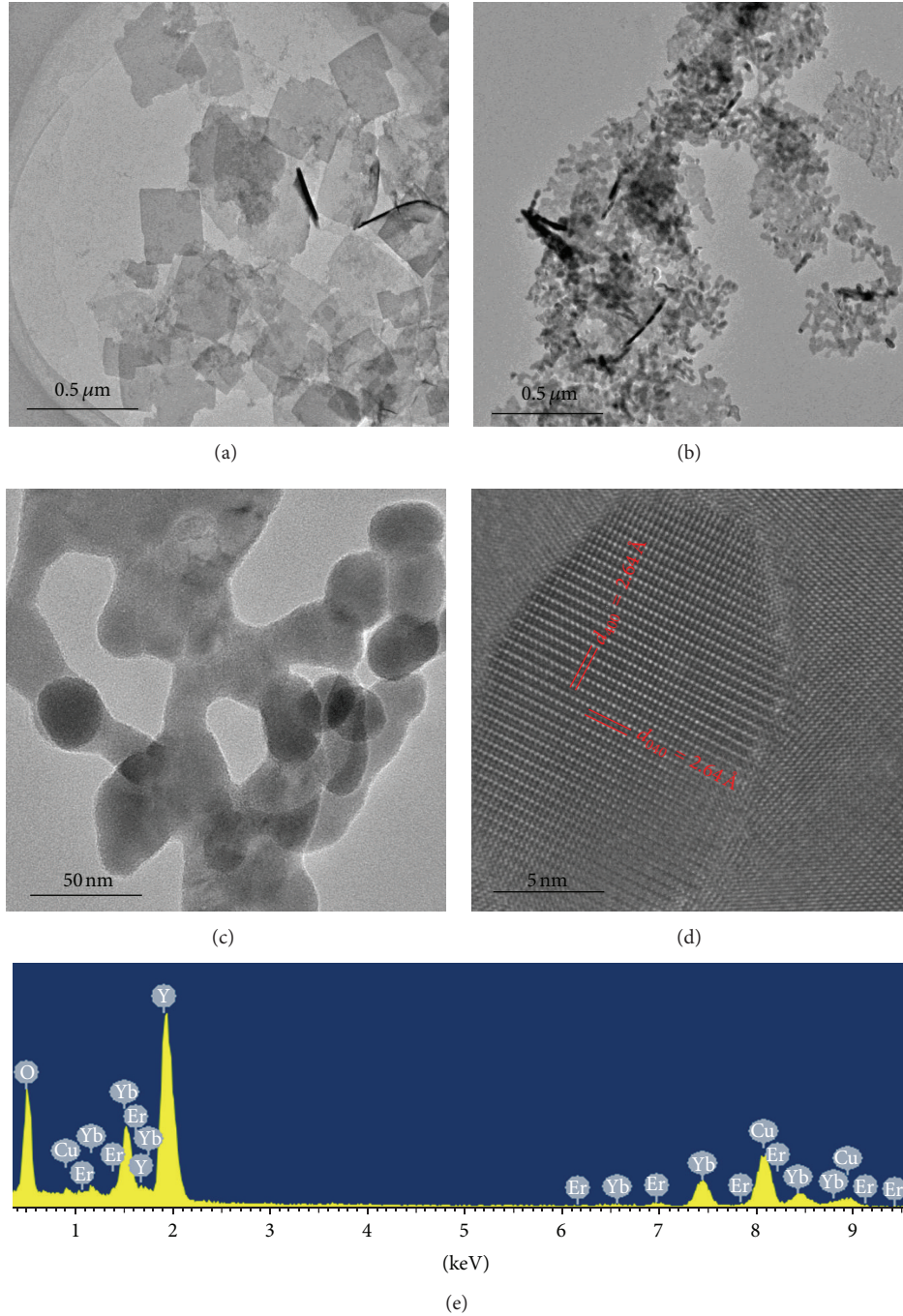


FIGURE 2: (a) TEM image of $Y(OH)_3:Yb/Er$ precursor; (b) low-magnification and (c) high-magnification TEM images of $Y_2O_3:Yb/Er$; (d) the HRTEM image of $Y_2O_3:Yb/Er$; (e) EDS of the $Y_2O_3:Yb/Er$ nanoparticles (mainly composed of Y, Er, Yb, and O elements).

following excited state absorption, transfer of energy from excited state Yb^{3+} resulted in populating the $^4F_{7/2}$ state of Er^{3+} . The excited state ($^4F_{7/2}$) electrons of Er^{3+} nonradiatively relax to the $^2H_{11/2}$, $^4S_{3/2}$, and $^4F_{9/2}$ levels (Er^{3+}). With high Yb^{3+} -doped concentration, the green emissions are almost quenched and the intensity ratio of the red to the green emission is large, which results in strong red emission [29]. The dominant red UC emission is mainly attributed to the

two energy-transfer processes $^4S_{3/2} (Er^{3+}) + ^2F_{7/2} (Yb^{3+}) \rightarrow ^4I_{13/2} (Er^{3+}) + ^2F_{5/2} (Yb^{3+})$ and $^4I_{13/2} (Er^{3+}) + ^2F_{5/2} (Yb^{3+}) \rightarrow ^4F_{9/2} (Er^{3+}) + ^2F_{7/2} (Yb^{3+})$ [25, 29, 30]. The three emission peaks around at 522 nm, 541 nm, and 660 nm can be assigned to the $^2H_{11/2} \rightarrow ^4I_{15/2}$ (green), $^4S_{3/2} \rightarrow ^4I_{15/2}$ (green), and $^4F_{9/2} \rightarrow ^4I_{15/2}$ (red) transitions of Er^{3+} , respectively. As demonstrated in Figure 3(b), the relative intensity of green ($^3S_2/^5F_4 \rightarrow ^5I_8$) to red ($^5F_5 \rightarrow ^5I_8$)

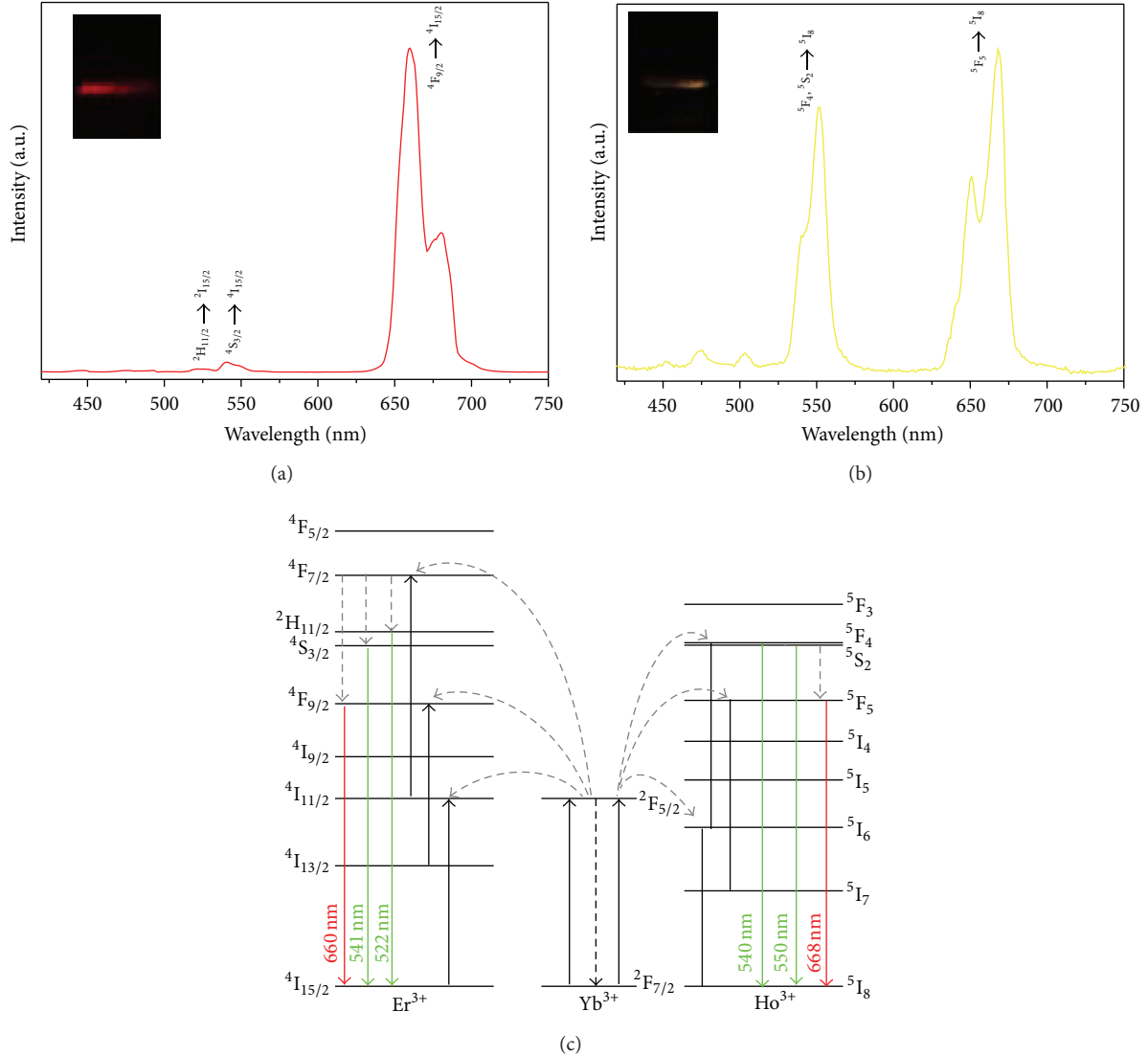


FIGURE 3: Upconversion luminescence spectra of Y_2O_3 nanoparticles doped with (a) 20% Yb, 2% Er; (b) 20% Yb, 2% Ho. (c) Simplified energy-level diagram of $\text{Yb}^{3+}/\text{Er}^{3+}$ and $\text{Yb}^{3+}/\text{Ho}^{3+}$ doped Y_2O_3 samples. The insets of (a) and (b) are the corresponding digital photographs of the water solutions of these nanoparticles.

emission of the Ho^{3+} ion is stronger than the ratio of green to red emission of Er^{3+} . The insets of Figures 3(a) and 3(b) show the corresponding digital photographs of the water solution of the $\text{Y}_2\text{O}_3:\text{Yb}/\text{Er}$ and $\text{Y}_2\text{O}_3:\text{Yb}/\text{Ho}$, respectively. As demonstrated, the eye-visible red and yellow light can be readily observed.

To further reveal the UC multicolor output, we have calculated the CIE chromaticity coordinates of $\text{Y}_2\text{O}_3:\text{Yb}^{3+}/\text{Er}^{3+}$ and $\text{Y}_2\text{O}_3:\text{Yb}^{3+}/\text{Ho}^{3+}$. As shown in Figure 4, the chromaticity coordinates for $\text{Y}_2\text{O}_3:\text{Yb}^{3+}/\text{Er}^{3+}$ ($X = 0.6611$, $Y = 0.3357$) (Figure 4, point a) and $\text{Y}_2\text{O}_3:\text{Yb}^{3+}/\text{Ho}^{3+}$ ($X = 0.3884$, $Y = 0.6026$) (Figure 4, point b) are fallen into the red and yellow region, respectively, which is consistent with the results of the UC spectra and the digital photographs. The CIE diagram indicates that the UC colors including strong red and yellow

can be obtained via co-doping $\text{Yb}^{3+}/\text{Er}^{3+}$ and $\text{Yb}^{3+}/\text{Ho}^{3+}$ in Y_2O_3 host material, respectively.

4. Conclusions

In summary, we have successfully synthesized spherical-like cubic phase Y_2O_3 nanoparticles with tunable multicolor UC emissions by using facile hydrothermal method. On the basis of the analysis of the XRD and TEM, the as-prepared $\text{Y}(\text{OH})_3:\text{Yb}/\text{Er}$ nanocrystals are composed of nanosheet and frizzy nanosheet and then the $\text{Y}_2\text{O}_3:\text{Yb}/\text{Er}$ nanoparticles with a quasispherical cubic phase structure were obtained by calcining precursor. Under the excitation of the 980 nm laser, multicolor visible emissions including strong red and yellow can be obtained via co-doping $\text{Yb}^{3+}/\text{Er}^{3+}$ and $\text{Yb}^{3+}/\text{Ho}^{3+}$

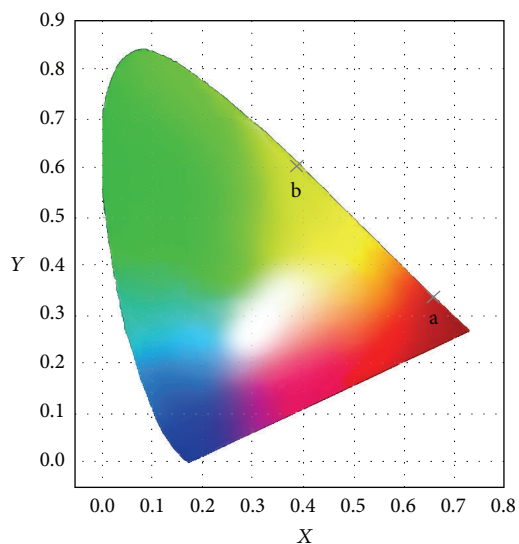


FIGURE 4: The CIE chromaticity diagram of Y_2O_3 nanoparticles doped with (a) 20% Yb, 2%Er (0.6611, 0.3357); (b) 20% Yb, 2% Ho (0.3884, 0.6026).

in Y_2O_3 host material, respectively. These UC nanoparticles with multicolors suggest that they have potential application in color displays and biolabels.

Acknowledgments

This work was supported by the National Natural Science Foundation of China (nos. 51102202 and 91230116), Specialized research fund for the Doctoral Program of Higher Education of China (no. 20114301120006), Hunan Provincial Natural Science Foundation of China (Nos. 12JJ4056 and 13JJ1017), the Scientific Foundation of Ministry of Education (212119), and Scientific Research Fund of Hunan Provincial Education Department (13B062).

References

- [1] F. Auzel, "Upconversion and anti-stokes processes with f and d ions in solids," *Chemical Reviews*, vol. 104, no. 1, pp. 139–174, 2004.
- [2] J. F. Suyver, A. Aebischer, D. Biner et al., "Novel materials doped with trivalent lanthanides and transition metal ions showing near-infrared to visible photon upconversion," *Optical Materials*, vol. 27, no. 6, pp. 1111–1130, 2005.
- [3] H. B. Wang, Z. G. Yi, L. Rao, H. R. Liu, and S. J. Zeng, "High quality multi-functional $NaErF_4$ nanocrystals: structure-controlled synthesis, phase-induced multi-color emissions and tunable magnetic properties," *Journal of Materials Chemistry C*, vol. 1, no. 35, pp. 5520–5526, 2013.
- [4] T. Hase, T. Kano, E. Nakazawa, and H. Yamamoto, "Phosphor materials for cathode-ray tubes," in *Advances in Electronics and Electron Physics*, W. H. Peter, Ed., vol. 79, pp. 271–373, Academic Press, 1990.
- [5] F. Vetrone, J.-C. Boyer, J. A. Capobianco, A. Speghini, and M. Bettinelli, "A spectroscopic investigation of trivalent lanthanide doped Y_2O_3 nanocrystals," *Nanotechnology*, vol. 15, no. 1, pp. 75–81, 2004.
- [6] R. Deng, X. Xie, M. Vendrell, Y.-T. Chang, and X. Liu, "Intracellular glutathione detection using MnO_2 -nanosheet-modified upconversion nanoparticles," *Journal of the American Chemical Society*, vol. 133, no. 50, pp. 20168–20171, 2011.
- [7] Q. Liu, M. Chen, Y. Sun et al., "Multifunctional rare-earth self-assembled nanosystem for tri-modal upconversion luminescence/fluorescence/positron emission tomography imaging," *Biomaterials*, vol. 32, no. 32, pp. 8243–8253, 2011.
- [8] H. R. Liu, W. Lu, H. B. Wang et al., "Simultaneous synthesis and amine-functionalization of single-phase $BaYF_5:Yb/Er$ nanoprobe for dual-modal in vivo upconversion fluorescence and long-lasting X-ray computed tomography imaging," *Nanoscale*, vol. 5, no. 13, pp. 6023–6029, 2013.
- [9] J. A. Capobianco, J. C. Boyer, F. Vetrone, A. Speghini, and M. Bettinelli, "Optical spectroscopy and upconversion studies of Ho^{3+} -doped bulk and nanocrystalline Y_2O_3 ," *Chemistry of Materials*, vol. 14, no. 7, pp. 2915–2921, 2002.
- [10] S. J. Zeng, M. K. Tsang, C. F. Chan, K. L. Wong, and J. H. Hao, "PEG modified $BaGdF_5:Yb/Er$ nanoprobes for multi-modal upconversion fluorescent, in vivo X-ray computed tomography and biomagnetic imaging," *Biomaterials*, vol. 33, no. 36, pp. 9232–9238, 2012.
- [11] J. McKittrick, L. E. Shea, C. F. Bacalski, and E. J. Bosze, "Influence of processing parameters on luminescent oxides produced by combustion synthesis," *Displays*, vol. 19, no. 4, pp. 169–172, 1999.
- [12] S. Zeng, J. Xiao, Q. Yang, and J. Hao, "Bi-functional $NaLuF_4:Gd^{3+}/Yb^{3+}/Tm^{3+}$ nanocrystals: structure controlled synthesis, near-infrared upconversion emission and tunable magnetic properties," *Journal of Materials Chemistry*, vol. 22, no. 19, pp. 9870–9874, 2012.
- [13] G.-Y. Adachi and N. Imanaka, "The binary rare earth oxides," *Chemical Reviews*, vol. 98, no. 4, pp. 1479–1514, 1998.
- [14] S. F. Lim, R. Riehn, W. S. Ryu et al., "In vivo and scanning electron microscopy imaging of upconverting nanophosphors in *Caenorhabditis elegans*," *Nano Letters*, vol. 6, no. 2, pp. 169–174, 2006.
- [15] T. R. Hinklin, S. C. Rand, and R. M. Laine, "Transparent, polycrystalline upconverting nanoceramics: towards 3-D displays," *Advanced Materials*, vol. 20, no. 7, pp. 1270–1273, 2008.
- [16] R. Si, Y.-W. Zhang, H.-P. Zhou, L.-D. Sun, and C.-H. Yan, "Controlled-synthesis, self-assembly behavior, and surface-dependent optical properties of high-quality rare-earth oxide nanocrystals," *Chemistry of Materials*, vol. 19, no. 1, pp. 18–27, 2007.
- [17] Y. C. Cao, "Synthesis of square gadolinium-oxide nanoplates," *Journal of the American Chemical Society*, vol. 126, no. 24, pp. 7456–7457, 2004.
- [18] H. Wang, M. Uehara, H. Nakamura, M. Miyazaki, and H. Maeda, "Synthesis of well-dispersed $Y_2O_3:Eu$ nanocrystals and self-assembled nanodisks using a simple non-hydrolytic route," *Advanced Materials*, vol. 17, no. 20, pp. 2506–2509, 2005.
- [19] R. Si, Y.-W. Zhang, L.-P. You, and C.-H. Yan, "Rare-earth oxide nanopolyhedra, nanoplates, and nanodisks," *Angewandte Chemie—International Edition*, vol. 44, no. 21, pp. 3256–3260, 2005.
- [20] D. K. Williams, B. Bihari, B. M. Tissue, and J. M. McHale, "Preparation and fluorescence spectroscopy of bulk monoclinic $Eu^{3+}:Y_2O_3$ and comparison to $Eu^{3+}:Y_2O_3$ nanocrystals," *Journal of Physical Chemistry B*, vol. 102, no. 6, pp. 916–920, 1998.

- [21] N. Niu, P. P. Yang, F. He et al., "Tunable multicolor and bright white emission of one-dimensional $\text{NaLuF}_4:\text{Yb}^{3+}, \text{Ln}^{3+}$ ($\text{Ln} = \text{Er}, \text{Tm}, \text{Ho}, \text{Er}/\text{Tm}, \text{Tm}/\text{Ho}$) microstructures," *Journal of Materials Chemistry*, vol. 22, no. 21, pp. 10889–10899, 2012.
- [22] G. Ren, S. Zeng, and J. Hao, "Tunable multicolor upconversion emissions and paramagnetic property of monodispersed bifunctional lanthanide-doped NaGdF_4 nanorods," *Journal of Physical Chemistry C*, vol. 115, no. 41, pp. 20141–20147, 2011.
- [23] F. Wang and X. Liu, "Upconversion multicolor fine-tuning: visible to near-infrared emission from lanthanide-doped NaYF_4 nanoparticles," *Journal of the American Chemical Society*, vol. 130, no. 17, pp. 5642–5643, 2008.
- [24] J.-C. Boyer, F. Vetrone, L. A. Cuccia, and J. A. Capobianco, "Synthesis of colloidal upconverting NaYF_4 nanocrystals doped with $\text{Er}^{3+}, \text{Yb}^{3+}$ and $\text{Tm}^{3+}, \text{Yb}^{3+}$ via thermal decomposition of lanthanide trifluoroacetate precursors," *Journal of the American Chemical Society*, vol. 128, no. 23, pp. 7444–7445, 2006.
- [25] G. Glaspell, J. Anderson, J. R. Wilkins, and M. S. El-Shall, "Vapor phase synthesis of upconverting Y_2O_3 nanocrystals doped with $\text{Yb}^{3+}, \text{Er}^{3+}, \text{Ho}^{3+}$, and Tm^{3+} to generate red, green, blue, and white light," *Journal of Physical Chemistry C*, vol. 112, no. 30, pp. 11527–11531, 2008.
- [26] F. Zhang and D. Zhao, "Synthesis of uniform rare earth fluoride (NaMF_4) nanotubes by in Situ ion exchange from their hydroxide $[\text{M}(\text{OH})_3]$ parents," *ACS Nano*, vol. 3, no. 1, pp. 159–164, 2009.
- [27] X. Wang and Y. Li, "Synthesis and characterization of lanthanide hydroxide single-crystal nanowires," *Angewandte Chemie—International Edition*, vol. 41, no. 24, pp. 4790–4793, 2002.
- [28] X. Teng, Y. H. Zhu, W. Wei et al., "Lanthanide-doped $\text{Na}_x\text{ScF}_{3+x}$ nanocrystals: crystal structure evolution and multicolor tuning," *Journal of the American Chemical Society*, vol. 134, no. 20, pp. 8340–8343, 2012.
- [29] Y. Li, J. Zhang, Y. Luo, X. Zhang, Z. Hao, and X. Wang, "Color control and white light generation of upconversion luminescence by operating dopant concentrations and pump densities in $\text{Yb}^{3+}, \text{Er}^{3+}$ and Tm^{3+} tri-doped Lu_2O_3 nanocrystals," *Journal of Materials Chemistry*, vol. 21, no. 9, pp. 2895–2900, 2011.
- [30] E. W. Barrera, M. C. Pujol, F. Díaz et al., "Emission properties of hydrothermal $\text{Yb}^{3+}, \text{Er}^{3+}$ and $\text{Yb}^{3+}, \text{Tm}^{3+}$ -codoped Lu_2O_3 nanorods: upconversion, cathodoluminescence and assessment of waveguide behavior," *Nanotechnology*, vol. 22, no. 7, Article ID 075205, pp. 1–15, 2011.

Research Article

Intense Red Upconversion Emission and Shape Controlled Synthesis of $\text{Gd}_2\text{O}_3:\text{Yb}/\text{Er}$ Nanocrystals

Zhigao Yi, Boyun Wen, Chao Qian, Haibo Wang,
Ling Rao, Hongrong Liu, and Songjun Zeng

College of Physics and Information Science and Key Laboratory of Low-Dimensional Quantum Structures and Quantum Control of the Ministry of Education, Hunan Normal University, Changsha, Hunan 410081, China

Correspondence should be addressed to Songjun Zeng; songjunz@hunnu.edu.cn

Received 5 October 2013; Accepted 23 October 2013

Academic Editor: Jianhua Hao

Copyright © 2013 Zhigao Yi et al. This is an open access article distributed under the Creative Commons Attribution License, which permits unrestricted use, distribution, and reproduction in any medium, provided the original work is properly cited.

Yb/Er codoped $\text{Gd}(\text{OH})_3$ was synthesized firstly via a simple hydrothermal treatment of the corresponding nitrate in the presence of alkali by tuning the pH values. The $\text{Gd}_2\text{O}_3:\text{Yb}/\text{Er}$ nanocrystals were obtained via sintering the corresponding hydroxides precursors. The as-prepared samples were characterized by the typical X-ray diffraction, energy-dispersive X-ray spectroscopy, transmission electron microscopy (TEM), high-resolution TEM, and spectrophotometer. The results revealed that two shapes of the as-prepared $\text{Gd}_2\text{O}_3:\text{Yb}/\text{Er}$ nanocrystals can be readily tuned from lemon-like particle to rod-like structure via tuning pH values from 7 to 14. Moreover, compared with the samples prepared at pH 7, the $\text{Gd}_2\text{O}_3:\text{Yb}/\text{Er}$ nanocrystals prepared at pH 14 exhibit enhanced red upconversion emission and higher upconversion luminescence intensity under the excitation of 980 nm laser.

1. Introduction

Rare-earth (RE) doped upconversion (UC) nanocrystals have been comprehensively used in high-quality lighting devices, magnets, and other functional materials due to their optical, electronic, and chemical properties arising from the 4f shell of their ions [1–6]. These capabilities are highly sensitive to the bonding states of RE ions. RE doping induced photoluminescence property in fluorides, and oxides systems have been universally reported [7–11]. For instance, Yb/Tm codoped Y_2O_3 nanocrystals can achieve remarkable green UC luminescent emission [8]. In Yb/Er codoped Lu_2O_3 system, UC spectra revealed that simultaneous green and red emissions can be obtained [11]. However, the intense UC emission located in the red region by doping Yb/Er is an enormous challenge owing to the fact that Yb/Er codoped UC materials have a multipeak emissions nature. Recently, Li's group have developed a simple and controlled synthetic method [3–5], in which the shape transformation, phase evolution, and UC emission tuning of a series of RE oxides nanocrystals can be reached by simply adjusting reaction parameters, such as pH value, reaction time, and temperature.

Among various developed RE-based oxides UC nanomaterials, gadolinium oxide (Gd_2O_3) has its unique UC luminescent and magnetic properties. Therefore, RE (Nd^{3+} , Er^{3+} , and Tm^{3+}) doped Gd_2O_3 nanocrystals have been selected for optical and magnetic studies, because of their high chemical durability, photothermal and photochemical stabilities, low photon-energy, and unpaired electrons of the 4f shell [12–17]. Of course, there are also many investigations of the UC luminescence nanocrystals mainly focused on the RE doped Gd_2O_3 with phase/structure control and UC luminescence tuning [15, 18–20]. Even though UC emissions of RE doped Gd_2O_3 nanocrystals can be enhanced via changing reaction parameters, intense red UC emission is still a large challenge for the various energy levels of RE ions. In general, these nanocrystals exhibit multipeak UC emissions due to the fact that the doped lanthanide ions have abundant energy levels. However, there are still limited reports about doping Yb/Er to achieve intense red UC emission.

In this work, the precursor $\text{Gd}(\text{OH})_3$ codoped with Yb^{3+} and Er^{3+} ions was synthesized at first via a simple hydrothermal reaction. After that, the nanoparticle and nanorod structures of $\text{Gd}_2\text{O}_3:\text{Yb}/\text{Er}$ were obtained by calcination of the

corresponding $\text{Gd}(\text{OH})_3$ precursors prepared at different pH values of 7 and 14, respectively. The UC properties of the $\text{Gd}_2\text{O}_3\text{:Yb/Er}$ samples with different shapes were studied. Interestingly, greatly enhanced pH red UC emission can be realized by simply tuning the pH value from 7 to 14, which will expand their application from optics to the biological field.

2. Experimental

2.1. Materials and Regents. $\text{RE}(\text{NO}_3)_3 \cdot 6\text{H}_2\text{O}$ ($\text{Gd}^{3+}/\text{Yb}^{3+}/\text{Er}^{3+}$, 99.99%) was purchased from Sigma-Aldrich. KOH was purchased from Sinopharm Chemical Reagent Co., China. All of the reagents were used as received with no further purification.

2.2. Synthesis of Yb/Er Codoped $\text{Gd}(\text{OH})_3$ and Gd_2O_3 Nanocrystals. $\text{Gd}(\text{OH})_3\text{:Yb/Er}$ nanocrystals were synthesized by using a simple hydrothermal treatment [5] of the corresponding nitrate in the presence of alkali. In a typical synthesis, 1 mmol of $\text{Gd}(\text{NO}_3)_3$ (0.5 M), $\text{Yb}(\text{NO}_3)_3$ (0.5 M), and $\text{Er}(\text{NO}_3)_3$ (0.5 M) with the designed molar ratio of 78 : 20 : 2 was added into 20 mL of deionized (DI) water. And then, aqueous KOH (10 wt%) solution was added dropwise into the mixture until the pH was adjusted to a designated value (7/14). After another stirring for 20 min, the formed colloidal mixture was transferred into a 50 mL Teflon-lined stainless steel autoclave and then sealed and maintained at 180°C for 12 h. After the reaction was completed, the reaction system was permitted to cool to room temperature naturally and the pure solid product $\text{Gd}(\text{OH})_3\text{:Yb/Er}$ was obtained by washing with deionized water several times and drying at 60°C for 24 h. In addition, the corresponding oxide nanocrystals ($\text{Gd}_2\text{O}_3\text{:Yb/Er}$) have been prepared by calcination of $\text{Gd}(\text{OH})_3\text{:Yb/Er}$ at 450°C for 6 h.

2.3. Characterizations. Typical X-ray diffraction (XRD) patterns were recorded by a D/max- γ A System X-ray diffractometer at 40 kV and 250 mA with Cu-K α radiation ($\lambda = 1.54056 \text{ \AA}$). The shape and structure of the as-prepared samples were characterized by transmission electron microscopy (TEM, JEOL-2100F) equipped with the energy-dispersive X-ray spectroscopy (EDS). The UC emissions were tested by a spectrophotometer (R500) equipped with a 980 nm laser diode.

3. Results and Discussion

Crystal phase of the as-prepared $\text{Gd}_2\text{O}_3\text{:Yb/Er}$ samples was identified by powder XRD pattern. After continuous heating for 6 hours at 450°C, $\text{Gd}(\text{OH})_3\text{:Yb/Er}$ (pH = 7) nanocrystals have completely transformed to $\text{Gd}_2\text{O}_3\text{:Yb/Er}$ and the corresponding XRD analysis is showed in Figure 1(a). In addition, the phase of $\text{Gd}_2\text{O}_3\text{:Yb/Er}$ (pH = 7) has transformed into pure cubic phase and no other peaks have been detected. When the pH value is tuned up to 14, pure cubic phase of as-synthesized products can be obtained as well as presented in Figure 1(b). The diffraction peaks of $\text{Gd}_2\text{O}_3\text{:Yb/Er}$ nanocrystals (pH = 7/14)

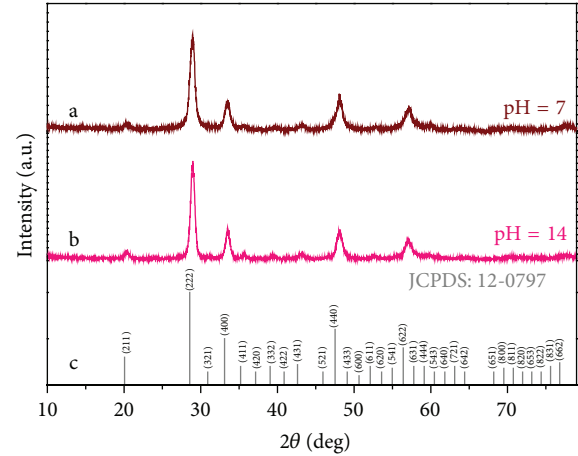


FIGURE 1: XRD pattern of (a) $\text{Gd}_2\text{O}_3\text{:Yb/Er}$ (pH = 7) and (b) $\text{Gd}_2\text{O}_3\text{:Yb/Er}$ (pH = 14) nanocrystals and (c) standard cubic phase Gd_2O_3 .

are well coincident with the peaks of the standard cubic phase Gd_2O_3 (JCPDS number 12-0797, Figure 1(c)).

To further investigate the morphology and structure of these nanocrystals, TEM, high-resolution TEM (HRTEM), and selected area electron diffraction (SAED) assays were carried out. As shown in Figure 2(a), the precursor ($\text{Gd}(\text{OH})_3\text{:Yb/Er}$, pH = 7) presented lemon-like shape. Figure 2(c) shows a typical TEM image of $\text{Gd}_2\text{O}_3\text{:Yb/Er}$ (pH = 7). As demonstrated, the samples presented lemon- and rod-like structures. The interplanar spacing in the HRTEM image (Figure 2(d)) of a single particle was measured to be 3.10 Å, corresponding to the 111 crystal plane of cubic phase Gd_2O_3 , which is matched well with the XRD analysis. Figure 2(e) shows the typical SAED result, further validating the formation of body-centered cubic phase structure. To further study the influence on morphology by tuning pH value, the TEM image of $\text{Gd}_2\text{O}_3\text{:Yb/Er}$ (pH = 14) is presented in Figure 2(f). As shown in Figure 2(f), compared with $\text{Gd}_2\text{O}_3\text{:Yb/Er}$ (pH = 7), the shape was completely changed to pure rod-like morphology. Figure 2(h) shows the typical HRTEM image taken from an individual nanorod (Figure 2(g)). The interplanar spacing was measured to be 2.68 Å, which agrees well with the 400 crystal plane of cubic phase Gd_2O_3 , indicating the formation of cubic phase rod-like structure. The SAED result of nanorods (Figure 2(i)) also presents the characterized polycrystalline diffraction rings of body-centered cubic phase, further demonstrating the formation of cubic phase rod-like structure. Therefore, tuning pH value from 7 to 14 can successfully achieve the morphology evolution of Yb/Er codoped Gd_2O_3 nanocrystals from lemon-like particle to rod. Figure 2(b) exhibits EDS analysis of the as-prepared $\text{Gd}_2\text{O}_3\text{:Yb/Er}$ (pH = 14), indicating that Gd, O, Yb, and Er are the major elements in these nanorods.

The UC luminescence property of the $\text{Gd}_2\text{O}_3\text{:Yb/Er}$ nanocrystals was studied at room temperature. As shown in Figure 3, $\text{Gd}_2\text{O}_3\text{:Yb/Er}$ (pH = 7) exhibits intense red and weak green emissions (green curve) under excitation by

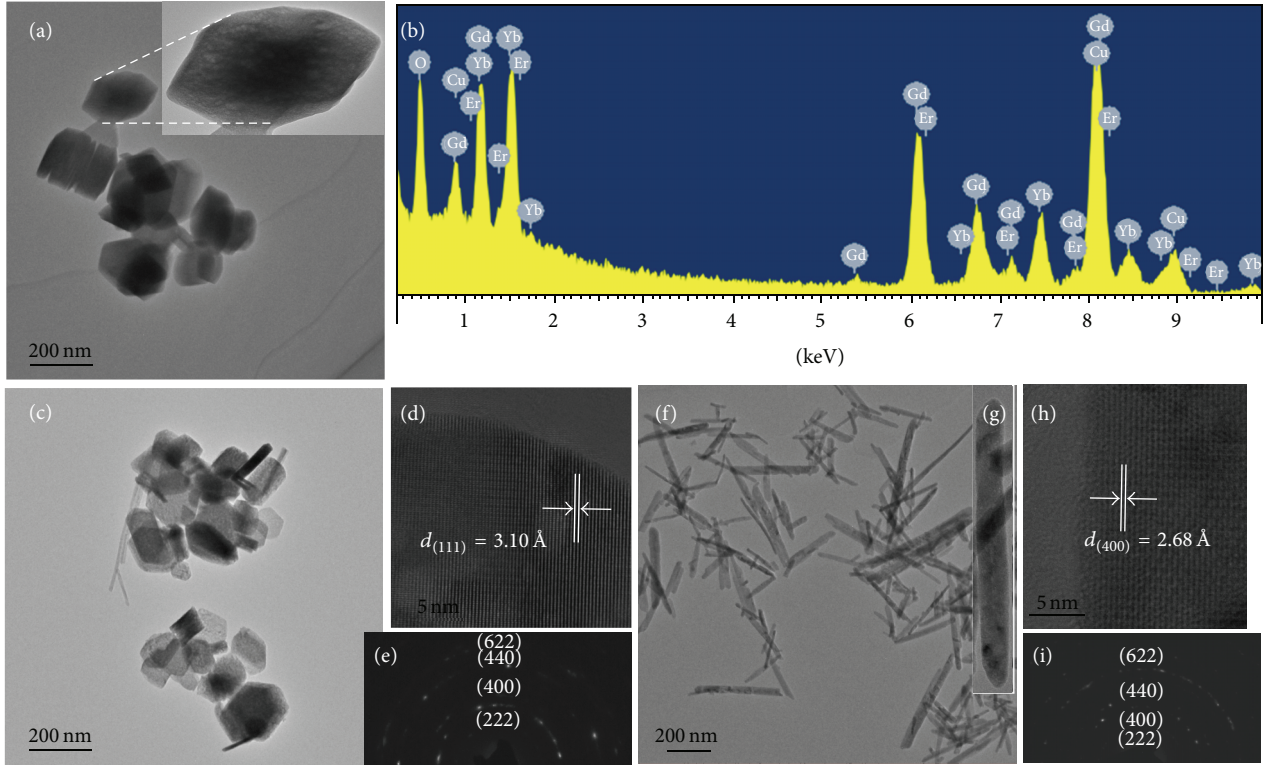


FIGURE 2: (a) TEM image of $Gd(OH)_3:Yb/Er$ ($pH = 7$). (b) EDS analysis of $Gd_2O_3:Yb/Er$ nanorods shown in (f). (c) TEM image of $Gd_2O_3:Yb/Er$ ($pH = 7$) and the corresponding (d) HRTEM and (e) SAED, respectively. (f) TEM image of $Gd_2O_3:Yb/Er$ ($pH = 14$). (g) TEM of a single nanorod and (h) the corresponding HRTEM image. (i) The SAED characterization of nanorods shown in (f).

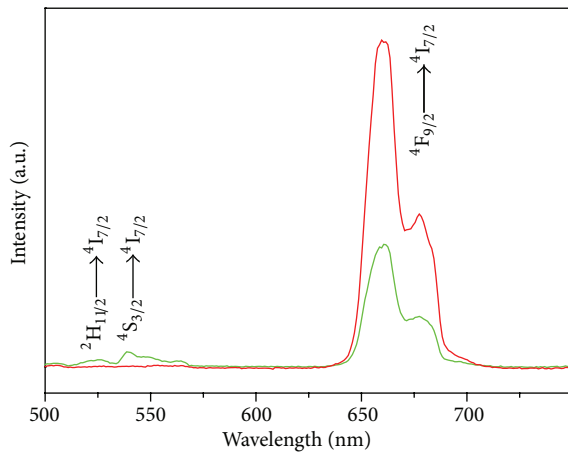


FIGURE 3: UC spectra of $Gd_2O_3:Yb/Er$ nanocrystals with different pH values. The blue curve stands for $pH = 7$, and the red one corresponds with $pH = 14$.

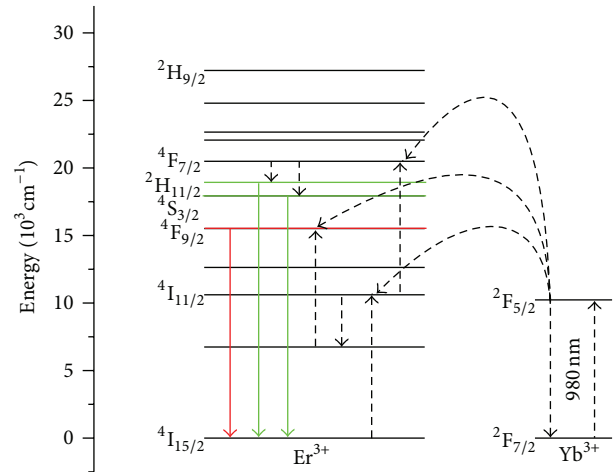


FIGURE 4: Schematic energy-level diagram of Yb^{3+} and Er^{3+} ions.

continuous-wave 980 nm laser diode. Moreover, the later CIE calculated chromaticity coordinates (Figure 6) reveal that yellow light can be obtained. However, via varying the pH value from 7 to 14, the red UC emission efficiency and emission intensity of $Gd_2O_3:Yb/Er$ have been extremely enhanced (red curve). As presented in Figure 4, the two green light

emissions (labeled by green arrows) are attributed to the electronic transitions $^2H_{11/2} \rightarrow ^4I_{15/2}$ and $^4S_{3/2} \rightarrow ^4I_{15/2}$, which correspond with the green emissions (Figure 3) centered in 525 and 538 nm, respectively. On the other hand, the red emission (labeled by the red arrow) is ascribed to the transition of $^4F_{9/2} \rightarrow ^4I_{15/2}$, which is well coincident with the red emission centered at 662 nm. To further reveal the UC emission property of these $Gd_2O_3:Yb/Er$ nanorods,

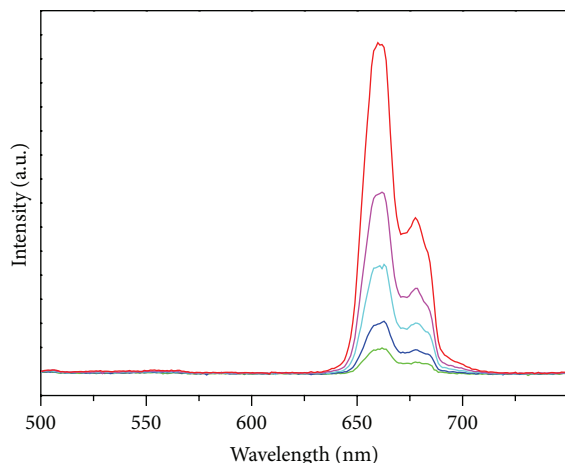


FIGURE 5: Dependence of PL spectra on pumping power in $\text{Gd}_2\text{O}_3:\text{Yb/Er}$ nanorods.

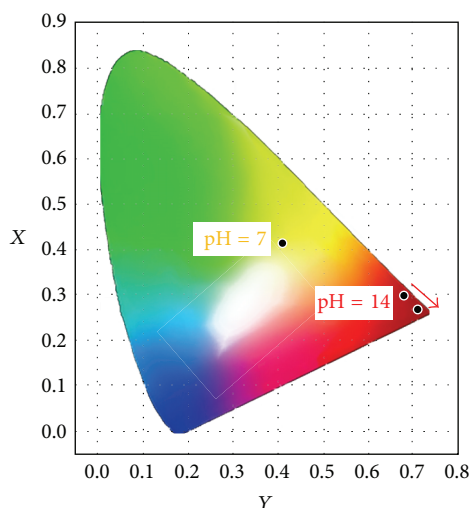


FIGURE 6: The CIE 1931 chromaticity diagram and calculated chromaticity coordinates. The red arrow indicates the changing tendency of chromaticity coordinate of $\text{Gd}_2\text{O}_3:\text{Yb/Er}$ nanorods (pH = 14) by increasing the excitation power.

power dependent UC spectra have been studied (Figure 5). With increasing excitation power, the as-synthesized samples exhibit the trend of enhancing UC luminescence, especially red emission, which can be observed obviously from the red arrow shown in the CIE diagram (Figure 6). It is noted that the dominant red UC emission with very weaker green UC emission in the Yb/Er doped system is mainly attributed to the fact that the intensity ratio of the red to green emissions increased rapidly and the green emissions almost quenched for high doped content of Yb^{3+} (20 mol%) [11, 21].

4. Conclusions

In conclusion, body-centered cubic phase $\text{Gd}_2\text{O}_3:\text{Yb/Er}$ nanocrystals with different shapes were successfully synthesized by a hydrothermal method and combination of

a subsequent calcination. By tuning the pH value of the reaction system, the shape of $\text{Gd}_2\text{O}_3:\text{Yb/Er}$ nanocrystals can be successfully tuned from lemon-like shape to rod. More interestingly, when adjusting the pH value from 7 to 14, the red UC emission and whole UC emission intensity have been remarkably enhanced. The bright red UC emission of these nanorods may expand their application varying from optics to the biological field.

Acknowledgments

This paper was supported by the National Natural Science Foundation of China (no. 51102202), specialized research Fund for the Doctoral Program of Higher Education of China (no. 20114301120006), Hunan Provincial Natural Science Foundation of China (no. 12JJ4056), and the Scientific Research Fund of Hunan Provincial Education Department (13B062).

References

- [1] G.-Y. Adachi and N. Imanaka, "The binary rare earth oxides," *Chemical Reviews*, vol. 98, no. 4, pp. 1479–1514, 1998.
- [2] J. A. Capobianco, J. C. Boyer, F. Vetrone, A. Speghini, and M. Bettinelli, "Optical spectroscopy and upconversion studies of Ho^{3+} -doped bulk and nanocrystalline Y_2O_3 ," *Chemistry of Materials*, vol. 14, no. 7, pp. 2915–2921, 2002.
- [3] X. Wang, X.-M. Sun, D. P. Yu, B.-S. Zou, and Y. D. Li, "Rare earth compound nanotubes," *Advanced Materials*, vol. 15, no. 17, pp. 1442–1445, 2003.
- [4] Z.-L. Wang, J. H. Hao, H. L. W. Chan, W.-T. Wong, and K.-L. Wong, "A strategy for simultaneously realizing the cubic-to-hexagonal phase transition and controlling the small size of $\text{NaYF}_4:\text{Yb}^{3+}, \text{Er}^{3+}$ nanocrystals for in vitro cell imaging," *Small*, vol. 8, no. 12, pp. 1863–1868, 2012.
- [5] X. Wang and Y. D. Li, "Synthesis and characterization of lanthanide hydroxide single-crystal nanowires," *Angewandte Chemie International Edition*, vol. 41, no. 24, pp. 4790–4793, 2002.
- [6] J. J. Zhou, G. X. Chen, E. Wu et al., "Ultrasensitive polarized up-conversion of $\text{Tm}^{3+}-\text{Yb}^{3+}$ doped $\beta\text{-NaYF}_4$ single nanorod," *Nano Letters*, vol. 13, no. 5, pp. 2241–2246, 2013.
- [7] G. Z. Ren, S. J. Zeng, and J. H. Hao, "Tunable multicolor upconversion emissions and paramagnetic property of monodispersed bifunctional lanthanide-doped NaGdF_4 nanorods," *Journal of Physical Chemistry C*, vol. 115, no. 41, pp. 20141–20147, 2011.
- [8] S. F. Zhou, N. J. Jiang, K. Miura et al., "Simultaneous tailoring of phase evolution and dopant distribution in the glassy phase for controllable luminescence," *Journal of the American Chemical Society*, vol. 132, no. 50, pp. 17945–17952, 2010.
- [9] S. J. Zeng, J. J. Xiao, Q. B. Yang, and J. H. Hao, "Bi-functional $\text{NaLuF}_4:\text{Gd}^{3+}/\text{Yb}^{3+}/\text{Tm}^{3+}$ nanocrystals: structure controlled synthesis, near-infrared upconversion emission and tunable magnetic properties," *Journal of Materials Chemistry*, vol. 22, no. 19, pp. 9870–9874, 2012.
- [10] S. J. Zeng, M.-K. Tsang, C.-F. Chan, K.-L. Wong, and J. H. Hao, "PEG modified $\text{BaGdF}_5:\text{Yb/Er}$ nanoprobes for multi-modal upconversion fluorescent, *in vivo* X-ray computed tomography and biomagnetic imaging," *Biomaterials*, vol. 33, no. 36, pp. 9232–9238, 2012.

- [11] E. W. Barrera, M. C. Pujol, F. Díaz et al., "Emission properties of hydrothermal Yb^{3+} , Er^{3+} and Yb^{3+} , Tm^{3+} -codoped Lu_2O_3 nanorods: upconversion, cathodoluminescence and assessment of waveguide behavior," *Nanotechnology*, vol. 22, no. 7, Article ID 075205, 2011.
- [12] H. Guo, N. Dong, M. Yin, W. P. Zhang, L. R. Lou, and S. D. Xia, "Visible upconversion in rare earth ion-doped Gd_2O_3 nanocrystals," *Journal of Physical Chemistry B*, vol. 108, no. 50, pp. 19205–19209, 2004.
- [13] H. Guo, Y. F. Li, D. Y. Wang et al., "Blue upconversion of cubic $\text{Gd}_2\text{O}_3:\text{Er}$ produced by green laser," *Journal of Alloys and Compounds*, vol. 376, no. 1-2, pp. 23–27, 2004.
- [14] T. Hirai and T. Orikoshi, "Preparation of $\text{Gd}_2\text{O}_3:\text{Yb}$, Er and $\text{Gd}_2\text{O}_2\text{S}:\text{Yb}$, Er infrared-to-visible conversion phosphor ultra-fine particles using an emulsion liquid membrane system," *Journal of Colloid and Interface Science*, vol. 269, no. 1, pp. 103–108, 2004.
- [15] D. Dosev, I. M. Kennedy, M. Godlewski, I. Gryczynski, K. Tomsia, and E. M. Goldys, "Fluorescence upconversion in Sm-doped Gd_2O_3 ," *Applied Physics Letters*, vol. 88, no. 1, Article ID 011906, 2006.
- [16] L. D. Sun, J. Yao, C. H. Liu, C. S. Liao, and C. H. Yan, "Rare earth activated nanosized oxide phosphors: synthesis and optical properties," *Journal of Luminescence*, vol. 87–89, pp. 447–450, 2000.
- [17] A. Brenier and G. Boulon, "Laser heated pedestal growth and spectroscopic investigations of Nd^{3+} -doped Gd_2O_3 single crystal fibres," *Journal of Luminescence*, vol. 82, no. 4, pp. 285–289, 1999.
- [18] A. Brenier, "Laser-heated pedestal growth of Er^{3+} -doped Gd_2O_3 single crystal fibres and up-conversion processes," *Chemical Physics Letters*, vol. 290, no. 4–6, pp. 329–334, 1998.
- [19] X. Bai, H. W. Song, G. H. Pan et al., "Improved upconversion luminescence properties of $\text{Gd}_2\text{O}_3:\text{Er}^{3+}/\text{Gd}_2\text{O}_3:\text{Yb}^{3+}$ core-shell nanorods," *Journal of Nanoscience and Nanotechnology*, vol. 9, no. 4, pp. 2677–2681, 2009.
- [20] M.-A. Fortin, R. M. P. Petoral Jr., F. Soderlind et al., "Polyethylene glycol-covered ultra-small Gd_2O_3 nanoparticles for positive contrast at 1.5 T magnetic resonance clinical scanning," *Nanotechnology*, vol. 18, no. 39, Article ID 395501, 2007.
- [21] Y. P. Li, J. H. Zhang, Y. S. Luo, X. Zhang, Z. D. Hao, and X. J. Wang, "Color control and white light generation of upconversion luminescence by operating dopant concentrations and pump densities in Yb^{3+} , Er^{3+} and Tm^{3+} tri-doped Lu_2O_3 nanocrystals," *Journal of Materials Chemistry*, vol. 21, no. 9, pp. 2895–2900, 2011.

Research Article

Phase Transition and Optical Properties for Ultrathin KNbO_3 Nanowires

Shulin Yang,¹ Yongming Hu,¹ Shengfu Wang,¹ Haoshuang Gu,¹ and Yu Wang²

¹ Hubei Collaborative Innovation Center for Advanced Organic Chemical Materials, Key Lab of Ferro- & Piezo Materials and Devices of Hubei Province, Faculty of Physics & Electronic Technology, Hubei University, Wuhan 430062, China

² Department of Applied Physics, The Hong Kong Polytechnic University, Hong Kong

Correspondence should be addressed to Yongming Hu; yongming.hu09@gmail.com

Received 28 October 2013; Accepted 7 November 2013

Academic Editor: Danyang Wang

Copyright © 2013 Shulin Yang et al. This is an open access article distributed under the Creative Commons Attribution License, which permits unrestricted use, distribution, and reproduction in any medium, provided the original work is properly cited.

Fascicular KNbO_3 nanowires with tetragonal perovskite structures and ultrasmall diameters are synthesized by hydrothermal route at about 150°C for 24 hours. The concentrations of medium alkalinity have influenced phase structures and the final morphologies of the products significantly by modifying the conditions in process. The as-prepared KNbO_3 nanowires exhibit three phase transitions at about 343, 454.7, and 623 K as the temperature increases from 250 to 700 K. The band gap is about 3.78 eV for KNbO_3 nanowires. Photoluminescence study at room temperature reveals two visible light emission bands peaking at ~ 551 and 597 nm, respectively, which may be due to the oxygen vacancies, site niobium (occupy the location of Nb), and antisite niobium (occupy the location of K) in KNbO_3 nanowires.

1. Introduction

Perovskite-type metallic oxides make a family of materials that share a common crystal structure, analogy to that of the natural crystal calcium titanate, yet exhibit a broad range of interesting physical properties [1]. With the advances in science and technology of integrated ferroelectrics, the size-dependent ferroelectric behaviors become crucial due to the dimensional confinement or the size of ferroelectrics decreasing [2]. 1D nanostructure of ferroelectric materials, such as nanorods, nanowires, and nanotubes, have attracted great attention due to their promising applications, such as miniaturized piezoelectric actuators, medical imaging detectors, and even ferroelectric memories [3, 4]. In recent years, the size-dependent physical properties, such as phase transition, polarizations, and energy band, in ferroelectric nanowires have been evaluated systematically. For instance, Naumov and Fu revealed that both the Curie temperature and the polarization of $\text{Pb}(\text{Zr}_{0.5}\text{Ti}_{0.5})\text{O}_3$ nanowire decreased with the reducing diameter [5]. Spanier et al. reported that phase transition temperature of BaTiO_3 nanowires fell below room

temperature as the diameter was ~ 3 nm [6]. Geneste et al. found that the ferroelectric properties of BaTiO_3 nanowire vanished when the diameter was less than 1.2 nm according to the first principle calculation [7]. However, Morozovska et al. reported that the Curie temperature of ferroelectric nanorods/nanowires could be higher than that of bulk materials from a direct variational method [8]. In addition, the author revealed that there was a blue-green emission for PbTiO_3 nanowires (with diameters of 10~20 nm) both the oxygen vacancies and lead-oxygen vacancy centers may be responsible for this phenomenon [9]. Despite very promising progress in theory, there is inconsistency for phase transition as the diameter of ferroelectric nanowires is decreased. Moreover, few reports have concerned the investigation of the phase transition behavior in experiments.

Potassium niobate (KNbO_3) is one of the most important ferroelectric perovskite oxides, which undergoes successive phase transitions upon cooling from its cubic phase, that is, from cubic to tetragonal at 435°C , tetragonal to orthorhombic at 225°C , and orthorhombic to rhombohedral at -10°C [10, 11]. This material attracts great interests for its multiple

applications, such as optical waveguides, frequency doublers, holographic storage systems, and other technological devices [12–14]. The great potential has stimulated research on the KNbO_3 nanowires. Therefore, the synthesis, phase transition, and optical properties of KNbO_3 nanowires are worth being investigated. Magrez et al. realized the growth of KNbO_3 nanowires with a narrow diameter distribution ~ 60 nm via a hydrothermal route at 150°C from a 38.7 wt% KOH, 0.4 wt% Nb_2O_5 , and 60.9 wt% H_2O mixture [15]. Baier-Saip et al. reported the influence of grain size on the phase transition of ferroelectric KNbO_3 [16]. Wang et al. found that the phase transition of orthorhombic to tetragonal and tetragonal to cubic of KNbO_3 nanorods with diameters of 100–300 nm occurred at lower temperatures than that of bulk counterpart due to finite size or disorder effects [17]. Nakayama et al. developed an electrode-free, continuously tunable coherent visible light source compatible with physiological environments from individual KNbO_3 nanowires, exhibiting efficient second harmonic generation, which could act as frequency converters, allowing the local synthesis of a wide range of colors via sum and difference frequency generations [18]. However, the diameters of the 1D nanostructure synthesized by most of the current routes are much larger than the critical size in ferroelectrics. It is still very challenging to obtain ferroelectric oxide nanowires with extremely small diameters (<10 nm) and a narrow size distribution, especially for niobate oxide. At the same time, the size effects and surface states have important impacts on the lattice distortion in the crystal, which will further result in the changes of the phase transition temperature. Thus, finding a feasible way to overcome those drawbacks discussed ahead is very essential. Herein, KNbO_3 nanowires with ultrathin diameters (down to 5 nm) are synthesized through two step method, that is, milling of raw materials followed by hydrothermal treatment at 150°C for 12 h. In addition, in the phase transition, room temperature photoluminescence properties of KNbO_3 nanowires are also investigated. The studies show that the KNbO_3 nanowires may be a promising candidate for fabricating piezoelectric sensors and other functional devices.

2. Experiments

2.1. Synthesis of KNbO_3 Nanowires. Niobium pentoxide (Nb_2O_5 , 99.95%) and potassium hydroxide (KOH, 95%) were used as raw materials and $\text{C}_{12}\text{H}_{25}\text{OH}$ as surfactant. Figure 1 shows the process illustration of KNbO_3 nanowires through two step hydrothermal method. Firstly, Nb_2O_5 powders of 13.29 g, KOH of 5.89 g, and $\text{C}_{12}\text{H}_{25}\text{OH}$ of 2 g were dispersed in 80 mL $\text{C}_2\text{H}_5\text{OH}$ together. The above mixture was milled at room temperature for 12 hours. Then the obtained precursor was dried by infrared lamp for 12 hours. After that, 20% amount of the above precursor, 20 mL $\text{C}_2\text{H}_5\text{OH}$, and 20 mL H_2O were transferred into the stainless steel autoclave (50 mL). The next step is to add 1.2 g KOH in the above mixture and stir for 30 min. Finally, KNbO_3 nanowires were synthesized after the mix was subjected to further hydrothermal treatment at 150°C for 12 h and cooled to room temperature.

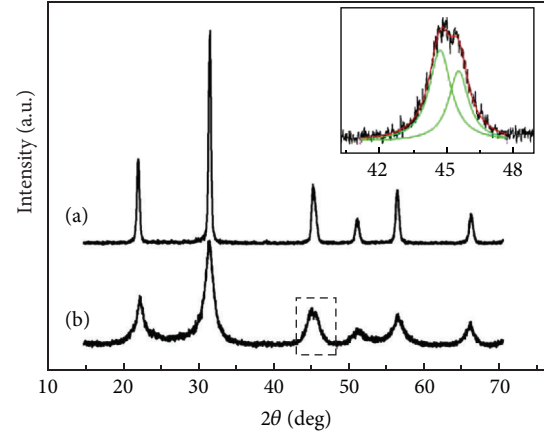


FIGURE 1: XRD patterns of (a) nanoparticles and (b) nanowires of KNbO_3 . Inset: the Lorentz fitting for diffraction peak of KNbO_3 nanowires located at 2θ of $\sim 45^\circ$.

2.2. Characterization of Materials. X-ray diffraction (XRD) measurements were performed on a Bruker AXS-D8-Advance X-ray Diffractometer system using $\text{CuK}\alpha$ ($\lambda = 1.5406 \text{ \AA}$) as the radiation source. Microstructures of the samples were determined on a field-emission scanning electron microscopy (FESEM) JEOL JSM-6700F and transmission electron microscopy (TEM) JEOL 2011 using an acceleration voltage of 200 kV. The phase transition properties of KNbO_3 nanowires were measured using a differential scanning calorimeter (DSC, Perkin-Elmer) in the range of 250 to 700 K at a heating and cooling rate of 10.0 K/min in a nitrogen atmosphere. The UV-vis absorption spectra were measured using Shimadzu UV-2550 spectrophotometer. The fluorescence spectrum of KNbO_3 nanowires was recorded with Edinburgh FLSP920 fluorimeter. Fluorescence intensities were corrected for inner filter effects according to standard methods.

3. Results and Discussions

We have conducted a series of experiments with various concentrations of medium alkalinity, which have significant effects on the phase structures and the final morphologies of the products. We find that KNbO_3 nanoparticles were obtained when the total weight of NaOH reached up to 15 grams, while KNbO_3 nanowires were synthesized as the weight was 7.09 grams during hydrothermal treatment. Figure 1 shows the XRD pattern of KNbO_3 particles (a) and nanowires (b) synthesized by means of hydrothermal method, respectively. One can see that the sharp diffraction peak indicated that KNbO_3 particles have better crystallization than nanowires. All the diffraction peaks of them are well consistent with that of Joint Committee on Powder Diffraction Standards (JCPDS) Cards no. 71-0946 and 71-0946, respectively, illustrating clearly that the samples are composed of KNbO_3 perovskite structure and there is no trace of any impurity phase in the samples. It is noted that KNbO_3 nanoparticles have the orthorhombic structure and KNbO_3 nanowires belong to the tetragonal structure, which

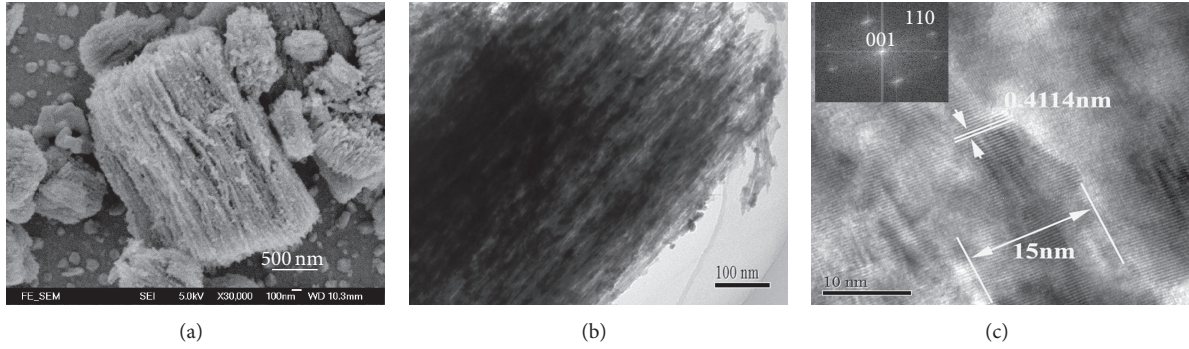


FIGURE 2: (a) SEM image, (b) low magnification TEM image, and (c) HRTEM image of the KNbO_3 nanowires. Inset: SAED pattern of individual nanowires.

can be identified by the splitting peak located at $2\theta \sim 45^\circ$ (shown in the inset in Figure 1). The refined lattice parameters obtained by Curve Fitting software are determined to be $a = 4.0124(3)$ and $c = 4.0456(5)$ Å for KNbO_3 nanowires, while that parameters for nanoparticles are $a = 3.9966(6)$, $b = 5.6535(5)$, and $c = 5.6577(6)$ Å for nanoparticles. At the same time, the strain in the samples has been studied. The consequences imply that the strain in KNbO_3 nanowires is about $33 \pm 2\%$, while it is about $10 \pm 3\%$ for KNbO_3 nanoparticles.

The typical SEM and TEM images of the KNbO_3 nanowires are shown in Figure 2. As can be seen in Figure 2(a), the parallel nanowires are arranged side by side and tend to form the fascicular structure due to the Van der Waals and/or electrostatic attraction force. Almost all of the nanowires grow into regular structure and distribute uniformly in both diameter and length. As demonstrated in Figure 2(b), the TEM image exhibits a large quantity of nanowires with diameters of 5~15 nm and length of up to several micrometers. The HRTEM image in Figure 2(c) shows the lattice fringes of the sample, indicating that the KNbO_3 nanowires are well crystallized and structurally uniform. The adjacent lattice spacing is about 0.4114 nm, corresponding to the (001) lattice plane of KNbO_3 . The SAED pattern (inset of Figure 2(c)), which is indexed by assuming the lattice constants refined from XRD measurements, is obtained from an entire nanowire. The result shows clear diffraction spots characteristic of crystalline KNbO_3 , demonstrating these nanowires are growing along [001] directions.

It is well known that the heat energy released from oxide materials when the phase transition occurs. Thus, differential scanning calorimeter (DSC) technique was selected to reveal the phase transition behavior of KNbO_3 nanowires with diameters of 5~15 nm. Figure 3 shows the DSC curve for KNbO_3 nanowires recorded in the temperature range from 250 to 700 K. It can be seen that the as-prepared nanowires go through three phase transitions at about 623, 454.7, and 343 K, respectively, as the temperature cools from 700 to 250 K. According to the studies in the literature, KNbO_3 crystal undergoes successive ferroelectric transitions upon cooling from its cubic ABO_3 perovskite phase [9]. Therefore, it can be concluded that the structure will transform from cubic to tetragonal when the sample is cooled to 623 K; it

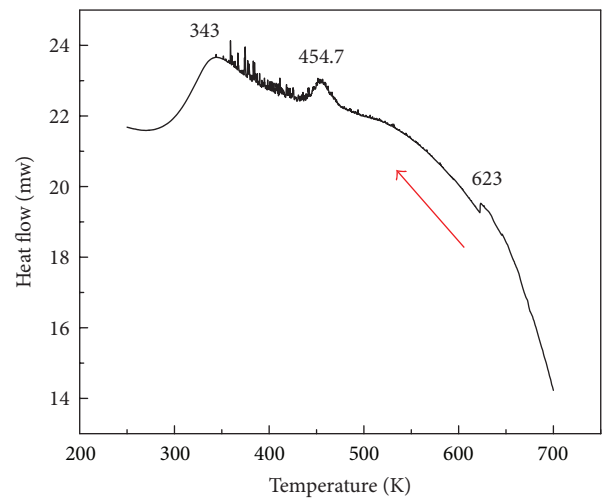


FIGURE 3: DSC curve for KNbO_3 nanowires recorded at the temperature range from 250 to 700 K.

will change to orthorhombic structure as the temperature reaches ~ 454.7 K, and it shows the rhombohedra structure when the sample is below ~ 343 K. However, Gopalan and Raj reported that the phase of the epitaxial KNbO_3 thin films would transform to be $210 \pm 10^\circ\text{C}$ for orthorhombic-tetragonal and $450 \pm 10^\circ\text{C}$ for tetragonal-cubic transitions, which was studied by in situ second harmonic generation measurements. It can be clearly seen that the phase transition temperature of KNbO_3 nanowires is much higher than that of epitaxial KNbO_3 thin films [19]. We consider that the obvious size and surface effect of KNbO_3 nanowires would have significant influences on the lattice distortion and phase transition, which may be also one of the important reasons for the differences discussed ahead.

In the earlier studies, we have found that the morphology of KNbO_3 nanostructures has considerable influences on the onsets of absorption. Figure 4 shows the UV-vis absorption spectrum of KNbO_3 nanowires dispersed in ethanol. It is clear that strong absorption happens as the wavelength is lower than 330 nm, while there is no obvious absorption band in the whole wavelength range (190~900 nm). The band gap of KNbO_3 nanowires is estimated to be 3.78 eV from the

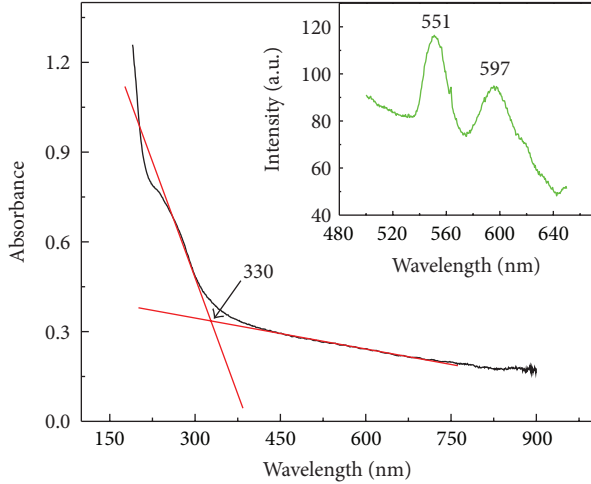


FIGURE 4: UV-vis absorption spectrum of KNbO_3 nanowires, the inset is the room temperature PL spectrum.

onsets of absorption, which is higher than that of KNbO_3 nanocubes with edge sizes of ~ 80 nm (~ 3.14 eV) [20]. The combined action of size and surface effect will result in the obvious blue shift of optical absorption or larger energy gap. The inset in Figure 4 exhibits the room temperature PL spectra of KNbO_3 nanowires excited at wavelengths of 400 nm. A green light emission band located at about 551 nm (2.25 eV) and a yellow light located at 597 nm (2.077 eV) were observed. As mentioned above, the energy gap of KNbO_3 nanowires is about 3.78 eV, which is higher than the excitation energy used in the present work. Therefore, the light emissions observed from 500 to 650 nm are not caused by a direct electron transition between the valence bands to the conduction bands. Similar results have also been found in PbTiO_3 nanowires [8]. It has been reported that oxygen vacancies in oxides would enhance the emission intensities and extend the radiative lifetime of self-trapped excitons. As it is well known, the smaller the diameters of nanowires, the higher the surface to volume ratio, and there is more concentration of surface oxygen vacancies. Fischer et al. have reported that the luminescence of LiNbO_3 can be ascribed to the recombination of the electrons captured by Nb^{5+} ions and holes captured by oxygen in an atomistic model: $\text{Nb}^{4+} + \text{O}^- = \text{Nb}^{5+} + \text{O}^{2-}$, and both the site niobium (occupy the location of Nb) and antisite niobium (occupy the location of Li) are responsible for the main emission in LiNbO_3 [21]. Therefore, the emission bands centered at wavelengths of about 551 and 597 nm would derive from the oxygen vacancies and the site niobium (occupy the location of Nb) and antisite niobium (occupy the location of K), respectively.

4. Conclusions

In conclusion, fascicular KNbO_3 nanowires with perovskite structures and ultrathin diameters of 5~15 nm were synthesized by hydrothermal treatment at low temperature. The KNbO_3 nanowires underwent successive phase transitions upon cooling from its cubic phase, that is, cubic \rightarrow

tetragonal at 623 K, tetragonal \rightarrow orthorhombic at ~ 454.7 K, and orthorhombic \rightarrow rhombohedral at ~ 343 K. The band gap of KNbO_3 nanowires is estimated to be 3.78 eV, which may be caused by the combined action of size effect and quantum size effect. There are two visible light emission peaks located at ~ 551 nm (2.25 eV) and 597 nm (2.077 eV) for KNbO_3 nanowires at room temperature. The oxygen vacancy, the site niobium (occupy the location of Nb), and antisite niobium (occupy the location of K) may have a response for these two emissions.

Acknowledgments

This work was financially supported by the National Science Foundation of China (NSFC) (Grant no. 50902046, and 61274073) and the National High Technology Research and Development Program of China (863 Program) (no. 2013AA031903), and the Youth Chenguang Project of Science and Technology, the Key Project of Science and Technology of Wuhan City, China (Grant no. 201150431133, 201160723217) and the Research Grants Council of Hong Kong (GRF no. PolyU 5309/08E).

References

- [1] Y.-Z. Wang, H. Zhong, X.-M. Li et al., "Electrochemiluminescence study of perovskite-type oxides LaTiO_3 -Ag_{0.1} with $\text{Ru}(\text{bpy})_3^{2+}$ modified electrode," *International Journal of Electrochemical Science*, vol. 8, pp. 1911–1919, 2013.
- [2] R. Grange, J.-W. Choi, C.-L. Hsieh et al., "Lithium niobate nanowires synthesis, optical properties, and manipulation," *Applied Physics Letters*, vol. 95, Article ID 143105, 3 pages, 2009.
- [3] J. Hong and D. Fang, "Size-dependent ferroelectric behaviors of BaTiO_3 nanowires," *Applied Physics Letters*, vol. 92, Article ID 012906, 3 pages, 2008.
- [4] Y. Li, X.-Y. Yang, Y. Feng, Z.-Y. Yuan, and B.-L. Su, "One-dimensional metal oxide nanotubes, nanowires, nanoribbons, and nanorods: synthesis, characterizations, properties and application," *Critical Reviews in Solid State and Materials Sciences*, vol. 37, no. 1, pp. 1–74, 2012.
- [5] I. I. Naumov and H. X. Fu, "Spontaneous polarization in one-dimensional $\text{Pb}(\text{ZrTi})\text{O}_3$ nanowires," *Physical Review Letters*, vol. 95, no. 24, Article ID 247602, 4 pages, 2005.
- [6] J. E. Spanier, A. M. Kolpak, J. J. Urban et al., "Ferroelectric phase transition in individual single-crystalline BaTiO_3 nanowires," *Nano Letters*, vol. 6, no. 4, pp. 735–739, 2006.
- [7] G. Geneste, E. Bousquet, J. Junquera, and P. Ghosez, "Finite-size effects in BaTiO_3 nanowires," *Applied Physics Letters*, vol. 88, Article ID 112906, 2006.
- [8] A. N. Morozovska, E. A. Eliseev, and M. D. Glinchuk, "Ferroelectricity enhancement in confined nanorods: direct variational method," *Physical Review B*, vol. 73, no. 21, Article ID 214106, 13 pages, 2006.
- [9] Y. Hu, H. Gu, X. Sun, J. You, and J. Wang, "Photoluminescence and Raman scattering studies on PbTiO_3 nanowires fabricated by hydrothermal method at low temperature," *Applied Physics Letters*, vol. 88, Article ID 193120, 2006.
- [10] C.-H. Wen, S.-Y. Chu, Y.-D. Juang, and C.-K. Wen, "New phase transition of erbium-doped KNbO_3 polycrystalline," *Journal of Crystal Growth*, vol. 280, no. 1-2, pp. 179–184, 2005.

- [11] Y. Lin, X. Chen, S. W. Liu et al., "Epitaxial nature and anisotropic dielectric properties of (Pb,Sr)TiO₃ thin films on NdGaO₃ substrates," *Applied Physics Letters*, vol. 86, Article ID 142902, 2005.
- [12] L. Goldberg, L. Busse, and D. Mehusy, "Blue light generation by frequency doubling of AlGaAs broad area amplifier emission," *Applied Physics Letters*, vol. 60, no. 9, pp. 1037–1039, 1992.
- [13] J. -S. Lee, Y. Li, Y. Lin, S. Y. Lee, and Q. X. Jia, "Hydrogen-induced degradation in epitaxial and polycrystalline (Ba,Sr)TiO₃ thin films," *Applied Physics Letters*, vol. 84, no. 19, pp. 3825–3827, 2004.
- [14] Q. X. Jia, B. Maiorov, H. Wang et al., "Comparative study of REBa₂Cu₃O₇ films for coated conductors," *IEEE Transactions on Applied Superconductivity*, vol. 15, no. 2, pp. 2723–2726, 2005.
- [15] A. Magrez, E. Vasco, J. W. Seo, C. Dicker, N. Setter, and L. Forró, "Growth of single-crystalline KNbO₃ nanostructures," *Journal of Physical Chemistry B*, vol. 110, no. 1, pp. 58–61, 2006.
- [16] J. A. Baier-Saip, E. Ramos-Moor, and A. L. Cabrera, "Raman study of phase transitions in KNbO₃," *Solid State Communications*, vol. 135, no. 6, pp. 367–372, 2005.
- [17] G. Z. Wang, S. M. Selbach, Y. Yu, X. Zhang, T. Grande, and M.-A. Einarsrud, "Hydrothermal synthesis and characterization of KNbO₃ nanorods," *CrystEngComm*, vol. 11, no. 9, pp. 1958–1963, 2009.
- [18] Y. Nakayama, P. J. Pauzauskie, A. Radenovic et al., "Tunable nanowire nonlinear optical probe," *Nature*, vol. 447, pp. 1098–1101, 2007.
- [19] V. Gopalan and R. Raj, "Domain structure and phase transitions in epitaxial KNbO₃ thin films studied by *in situ* second harmonic generation measurements," *Applied Physics Letters*, vol. 68, no. 10, pp. 1323–1325, 1996.
- [20] J. W. Liu, G. Chen, Z. H. Li, and Z. G. Zhang, "Hydrothermal synthesis and photocatalytic properties of ATaO₃ and ANbO₃ (A = Na and K)," *International Journal of Hydrogen Energy*, vol. 32, no. 13, pp. 2269–2272, 2007.
- [21] C. Fischer, M. Wohlecke, T. Volk, and N. Rubinina, "Influence of the damage resistant impurities Zn and Mg on the UV-excited luminescence in LiNbO₃," *Physica Status Solidi A*, vol. 137, no. 1, pp. 247–255, 1993.

Research Article

Simulation and Analysis of GaN Wafer Bowing on Sapphire Substrate

Wang Bin,¹ Qu Yu-xuan,² Hu Shi-gang,³ Tang Zhi-jun,³ Li Jin,³ and Hu Ying-lu⁴

¹ *The Center of Coordination and Support of State Administration of Science, Technology and Industry for National Defence, Beijing 100081, China*

² *Advanced Technology Generalization Institute of CNGC, Beijing 100089, China*

³ *School of Information and Electrical Engineering, Hunan University of Science and Technology, Xiangtan 411201, China*

⁴ *The 41st Institute of China Electronics Technology Group Corporation, Qingdao 266555, China*

Correspondence should be addressed to Hu Shi-gang; hsg99528@126.com

Received 17 June 2013; Accepted 14 August 2013

Academic Editor: Jianhua Hao

Copyright © 2013 Wang Bin et al. This is an open access article distributed under the Creative Commons Attribution License, which permits unrestricted use, distribution, and reproduction in any medium, provided the original work is properly cited.

During the process of heteroepitaxial growth, if the lattice constant of the growing film differs from that of the substrate, the wafer surface bows, regardless of whether the lattice mismatch occurs or not. As the growth in large-scale wafers speeds up, bowing effects are becoming more and more important. Wafer bowing has a direct impact on the yield in modern mass-production compound semiconductor industries. By using finite element analysis software, the bowing deformation of the GaN wafer on sapphire substrate can be studied. This paper summarizes the causes of bowing deformation, builds the mathematical model, and deduces the relation equation of the wafer bowing. The results show that epitaxial wafer bowing has a linear relationship with the square of the diameter of the substrate but has little relationship with the thickness of the substrate. Moreover, the relation equation of the wafer bowing is also simplified finally.

1. Introduction

Using MOCVD (metal-organic chemical vapor deposition) to analyze the growth of GaN-base photoelectric devices on the sapphire substrate is a common method in the semiconductor lighting industry [1–5]. In recent years, along with the unceasing enhancement of epitaxy technology and related technologies, larger sapphire substrates are needed. The optimization and improvement of MOCVD reaction chamber structure with large-scale epitaxial wafers have been studied by many domestic researchers [6–10]. Li et al. [11, 12] optimized high-frequency heating graphite base groove structure with eight-inch and twelve-inch substrates. Ying-lu et al. [13] studied the heating modulate curve of radiation heating MOCVD and proposed the design principles of the outer heater. To improve the production efficiency, some great MOCVD manufacturers also focus on how to improve and increase the MOCVD cavity and the sapphire substrate size in foreign countries. At present, two-inch and four-inch

epitaxial wafers are frequently used, so manufacturers who can produce six-inch SiC and Si substrate epitaxial wafers with high quality in foreign countries would sell chips abroad [14, 15].

With the growth of the III-nitrides, sapphire becomes the most extensively used substrate material [16]. Crystals of sapphire with good quality and low price can be easily got. Besides, sapphire is stable at high temperature and the growth technology of nitrides on sapphire is now fairly mature. However, the problem of wafer bowing, which results from the difference in thermal expansion coefficient between GaN epitaxial layer and sapphire, has become much more serious in larger-diameter wafers. It will deteriorate the contact between the substrates and the equipment stages or the subsectors during device process, which will result in degradation in the device uniformity or failures in lithography.

By using finite element simulation software, the relationship between the maximum wafer bowing and sapphire substrate size under characteristic temperature is studied in

the case of the growth of GaN in the sapphire substrate, and the wafer bowing relation equation is also deduced. The research work in this paper plays a foreshadowing role for later research sapphire epitaxial growth and MOCVD reaction chamber structure improvement.

2. Bowing Causes and Mathematical Model

2.1. Bowing Causes. The MOCVD growth process can be divided into four phases: a reactant input phase, a reactant mixing phase, an immediate boundary layer phase above the substrate, and the growth phase on the substrate surface itself. Growth complications that can occur in these phases include gas phase reactions during reactant mixing, reactant diffusion and/or pyrolysis in the boundary layer above the substrate, and thermodynamic or kinetic rejection of species from the substrate. The worst effects can be reduced or eliminated by providing appropriate equipment design and process conditions [17].

As shown in Figure 1, MOCVD growth system is composed of four parts including gas handle system, reactor, computer control, and vacuum and exhaust system.

The stress in the films often results from epitaxy in the growth processes and from thermal expansion coefficient (TEC) mismatch in the postgrowth processes of both metal-organic chemical vapor deposition and hydride vapor phase epitaxy. For example, the stress typically observed is dominated by thermal stress in the post-growth processes, which is usually considered to bring defects or damage to the films, such as, dislocation, buckling, and cracking. Cracks normally extend to the principal tensile stresses within the thin brittle layers and interact with the interfaces of GaN/sapphire. Due to the mismatch of TECs between the GaN film and sapphire, wafer bowing will occur when the GaN film is mechanically constrained by the sapphire after cooling. Thermal stress, wafer bending, and cracking are the main drawbacks that hamper the production of large-area GaN substrates and the application of GaN films. Wafer bowing and stress concentration significantly influence not only the devices' mechanical performance but also their optical, electrical, and magnetic properties. Therefore, reducing wafer bowing and stress concentration in GaN films is very important. To the best of our knowledge, there are no feasible methods for reducing GaN wafer bowing and few papers on wafer bowing have been published.

When GaN is grown on the sapphire substrate using MOCVD, bowing will happen in epitaxial wafers. There are three major factors for the wafer bowing. One is the temperature difference between the upper and lower interfaces of epitaxial wafers. The lower surface temperature is higher than that of the upper surface, so that the expansion of the lower surface can be larger than that of the upper surface, causing the epitaxial wafers concave. Another is the lattice mismatch between sapphire substrate and epitaxial material, which makes the sapphire suffer from tensile and compressive stress and produces concave or convex bowing. The third is thermal mismatch between epitaxial material and

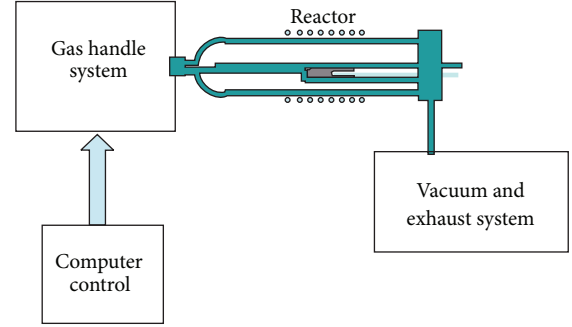


FIGURE 1: Schematic representation of MOCVD growth system.

the sapphire substrate, which occurs mainly in the case of a sudden jump or a sudden drop of the outside temperature.

2.2. Mathematical Model. This paper mainly studies the maximum bowing situation in the growth process. Since the epitaxial layer is much thinner than the sapphire substrate, considering the changes of temperature difference due to lattice mismatch and epitaxial layer heat transfer, the upper surface of epitaxial wafer is approximated to the thermal radiation condition of GaN. Since the condition is steady state, the thermal mismatch between epitaxial materials and sapphire substrate can be ignored. Therefore, the bowing of GaN epitaxial wafer with sapphire substrate is mainly due to the temperature difference between the upper and lower interfaces in this paper.

The solid lattice conforms to the Grüneisen lattice state equation generally:

$$P = -\frac{dE_0}{dV} + \gamma \frac{E_L}{V}. \quad (1)$$

The first item is known as static pressure, and the second item is called thermal pressure, where E_0 is a function of the crystal volume V , E_L is the average lattice vibration at the temperature T , and γ is called Grüneisen constant

$$E_L = \sum_j \left(\frac{1}{2} \hbar \omega_j + \frac{\hbar \omega_j}{e^{\hbar \omega_j / k_B T} - 1} \right), \quad (2)$$

$$\gamma = -\frac{d \ln \omega}{d \ln V}.$$

Solid thermal expansion refers to the change of volume along with temperature in the case without pressure. Making $P = 0$, we can get

$$\frac{dE_0}{dV} = \gamma \frac{E_L}{V}. \quad (3)$$

Because the change of volume is not big during general thermal expansion, dE_0/dV can be expanded near the lattice volume V_0 , and only one degree term of $\Delta V = V - V_0$ is retained, we can get

$$\frac{dE_0}{dV} = \left(\frac{dE_0}{dV} \right)_{V_0} + \left(\frac{d^2 E_0}{dV^2} \right)_{V_0} \Delta V. \quad (4)$$

Considering that the first term is equal to 0 and the definition of bulk modulus, then

$$K_0 = V_0 \left(\frac{d^2 E_0}{dV^2} \right) V_0, \quad \frac{dE_0}{dV} = K_0 \frac{\Delta V}{V_0}. \quad (5)$$

Substituting formula (3), we can get

$$\frac{\Delta V}{V_0} = \gamma \frac{E_L}{K_0 V}. \quad (6)$$

Solving the derivative of the formula above with respect to temperature and using the definition of heat capacity $C_V = \partial E_L / \partial T$, the volumetric thermal expansion coefficient is obtained:

$$\alpha = \gamma \frac{C_V}{K_0 V}. \quad (7)$$

For the solid material, the Grüneisen constants are between 1 and 2 generally. Assuming that the entire heat capacity of the graphite disc is the same, as well as the small temperature difference between the upper and lower surfaces of the epitaxial wafer, the thermal expansion of epitaxial wafer can be approximated as a linear expansion.

Without affecting the main results, the temperature of the lower surface of epitaxial wafer is set to the constant temperature 1220 K, which is close to the actual temperature. Assuming that the sapphire substrate is isotropic in a plane, its deformation meets the equation of thermal expansion:

$$L = \alpha L_0 (T - T_0) \quad (8)$$

L_0 and L are the amounts before and after the expansion, respectively, α is the coefficient of thermal expansion, and T_0 is the reference temperature.

Epitaxial wafer deformation models and geometrical parameter identification are shown in Figure 2. R is sapphire substrate radius size, d is the thickness of the epitaxial wafer, and B is the highest bowing degree of epitaxial wafer.

It is assumed that the bowing of the epitaxial wafer is caused by the different degrees of thermal expansion due to the average temperature difference between the upper and lower surfaces of the sapphire. As shown in Figure 3, we have set thermal expansion coefficient of sapphire for α , average temperature of the upper surface for T_1 , the average temperature of the lower surface for T_2 , reference temperature T_0 , radian formed by sapphire bowing for θ , and cambered radius of the upper surface for r .

By the law of thermal expansion and the geometric relationship, it can be got that

$$\begin{aligned} \alpha R (T_1 - T_0) &= \theta r, \\ \alpha R (T_2 - T_0) &= \theta (r + d). \end{aligned} \quad (9)$$

Deformation is quite slimly relative to the substrate size, so the angle θ is very small:

$$\frac{1}{2} \theta \approx \frac{1}{2} \tan \theta \approx \frac{B}{R}. \quad (10)$$

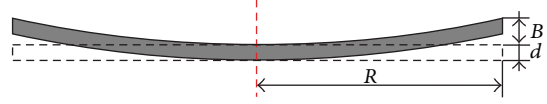


FIGURE 2: Epitaxial wafer model.

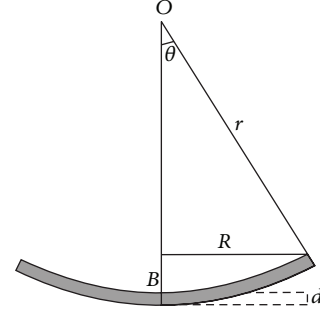


FIGURE 3: Epitaxial wafer bowing deformation schematic diagram.

Let $\Delta T = T_2 - T_1$; then it can be derived that

$$B \approx \frac{1}{2} \alpha R^2 \frac{\Delta T}{d}. \quad (11)$$

As can be seen from the above derivation, the maximum bowing is proportional to the square of the epitaxial wafer substrate radius, and the temperature difference between the upper and lower surfaces of epitaxial wafers is inversely proportional to the thickness of the epitaxial wafers.

3. Simulation Results and Analysis

3.1. Influence of Sapphire Size on the Deformation. To observe the bowing with the same thickness of 500 nm, the diameters of the sapphire substrate 2R with two inches, four inches, six inches, and eight inches were compared. The simulation results are shown in Figure 4.

With the increase of size, the degree of bowing is also growing. When the diameter of the substrate is eight inches, its bowing has reached nearly 500 nm, similar to the thickness of the epitaxial wafers of sapphire substrate, which can lead to the rejection of disk accident. It is obviously one of the main problems needed to be solved when large-area sapphire substrate is epitaxial. As shown in Figure 5, the bowing amount and the square of sapphire diameter (radius) are seen in a roughly linear relationship; that is to say, $B \approx AR^2$, where A is a constant.

3.2. Influence of the Thickness of Sapphire Size on the Deformation. Under the same heating condition, we researched the bowing degree of several four-inch substrates of which the thickness is 300 nm, 400 nm, 500 nm, and 600 nm, respectively. It can be seen in Figure 6, in the case of different thicknesses, the degree of the bowing only changes by a few nanometers, which can be neglected, that is, the thickness has less influence on the bowing.

There are a few differences between this conclusion and the above theoretical result. It is considered that the temperature difference between the upper and lower substrate

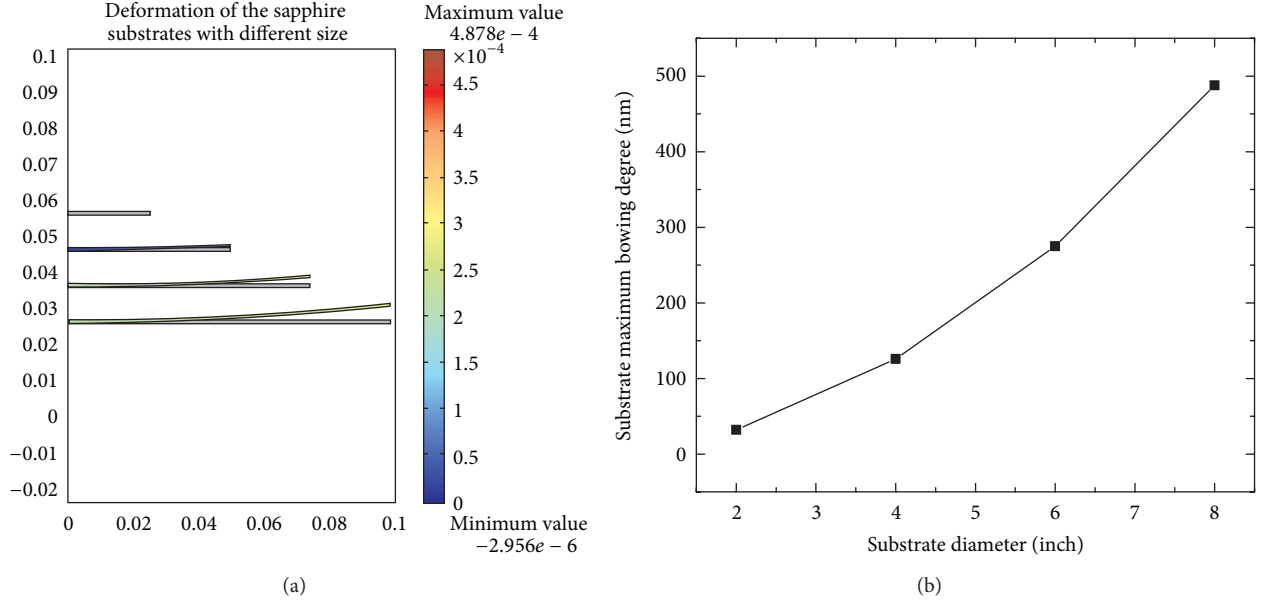


FIGURE 4: Simulation results of bowing amount of different size substrate (a) deformation of sapphire substrate with different sizes (10 times effect), (b) relation curve of maximum amount of bowing and substrate diameter.

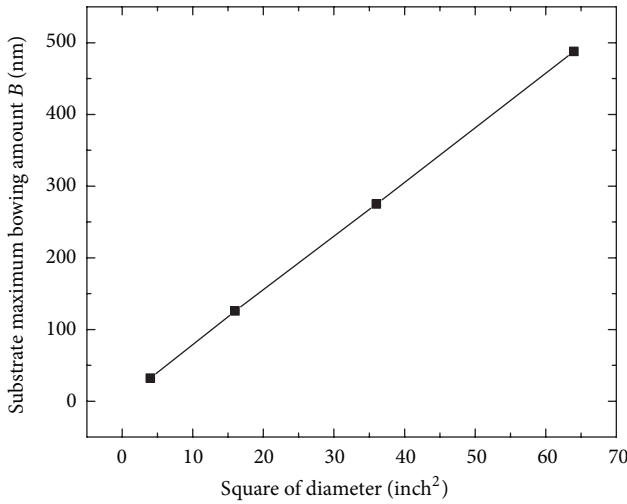


FIGURE 5: The linear relationship between the bowing amount and the square of sapphire diameter.

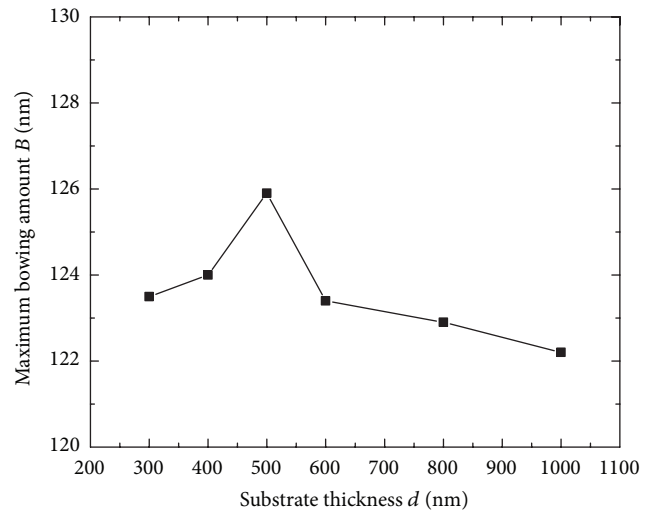


FIGURE 6: Bowing with different substrate thicknesses.

surfaces also changes. The average temperature difference between the upper and lower surfaces is calculated, and its relationship with the thickness d of the substrate is shown as in Figure 7. A roughly linear relationship can be seen between the two; that is, $\Delta T/d \approx C$. The result shows that the thickness of the substrate is the main reason for the temperature difference between the upper and lower substrate surfaces, and generally there is a direct proportion linear relationship between them. Based on formula (11), to further simplify the result, we can get

$$B \approx \frac{1}{2} \alpha R^2 \frac{\Delta T}{d} = \frac{1}{2} \alpha R^2 C = \left(\frac{1}{2} \alpha C \right) R^2 = AR^2. \quad (12)$$

4. Conclusions

The bowing of epitaxial wafer is the main reason leading to plate deformation and is also one of the major difficulties in the growth of large-size epitaxial wafer; the degree of bowing can influence the uniformity of surface temperature field and flow field. In this paper, through the simulation and mathematical derivation, the bowing deformation of the GaN wafer on sapphire substrate is studied in detail. It is found that the epitaxial wafer bowing has a linear relationship with the square of the diameter of the substrate. Within a certain range, there is little relationship between the degree of bowing of the epitaxial wafer and its thickness. This is

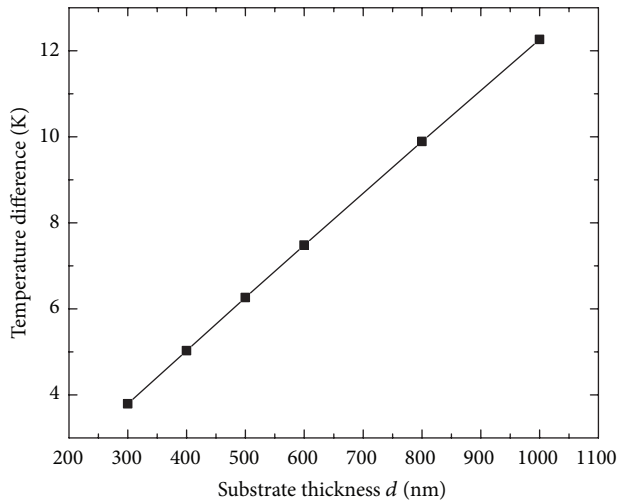


FIGURE 7: Relationship between substrate thickness and surface temperature difference.

due to the direct proportion linear relationship between the temperature difference of the upper and lower surfaces and thickness. The mathematical derivation demonstrates that the epitaxial wafer bowing amount can be represented by using the formula $B \approx (1/2)\alpha(\Delta T/d)R^2$. Under normal circumstances, $\Delta T/d$ is approximately constant.

Acknowledgment

This project is supported by the National Natural Science Foundation of China (Grant nos. 61376076, 61274077, 61274026, and 61377024); the Science and Technology Plan Foundation of Hunan Province (Grant nos. 2013FJ2011 and 2013FJ4232); the Scientific Research Fund of Hunan Provincial Education Department (Grant nos. 12C0108 and 13C321).

References

- [1] J. Xue, J. Zhang, Y. Hou, H. Zhou, J. Zhang, and Y. Hao, "Pulsed metal organic chemical vapor deposition of nearly latticed-matched InAlN/GaN/InAlN/GaN double-channel high electron mobility transistors," *Applied Physics Letters*, vol. 100, no. 1, Article ID 013507, 2012.
- [2] Y. Lianqiao, C. Zunmiao, Z. Jianhua, and A. G. Li, "Transport phenomena in a novel large MOCVD reactor for epitaxial growth of GaN thin films," *IEEE Transactions on Semiconductor Manufacturing*, vol. 25, no. 1, pp. 16–18, 2012.
- [3] Z.-Q. Cheng, S. Hu, W.-J. Zhou, and J. Liu, "Effect of composited-layer AlyGal-yN on performances of AlGaN/GaN HEMT with unintentionally doping barrier AlxGa 1-xN," *Microwave and Optical Technology Letters*, vol. 53, no. 6, pp. 1206–1209, 2011.
- [4] Z.-Q. Cheng, S. Hu, J. Liu, and Q.-J. Zhang, "Novel model of a AlGaN/GaN high electron mobility transistor based on an artificial neural network," *Chinese Physics B*, vol. 20, no. 3, Article ID 036106, 2011.
- [5] H. O. Li, C. W. Tang, K. J. Chen, and K. M. Lau, "Metamorphic InAlAs/InGaAs HEMTs on GaAs substrates grown by MOCVD," *Electron Device Letters*, vol. 29, no. 6, pp. 561–564, 2008.
- [6] M. H. Lo, P. M. Tu, C. H. Wang et al., "High efficiency light emitting diode with anisotropically etched GaN-sapphire interface," *Applied Physics Letters*, vol. 95, no. 4, Article ID 041109, 2009.
- [7] Y. J. Lee, J. M. Hwang, T. C. Hsu et al., "Enhancing the output power of GaN-based LEDs grown on wet-etched patterned sapphire substrates," *IEEE Photonics Technology Letters*, vol. 18, no. 10, pp. 1152–1154, 2006.
- [8] T. Tao, Z. Zhang, L. Liu et al., "Surface morphology and composition studies in InGaN/GaN film grown by MOCVD," *Journal of Semiconductors*, vol. 32, no. 8, Article ID 083002, 2011.
- [9] Y. Wang, J. Li, S. Li, H. Chen, D. Liu, and J. Kang, "X-ray reflectivity and atomic force microscopy studies of MOCVD grown AlxGal-xN/GaN superlattice structures," *Journal of Semiconductors*, vol. 32, no. 4, Article ID 043006, 2011.
- [10] Y. Liu, H. Chen, and S. Fu, "CFD simulation of flow patterns in GaN-MOCVD reactor," *Chinese Journal of Semiconductors*, vol. 25, no. 12, pp. 1639–1646, 2004.
- [11] Z. M. Li, S. R. Xu, J. C. Zhang et al., "Finite Element Analysis of the Temperature Field in a Vertical MOCVD Reactor by Induction Heating," *Journal of Semiconductors*, vol. 33, no. 11, Article ID 113004, 5 pages, 2009.
- [12] Z. M. Li, Y. Hao, J. C. Zhang et al., "Thermal transportation simulation of a susceptor structure with ring groove for the vertical MOCVD reactor," *Journal of Crystal Growth*, vol. 311, no. 23–24, pp. 4679–4684, 2009.
- [13] H. Ying-lu, L. Pei-xian, L. Zhi-ming et al., "Simulation and analysis of temperature modulate curve in MOCVD with the chipped infrared heating system," *Electronic Science and Technology*, vol. 25, no. 1, pp. 108–111, 2012.
- [14] S.-Q. Zhong, X.-M. Ren, Q. Wang et al., "Numerical simulation of flow and temperature field in MOCVD reactor," *Journal of Synthetic Crystals*, vol. 37, no. 6, pp. 1342–1348, 2008.
- [15] S. R. Xu, Y. Hao, J. C. Zhang et al., "Yellow luminescence of polar and nonpolar gan nanowires on r-plane sapphire by metal organic chemical vapor deposition," *Nano Letters*, vol. 13, pp. 3654–3657, 2013.
- [16] Q. Xu, R. Zuo, and H. Zhang, "Design and simulation of reverse-flow showerhead MOCVD reactors," *Journal of Synthetic Crystals*, vol. 34, no. 6, pp. 1059–1064, 2005.
- [17] G.-B. Wang, R. Zuo, Q. Xu, H. Li, H.-Q. Yu, and J.-S. Chen, "Design and numerical simulation of MOCVD reactor with tangential inlets," *Journal of Synthetic Crystals*, vol. 39, no. 1, pp. 267–271, 2010.

Research Article

Effect of Annealing Temperature on the Morphology and Piezoresponse Characterisation of Poly(vinylidene fluoride-trifluoroethylene) Films via Scanning Probe Microscopy

K. Lau,¹ Y. Liu,¹ H. Chen,² and R. L. Withers¹

¹ Research School of Chemistry, The Australian National University, Canberra, ACT 0200, Australia

² Centre for Advanced Microscopy, The Australian National University, Canberra, ACT 0200, Australia

Correspondence should be addressed to K. Lau; ktslau@rsc.anu.edu.au and Y. Liu; yliu@rsc.anu.edu.au

Received 6 June 2013; Accepted 30 September 2013

Academic Editor: Jianhua Hao

Copyright © 2013 K. Lau et al. This is an open access article distributed under the Creative Commons Attribution License, which permits unrestricted use, distribution, and reproduction in any medium, provided the original work is properly cited.

Poly(vinylidene fluoride-trifluoroethylene) (PVDF-TrFE (70/30)) films were synthesized on a gold/glass substrate via spin coating. The films were annealed at a temperature between 125°C and 180°C. Nanoscale characterisation of the morphology, polarization switching, and local piezoresponse hysteresis loops of PVDF-TrFE film was studied using a scanning probe microscope (SPM). Ferroelectric switchable domains were identified by piezoresponse force microscopy (PFM) for all films. Small grains, with weak piezoresponse character, were observed for films annealed just above the Curie temperature. Acicular grains were obtained when the annealing temperature approached the melting point and the piezoresponse increased. Annealing above the melting point decreased the piezoresponse and the morphology changed dramatically into plate-like structures.

1. Introduction

Poly(vinylidene fluoride) (PVDF) and its copolymers, especially with trifluoroethylene (TrFE), are organic ferroelectric polymers that have been extensively studied due to their application in diverse fields such as high performance actuators [1], nonvolatile memory devices [2], energy harvesters [3], and artificial organs [4]. This broad spectrum of applications is due to the large remnant polarization, short switching time, low processing temperature, chemical stability, and excellent electromechanical properties [5]. These polymers can crystallise into four different phases: β , α , γ , and δ [5]. Only the β phase is ferroelectric. It consists of an all *trans* configuration. The dominant phase can be controlled by manipulating the deposition method, thermal treatment, or mechanical treatment of the polymer [5]. Alternatively, the addition of trifluoroethylene within the range of 10–50% increases and stabilizes the β phase [6].

One disadvantage in the applications of PVDF-TrFE is the high coercive field of approximately 50 MV m⁻¹ [7]. Thus,

in order to facilitate the development of devices with low operating voltages, PVDF-TrFE films with thickness less than 100 nm are necessary. Such films are commonly prepared by spin coating [8] or Langmuir-Blodgett technique [9].

The ferroelectric properties of PVDF-TrFE are determined by its crystallinity. Crystallinity is usually increased by annealing PVDF-TrFE copolymers between the Curie temperature (110°C) and melting temperature (150°C) [10]. Macroscopic polarization voltage hysteresis loops for films annealed between 120 and 155°C demonstrate optimal remnant polarization for films annealed at 140°C [11]. However, the recrystallization behaviour of PVDF-TrFE copolymers annealed above the melting point is not as well understood. Li et al. [12] have shown that the morphology of PVDF-TrFE films changes dramatically if it is annealed above the melting temperature while the structure is invariant. However, this morphology depends on the thickness of the sample. For 5 μ m thick films, acicular grains are produced while for 30 nm thick samples, nanomesa morphology is obtained. Zeng et al. [11] demonstrated that films above the melting

point retain ferroelectric character. Recently, piezoresponse force microscopy is used for nanoscale characterisation of ferroelectric domains and polarization related processes in PVDF-TrFE films annealed below the melting point [13, 14]. In this work, nanoscale characterisation of the morphology, polarization switching, and local piezoresponse hysteresis loops for PVDF-TrFE films annealed within the range 125 to 180°C is presented. This temperature range spans from above the Curie temperature to above the melting point.

2. Experimental

PVDF-TrFE (70/30 mol%) powder (Piezotech) was dissolved in butan-2-one without further purification to obtain a solution with 1 wt% concentration. The solution was then spin-coated onto an Au sputtered glass slide. As-deposited PVDF-TrFE was removed from the substrate and pressed into a pellet for differential scanning calorimetry (DSC) characterisation. The heating rate for the DSC measurement was 5°C/minute while the cooling rate was 3°C/min. The film was annealed at 125°C, 150°C, or 180°C for 4 hours in an oven and then allowed to cool to room temperature. Surface topography, piezoresponse image, and switching spectroscopy were performed with a commercial atomic force microscope (Cypher, Asylum Research) under ambient conditions with platinum coated silicon probes (spring constant ~2 N/m, tip radius ~28 nm). Surface roughness was determined by Igor Pro. To verify the presence of polarization switchable domains within the film, after the background poling of the film by applying +20 V bias to the AFM tip, a smaller square was poled in the opposite direction at a bias of -15 V. The thickness of the as-deposited films was about 70 nm as determined by AFM. Piezoresponse loops were obtained by superimposing a 0.5 Hz triangular square step wave on a 300 kHz ac signal with bias window up to ±30 V.

3. Results and Discussion

Consistent with previous reports [16, 17], from the DSC of as-deposited PVDF-TrFE, the Curie temperature is observed at 111°C upon heating (T_{C1}) and around 68°C upon cooling (T_{C2}). The melting and crystallization temperature are at 152°C and 142°C, respectively (Figure 1). PVDF-TrFE films are generally annealed between the Curie and melting temperature because the chain mobility is higher in the paraelectric phase as compared to the ferroelectric phase [16]. Moreover, chain mobility increases as a function of temperature [18]. A higher chain mobility favours the lowest energy conformation (all *trans*) thereby increasing its ferroelectric character [5]. In this work, the annealing temperatures are at 125°C, 150°C, and 180°C. The film annealed at 125°C has the lowest chain mobility so the degree of crystallization is expected to be low. The degree of crystallinity of the film annealed at 150°C is higher due to the higher annealing temperature. Chain mobility in the film annealed at 180°C is the highest, however, it will be recrystallized as it cools to room temperature. The degree of crystallinity, chain mobility, and whether recrystallization takes place are likely to affect the

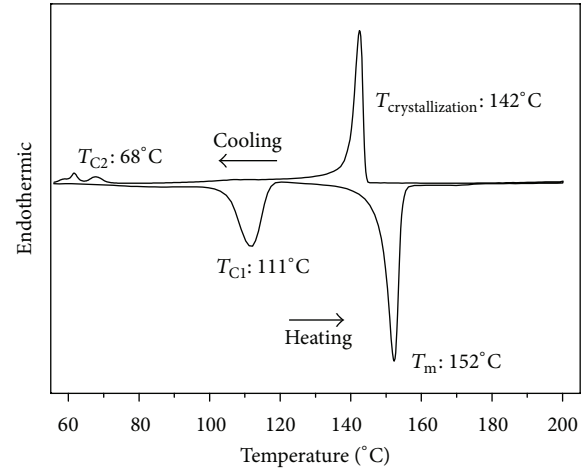


FIGURE 1: DSC curve for as-deposited PVDF-TrFE (70/30 mol%).

morphology, polarization switching, and local piezoresponse hysteresis loops.

The AFM images of the resulting film after annealing at different temperatures are shown in Figures 2(a)–2(c). After annealing at 125°C, the grains are relatively small with an average length of 130 nm and 70 nm diameter. As the annealing temperature is increased to 150°C, the grains coalesce and acicular grains are obtained with an average length of 1.5 μm and diameter of 160 nm. There is a concomitant increase in surface roughness. The surface roughness is 3.3 nm and 12.7 nm, respectively, for the film annealed at 125°C and 150°C. This is in agreement with works by other authors [12, 19, 20]. In the needle like grains, the molecular chains are preferentially oriented parallel to the substrate in lamellar crystals which are perpendicular to the substrate (Figure 3(a)) [7, 15]. These edge-on lamellae form acicular grains. Above the melting point, the morphology changes drastically due to the melting and recrystallization of the film. In this situation, the chain axis is dominantly normal to the surface, and the crystalline lamellae stack on top of one another resulting in a relatively smooth topography (Figure 3(b)) [15]. The surface roughness is 6.3 nm.

In the PFM phase image (Figures 2(d)–2(f)), purple regions correspond to a c^- domain (polarization antiparallel to surface normal), and yellow regions correspond to a c^+ domain (polarization parallel to surface normal). Polarization switchable domains are present in the PVDF-TrFE films, regardless of the annealing temperature, as a smaller square of opposite polarization can be poled at -15 V after background poling at +20 V. The quality of the pattern appears to be optimum for the film annealed at 150°C. This is probably due to its high degree of crystallinity and low number of defects [12]. The irregularities in the film annealed at 125°C are presumably due to its lower degree of crystallinity [11]. Similarly, the lower crystallinity of films annealed at 180°C [11] affects the quality of the switching.

A comparison of typical local piezoresponse loops for a single point obtained from PFM for PVDF-TrFE films annealed at different temperatures is presented in Figure 4. The loops are slightly shifted to a negative voltage. This is

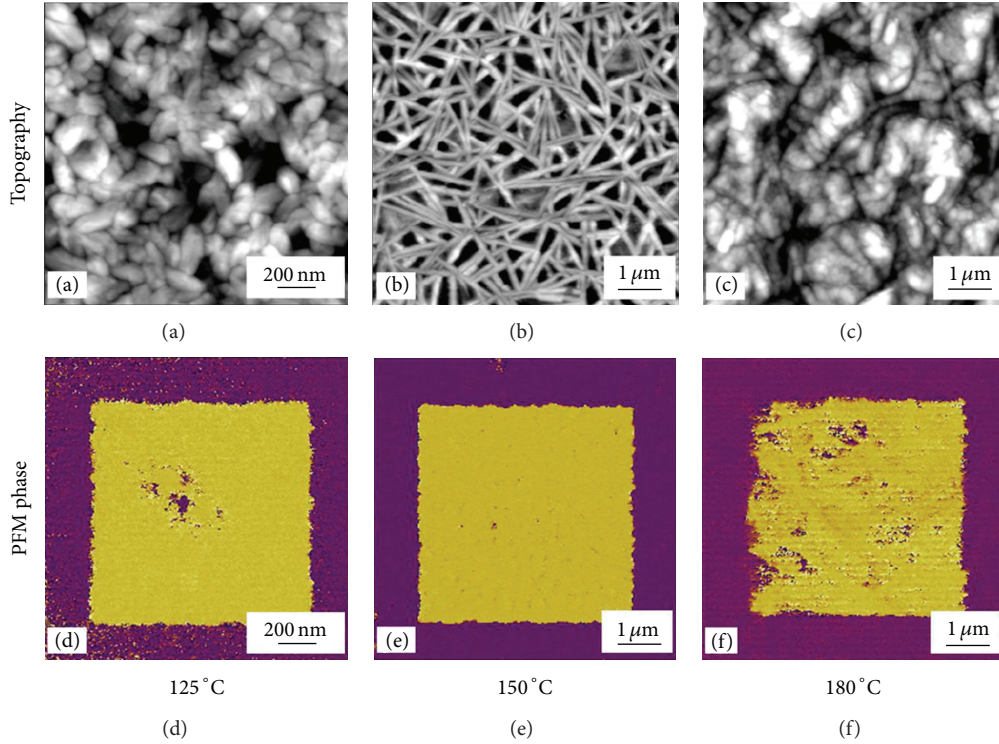


FIGURE 2: Surface topography obtained by AFM for films annealed at (a) 125°C, (b) 150°C, and (c) 180°C. White regions are higher than black regions. The scan size is (a) $1 \times 1 \mu\text{m}$ and (b), (c) $5 \times 5 \mu\text{m}$. The black to white contrast is (a) 12 nm, (b) 50 nm, and (c) 30 nm. (d), (e), and (f) PFM phase image of the corresponding area after background poling at +20 V tip bias followed by a poling of a smaller square at -15 V tip bias. c^- domains are purple, and c^+ domains are yellow.

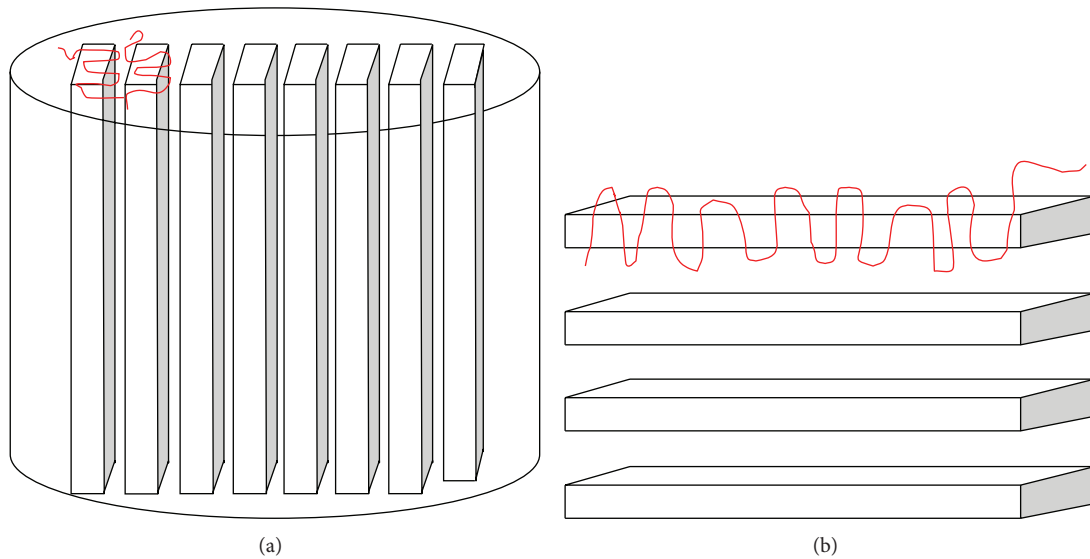


FIGURE 3: Schematic structure of (a) edge-on (b) face-on lamellar structure for films annealed (a) below the melting temperature, (b) above the melting temperature. The red lines are representative of a single PVDF-TrFE molecular chain folding to form crystalline lamellae [15].

commonly attributed to the presence of an internal field or to the asymmetry of the tip/polymer/electrode sample [14]. All films demonstrate ferroelectricity with comparable coercive voltages. As expected, the piezoresponse is highest for the film annealed at 150°C, lowest for the film annealed at 125°C, and intermediate for the film annealed at 150°C.

This trend is consistent with the degree of crystallinity. Moreover, macroscopic polarization voltage hysteresis loops of 550 nm PVDF-TrFE (72/28 mol%) demonstrate a similar trend [12]. The vertical shift in the loops is likely to be caused by nonswitchable dipoles in the film [21]. Contrary to the quality of the switching pattern, the piezoresponse for the film

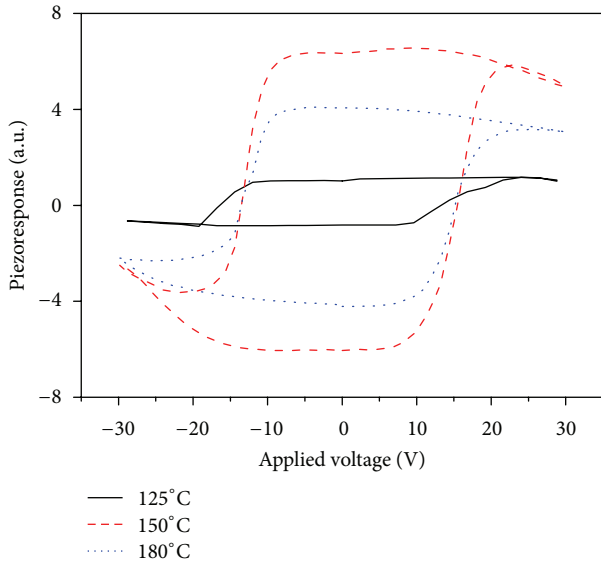


FIGURE 4: Typical piezoresponse hysteresis loops for PVDF-TrFE films annealed at different temperatures.

annealed at 150°C is greater than that for the film annealed at 125°C. This could be caused by a large local variation in piezoresponse for the film annealed at 150°C. Thus, the local hysteresis loop shows good piezoresponse, however, the quality of the switching pattern is not as desirable.

4. Conclusion

The effect of annealing PVDF-TrFE spin-coated films across a broad range of annealing temperatures was studied. For films annealed below the melting point, PVDF-TrFE edge-on crystalline lamellae grains are observed. As the temperature is increased the crystalline grain enlarges as the grains coalesce. Annealing above the melting point drastically changes the morphology since face-on lamellae are formed. Irrespective of the annealing temperature, all the films produced demonstrate polarization switchable domains as evidenced by poling a small square of opposite polarization after background poling. The film annealed at 150°C exhibits the best ferroelectric character due to the quality of the switching pattern and the high local piezoresponse.

Acknowledgment

K. Lau, Y. Liu, and R. L. Withers acknowledge financial support from the Australian Research Council (ARC) in the form of an ARC Discovery Project. Y. Liu thanks the ARC Future Fellowship for funding.

References

[1] E. Edqvist and E. Hedlund, "Design and manufacturing considerations of low-voltage multilayer P(VDF-TrFE) actuators," *Journal of Micromechanics and Microengineering*, vol. 19, no. 11, Article ID 115019, 2009.

[2] T. J. Reece, S. Ducharme, A. V. Sorokin, and M. Poulsen, "Nonvolatile memory element based on a ferroelectric polymer Langmuir-Blodgett film," *Applied Physics Letters*, vol. 82, no. 1, pp. 142–144, 2003.

[3] G. W. Taylor, J. R. Burns, S. M. Kammann, W. B. Powers, and T. R. Welsh, "The energy harvesting Eel: a small subsurface ocean/river power generator," *IEEE Journal of Oceanic Engineering*, vol. 26, no. 4, pp. 539–547, 2001.

[4] T. Okoshi, "New concept of microporous structure in small diameter vascular prostheses," *Artificial Organs*, vol. 19, no. 1, pp. 27–31, 1995.

[5] A. J. Lovinger, "Ferroelectric polymers," *Science*, vol. 220, no. 4602, pp. 1115–1121, 1983.

[6] T. Furukawa, "Structure and functional properties of ferroelectric polymers," *Advances in Colloid and Interface Science*, vol. 71-72, pp. 183–208, 1997.

[7] Y. J. Park, S. J. Kang, C. Park et al., "Irreversible extinction of ferroelectric polarization in P(VDF-TrFE) thin films upon melting and recrystallization," *Applied Physics Letters*, vol. 88, no. 24, Article ID 242908, 2006.

[8] F. Xia, B. Razavi, H. Xu, Z.-Y. Cheng, and Q. M. Zhang, "Dependence of threshold thickness of crystallization and film morphology on film processing conditions in poly(vinylidene fluoride-trifluoroethylene) copolymer thin films," *Journal of Applied Physics*, vol. 92, no. 6, p. 3111, 2002.

[9] M. Bai and S. Ducharme, "Ferroelectric nanomesa formation from polymer Langmuir-Blodgett films," *Applied Physics Letters*, vol. 85, no. 16, pp. 3528–3530, 2004.

[10] F. Xia, B. Razavi, H. Xu, Z.-Y. Cheng, and Q. M. Zhang, "Dependence of threshold thickness of crystallization and film morphology on film processing conditions in poly(vinylidene fluoride-trifluoroethylene) copolymer thin films," *Journal of Applied Physics*, vol. 92, no. 6, p. 3111, 2002.

[11] Z.-G. Zeng, G.-D. Zhu, L. Zhang, and X.-J. Yan, "Effect of crystallinity on polarization fatigue of ferroelectric P(VDF-TrFE) copolymer films," *Chinese Journal of Polymer Science*, vol. 27, no. 4, pp. 479–485, 2009.

[12] W. Li, L. Yu, Y. Zhu et al., "Annealing effect on poly(vinylidene fluoride/trifluoroethylene) (70/30) copolymer thin films above the melting point," *Journal of Applied Polymer Science*, vol. 116, no. 2, pp. 663–667, 2010.

[13] Y. Kim, W. Kim, H. Choi et al., "Nanoscale domain growth dynamics of ferroelectric poly(vinylidene fluoride-co-trifluoroethylene) thin films," *Applied Physics Letters*, vol. 96, no. 1, Article ID 012908, 2010.

[14] Y.-Y. Choi, J. Hong, S. Hong, H. Song, D.-S. Cheong, and K. No, "Nanoscale piezoresponse of 70 nm poly(vinylidene fluoride-trifluoroethylene) films annealed at different temperatures," *Physica Status Solidi*, vol. 4, no. 3-4, pp. 94–96, 2010.

[15] J. S. Lee, A. A. Prabu, and K. J. Kim, "Annealing effect upon chain orientation, crystalline morphology, and polarizability of ultra-thin P(VDF-TrFE) film for nonvolatile polymer memory device," *Polymer*, vol. 51, no. 26, pp. 6319–6333, 2010.

[16] G. Teyssedre, A. Bernes, and C. Lacabanne, "DSC and TSC study of a VDF/TrFE copolymer," *Thermochimica Acta*, vol. 226, pp. 65–75, 1993.

[17] G. Teyssedre, A. Bernes, and C. Lacabanne, "Cooperative movements associated with the Curie transition in P(VDF-TrFE) copolymers," *Journal of Polymer Science, Part B*, vol. 33, no. 6, pp. 879–890, 1995.

- [18] G. Teyssedre, M. Grimau, A. Bernes, J. J. Martinez, and C. Lacabanne, " α -Relaxation/retardation mode in semicrystalline polymers with flexible chains," *Polymer*, vol. 35, no. 20, pp. 4397–4403, 1994.
- [19] K. El-Hami, A. Ribbe, S. Isoda, and K. Matsushige, "Structural analysis of the P(VDF/TrFE) copolymer film," *Chemical Engineering Science*, vol. 58, no. 2, pp. 397–400, 2003.
- [20] K. Kimura, K. Kobayashi, H. Yamada, T. Horiuchi, K. Ishida, and K. Matsushige, "Orientation control of ferroelectric polymer molecules using contact-mode AFM," *European Polymer Journal*, vol. 40, no. 5, pp. 933–938, 2004.
- [21] Y. Kim, W. Kim, H. Choi et al., "Nanoscale domain growth dynamics of ferroelectric poly(vinylidene fluoride-co-trifluoroethylene) thin films," *Applied Physics Letters*, vol. 96, no. 1, Article ID 012908, 2010.

Research Article

Phase Relations in $\text{Ba}_{6-3x}\text{Ln}_{8+2x}\text{Ti}_{18}\text{O}_{54}$ (Ln = Nd & Sm) Electroceramics

Amanda L. Snashall,¹ Yun Liu,¹ Frank Brink,² Ray L. Withers,¹ and Steven Cooper³

¹ Research School of Chemistry, Australian National University, Acton, Australian Capital Territory 0200, Australia

² Centre for Advanced Microscopy, Australian National University, Acton, Australian Capital Territory 0200, Australia

³ Mesaplexx Pty. Ltd., 31 Kurilpa Street, West End, Brisbane, Queensland 4101, Australia

Correspondence should be addressed to Yun Liu; yliu@rsc.anu.edu.au

Received 31 May 2013; Accepted 28 July 2013

Academic Editor: Danyang Wang

Copyright © 2013 Amanda L. Snashall et al. This is an open access article distributed under the Creative Commons Attribution License, which permits unrestricted use, distribution, and reproduction in any medium, provided the original work is properly cited.

A careful, systematic investigation of $\text{Ba}_{6-3x}\text{Ln}_{8+2x}\text{Ti}_{18}\text{O}_{54}$ (BLnTss) ceramics has been performed in order to understand the relationship between composition, microstructure evolution, and microwave dielectric properties. In this paper, we report the effects of composition, morphology, and sintering time on the phase relations and properties of BLnTss (Ln = Nd, Nd/Sm, Sm) ceramics. The microwave dielectric properties of the materials are reported in addition to phase characterisation and structural analysis via X-ray diffraction and field emission scanning electron microscopy coupled with energy dispersive X-ray spectroscopy. BLnTss, $x = 0.33$, ceramics with high Sm content are found to experience a severe degradation of Qf and changes in τ_{cf} trending, associated with the onset of globular and needle-like grain morphology and a Ba-Ti rich phase. $x = 0.67$ ceramics with high Nd content are found to exhibit a secondary phase ($\text{Nd}_2\text{Ti}_2\text{O}_7$) upon prolonged sintering which resulted in beneficial changes to Qf and τ_{cf} without affecting ϵ_r . Two BLnTss ceramics compositions with near-zero τ_{cf} were successfully synthesised with high Qf and ϵ_r values.

1. Introduction

Dielectric ceramics are fundamental building blocks of modern microwave telecommunications technology, being widely used as resonators in filters, phase shifters, and dielectric resonator antennas [1]. $\text{Ba}_{6-3x}\text{Ln}_{8+2x}\text{Ti}_{18}\text{O}_{54}$ solid solutions (BLnTss, Ln = lanthanide) in ceramic form have attracted significant interest since their discovery in 1968 [2] and subsequent investigation in 1981 [3] due to their high dielectric permittivity (ϵ_r), comparatively high quality factor (Qf), and moderate temperature coefficient of resonant frequency (τ_{cf}) at microwave frequencies [4].

The tungsten bronze-type structure of these BLnTss ceramics is composed of corner sharing blocks of TiO_6 -octahedra of perovskite-like structure. These perovskite-like blocks are in turn corner-connected to one another leading to three distinct potential locations for Ba and Ln cation insertion, forming channels running parallel to the

b-axis; 12-coordinate rhombohedral sites (A1-sites within the perovskite-like block regions) preferentially occupied by Ln^{3+} cations, 15-coordinate pentagonal sites (A2-sites) preferentially filled with Ba^{2+} , and 9-coordinate trigonal sites (C-sites) that remain vacant due to their restrictive size [5]. In order to form the upper limit of the $\text{Ba}_{6-3x}\text{Ln}_{8+2x}\text{Ti}_{18}\text{O}_{54}$ solid solution, Ba^{2+} substitutes for Ln^{3+} and vacancies on A1-sites, while the lower limit of the solid solution is determined by excessive vacancy formation in the A1- and A2-sites which destabilises the BLnTss structure. The dielectric properties of BLnTss ceramics vary substantially with the Ba/Ln ratio as well as with the selection of the lanthanide, as each results in a distortion of the ideal structure and its resultant properties [6]. BLnTss ceramics with Ln = La, Pr, and Nd have been reported to display a positive τ_{cf} while Ln = Sm, Eu, and Gd display negative τ_{cf} [5]. BLnTss compounds combining lanthanides with opposite τ_{cf} characteristics have been found

to form a final product with a near-zero τ_{cf} when mixed in correct proportions [7], resulting in high commercial demand for compounds of this type [8].

It is noteworthy that the BLnTss system does not have a well-defined crystallisation temperature [9] and its X-ray diffraction patterns are rather too complicated to determine the phase composition, with common secondary phases “masked” by superposition of main diffraction peaks. As a result, there is some uncertainty surrounding the solid solubility limits for both the Ln = Sm and Ln = Nd analogues of $Ba_{6-3x}Ln_{8+2x}Ti_{18}O_{54}$ [9]. In this paper we report the effects of composition, sintering temperature, and time on the properties of BLnTss (Ln = Nd, Sm, and Nd-Sm) ceramics. A careful, systematic investigation is performed to build a relationship between composition, microstructure evolution, and microwave dielectric properties. This investigation, particularly, focuses on changes in morphology and the effects of prolonged annealing, which had previously been shown to result in unexplained cell parameter and dielectric properties variation deserving of further attention [10].

2. Materials and Methods

$Ba_{6-3x}(Nd_{1-y}Sm_y)_{8+2x}Ti_{18}O_{54}$ electroceramics were synthesised via solid state reaction using $BaCO_3$ (>2N, May and Baker), Nd_2O_3 (3N, Pi-KEM), Sm_2O_3 (3N, Pi-KEM), and TiO_2 (4N, PiKEM, 20 nm). The reported solid solution range of BLnTss (Ln = Sm, Nd) compounds is approximately $0.25(5) \leq x \leq 0.75(5)$ [8, 11–13]; therefore the compositions investigated in this paper were $x = 0.33, 0.5, 0.67$, henceforth referred to as compositions A, B, and C, respectively. To observe the effects of varying the size of the lanthanide, for each composition A, B, and C, samples for $y = 0, 0.2, 0.4, 0.6, 0.8, \text{ and } 1$ were synthesised, henceforth referred to as A0, A2, A4, and so forth. All starting materials were thoroughly dried prior to weighing, with Nd_2O_3 and Sm_2O_3 undergoing an additional high temperature (1000°C) treatment prior to weighing to minimise stoichiometric errors due to the formation of $Ln_xO_y(OH)_{3x-2y}$.

Reagents were mixed in appropriate ratios, ball-milled for 12 hours under ethanol (polyoxymethylene canisters, stabilised ZrO_2 balls) and then dried in an oven to vaporise residual milling solvent. These powders were then sieved to a particle size $<125\ \mu\text{m}$ and calcined at 1100°C for 4 hours in air. Individual cylindrical samples were formed via 5 tonne anisotropic pressing using polyvinyl alcohol as a binding agent. Batches of each composition were subsequently sintered at temperatures between 1250 and 1375°C on platinum foil within an alumina crucible. To promote solid-state reaction characteristics and mitigate potential compositional variation effects, nanoscale TiO_2 was used as a starting reagent, and a minimum sintering period of 4 hours was selected [14, 15]. The optimum sintering temperature was found to be 1375°C with samples of each composition sintered for 4 hours (e.g., A0-4) and 60 (e.g., A0-60) hours to observe the effects of prolonged heat treatment. Densification was determined via the Archimedes method.

Phase composition was investigated via XRD (Siemens D-5000). Field emission scanning electron microscopy (FESEM) was used to characterise both morphology (Zeiss UltraPLUS FESEM) and phase distribution (Hitachi 4300SE/N FESEM). Quantitative analyses were undertaken via electron probe microanalysis (EPMA on Hitachi: 15 kV, 600 pA) with $Nd_2Ti_2O_7$, SmP_5O_{14} , and $BaSO_4$ used as calibration standards.

A network analyser (Agilent E5062A) was used to characterise microwave dielectric properties based on the TE_{011} resonant mode. Q values were calculated using “QZERO for Windows”. The dielectric constant (ϵ_r) was obtained using a 3D finite element analysis (FEA) *eigenmode* solver. The temperature coefficient of resonant frequency (τ_{cf}) was calculated via the relation $\tau_{cf} = \Delta f / f \Delta T$ (ppm/K).

3. Results and Discussion

All A-Series samples were initially identified as single phase via XRD. Sintered surface morphology displayed a significant increase in density with prolonged sintering time (Figures 1(a) and 1(b)) and increasing Sm content (Figures 1(a), 1(c), and 1(d)). All A-series samples displayed the formation of columnar-type grains characteristic of BLnTss ceramics, in good agreement with previous reports [9, 10]. Smooth “globular” shaped grains (indicated in Figure 1(c)) were evident in A-series samples with $y \geq 0.4$, and needle-like characteristics were observed for some grains within the $y = 1.0$ sample (as indicated in Figure 1(d)). SEM backscatter imaging displayed distinct differential contrast between the columnar grains typical of BLnTss and the needle-like grains observed for A10-4 (Figure 1(e)) and A10-60, indicating the presence of a secondary phase.

EPMA compositional analysis of both the main phase and the contrasting phase was undertaken on the “as-sintered” surface of the A10-60 sample. Due to the restrictive grain size of the darker contrast regions, an exact composition could not be determined; however these areas indicated increased levels of Ba and Ti and a significant reduction in Sm content when compared with the main phase (Table 1 (a)-(b)). In order to better identify the phase nature of the needle-type morphology grains, the A10-60 sample was polished and reexamined.

When polished, there was no detectable secondary phase in the A10-60 sample at low-to-medium magnification, with spot and area analyses confirming the nominal stoichiometry within the limits of experimental error. At high magnification, FESEM images were compared with the corresponding backscattered images (Figure 2(a)), to reveal darker patches almost indistinguishable at maximum backscatter detector contrast. Due to their small surface area, EPMA quantitative analysis of these darker areas was not feasible; however spot analysis (Table 1 (c)-(d)) concentrated on such grain regions and surface mapping (Figures 2(b)–2(d)) of the sample revealed the existence of regions rich in Ba and Ti, with reduced Sm content when compared to the main phase. These results, in good agreement with the EPMA compositional analysis of the as-sintered surface, indicate the presence of

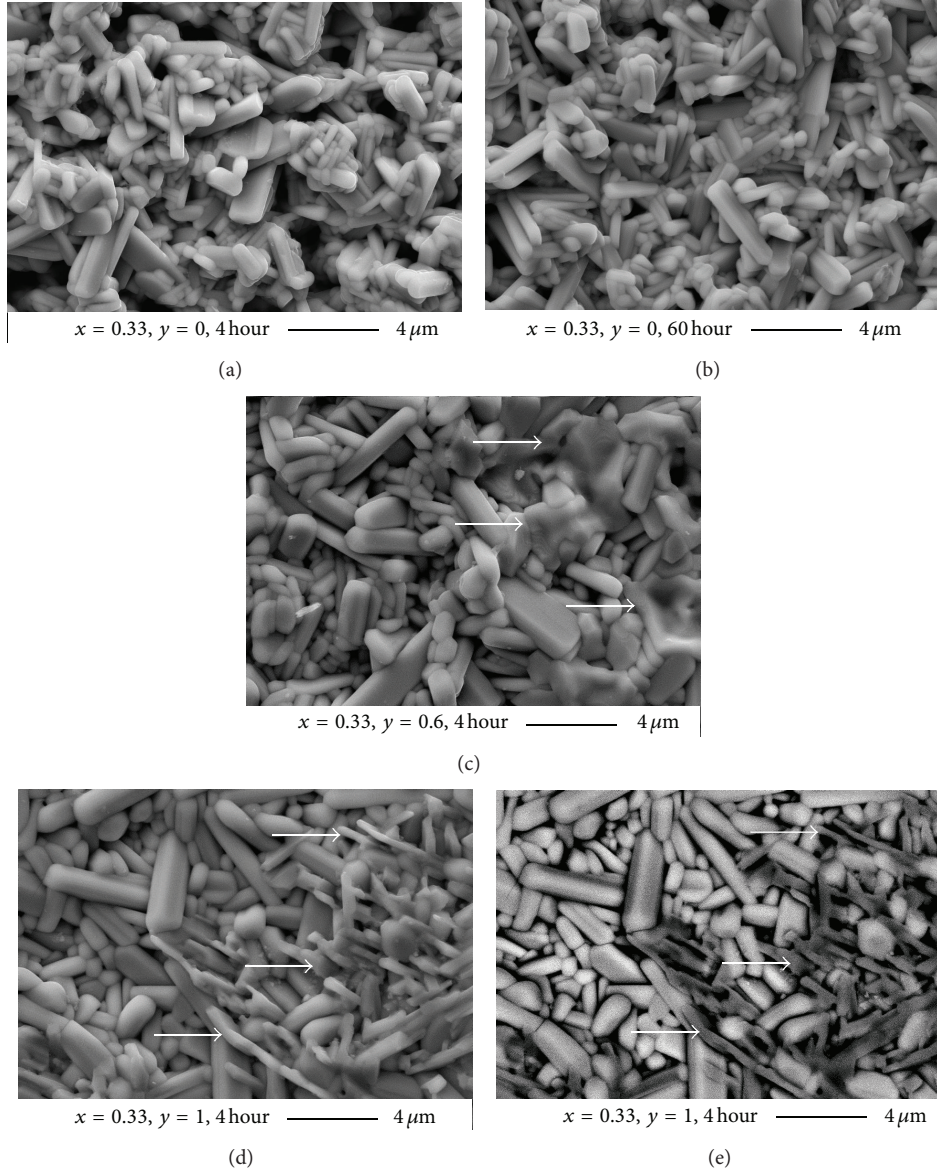


FIGURE 1: SEM images of $x = 0.33$ samples sintered at 1375°C for either 4 or 60 hours. Secondary electron images of (a) A0-4, (b) A0-60, (c) A6-4, and (d) A10-4 and matching backscattered electron images for (e) A10-4.

TABLE 1: EPMA quantitative results for A10-60 sample, for “as-sintered” (a, b) and polished surfaces (c, d).

Area under analysis	Surface type	Ba [At. %]	Sm [At. %]	Ti [At. %]
(a) Column-like (BSE lighter)	As-sintered	5.72 (9)	10.36 (13)	20.89 (16)
(b) Needle-like morphology (BSE darker)*	As-sintered	8.29 (11)	3.55 (51)	24.85 (37)
(c) BSE light contrast region	Polished	5.68 (14)	10.20 (12)	21.05 (10)
(d) BSE dark contrast region*	Polished	12.49 (1.19)	5.21 (74)	20.66 (18)

* Analysis represents a composite of the main phase and the dark contrast region due to restrictive grain size.

a Ba/Ti-rich secondary phase, either extremely poor in or completely devoid of Sm, and not previously reported for this composition. This secondary phase was unable to be further defined, as grain size limited the effectiveness of EPMA analysis, while the complex nature of the main phase X-ray diffraction pattern concealed this Bi/Ti-rich secondary phase.

Figure 3(a) presents the microwave dielectric properties of the A-series samples. For $y = 1$, both the A10-4 and A10-60 samples were found to correlate well with the reported dielectric properties for single-phase Sm-BLnTss, with an extremely low Q_f , a moderate ϵ_r , and a highly negative τ_{cf} measured [16]. The Q_f and τ_{cf} of the A-Series samples

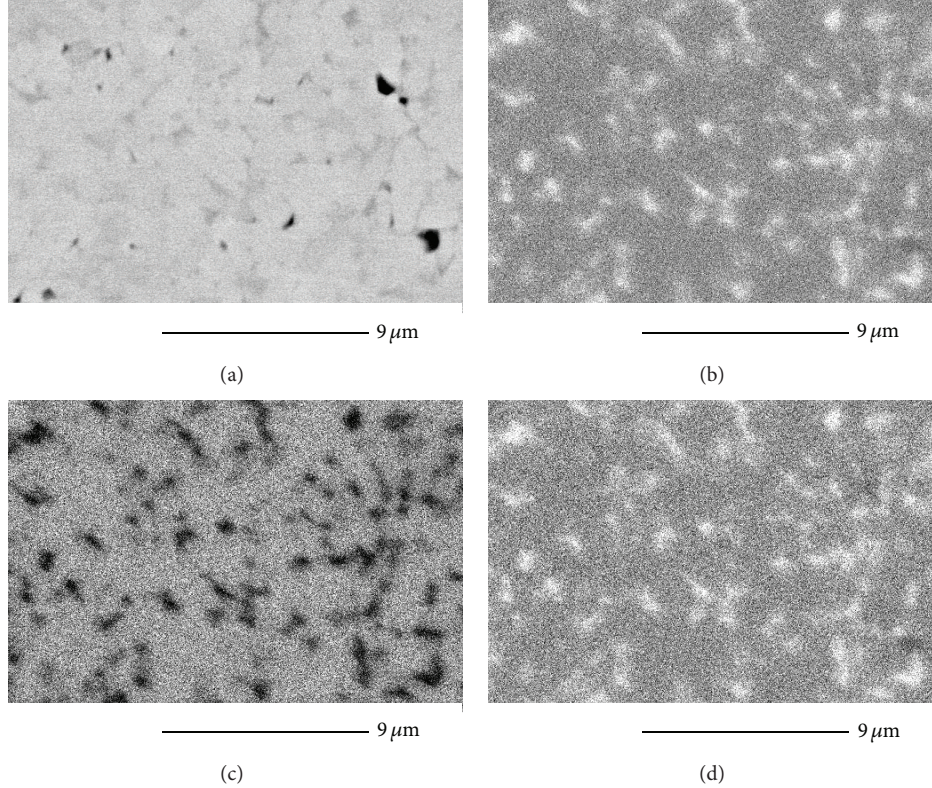


FIGURE 2: (a) SEM backscatter image and matching EPMA surface elemental mapping for (b) Ba, (c) Sm, and (d) Ti content for the A10-60 sample revealing the Ba- and Ti-rich secondary phase contained within the A10-60 sample. Brighter contrast in (b), (c), and (d) indicates a higher proportion of that element in comparison with darker areas.

display a nonlinear deterioration in Qf and a considerable decrease in τ_{cf} with increasing Sm content. The negative trend in τ_{cf} observed as Sm content increases originates from the contrasting contributions of the positive τ_{cf} Nd-BLNtss analogue and the negative τ_{cf} Sm-BLNtss analogue. The primary driver behind these differing τ_{cf} contributions is attributed to the TiO_6 octahedral tilting resultant from Nd and Sm positioning within the perovskite-like matrix of BLNtss [17].

It was found that Qf significantly deteriorated for $y \geq 0.4$ compositions, and the near-linear slope of τ_{cf} was altered for the same range of compositions (Figure 3(a)). These changes appear to correlate well with the appearance of noncolumnar grain morphologies for these samples (Figures 1(c)-1(d)). Qf begins to degrade as globular grains become apparent, with deleterious effects amplifying with increasing proportions of noncolumnar grain shapes. It is therefore suggested that this degradation in Qf is primarily due to the heterogeneous nature of the phase composition and morphologies in these samples, (i.e., significant variations in composition and a strong deleterious effect of the Ba/Ti-rich second phase). The composition and dielectric characteristics of this Ba/Ti-rich secondary phase are worth investigating further.

The dielectric constant was found to increase slightly with increased Sm content (y -value). Generally speaking, the introduction of smaller isovalent lanthanides (Sm) within the tungsten bronze-type structure results in a lower

dielectric permittivity, as the smaller average cell volume decreases the magnitude of potential off-centre Ti ion displacements within the TiO_6 octahedral framework [9]. Accordingly, increased Sm content should lower the dielectric permittivity of BLNtss ceramics. Our results exhibit a different trend, however, with the dielectric permittivity of BLNtss increasing with Sm content. As dielectric permittivity is also highly dependent on the extent to which the sample has undergone densification and crystallisation [1], this is attributed to similar polarisation of both end-members as reported previously [16] and a significant increase in densification observed in the Sm-rich compositions.

With increased sintering time, all A-series samples demonstrated an improved Qf as well as a change in value of τ_{cf} for each composition. An improved linearity of the τ_{cf} transition from positive to negative is also observed with increased sintering time. Improvements in Qf are attributed to an increase in crystallisation, homogenisation of grain size and composition, and a reduction in grain-boundary defects. This is evidenced by improved densification, a reduction in the proportion of globular and needle-like grains, and an observed change in the distribution of the Ba/Ti-rich secondary phase with prolonged sintering. The dielectric constant of the BLNtss ceramics remains almost unchanged as a function of sintering time, suggesting that the samples have been well sintered during the 4-hour sinter and have

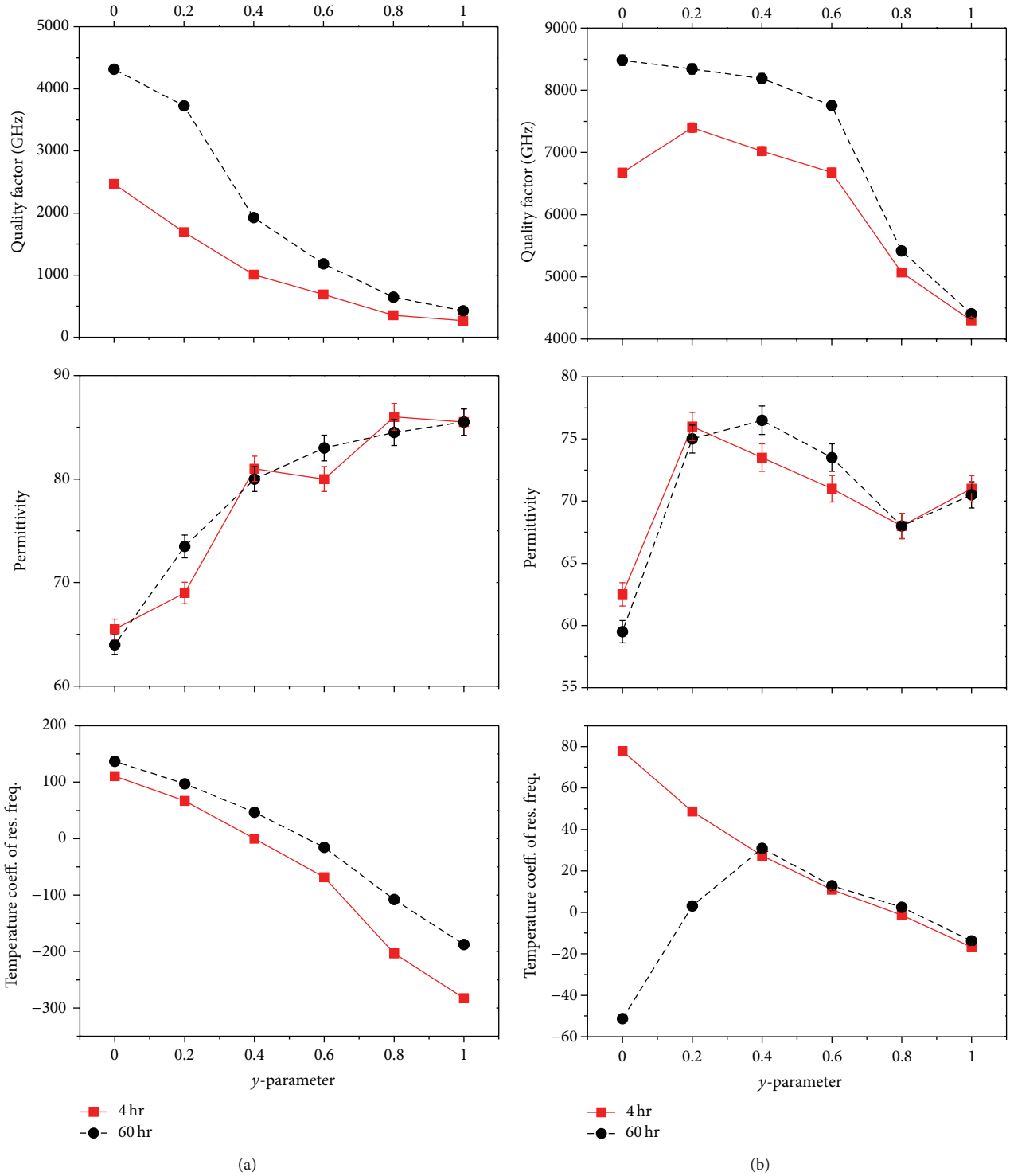


FIGURE 3: Microwave dielectric properties of $\text{Ba}_{6-3x}(\text{Nd}_{1-y}\text{Sm}_y)_{8+2x}\text{Ti}_{18}\text{O}_{54}$ samples (a) A-Series ($x = 0.33$) and (b) C-Series ($x = 0.67$), sintered for 4 hours (red, solid line) and 60 hours (black, dashed line) at 1375°C . Error bars are displayed for all measurements; however in some cases error range is smaller than data points.

primarily undergone compositional homogenisation over the prolonged sintering period.

C-Series BLnTss samples sintered for 4 hours (Figure 3(b)) also displayed a nonlinear degradation in Qf, a

slight increase in ϵ_r , and a considerable decrease in τ_{cf} with increasing Sm content. Prolonged sintering of C-Series samples was shown to significantly improve crystallisation of Nd-rich samples, while little change was observed for the

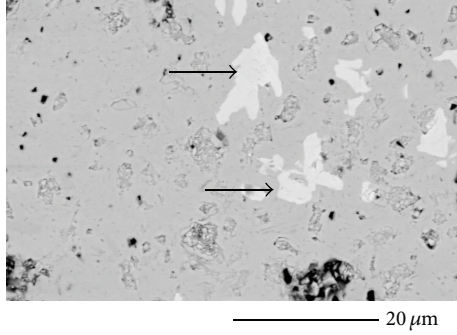


FIGURE 4: Polished BSE SEM image of C0-60 displaying secondary phase ($\text{Nd}_2\text{Ti}_2\text{O}_7$).

Sm-Rich samples. With prolonged sintering there were two significant changes in dielectric properties observed for the C0-60 and C2-60 samples: a significant improvement in Qf and a distinct change in the τ_{cf} characteristics.

All C-Series samples were initially identified as single phase via XRD. Further investigation via SEM analysis revealed that while the Nd-rich 4-hour samples were single phase, the 60-hour samples displayed segments of distinctly different backscatter contrast (Figure 4) for low Sm content compositions (C0-60 to C6-60). The higher the proportion of Nd in the 60-hour samples, the higher the amount of observed secondary phase. EPMA analysis of these areas confirmed the presence of a secondary phase ($\text{Nd}_2\text{Ti}_2\text{O}_7$).

$\text{Nd}_2\text{Ti}_2\text{O}_7$ has been reported to have a lower permittivity than BLnTss ($\epsilon_r = 36$), a higher quality factor (Qf = 16,400), and a highly negative temperature coefficient ($\tau_{cf} = -118$ ppm/K) [18]. Improvements in Qf for C-Series Nd-rich samples undergoing extended sintering are therefore attributed to improved crystallisation, a reduction in grain-boundary defects due to increased grain size, improved homogeneity of the main BLnTss phase composition, and excretion of a high-Qf secondary phase. The observed changes in τ_{cf} with prolonged sintering indicate that the highly negative τ_{cf} of $\text{Nd}_2\text{Ti}_2\text{O}_7$ compensates for the positive τ_{cf} of BLnTss, Ln = Nd. Significant improvements in both τ_{cf} and Qf are therefore achieved through the formation of $\text{Nd}_2\text{Ti}_2\text{O}_7$ as a secondary phase.

Prolonged sintering of BLnTss (Ln = Nd) compounds is therefore shown to provide a simplified, one-step method for embedding $\text{Nd}_2\text{Ti}_2\text{O}_7$ into a dense BLnTss matrix. This result effectively enables tuning of the τ_{cf} of BLnTss (Ln = Nd) compounds to near-zero values, whilst improving the density and compositional homogeneity of the primary phase. One multiphase composition with near-zero τ_{cf} was identified for BLnTss prolonged sinter samples; C2-60 with a Qf of 8343, $\epsilon_r = 75$, and a τ_{cf} of +3.0 ppm/K. While previous reports state that $\text{Ln}_2\text{Ti}_2\text{O}_7$ is one of the precursor compounds of BLnTss [9, 15], there has been no suggestion until now that Nd-BLnTss is metastable for the $x = 0.67$ composition. It is suggested that previous investigations have not revealed the metastable nature of Nd-BLnTss $x = 0.67$, due to their use of microscale reagents and shorter sintering periods. It is

proposed that this study, through the use of nanoscale TiO_2 and extended sintering periods, enhanced solid-state reaction characteristics exposing the metastable nature of Nd-BLnT $x = 0.67$.

BLnTss is reported to have the lowest structural strain for the C-Series composition [16], with apparent bond valence values closest to their ideal values for this composition [14]. Through phase segregation of a Nd- and Ti-rich secondary phase, the BLnTss primary phase would move toward a more Ba-rich composition, significantly increasing the global instability index (GII) of the compound based on previous reports [14]. Details of this are worth further investigation.

For B-Series samples, similar trends to the A and C-series samples were observed with regard to improved density and crystallisation with increased Sm content and sintering time. One composition with near-zero τ_{cf} was identified, B8-60 with a Qf of 8044, $\epsilon_r = 76.5$, and a τ_{cf} of +3.8 ppm/K.

4. Conclusions

$x = 0.33$ ceramics with high Sm content were found to experience a severe degradation of Qf and extreme negative trending of τ_{cf} corresponding with the onset of globular and needle-like grain morphology and the formation of a Ba/Ti-rich secondary phase at BLnTss grain-boundary regions. $x = 0.67$ ceramics with high Nd content were found to exhibit a secondary phase ($\text{Nd}_2\text{Ti}_2\text{O}_7$) upon prolonged sintering which resulted in beneficial changes to Qf and τ_{cf} without affecting ϵ_r . Two ceramics compositions with near-zero τ_{cf} were synthesised; $x = 0.5$, $y = 0.8$ (Qf = 8044, $\epsilon_r = 76.5$, and $\tau_{cf} = +3.8$ ppm/K) and $x = 0.67$, $y = 0.2$ (Qf = 8343, $\epsilon_r = 75$, and $\tau_{cf} = +3.0$ ppm/K).

Acknowledgments

Amanda L. Snashall, Yun Liu, and Ray L. Withers thank the Australian Research Council for financial support in the form of ARC Linkage Grants. Amanda L. Snashall is grateful for the funding supplied via her Australian Postgraduate Award Industry scholarship.

References

- [1] M. T. Sebastian, *Dielectric Ceramics For Wireless Communication*, 1st edition, 2008.
- [2] R. L. Bolton, *Temperature Compensating Ceramic Capacitors in the System Barium Oxide-Rare Earth Oxide-Titania*, 1968.
- [3] A. M. Gens, M. B. Varfolomeev, V. S. Kostomarov, and S. S. Korovin, "Crystal-chemical and electrophysical properties of complex titanates of rare earth elements and barium," *Zhurnal Neorganicheskoi Khimii*, vol. 26, no. 4, pp. 896–898, 1981.
- [4] H. Ohsato, "Research and development of microwave dielectric ceramics for wireless communications," *Journal of the Ceramic Society of Japan*, vol. 113, no. 1323, pp. 703–711, 2005.
- [5] D. Suvorov, M. Valant, and D. Kolar, "The role of dopants in tailoring the microwave properties of $\text{Ba}_{6-3x}\text{Ln}_{8+2x}\text{Ti}_{18}\text{O}_{54}$ R = (La-Gd) Ceramics," *Journal of Materials Science*, vol. 32, no. 24, pp. 6483–6488, 1997.

- [6] M. Valant, D. Suvorov, and C. J. Rawn, "Intrinsic reasons for variations in dielectric properties of $Ba_{6-3x}Ln_{8+2x}Ti_{18}O_{54}$ $R = (La-Gd)$ solid solutions," *Japanese Journal of Applied Physics*, vol. 38, no. 5, pp. 2820–2826, 1999.
- [7] H. Ohsato, J. Sugino, A. Komura, S. Nishigaki, and T. Okuda, "Microwave dielectric properties of $Ba_4(Nd_{28/3-y}R_y)Ti_{18}O_{54}$ ($R = Eu, Dy, Ho, Er$ and Yb) solid solutions," *Japanese Journal of Applied Physics*, vol. 38, no. 9, pp. 5625–5628, 1999.
- [8] T. Negas and P. K. Davies, "Influence of chemistry and processing on the electrical properties of $Ba_{6-3x}Ln_{8+2x}Ti_{18}O_{54}$ solid solutions," *Ceramic Transactions*, vol. 53, pp. 179–196, 1995.
- [9] S.-F. Wang, Y.-F. Hsu, Y.-R. Wang et al., "Densification, microstructural evolution and dielectric properties of $Ba_{6-3x}(Sm_{1-y}Nd_y)_{8+2x}Ti_{18}O_{54}$ microwave ceramics," *Journal of the European Ceramic Society*, vol. 26, no. 9, pp. 1629–1635, 2006.
- [10] Y. Li and X. M. Chen, "Effects of sintering conditions on microstructures and microwave dielectric properties of $Ba_{6-3x}(Sm_{1-y}Nd_y)_{8+2x}Ti_{18}O_{54}$ ceramics ($x=2/3$)," *Journal of the European Ceramic Society*, vol. 22, no. 5, pp. 715–719, 2002.
- [11] K. M. Cruickshank, X. Jing, G. Wood, E. E. Lachowski, and A. R. West, "Barium neodymium titanate electroceramics: phase equilibria studies of $Ba_{6-3x}Ln_{8+2x}Ti_{18}O_{54}$ solid solution," *Journal of the American Ceramic Society*, vol. 79, no. 6, pp. 1605–1610, 1996.
- [12] L. Zhang, X. M. Chen, N. Qin, and X. Q. Liu, "Upper limit of x in $Ba_{6-3x}Ln_{8+2x}Ti_{18}O_{54}$ new tungsten bronze solid solution," *Journal of the European Ceramic Society*, vol. 27, no. 8-9, pp. 3011–3016, 2007.
- [13] H. Ohsato, T. Ohhashi, S. Nishigaki, T. Okuda, K. Sumiya, and S. Suzuki, "Formation of solid solutions of new tungsten bronze-type microwave dielectric compounds $Ba_{6-3x}Ln_{8+2x}Ti_{18}O_{54}$ ($R = neodymium$ and $samarium$, $0 < X < 1$)," *Japanese Journal of Applied Physics*, vol. 32, no. 9, pp. 4323–4326, 1993.
- [14] A. L. Snashall, L. Norén, Y. Liu, T. Yamashita, F. Brink, and R. L. Withers, "Phase analysis and microwave dielectric properties of $BaO-Nd_2O_3-5TiO_2$ composite ceramics using variable size TiO_2 reagents," *Ceramics International*, vol. 38, no. 1, pp. S153–S157, 2012.
- [15] A. G. Belous, O. V. Ovchar, M. Valant, and D. Suvorov, "Solid-state reaction mechanism for the formation of $Ba_{6-x}Ln_{8+2x/3}Ti_{18}O_{54}$ ($Ln = Nd, Sm$) solid solutions," *Journal of Materials Research*, vol. 16, no. 8, pp. 2350–2356, 2001.
- [16] H. Ohsato, "Science of tungstenbronze-type like $Ba_{6-3x}Ln_{8+2x}Ti_{18}O_{54}$ ($R = rare\ earth$) microwave dielectric solid solutions," *Journal of the European Ceramic Society*, vol. 21, no. 15, pp. 2703–2711, 2001.
- [17] I. M. Reaney, "Effect of octahedral tilt transitions on the properties of perovskites and related materials," *Ferroelectrics*, vol. 222, no. 1–4, pp. 401–410, 1999.
- [18] J. Takahashi, K. Kageyama, and K. Kodaira, "Microwave dielectric properties of lanthanide titanate ceramics," *Japanese Journal of Applied Physics*, vol. 32, no. 9, pp. 4327–4331, 1993.

Research Article

Effect of Electric Field and Temperature on Average Structure and Domain Wall Motion in $0.93\text{Bi}_{0.5}\text{Na}_{0.5}\text{TiO}_3\text{-}0.07\text{BaTiO}_3$ Ceramic

Jian Wang,¹ Yun Liu,¹ Andrew Studer,² Lasse Norén,¹ and Ray Withers¹

¹ Research School of Chemistry, The Australian National University, Canberra, ACT 0200, Australia

² Bragg Institute, ANSTO, Lucas Heights, NSW 2232, Australia

Correspondence should be addressed to Yun Liu; yliu@rsc.anu.edu.au

Received 3 June 2013; Accepted 24 June 2013

Academic Editor: Danyang Wang

Copyright © 2013 Jian Wang et al. This is an open access article distributed under the Creative Commons Attribution License, which permits unrestricted use, distribution, and reproduction in any medium, provided the original work is properly cited.

In situ neutron powder diffraction patterns and dielectric spectra of $0.93\text{Bi}_{0.5}\text{Na}_{0.5}\text{TiO}_3\text{-}0.07\text{BaTiO}_3$ ceramic were investigated under different electrical fields and temperatures. An electric-field-induced phase transition from metrically cubic to metrically tetragonal, associated with strong domain wall motion, occurs. Such induced phase and domain wall motion are unchanged until the high-temperature phase transition occurs from metrically tetragonal to metrically cubic. All these changes are irrelevant to the observed depolarization temperature (75°C). The depolarization behaviour is thus suggested to be associated with the local structure caused by the octahedral tilt twinning disorder.

1. Introduction

Piezoelectric materials are used in a variety of devices such as stress sensors, ultrasound emitters, and large-strain actuators. The ultrahigh strain (~1.7%) in (001) oriented rhombohedral $\text{Pb}(\text{Zn}_{1/3}\text{Nb}_{2/3})\text{O}_3\text{-PbTiO}_3$ and $\text{Pb}(\text{Mg}_{1/3}\text{Nb}_{2/3})\text{O}_3\text{-PbTiO}_3$ single crystals is suggested to be a result of the electric-field-induced rhombohedral-tetragonal phase transition [1–4]. Lead-free BiFeO_3 films have a reversible electric-field-induced strain of over 5% that arises from moving the boundaries between tetragonal- and rhombohedral-like phases [5]. In fact, such electric-field-induced structural transition is found to be universal in rare-earth-substituted BiFeO_3 [6], resulting from isostructural transitions, disappearance and reappearance of the tilting of the oxygen octahedral, and reentrance into specific crystallographic classes [7]. This phenomenon also occurs in other lead-free piezoelectric material systems [8, 9].

$(1-x)\text{Bi}_{0.5}\text{Na}_{0.5}\text{TiO}_3\text{-}x\text{BaTiO}_3$ (BNTBT) ceramic has been intensively studied as a candidate for lead-free piezoelectric materials due to the high strain that appeared in the morphotropic phase boundary compositions ($0.06 \leq x \leq 0.08$) [10]. Such high strain is suggested to be related

to the electric-field-induced structural changes [11–13]. It is found that BNTBT undergo a ferroelectric to antiferroelectric transition above a so-called depolarization temperature (T_d) above which the piezoelectric properties deteriorate [14]. In this paper, we aim to investigate the variation in the structure and domain texture of $0.93\text{Bi}_{0.5}\text{Na}_{0.5}\text{TiO}_3\text{-}0.07\text{BaTiO}_3$ ($x = 0.07$, abbreviated as BNTBT7 hereafter) ceramic under the electrical field and with increasing temperature via *in situ* neutron diffraction technique in order to understand the relationship between the structural change under the applied electric field and the depolarisation behaviour at elevated temperature.

2. Experimental

BNTBT7 ceramic was synthesized by a solid state reaction. High purity Na_2CO_3 , Bi_2O_3 , BaCO_3 , and TiO_2 were used as starting materials. Mixtures of the starting materials were first ball-milled for 5 h. The dried mixture of powder was then calcined at 800°C for 3 h, followed by ball-milling again for 2 h. The resultant powders were then pressed into pellets under a uniaxial pressure of 200 MPa, using poly(vinyl

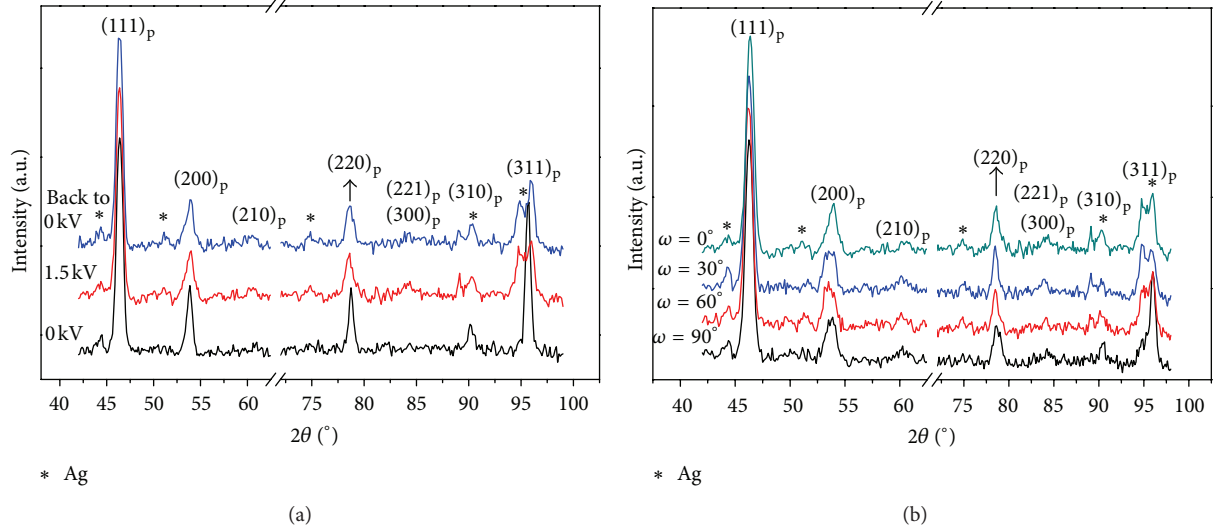


FIGURE 1: Neutron diffraction patterns of BNTBT7 collected at room temperature (a) under different applied electric fields and at $\omega = 0^\circ$ and (b) under 1.5 kV and at different ω angles.

alcohol) as a binder. Finally, the as-sintered ceramics were polished on both sides down to 0.8 mm thickness and coated with silver paste, followed by the heat treatment at 500°C for 5 min. The dielectric properties of the sample were measured using a high precision LCR meter (HP 4284A).

In situ neutron powder diffraction measurements were carried out as a function of applied electric field and temperature. These measurements were completed using the WOMBAT instrument on the OPAL reactor at the Australian Nuclear Science and Technology Organisation (ANSTO). A Ge (115) monochromator was used to select a wavelength of $\lambda = 1.727 \text{ \AA}$. The sample was fixed perpendicular to a central stage on WOMBAT. Conducting wires were attached to the silver coating on either side of the sample to enable a voltage to be applied. The sample was rotated with the cylindrical axis of the stage to vary the angle (ω) between the incident beam and the poling direction from 90° to 0° in 30° increments.

3. Results and Discussion

Figure 1(a) shows the room temperature diffraction pattern of BNTBT7 ceramic collected under different electric fields and at $\omega = 0^\circ$. There is no apparent peak splitting in BNTBT7 prior to the application of electric field, suggesting that its average structure is metrically cubic. Once the electric field is applied (e.g., 1.5 kV), we can see a clear peak splitting in $(200)_p$, $(220)_p$, and $(311)_p$ diffraction peaks, but not in $(111)_p$ peak. This demonstrates a clear phase transition from metrically cubic to metrically tetragonal. Note that both $(113)_p$ and $(311)_p$ peak intensities are almost identical. After, withdrawal of the electric field, their intensities are different, even though the peak splitting profile is retained. This suggests that the metrically tetragonal phase would be partially reversed after the withdrawal of the electric field. Figure 1(b) is the diffraction patterns under an applied electric field of 1.5 kV as a function of ω . There is a clear splitting of $(200)_p$, $(220)_p$, and

$(311)_p$ peaks once ω changes, where the relative intensity of these splitting peaks is different. The results are in accordance with Daniels' work [11]. The applied electric field causes non- 180° domain wall motion, which can be detected using *in situ* neutron diffraction or X-ray diffraction as a consequence of the variation in the relative intensities of some diffraction peaks. For example, a 90° domain switching in tetragonal phase is demonstrated through the relative intensity change, for example, between the (002) and $(200)/(020)$ peaks, or between the $(202)/(022)$ and (220) peaks [15]. It is apparent that the relative intensity of the peak and its shoulder within the $(220)_p$ varies significantly in different situations (at 0 kV and 1.5 kV, and back to 0 kV), indicating that the 90° domain wall motion appears under an electric field and leading to the domain texture-related preferred orientation in the structure as shown in Figure 1(b).

Figure 2(a) shows the dielectric constant and loss tangent of poled BNTBT7 ceramics as a function of temperature. A small jump in the dielectric constant and loss tangent is observed at about 70°C which is regarded as the depolarization temperature T_d for the sample. Figure 2(b) shows *in situ* neutron powder diffraction patterns collected at different temperatures up to 200°C at $\omega = 0^\circ$. Note that a dc bias of 0.5 kV is applied during the measurement to enhance the depolarization effect. The intensity and the profile of the diffraction peaks below 100°C are almost the same. The splitting of $(310)_p$ and $(311)_p$ peaks as well as the shoulders of the $(200)_p$ and $(220)_p$ peaks disappears at 150°C . This indicates that a transition from metrically tetragonal to metrically cubic occurs in the vicinity of this temperature. This phase transition narrows the dielectric polarisation relaxation in the corresponding temperature range (see Figure 2(a)). Figure 2(c) shows the diffraction patterns of the $(311)_p$ peak at different temperatures (room temperature, 75°C , and 100°C) and different ω angles in order to investigate the structural evolution at T_d . For all selected temperatures, the intensity

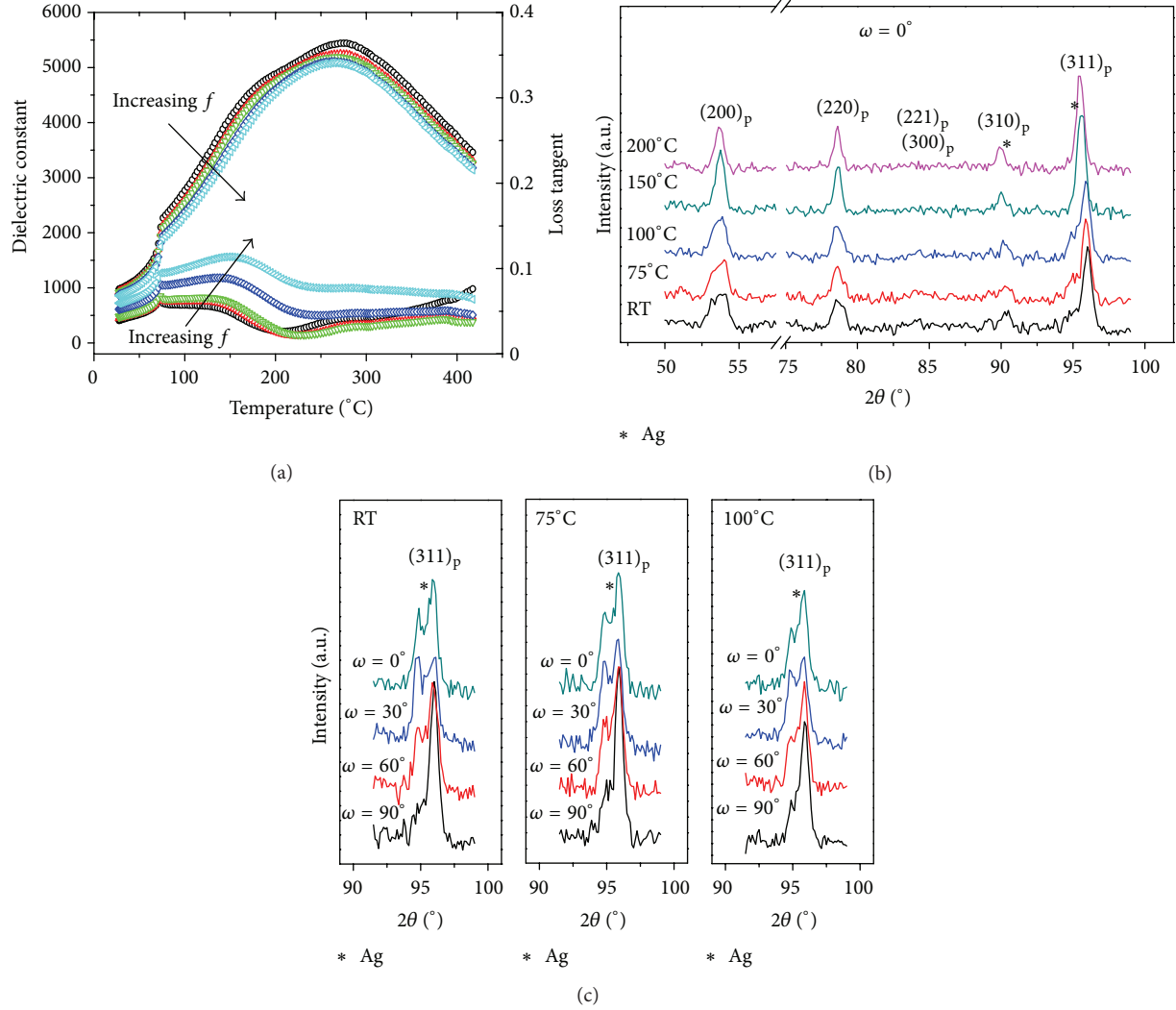


FIGURE 2: (a) Temperature dependence on dielectric spectra of BNTBT7 ceramic and (b) its neutron diffraction patterns at $\omega = 0^\circ$ as well as (c) a typical $(311)_p$ diffraction peak at different temperatures and different ω angles.

of the induced (113) peak (left hand side one) increases with respect to the ω angle and reaches the highest value relative to the (311) peak (right hand side one) at $\omega = 60^\circ$. There is no change in the preferred domain orientation with increasing temperature that can be revealed by neutron diffraction, indicating that the depolarization behaviour is not determined by the domain wall motion. Thus, we conclude that both the average structure and domain wall motion follow the same trend as the temperature increases, and there is no observable difference below and above T_d .

In BNTBT ceramics, the octahedral tilt twin disordering and the resultant orthorhombic $Pnma$ interfacial phase in the material matrix have been reported [14]. As a result, an increasing volume of such local structure with respect to the electrical field results in an observable metrically tetragonal phase. The T_d is irrelevant to or at least not dominated by the average structure and domain wall motion. Taking into consideration its local structure, it is highly possible that the T_d is the balancing sequence of the following

possible co-existing factors: an incomplete poling and/or unpoled parts within the ceramic, which still keep the original metrically cubic phase; the octahedral tilt twinning disorder; and high temperature metrically cubic phase induced with the increasing temperature.

4. Conclusions

An electric-field-induced phase transition from metrically cubic to metrically tetragonal, which is associated with a strong 90° domain wall motion, is observed in BNTBT7 ceramic. The temperature-dependent diffraction patterns show that a high-temperature phase transition from induced metrically tetragonal to metrically cubic occurs between 100°C and 150°C , as the temperature increases. However, neither the average structure nor the domain wall motion induced orientation changes are relevant to the depolarization temperature.

Acknowledgments

Jian Wang, Yun Liu, and Ray Withers acknowledge the financial support from the Australian Research Council (ARC) in the form of an ARC Discovery Grant. Yun Liu also acknowledges support from the ARC Future Fellowships program. Jian Wang, Yun Liu, and Andrew Studer also thank the Australian Institute of Nuclear Science and Engineering (ANSIE) for the financial support to access the national neutron facilities at ANSTO.

References

- [1] S.-E. Park and T. R. Shrout, "Ultrahigh strain and piezoelectric behavior in relaxor based ferroelectric single crystals," *Journal of Applied Physics*, vol. 82, no. 4, pp. 1804–1811, 1997.
- [2] M. Davis, D. Damjanovic, and N. Setter, "Electric-field-, temperature-, and stress-induced phase transitions in relaxor ferroelectric single crystals," *Physical Review B*, vol. 73, no. 1, Article ID 014115, 2006.
- [3] H. Y. Chen, C. S. Tu, C. M. Hung et al., "Poling effect and piezoelectric response in high-strain ferroelectric 0.70Pb(Mg_{1/3}Nb_{2/3})O₃-0.30 PbTiO₃ crystal," *Journal of Applied Physics*, vol. 108, no. 4, Article ID 044101, 2010.
- [4] C. Zhan, J. Wu, S. Yin, and X. Jiang, "Strong, high-frequency, ac electric-field-induced rhombohedra-tetragonal phase transition in Pb(Mg_{1/3}Nb_{2/3})O₃-PbTiO₃ single crystal," *Journal of Applied Physics*, vol. 97, no. 7, Article ID 074107, pp. 1–4, 2005.
- [5] J. X. Zhang, B. Xiang, Q. He et al., "Large field-induced strains in a lead-free piezoelectric material," *Nature Nanotechnology*, vol. 6, no. 2, pp. 98–102, 2011.
- [6] D. Kan, L. Pálová, V. Anbusathaiah et al., "Universal behavior and electric-field-induced structural transition in rare-earth-substituted BiFeO₃," *Advanced Functional Materials*, vol. 20, no. 7, pp. 1108–1115, 2010.
- [7] S. Lisenkov, D. Rahmedov, and L. Bellaiche, "Electric-field-induced paths in multiferroic BiFeO₃ from atomistic simulations," *Physical Review Letters*, vol. 103, no. 4, Article ID 047204, 2009.
- [8] A. J. Royles, A. J. Bell, J. E. Daniels, S. J. Milne, and T. P. Comyn, "Observation of a time-dependent structural phase transition in potassium sodium bismuth titanate," *Applied Physics Letters*, vol. 98, no. 18, Article ID 182904, 2011.
- [9] M. Hinterstein, M. Knapp, M. Hölzel et al., "Field-induced phase transition in Bi_{1/2}Na_{1/2}TiO₃-based lead-free piezoelectric ceramics," *Journal of Applied Crystallography*, vol. 43, no. 6, pp. 1314–1321, 2010.
- [10] T. Takenaka, K. I. Maruyama, and K. Sakata, "(Bi_{1/2}Na_{1/2})TiO₃-BaTiO₃ system for lead-free piezoelectric ceramics," *Japanese Journal of Applied Physics*, vol. 30, no. 9 B, pp. 2236–2239, 1991.
- [11] J. E. Daniels, W. Jo, J. Rödel, and J. L. Jones, "Electric-field-induced phase transformation at a lead-free morphotropic phase boundary: case study in a 93%(Bi_{0.5}Na_{0.5})TiO₃-7%BaTiO₃ piezoelectric ceramic," *Applied Physics Letters*, vol. 95, no. 3, Article ID 032904, 2009.
- [12] H. Simons, J. Daniels, W. Jo et al., "Electric-field-induced strain mechanisms in lead-free 94%(Bi_{1/2}Na_{1/2})TiO₃-6%BaTiO₃," *Applied Physics Letters*, vol. 98, no. 8, Article ID 082901, 2011.
- [13] C. Ma, X. Tan, E. Dul'Kin, and M. Roth, "Domain structure-dielectric property relationship in lead-free (1-x)(Bi_{1/2}Na_{1/2})TiO₃-xBaTiO₃ ceramics," *Journal of Applied Physics*, vol. 108, no. 10, Article ID 104105, 2010.
- [14] Y. Guo, Y. Liu, R. L. Withers, F. Brink, and H. Chen, "Large electric field-induced strain and antiferroelectric behavior in (1-x)(Na_{0.5}Bi_{0.5})TiO₃-xBaTiO₃ ceramics," *Chemistry of Materials*, vol. 23, no. 2, pp. 219–228, 2011.
- [15] J. L. Jones, "The use of diffraction in the characterization of piezoelectric materials," *Journal of Electroceramics*, vol. 19, no. 1, pp. 67–79, 2007.